Dynamics in stellar chromospheres

Candidatus Scientiarum Thesis

Roar Skartlien
Institute of Theoretical Astrophysics, Oslo

May 1994

Preface

I have been fascinated by astronomy since I was a teenager. I joined the local astronomy club (GOTAF) as an amateur astronomer, where we could share each others knowledge and experiences. After a few years I decided to take a further step in this direction. I started to study astronomy and physics at the University of Oslo. This candidatus scientiarum thesis is the product of this education. My interest for astronomy has grown considerably during this time at the University.

There is a star 150 million km. from the Earth in the center of the solar system that reveal wondrous things even in small telescopes. We may also pick up photons from stars at enormous distances compared to the distance to our Sun. A key to understand the stars around us is to learn the meaning of the photons we receive from the Sun. I will make some attempts to understand the dynamics in stellar chromospheres in this thesis on the basis of solar observations and numerical models.

I wish to thank professor Mats Carlsson for sharing his insights in the field of stellar atmospheres, and for being my supervisor. Mats Carlsson and Robert Stein are thanked for letting me work with their radiation-hydrodynamic models. The professors Egil Leer and Jan Trulsen are thanked for stimulating and fruitful lectures in astrophysics. Franz Kneer is thanked for constructive suggestions and illuminating ideas during a discussion of the solar chromosphere. Rob Rutten and Bruce Lites are thanked for letting me work with their observational data of the Sun.

The computations were supported by a grant from the Norwegian Research council, Tungregneutvalget.

Roar Skartlien

Institute of Theoretical Astrophysics, Oslo, May 1994.

The *cover picture* is a spectroheliogram of the solar chromosphere, revealing the "bright grains" of singly ionized calcium. These are seen as the smallest bright dots, and they originate from specific chromospheric wave patterns. Much attention has been given to the bright grains in this thesis. The spectroheliogram was taken by Bruce Gillespie with the east auxiliary of the McMath Solar Telescope, National Solar Observatory.

Contents

1 Introduction

Almost all of the information we receive from a star is in the form of electro-magnetic radiation. The energy contained in this radiation is originally released in the stellar interior by nuclear fusion. The energy is transported from the interior by radiation, convection and conduction. Finally the energy flux enters the stellar atmosphere, where photons are created, destroyed and scattered as they interact with the plasma. At last the photons escape into space, and information about the star propagates with the speed of light to other parts of the Universe. Some of these light quanta enters the astronomers telescope, and the information can be decoded.

It is necessary to understand the physical processes in stellar atmospheres, in order to understand this information. The physics of thermodynamics, quantum physics, radiation magneto-hydrodynamics and plasma physics are included in this field of astrophysics. Astrophysical topics that are closely connected to this area are stellar evolution and solar physics. Since our own sun is easy to observe compared to the stars, it has been the main laboratory for understanding stellar atmospheres.

The field of stellar atmospheres has until recently been dominated by static, plane-parallel models. Many conclusions have been based on this assumption. The introduction of a chromospheric temperature rise, microturbulence to explain the widths of spectral lines, determination of element abundances for cosmological theories, and determination of wave phase velocities and modes of oscillation in the solar atmosphere are a few examples.

Observations have revealed inconsistencies in solar static models. Spectral lines formed by solar carbon monoxide indicate that the time-, and spatially averaged temperature above the temperature minimum decrease towards the chromosphere. Other spectral lines and the continua indicate a temperature rise. This has been interpreted as a non-homogeneous composition in the horizontal direction (a bifurcation), making the one-dimensional model a poor assumption.

The assumption of a static plane-parallel (one-dimensional) atmosphere is at best a very crude one. A first step towards a better understanding is to extend the static models to dynamic ones. In the future, the computers will be fast enough so that it will be practical to take into account all three dimensions. This is important in order to determine if one-dimensional models are able to represent the three-dimensional world.

Dynamic signatures are observed in solar spectral lines. The five-minute p-mode oscillations in the photosphere are an observational fact. Theories have been developed to explain these phenomena of low velocity amplitude, and these are theories of perturbation on a static atmosphere, ie. linear theories. This approach has been successful in the photospheric layers where the velocity amplitudes are small compared to the speed of sound. Together with the theory of helioseismology, the five-minute p-mode observations have been explained as exitation of the eigenmodes of the sun by the motions in the convection zone.

A fraction of the wave energy that is generated by the convection zone penetrates the temperature minimum region. The waves are propagating into the low-density chromosphere where radiating shock-trains of high Mach number are formed. Especially the calcium lines H and K reveal Doppler-fluctuations of such shock waves. The bright-grains

of calcium are also a product of such non-linearities.

Energy can be extracted from these waves, by e.g. dissipation at the shock fronts. The energy input or heating from this process serves to rise the average chromospheric temperature above the radiative equilibrium value. This can be indirectly observed in continua, and spectral lines. The chromosphere in semiempirical models is identified as the temperature rise and the temperature plateau above the temperature minimum. This also requires heating, but a semiempirical model can not give any explanation for dynamic heating mechanisms because it is static. The strong non-linear perturbations in the solar chromosphere rises the question of whether or not semiempirical models can be used to estimate the magnitude of chromospheric heating, and if they can be used to constrain dynamic heating mechanisms.

Temperature changes of several thousand Kelvin occurs on very short height scales when shocks are present. A definition of the chromosphere as a semiempirical temperature plateau above the temperature minimum with small dynamic perturbations imposed, is thus quite suspect if the purpose of the model is to help us gain insight in the dynamic and non-linear solar chromosphere.

How can the dynamic behavior of the outer low density layer of a stellar atmosphere be analyzed from observations of spectral lines? It is obvious that we have to reproduce some of the observed behavior by using a dynamic model that is built on relevant physics. Only then can the atmospheric behavior be understood. We will then also be able develop diagnostic methods that link specific signatures of observations to the corresponding dynamic behavior. As the waves enter the chromosphere, we are leaving the linear regime. Non-linear models are then required. As far as we know, the only way to do this is to make numerical simulations of the complete dynamic equations involved. These equations describe mass motion and photon interactions. Such simulations have been carried out, and results from these are analyzed in this thesis.

Some important problems have developed since the dawn of solar physics and the field of stellar atmospheres. A few examples are:

1. What are the dynamic properties of stellar atmospheres?

2. To what extent can spectral lines be used to reveal the dynamic properties?

3. What are the sources of chromospheric heating?

4. To what extent can we use static models to understand chromospheric heating and the formation of spectral lines?

Dynamic self-consistent simulations will illuminate and probably solve these problems that have not yet been fully understood. We have to restrict ourselves to a few problems in this thesis, and these are summarized here:

1. It is common to use the radiative cooling (radiative losses) in a semiempirical model to constrain the heating mechanisms of the solar chromosphere. The validity of this assumption is investigated.

We determine the different dynamic heating terms that balances the dynamic radiative cooling. We compare the time average of the dynamic cooling with the semiempirical cooling to determine the correspondence between semiempirical and dynamic cooling. We also determine the cooling distribution among lines and continua in both dynamic and static models.

2. The H2V and K2V bright grains in the CaII lines can be seen in spectroheliograms. It has been thought that these features directly reveal fundamental dynamic properties of the solar chromosphere.

   We are able to reproduce these grains rather well by one of our models. The physics responsible for the bright grains is explained by using this model. We also make some prospects for bright grain diagnostics that can be used to determine some aspects of chromospheric dynamics.

3. The time dependent behavior of the CaII spectral lines has been used as a diagnostic tool for solar chromospheric dynamics. The assumptions necessary to interpret this dynamic behavior have been based on linear wave theory.

   One of our non-linear dynamic models is capable of reproducing the observed time resolved CaII profiles rather well. An interpretation of the phase relations between Doppler shifts and intensities in the line cores is thus given in terms of non-linear dynamics. A comparison with interpretations of observed phase relations made by other authors is done.

4. Many attempts have been made by several authors to reproduce line profiles formed in the solar chromosphere by semiempirical models. Dynamics in the chromosphere will certainly influence the temporally and spatially averaged solar profiles which can not be fully accounted for by using semiempirical or static models.

   We determine the line profile responses to different microturbulent velocities in both dynamic and semiempirical models. Then we investigate if it is possible to fit semiempirical line profiles to the averaged profiles by using micro- and macroturbulence or mesoturbulence. The dynamic properties that control the shape of the time averaged simulated profiles of the CaII lines are determined.

Section 2 describes the properties of the two dynamic models we use and the methods to obtain them. These models have recently been developed by Mats Carlsson and Robert F. Stein, and we study only the simulation results in this thesis. We give an overview of the methods and the code (RADYN) used to solve the radiation-hydrodynamic equations. Further calculations with another code (MULTI) on the resulting dynamic atmospheres are needed to examine the effects of different microturbulence and to calculate contribution functions. This code is also described. One model is heated by acoustic waves only and it is used in section 6. We denote it by the *acoustically heated model.* The other model includes an additional heating term and it is used in section 7. We denote it by the *pre-heated model.* Its physical properties are denoted by *shock perturbation on constant heating.*

We give a description of the hydrogen model atom and the CaII model atom in section 3.

We develop a method to produce semiempirical models from a given continuum spectrum. This is used on the dynamic models to compare static and dynamic quantities. The method can be used on solar and stellar spectra as well. A description of the method is given in in section 4, and we use it in sections 6 and 7.

We review some radiative transfer theory in section 5, and we use the results in sections 6 and 7.

The semiempirical model of the acoustically heated model is given in section 6.1. The semiempirical and the dynamic energy balance of the acoustically heated model are discussed in section 6.2.

Section 7.1 reviews the observed temporal behavior of the CaII H-line. The simulated profile of the pre-heated model reproduces most of the observed behavior. We thus explain the physics of the H2V bright grains in the simulation, and connect the findings to chromospheric dynamics in section 7.2.

An interpretation of the phase relations between the CaII lines is given in section 7.3.

The semiempirical model of the pre-heated model is given in section 7.4. A comparison between semiempirical line profiles and time averaged line profiles produced by the pre-heated model is given in section 7.5.

Section 8 gives a summary of the results.

2 Dynamic models and methods

First, we describe the two dynamic models we use, and we give the motivation for choosing these models. Then we give an overview of the methods implemented in the RADYN radiation-hydrodynamics code (Carlsson & Stein 1992b), and of the physics involved. We use another program, MULTI (Carlsson 1986), on the RADYN atmospheres to calculate contribution functions. The application of this code is also briefly described.

2.1 The two models

The dynamic models are made for the purpose of investigating vertical propagation of acoustic waves in the solar atmosphere, and the interactions between dynamics and radiation. The models are one-dimensional and plane parallel. Only vertical acoustic wave propagation can then be studied. It is assumed that electrons and ions have Maxwellian distributions at equal temperatures, and we assume that both species move with the same velocity.

Magnetic fields and plasma physics are left out to reduce the complexity of the problem. The dynamic behavior without magnetic fields should be understood to begin with. The models can thus at best describe non-magnetic regions of the sun and other stars.

Both models are exited by moving pistons with realistic velocities as a lower boundary. In this way we simulate the convective motions in the lower photosphere. It is assumed that no other form of exitation occurs. The waves propagate from the photosphere to the chromosphere. As the density of the atmosphere falls rapidly above the temperature minimum, the phase velocities of the wave approaches the speed of sound. High density parts of the wave overtake the low density parts such that shocks are formed in the chromosphere.

Shock formation in upper layers of stellar atmospheres was first proposed by Biermann (1946) and by Schwarzschild (1948). Further discussions can be found in e.g. Stein & Schwartz (1972). The atmospheric structure with the propagation and development of shocks can be seen for one of our models in figure 1 and 2.

The specific properties and the applications of the two models are:

1. *The acoustically heated model.*

   This model is included to investigate the energy balance during the influence from acoustic waves and shocks only. A semiempirical model is made from this model to study differences between semiempirical and dynamic radiative losses (cooling), and the differences between the cooling distributions between lines and continua.

   A heating term is added to the energy equation in the lower photosphere to account for the convective heat flux. This heating term is deduced from the mixing length theory for convection. We use radiative equilibrium as an initial condition in the chromosphere.

   The chromosphere is heated due to the dissipative properties of the shocks, and external compression work. This heating will slowly rise the atmospheric mean temperature and thus the internal energy. Increased radiative cooling will eventually

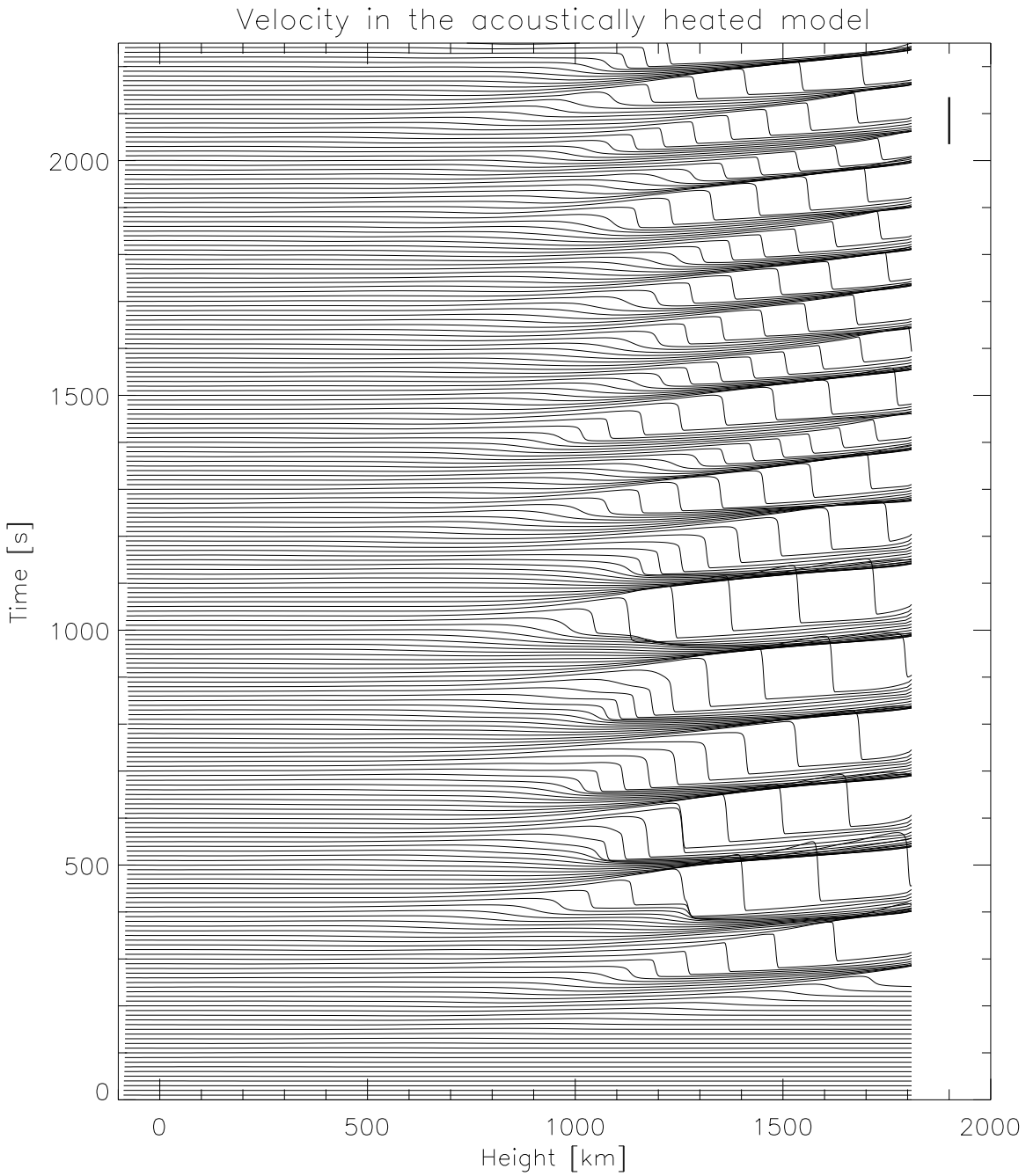

Figure 1: The macroscopic velocity as a function of height and time in the acoustically heated model. The velocity curves are shifted a step upwards at each time step. The time steps are 10 seconds apart. The velocity differences between pre- and post shock regions are typically 20km/s in chromospheric layers. The bar in the upper right corner shows a velocity difference of 20km/s.

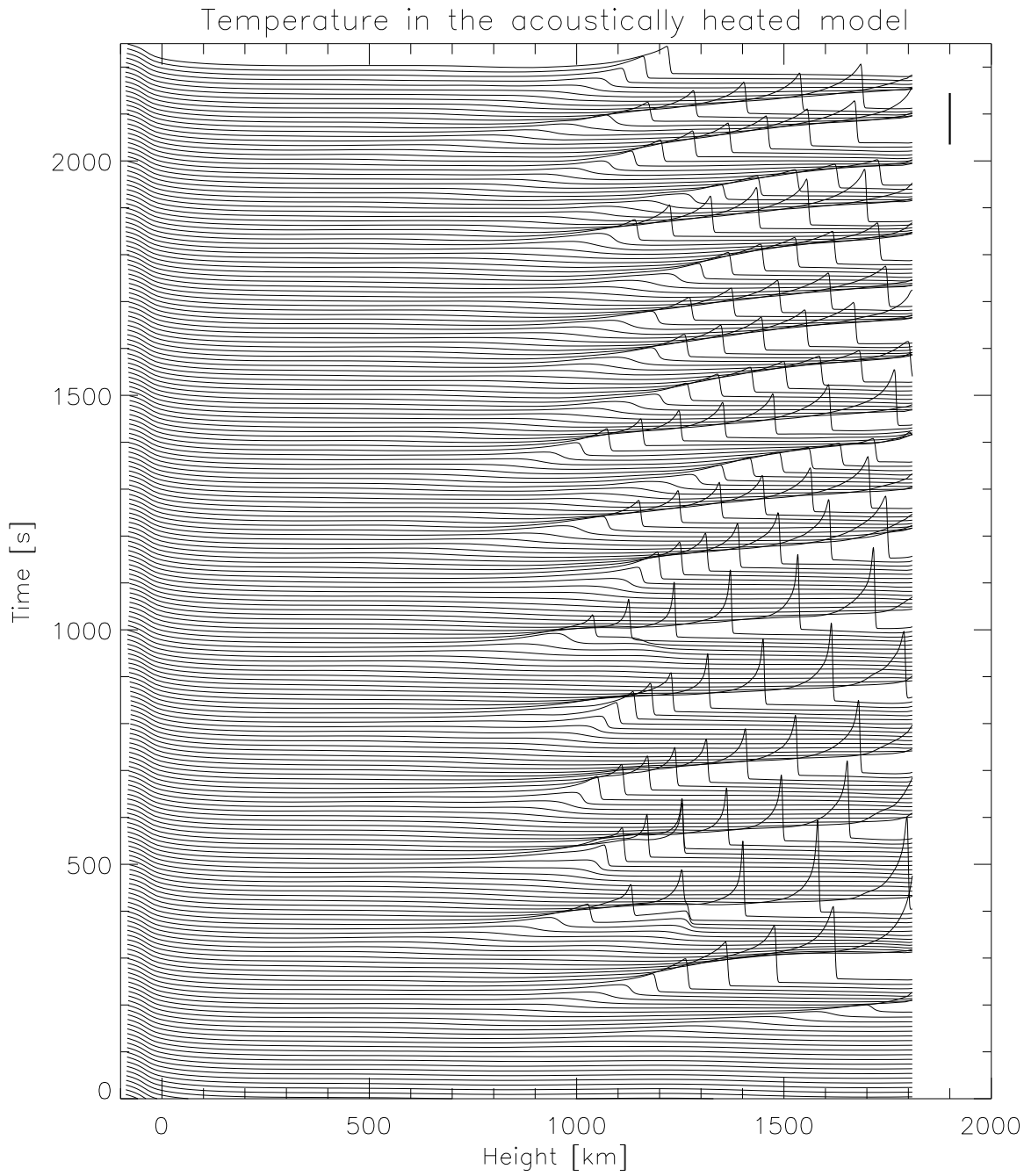

Figure 2: The temperature as a function of height and time in the acoustically heated model. The temperature curves are shifted a step upwards at each time step. The time steps are 10 seconds apart. The temperature differences between pre- and post shock regions are typically 10000K in chromospheric layers. The bar in the upper right corner shows a temperature difference of 10000K.

balance the heating such that a quasi-static state is achieved. This relaxation time is longer than the duration of the simulation.

2. *The pre-heated model.*

   We assume that the quasi-static state can be approximated by introducing an artificial heating term which accounts for increased internal energy compared to the acoustically heated model.

   Another justification for extra heating is that this model reproduces some of the evolution patterns in the solar CaII lines in regions of weak magnetic fields, such as the bright grains in the H and K lines and the line core excursions and intensity fluctuations. It is important that some of the observed details are reproduced, such that we can assume dynamic conditions comparable to those in the solar chromosphere.

   A temperature structure similar to VAL3C (Vernazza et al. 1981) without a transition region was used as an initial condition. To make the initial atmosphere consistent with the energy equation, the radiative losses are calculated and an equal heating term is added. This term is kept constant on the Lagrangian frame (column mass scale) during the simulation.

   We denote the chromospheric physical properties of this model by *shock perturbation on constant heating.*

2.2 Simulation methods

2.2.1 Methods of the RADYN simulations

The lower boundary is a reflecting piston located 100 km below $\tau_{5000} = 1$ with prescribed velocity as a function of time. The velocity is taken from the Doppler shifts from solar observations of the photospheric FeI line at λ3966.8Å (Lites et al. 1993). This is in the wing of the CaII H-line. The Doppler measurements are taken from a location where H2V bright grains occurs. The same velocity field is used for both models.

The line core is formed at approximately 280 km above $\tau_{5000} = 1$. The observed velocity amplitude is thus scaled with the expected amplitude difference between the height of formation and the height of piston location. The amplitudes with oscillation periods longer than 5 minutes are damped in the upwards direction. The low frequency amplitudes are thus amplified to compensate for this damping. This velocity field is assumed to be representative for the upper layer of the convection zone.

The piston could not be located at the formation height of the FeI line due to difficulties with too small optical depths at those wavelengths that are formed deepest is the photosphere.

The upper boundary is transmitting. Only a small fraction of the wave energy is reflected. The material that has crossed this boundary is lost as "stellar wind". We have not included a transition region. The one-dimensional conservation equations of:

1. Mass

2. Charge
3. Momentum
4. Energy

are solved together with the equations of:

1. Radiative transfer
2. Statistical equilibrium (NLTE rate equations)

These equations are given in the appendix. The equations are set up using an implicit finite difference scheme, and they are formulated on an adaptive grid (Dorfi & Drury 1987). The grid point locations are solved for together with the rest of the equations. The grid equation is set up such that the grid points gather where there are large gradients, thus giving maximum resolution where it is needed. This approach, together with artificial viscosity resolves the shock structure. The time steps of the computation are controlled by the rate of change of the variables. The advection terms in the equations are treated using Van Leer's second order upwind scheme (Van Leer 1977) to ensure stability and monotonicity in the presence of shocks.

The rate equations are dominated by radiative transitions. The radiative rates are proportional to the mean intensity which in general depends on the population densities over the whole atmosphere through the radiative transfer. The motions and the temperature structure of the atmosphere affect the density and population numbers. Thus a global time dependent NLTE coupling is introduced by the radiative transfer which is treated using Scharmer's method (Scharmer 1981, Scharmer & Carlsson 1985, Carlsson 1986).

The energy equation couples radiative heating of the material, viscous dissipation, conduction, and external compression work to the internal energy of the gas. This energy is in the form of exitation energy, ionization energy and thermal energy.

The main contributor from calcium in the solar photosphere and chromosphere is CaII. The great diagnostic potential of the H,K and IR lines, and their large contribution to radiative losses from the chromosphere are the reason to include CaII in the simulation. Hydrogen is the main contributor of radiative losses in in the upper chromosphere.

The NLTE radiation is treated with five level plus continuum model atoms for hydrogen and calcium (CaII). All bond-bound transitions and the five bound-free transitions are treated in detail for each atom. The H,K and the IR lines for CaII are treated, and the Lyman, Balmer, Paschen, Pfundt, and Brackett levels for hydrogen are included. Voigt line profiles with complete redistribution (CRD) are assumed for all lines. The Lyman line profiles are truncated at six Doppler widths to mimic effects of partial redistribution (PRD) (Milkey & Mihalas 1973). Constant microturbulence on a column mass scale was included in the RADYN simulations to account for observed line broadening and H2V bright grain displacement from the line center.

Other elements are included as electron donors and in the continuum opacity. These are all treated in LTE.

The simulations were run on a CRAY Y-MP 464. A typical simulation of 2000 seconds in solar time takes approximately 50 CPU hours, and about 200 Mbytes of output data are produced. All RADYN runs have kindly been provided by Carlsson and Stein.

2.2.2 Methods of the MULTI simulations

The MULTI program solves the radiative transfer for an impurity spices in moving or static atmospheres (Carlsson 1986). Scharmers' method is also applied in this code (Scharmer 1981, Scharmer & Carlsson 1985).

The radiative transfer of other elements than those included in RADYN can be calculated in NLTE by MULTI. One atom at a time can be treated. Each time step from the RADYN simulation produces an atmosphere which contains the temperature structure, electron densities, velocity field, microturbulence and hydrogen densities and populations. This atmosphere will then be input to the MULTI simulations together with the selected atom.

Secondary calculations on the RADYN atmospheres with CaII are needed to obtain contribution functions to intensity, and relative absorption. They are also needed to alter the microturbulent broadening of the CaII line profiles to determine its effect on time averaged profiles. The MULTI calculations are also necessary in obtaining a time averaged reference spectrum in the continua for the semiempirical computations. All of the static computations involved to obtain semiempirical temperature structures are done with MULTI.

It is assumed that CaII with altered microturbulence can be treated as an impurity spices, i.e. that it will not have any significant impact on the dynamics if it was included in the RADYN simulations. This is justified, since the same CaII model atom was run in the RADYN simulations. The advection term in the rate equations is not included in MULTI. This will give only minor changes in the radiative transfer, less than the effect of altered microturbulence.

3 Atomic models

3.1 Hydrogen

The hydrogen model includes five energy levels from n=1 to n=5 plus a continuum level. These are the Lyman, Balmer, Paschen, Pfundt and Brackett levels. All ten bound-bound transitions and the bound-free transitions are given the full NLTE treatment. The energy levels with bound-bound and bound-free radiative transitions are shown in figure 3. Wavelengths above 2000Å are given as air wavelengths, and wavelengths below 2000Å are given in vacuum.

Level energies were taken from Bashkin & Stoner (1975). Radiative bound-bound transition probabilities come from Johnson (1972), bound-free Gaunt-factors from Karzas & Latter (1961) and Menzel & Pekeris (1935), and collisional transition probabilities from Vriens & Smeets (1980).

3.2 CaII

The CaII model includes five energy levels plus a continuum level, which give rise to the H and K lines and the IR triplet. The bound-bound and bound-free transitions are given the full NLTE treatment. The energy levels with bound-bound and bound-free radiative transitions are shown in the Grotrian diagram in figure 4. Level energies and other atomic data were taken from Shine & Linsky (1972).

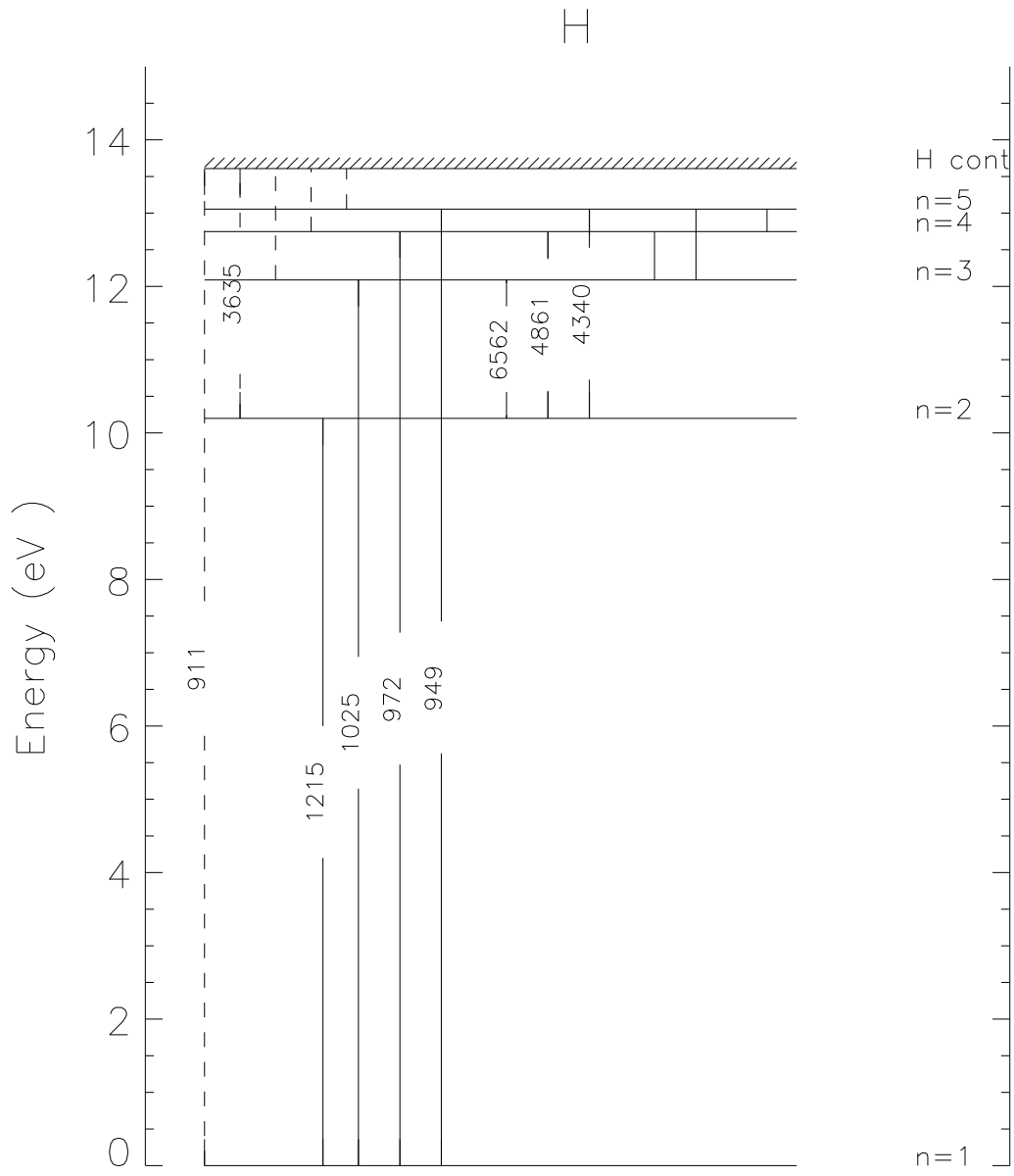

Figure 3: The hydrogen model atom. The wavelengths for the radiative transitions are given in Ångström. Dashed lines are bound-free transitions, and solid lines are bound-bound transitions.

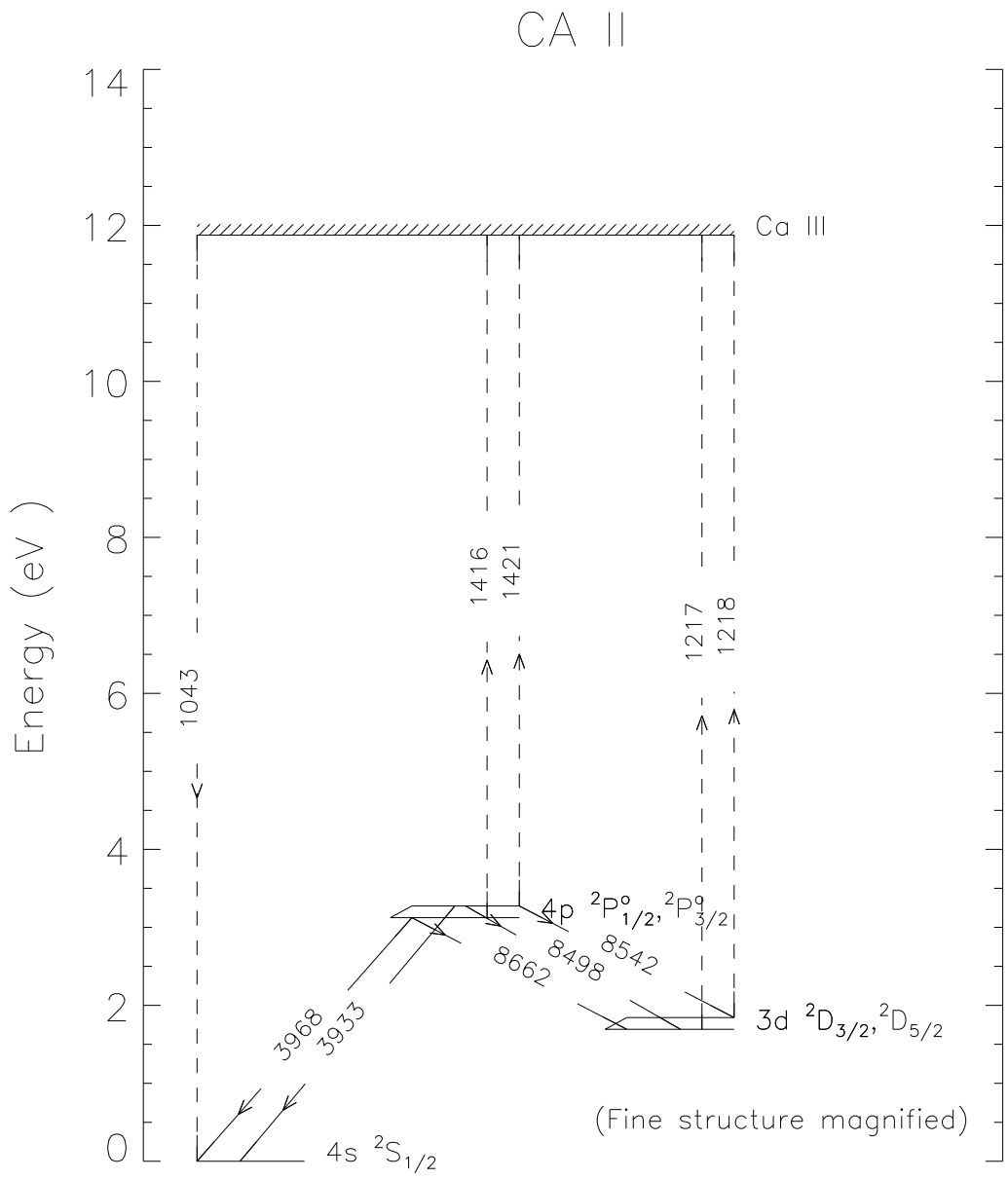

Figure 4: The calcium model atom. The wavelengths for the radiative transitions are given in Ångström. Dashed lines are bound-free transitions, and solid lines are bound-bound transitions.The H line arise from the 3968Å transition, the K-line from the 3933Å transition, and the IR triplet from the 8498Å ,8542Å and 8662Å transitions. Only collisional rates can occur between the metastable D-levels and the ground level.

4 The semiempirical method

In this section we describe the methods used to construct a semiempirical atmosphere. These methods are applied on the dynamic models in sections 6 and 7 to construct their corresponding semiempirical models. In these sections we compare semiempirical interpretations of energy balance and spectral lines with dynamic interpretations.

We follow the standard method of replacing the equation of radiative equilibrium by a temperature structure that reproduces the averaged continuum spectrum of the dynamic stellar atmosphere. The average is spatial and temporal in the case for semiempirical models of the solar atmosphere (Vernazza et al. 1981). In this thesis we produce semiempirical models of one-component dynamic models. We therefore use the temporally- or time averaged continuum spectrum. We hereafter denote the time averaged continuum spectrum as the reference spectrum for the semiempirical model. The methods described here are general, and they can be applied on observed stellar continuum spectra as well.

First, we make some considerations about the connections between spatially and temporally averaged reference spectra, and about the connections between temperature and continuum intensity. Second, we give an overview of the semiempirical calculations, and we give a detailed description of the semiempirical iteration method needed to obtain a close agreement with the reference spectrum. Third, we describe the constraints used to get a smooth and monotone temperature structure. Finally we give the methods needed to calculate the accuracy of the obtained temperature structure.

4.1 Connections between spatially and temporally averaged reference spectra

An exposure of short duration of a specific area of the sun contains different small scale features at different positions. We can construct a semiempirical model by averaging the spectrum over areas with similar features, e.g. internetwork areas where magnetic fields are relatively weak. This approach has been used for the VAL model of the solar atmosphere (Vernazza et al. 1981). This model consists of several different components, A to F, that each represents different characteristic areas. Model F is averaged over the magnetically active areas and model A over granular cell interiors (internetwork areas). Model C represents the average quiet sun over all areas. One can assume that the dynamic behavior does not change much from point to point in such areas. One could then in principle obtain the same reference spectrum by the time average of a sufficiently long time series of a relatively small area.

This is the approach when a semiempirical model of a dynamic model is constructed, since dynamic models so far only are plane parallel or one-dimensional. Dynamic plane parallel models are one-component models in the same sense as plane parallel semiempirical models. The typical horizontal length scale for thermodynamic changes and for changes in the radiation field of the real solar atmosphere must be greater than its thickness if the temporally averaged spectrum of a plane parallel dynamic model is a physically reasonable description for a spatially averaged area of the sun.

We are not able to take into account horizontal inhomogeneities on scales shorter than the thickness of the atmosphere, since our dynamic models are plane parallel. This limitation can only be overcome by three dimensional dynamic models. We have therefore not made any attempts to reproduce semiempirical solar models. Instead, we treat the dynamic model as the actual atmosphere, and thereafter we study the ability of the semiempirical model to describe the dynamic "reality".

4.2 Continuum intensities and atmospheric temperatures

It is important to notice that the time averaged intensity is sensitive to the wavelength range when LTE conditions dominate. This will often be the case for continuum radiation. In the Wien-limit (ultraviolet) the Planck function responds exponentially to the temperature, and in the Rayleigh-Jeans-limit (infrared) it responds linearly.

If the continuum intensities are formed under LTE conditions, in both semiempirical and dynamic atmospheres, the temperatures at the formation heights of UV-wavelengths will be overestimated in the semiempirical model.

One can thus not expect that the static temperature structure is an accurate time averaged measure of the dynamic temperature, especially if the dynamic perturbations are great relative to the ambient atmosphere. Such great perturbations occur in chromospheric layers due to shock formation. Relatively small perturbations occur in the photosphere, and modelling in the IR range will in addition serve to make the photospheric temperatures of a semiempirical model a reasonable estimate of the time average.

The assumptions above will be altered in NLTE. NLTE effects in the continua will be introduced for singly ionized calcium and hydrogen which are treated self-consistently in the dynamic simulations, and for hydrogen in the semiempirical model.

4.3 An overview of the semiempirical calculations

The static calculations require wavelength points that cover continuum radiation formed in the deepest layers in the photosphere (infrared) and up to the highest layers of the chromosphere (ultraviolet). The points are located in pairs below and above opacity edges for 81 bound-free transitions. Table 1 gives the wavelengths and the associated elements. All the points in the chromosphere lie in the EUV (extreme ultraviolet) or UV (ultraviolet) range, as for the VAL models. Modelling in the IR (infrared) part of the spectrum at these heights would serve as a test for consistency of the semiempirical method. UV and IR modelling should give the same temperature structure. This is not done here.

The radiation temperatures of the reference spectrum and the semiempirical spectrum are calculated according to the Planck distribution for black-body radiation at each frequency point. The differences between the radiation temperatures at each point is taken as a measure of the temperature deviation at the corresponding continuum formation height. These differences are then used to adjust the temperature structure to get a better agreement between the reference radiation temperature and the semiempirical radiation temperature. This process is thus iterative. The continuum radiation emerging from the atmosphere with the corrected temperature structure is calculated by the program MULTI.

Ion	Wavelength above edge [Å]	Wavelength below edge [Å]
H-	16450.00	16250.00
HI	8208.00	8206.00
MgI	3757.00	3755.00
H	3648.00	3646.00
MgI	2515.00	2513.00
FeI	2488.00	2486.00
FeI	2335.00	2333.00
FeI	2269.00	2267.00
FeI	2267.00	2265.00
AlI	2071.00	2069.00
SiI	1986.00	1984.00
FeI	1943.00	1941.00
FeI	1769.00	1767.00
SiI	1682.00	1680.00
MgI	1623.00	1621.00
FeI	1576.00	1574.00
SiI	1521.00	1519.00
CI	1240.00	1238.00
CaII	1219.00	1216.00
SI	1201.00	1199.00
MgII	1170.00	1168.00
SiII	1128.00	1122.00
CI	1101.00	1099.00
HI	913.00	911.00
HeI	505.00	503.00

Table 1: 81 continuum wavelengths are used in the semiempirical modelling. 50 of these are located at each side of the 25 absorption edges of bound-free transitions given in the table. The remaining are intermediate wavelengths from 17000Å to 300Å used to obtain an even distribution. *Wavelength below edge* denote the short wavelength side of the opacity edge. *Wavelength above edge* denotes the long wavelength side of the opacity edge. The helium continuum on the short wavelength side of 504Å was not taken into consideration in the determination of the temperature corrections due to neglected helium ionization in the dynamic model.

Hydrogen is calculated in NLTE and the rest of the elements are calculated in LTE. Hydrostatic equilibrium integrations (HSE) provide consistency between temperature and densities.

The sensitivity and response to temperature change in the static models are difficult to predict. This is due to non-local coupling of radiation (NLTE) through the atmosphere and global changes due to hydrostatic equilibrium integrations. With this view in mind the temperature corrections will only be approximate, unless one is able to get the exact response functions which is unlikely due to the non-linearity of the problem.

A multi-dimensional Newton-Raphson iterative process solves this problem. If the approximate temperature corrections always are in the right direction and decreasing in magnitude as the iterations goes on, we will eventually have a solution. The problem of finding the suitable temperature corrections will therefore be to find the approximate radiation temperature response functions to atmospheric temperature change.

4.4 The response matrix

The radiation temperature deviations at all frequency points in continuum have to be used in order to get maximum information about the atmospheric temperature deviations. The radiation temperature response functions to temperature change connects the deviations in radiation temperature to atmospheric temperature corrections. We get a linear set of equations with the temperature corrections as unknowns. The coefficients of these equations are called the response matrix. The radiation temperature response function is defined by Magain (1986):

$$\delta T_R(\nu) = \int_{-\infty}^{\infty} R_{T_R,T}(\nu, x)\delta T(x)dx \tag{1}$$

where $x = lg(column\ mass)$. It is reasonable to assume that the normalized contribution function to intensity is a reasonable choice of a response function, since the contribution function to intensity peaks where the sensitivity to atmospheric temperature is maximum. We define:

$$R_{T_R,T}(\nu, x) = \frac{C_{I_\nu}(x)}{I_\nu} \tag{2}$$

The integral over depth must be replaced by a sum in order to create the linear equations we are seeking. The pair (ν, x) is replaced by the indexes of frequency and depth (j, i):

$$\delta T_{R,j} = \sum_{i=1}^{N} \frac{C_I(j,i)}{I_j}\delta T_i \Delta x_i = \sum_{i=1}^{N} A_{i,j}\delta T_i \tag{3}$$

Which is equivalent to:

$$\delta\vec{T_R} = [A]\delta\vec{T} \tag{4}$$

$A_{i,j}$ will then be the matrix elements in the response matrix $[A]$.

One finds that the contribution functions to intensity are very similar as a function of depth for neighboring frequency points. This will then also be the case for the response functions. This leads to similar matrix coefficients in neighboring rows, and the matrix becomes singular.

This problem is solved by replacing the response functions by delta functions of unity value at depths which are closest to their centroids. The previous notation of the equations is unchanged by using these delta functions.

This leads to some matrix columns with zeroes only, and these are removed from the matrix. The depth grid will now be undersampled compared to the original resolution. The resulting matrix contains elements of unity value. There is one element for each frequency index, and one or more for each depth index.

The number of unknown temperature corrections will be smaller than the number of frequency points. The resulting response matrix has dimensions (N, M) where $M > N$.

4.5 The solution method

$\delta\vec{T}$ is solved by the least squares method by using the normal equations of linear algebra since we have an overdetermined set of equations. We will then obtain temperature corrections that minimizes the radiation temperature deviation over the whole spectrum.

The best solution vector $\delta\vec{T}$ is the one that minimizes the residual:

$$\Omega = \sum_{j=1}^{M}[\delta T_{R,j} - \sum_{i=1}^{N} A_{i,j}\delta T_i]^2 = [\delta\vec{T_R} - [A]\delta\vec{T}]^2 \tag{5}$$

The value of Ω can be used as a measure of convergence in the iterative procedure. One finds the solution effectively by LU decomposition and back-substitution of the set:

$$[A]^T[A]\delta\vec{T} = [A]^T\delta\vec{T_R} \tag{6}$$

Which is equivalent to:

$$[W]^*\delta\vec{T} = -\delta\vec{T_R} \tag{7}$$

We denote $[W]^*$ by the approximate operator.

4.6 The iteration procedure

The atmospheric response to temperature can be written as an operator equation. The solution of the temperature structure is determined by the radiation temperature of the reference spectrum $\vec{T}_{R_0}$:

$$[W]\vec{T} = \vec{T}_{R_0} \tag{8}$$

A current estimate of the temperature, $\vec{T}_n$ gives a deviation $\delta\vec{T}_{R,n}$ from the reference radiation temperature:

$$[W]\vec{T}_n = \vec{T}_{R_0} + \delta\vec{T}_{R,n} \tag{9}$$

Let $\delta\vec{T}_n$ be the correction to obtain the solution $\vec{T}$. We then have:

$$[W](\vec{T}_n + \delta\vec{T}_n) = \vec{T}_{R_0} \tag{10}$$

Subtraction of the last two equations gives:

$$[W](\vec{T}_n + \delta\vec{T}_n) - [W]\vec{T}_n = -\delta\vec{T}_{R,n} \tag{11}$$

By linearizing the exact operator $[W]$ to $[W]^*_n$, and assuming small atmospheric temperature changes $\delta\vec{T}_n$, we have:

$$[W]^*_n\delta\vec{T}_n \approx -\delta\vec{T}_{R,n} \tag{12}$$

The approximate operator $[W]^*_n$ is indexed by n since it changes after each iteration. Let $\delta\vec{T}_n$ be defined by the corresponding equality. The iteration procedure to get the solution will then be:

$$\delta\vec{T}_{R,n} = [W]\vec{T}_n - \vec{T}_{R_0} \tag{13}$$

$$\delta\vec{T}_n = [W]^{*-1}_n(-\delta\vec{T}_{R,n}) \tag{14}$$

$$\vec{T}_{n+1} = \vec{T}_n + \delta\vec{T}_n \tag{15}$$

The approximate operator and the deviation in radiation temperature are taken from the current atmosphere denoted by n. Since the atmosphere is calculated by MULTI, the exact operator $[W]$ is associated with the physics that the code describes. This iteration procedure is coded in IDL (interactive data language) as a loop that runs automatically until the user terminates the process manually. The code is available upon request from the author. A "users guide" to the code is given in the appendix. The details of the procedure can be summarized:

1. Choose an arbitrary temperature structure on a column mass scale as an initial solution. By some reasoning this should be chosen as close to the final solution as possible to get fast convergence.

2. Compute the atmosphere in HSE to get self-consistent densities and temperatures. The five level hydrogen atom is calculated in NLTE. Background opacities from other elements are calculated in LTE. The emergent spectrum is thus produced, or equivalently the exact operator.

3. Use the Planck function to compute the radiation temperatures at each continuum point using the intensities from the MULTI-calculation. Compute the deviations from the reference radiation temperatures. This is equation 13.

4. Construct the approximate operator from the contribution functions to intensity, and solve equation 14.

5. Terminate the iteration if the temperature corrections are sufficiently small, or if the average radiation temperature deviation is below a chosen threshold.

6. Replace the atmospheric temperatures in the current HSE integrated atmosphere by using equation 15. Temperature corrections between depth points determined by the contribution function centroids are found by interpolation. The interpolated correction is then added to the HSE atmosphere. This will be the input atmosphere for the next calculation.

7. Go to step 2.

4.7 Constraints on the temperature structure

We wish to have a smooth temperature structure. This requires that the temperature corrections have to be done on relatively few depth points at each iteration step. This is provided by the under-sampling caused by the centroids of the contribution functions to intensity. Smooth transitions between the correcting depths are achieved by interpolation. It must be noted that the correcting depths change during the iteration process.

The final temperature structure can have several extremal points even if the depth grid is sufficiently undersampeled. It is thus necessary to lay constraints on the temperature structure in order to obtain similarities to other semiempirical models. These constraints are built into the temperature correction interpolations which we will describe here.

Two constraints have been developed for semiempirical models with chromospheres over the past two decades (see e.g. the VAL model). These are:

1. There is only one extremal point, the temperature minimum.

2. The highest degree of smoothness is seeked. This means that the second derivative should have the lowest possible absolute value.

These constraints will reduce the possible number of temperature structure solutions, and they will be comparable to earlier models such as the VAL model.

It is not trivial to satisfy these constraints, and a lot of trial and error have been done. The most obvious method would be to fit the coefficients of an analytical temperature function with these properties by a least squares method. The temperatures to be approximated by this function would be the previous temperature structure with the temperature corrections added. The problem arising here is to find the analytical function that gives sufficient accuracy both in the chromosphere and in the photosphere. Another approach that solves this problem was found, and we call it the "hybrid" method:

1. The deviation from a radiative equilibrium temperature structure is fitted by a fifth order polynomial at the correcting depths by the least squares method to obtain monotonicity and sufficient smoothness in the chromosphere. The deviations are

roughly increasing outwards, implying a monotone polynomial provided that the degree is sufficiently low. Sufficient accuracy is obtained by choosing a degree that is not too low. The resulting temperature structure is obtained by adding the radiative equilibrium structure.

A few important steps has to be carried out to obtain monotonicity in the uppermost parts. If the uppermost correcting point lies above a maximum point in the resulting temperature structure, the temperature from the maximum point and upwards is substituted by this maximum temperature. If the uppermost correcting point lies below a maximum which can either be an extremum or the end point, the temperature from the uppermost correcting point and upwards is substituted by the temperature at this point.

2. Since the initial solution can be more accurately determined in the photosphere, the corrections here will not be large. A reasonable initial solution here is the initial state of the dynamic simulation.

   Monotonicity is achieved in the photosphere by the steep temperature gradient if the corrections are sufficiently small. A direct spline interpolation at the correcting depths is thus sufficient.

3. A weighted mean is used to make a smooth transition from the photospheric spline interpolation to the chromospheric polynomial interpolation. The weights are chosen from a fifteenth order Butterworth-function that weighs the two parts equally at $lg(column\ mass) = -1$. The two interpolatives are extended beyond this point at each side to avoid end-effects. The high order weighting function provides a swift transition between the two interpolatives.

The response matrix, and the solution of the temperature correction at an iteration step with the given constraints can be seen in figure 5.

4.8 Uniqueness and accuracy of the temperature structure

Uniqueness

Different initial temperature structures should converge to approximately the same final temperature structure if the iteration method is robust. This has been confirmed by experiments. Each initial structure converged to approximately the same final temperature structure within five iterations. The final temperature structure is nevertheless dependent on the constraints laid on them and the methods to obtain the temperature corrections.

Accuracy

It is impossible to obtain semiempirical radiation temperatures that exactly match the reference radiation temperatures with a smooth temperature structure. We are therefore satisfied if the average deviation is within a certain limit, say +/-20K.

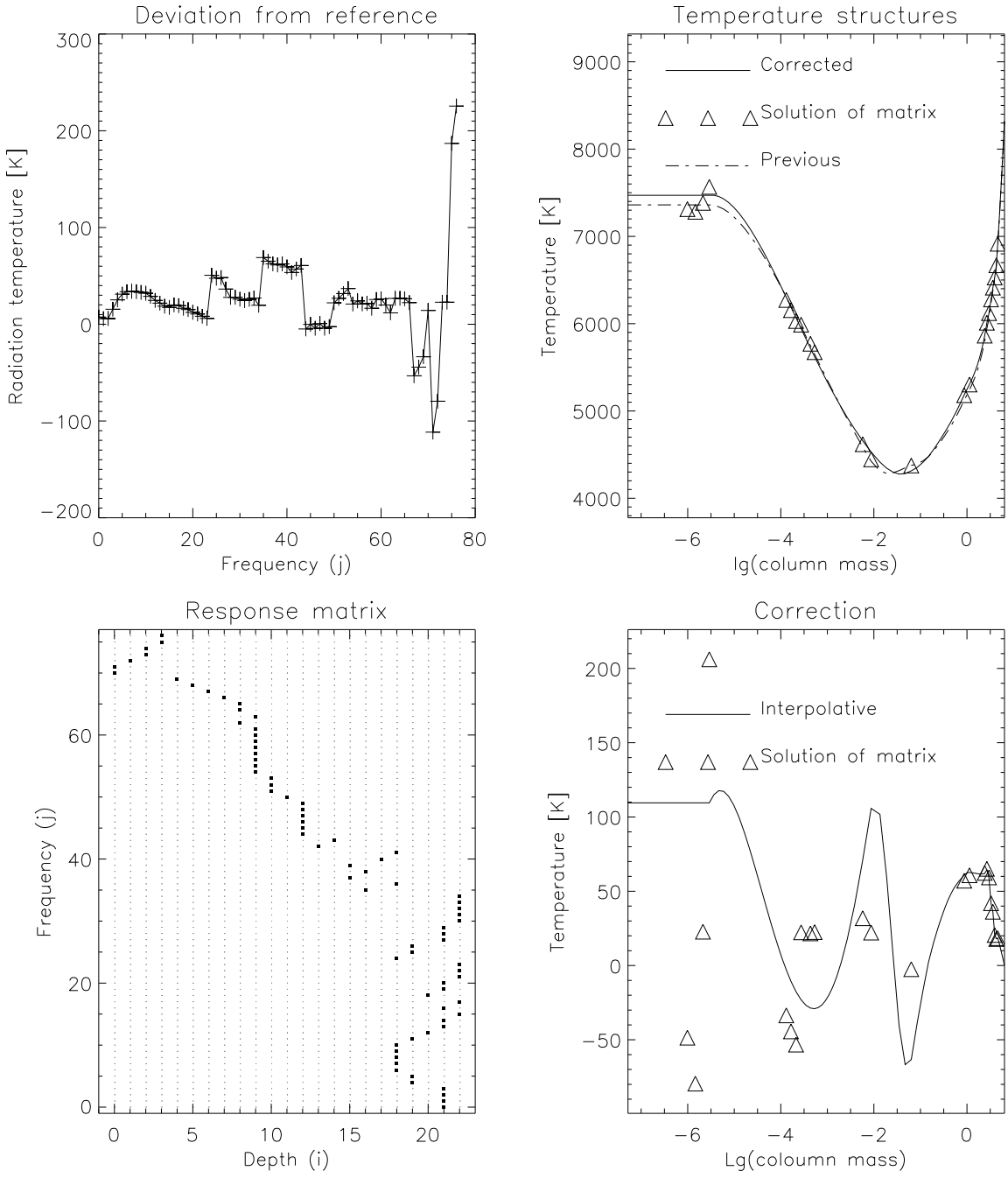

Figure 5: *Upper left panel.* The change of semiempirical radiation temperature needed to match the reference radiation temperature as a function of frequency index. High numbered indexes correspond to short wavelengths. *Lower left panel.* The response matrix with delta functions. The depth grid is resampled by the centroids of the contribution functions to intensity. *Upper right panel.* The solution of the matrix (diamonds) denotes here the corrections with the previous temperatures added. Polynomials are used to obtain a smooth temperature structure with only one extremal point at the temperature minimum. *Lower right panel.* The resulting temperature correction at every depth point (interpolative) is shown together with the solution obtained from the response matrix.

It is possible to eliminate the deviations within a limited frequency range by adjusting the temperature at a limited depth interval. These adjustments will not lead to an improvement if they are applied on the entire temperature structure because the resulting temperature structure will not obey the smoothness constraint.

We can nevertheless use these adjustments to determine the temperature interval in which the temperature structure that matches the reference spectrum exactly is located. This interval is bounded by the deviation limits.

The temperature correction in a certain depth interval is determined by minimizing a typical deviation (e.g. 20K) over the whole spectrum by the least squares method. We thus use the same principles as in the solution of the response matrix, but now only for a limited depth interval.

We define the upper deviation limit of the semiempirical temperature structure as this correction added to the temperature structure. The lower deviation limit corresponds to a subtraction of this correction.

These deviation limits are set by the reciprocal of the radiation temperature response functions. A relatively great change in atmospheric temperature is necessary to obtain a certain change in radiation temperature if the radiation temperature response function is relatively small. The separation between the deviation limits will thus be relatively great.

The deviation limits for the final temperature structure are found by computing the actual radiation temperature response functions to temperature change, $R_{T_R,T}(\nu, x)$. These are given by:

$$\delta T_R(\nu) = \int_{-\infty}^{\infty} R_{T_R,T}(\nu, x)\delta T(x)dx \tag{16}$$

By letting the temperature perturbation to be constant $\delta T = 100K$ over the interval $< -\infty, x_0]$ and elsewhere zero, the response can be written:

$$\delta T_R(\nu, x_0) = \delta T \int_{-\infty}^{x_0} R_{T_R,T}(\nu, x)dx \tag{17}$$

$\delta T_R(\nu, x_0)$ is found by perturbing the atmosphere in successive steps. This is done at every second depth point. The response function is found by differentiating this quantity:

$$\frac{1}{\delta T}\frac{d\delta T_R(\nu, x_0)}{dx_0} = R_{T_R,T}(\nu, x_0) \tag{18}$$

The depth variable is taken as the logarithm of the column mass in these equations. The normalized deviation at each depth point is defined to be the temperature change at this depth that minimizes by the least squares method a 1 Kelvin perturbation in radiation temperature over the whole spectrum. The temperature change is extended over an interval of $\Delta lg(m_c) = 1$ at each side of this depth. The least squares minimum for one depth can then be written:

$$\delta T = \frac{1 + \sum_{i \neq j} \frac{R_i}{R_j}}{R_j(1 + \sum_{i \neq j} (\frac{R_i}{R_j})^2)}\delta T_R \tag{19}$$

Where $R_j = max(R) > R_i$. The temperature change δT will be higher by taking into account the lesser valued responses R_i. This is due to the exponent in the fractional sum in the denominator. We ignore the R_i's, and define the normalized deviation as:

$$\delta T = +/- \frac{1K}{max(R)} \tag{20}$$

The maximum valued response function is here assumed to be constant over the depth interval in order to obtain the equality. The absolute deviation limits can be found by multiplying the typical deviation from the reference radiation temperature (e.g. 20K) with the normalized deviation.

5 Probabilistic radiative transfer

In this section we will use the concepts of probabilistic radiative transfer to get physical insight in the different processes that create spectral lines. We will derive a general equation of the NLTE line source function in terms of destruction- and escape probabilities in a medium with velocity gradients and a variable profile function. This result is specialized to the familiar second order expression for the line source function. We use this result to derive an expression for the population departures from LTE for the upper and lower energy levels associated with the spectral line. The results we obtain here are used extensively in section 7.

5.1 NLTE line source function

The emission profile is equal to the absorption profile in *complete redistribution* (CRD). The line source function is then given by:

$$S_{ij} = \frac{n_j A_{ji}}{n_i B_{ij} - n_j B_{ji}} \tag{21}$$

A_{ji},B_{ij} and B_{ji} are the Einstein coefficients for spontaneous emission, absorption and stimulated emission respectively. n_i is the number density or population number for the lower energy level, and n_j is the number density or population number for the upper energy level.

When the rate of stimulated emission is small in the limit of short wavelengths and low temperatures, the term $n_j B_{ji}$ can be omitted and we can write a relation to the Planck distribution, B, in terms of the population departures:

$$S_{ij} = \frac{b_j}{b_i} B \tag{22}$$

For any level, say k, the population departure b_k is:

$$b_k = \frac{n_k}{n_k^*} \tag{23}$$

where n_k^* is the LTE population determined by the Boltzmann distribution. If the line opacity is much greater than the background opacity, the total source function can be approximated by the line source function.

The line source function for a transition in a multilevel atom can be written as for the two level atom:

$$S_{ij} = (1 - \epsilon)\overline{J} - \epsilon B \tag{24}$$

$\overline{J}$ is the specific intensity weighted by the normalized line profile, and averaged over all solid angles and frequencies. ϵ is the *thermal coupling parameter* or the *destruction probability* if we are considering a two level atom. This is given by:

$$\epsilon = P_d = \frac{C_{ji}}{A_{ji} + C_{ji}} \tag{25}$$

which is the probability for collisional de-exitation. This process returns the exitation energy to the thermal pool or the electron gas.

High density plasmas provide dominant collisional rates compared to the spontaneous emission rate. A photon will then most probably be destroyed a mean free path away once it is emitted. This distance is short compared to the characteristic distances over which thermodynamic variables change. The radiation field is therefore controlled by the local temperature, and the line source function is very close to the Planck distribution. Populations are close to the Boltzmann distribution. This is *Local Thermodynamic Equilibrium* or LTE.

For a more dilute plasma, the mean free path is increased, and the collisional rate is decreased. The scattering term in the line source function will begin to dominate, and the radiation field becomes non-local. At a given location, the population numbers are controlled by the nonlocal radiation field, which in turn depends on the nonlocal population numbers through the radiative transfer. The source function is then dependent on the global atmospheric state. This is *Non-Local Thermodynamic Equilibrium* or NLTE. The population numbers are found from the rate equations for each energy level:

Rate of population change = Net rate into the level - Net rate out of the level

In a multilevel atom, ϵ is dependent on parameters in other atomic transitions in addition to the destruction probability in the transition we are considering. This quantity will then become non-local through the radiation field in other lines.

5.2 Escape probability

The probability for photon escape from a given atmospheric location without scattering is defined to be the *escape probability*. The transport of radiation through an atmosphere is characterized by exponential extinction. The solution of the transfer equation for the emergent intensity gives a sum or an integral of the source function weighted by this exponential term that is interpreted as a probability of escape. *The monochromatic escape probability* at $\vec{r}$ along a ray in the direction $\vec{n}$ where τ_ν is the optical depth to the boundary thus be written as:

$$p_\nu(\vec{r}, \vec{n}) = e^{-\tau_\nu} \tag{26}$$

The escape probability for a photon that can interact with an atomic transition is obtained by averaging this quantity over the normalized emission profile and over all directions in space:

$$P_e(\vec{r}) = \frac{1}{4\pi} \int_\Omega \int_0^\infty p_\nu(\vec{r}, \vec{n}(\Omega))\phi_\nu d\nu d\Omega \tag{27}$$

5.3 Core saturation and a probabilistic equation for the line source function

We will here use core saturation methods (Kalkofen 1984) to derive an equation for the line source function in terms of escape- and destruction probabilities.

At great optical depths, the specific intensity can be approximated by the local source function at all frequencies. This means that any photon is assumed to be absorbed at the point where it was emitted. The local source function is, under this condition, equal to the profile averaged intensity. This concept of *complete saturation* can be modified to *partial saturation* such that the source function is equal to the specific intensity only for a limited set of frequencies which depends on the atmospheric location. This limited set is called the *core*. The unsaturated frequency range is called the *wing*.

The saturated core region at a certain depth is defined by those frequencies where the monochromatic optical depth is greater than some chosen value γ. γ is denoted by the *saturation depth*.

In the limit of $\gamma \rightarrow \infty$, the whole frequency range becomes the wing region, and the core saturation method reduces to the exact theory. The wing region is taken to be completely *transparent*, i.e. an emitted photon escapes if it is directed towards the outer hemisphere. By using the two stream model, and by assuming zero incoming radiation at the boundary, one obtains:

$$J_{core}(\tau_\nu) = S(\tau_\nu); \tau_\nu > \gamma \tag{28}$$

$$J_{wing}(\tau_\nu) = \frac{1}{2} S(\gamma); \tau_\nu < \gamma \tag{29}$$

The saturation frequency ν_s at a given reference depth τ_0 is given by $\tau_{\nu_s}(\tau_0) = \gamma$. This quantity is taken from the simulations, and it is in general different for blue and red wings in the presence of velocity fields. The following discussion assumes that ν_s is a monotone function of τ_0 at each side of the Doppler-core throughout the atmosphere. This is verified by the simulations.

The line source function contains the profile averaged mean intensity. Elimination of this quantity is necessary to get a simple expression of the source function in terms of the escape probability. The differential $d\overline{J}$ is investigated rather than $\overline{J}$ itself. This will result in a first order differential equation for $S(\tau_0)$.

The change in $\overline{J}_{wing}$ that occurs in the blue wing, when a displacement in optical depth $d\tau_0$ is carried out, can be written in the following way taking into account a depth variable profile function:

$$d\overline{J}^{blue}_{wing} = \int_{\nu_s+d\nu}^{\infty} J(\nu')\phi(\nu', \tau_0 + d\tau_0)d\nu' - \int_{\nu_s+d\nu}^{\infty} J(\nu')\phi(\nu', \tau_0)d\nu' - \int_{\nu_s}^{\nu_s+d\nu} J(\nu')\phi(\nu', \tau_0)d\nu' \tag{30}$$

$d\nu$ is the change in saturation frequency, and ν_s is the saturation frequency at τ_0 which in general are unequal for red and blue wing. ϕ is dependent on velocity, temperature

and microturbulence. A similar expression results for the red wing. Substituting the mean intensity in the wing (eq. 29), we get:

$$d\overline{J}^{blue}_{wing} = \frac{1}{2}\int_{\nu_s+d\nu}^{\infty} S(\tau_0(\nu'))d\phi(\nu',\tau_0)d\nu' - \frac{1}{2}S(\tau_0(\nu_s))\phi(\nu_s,\tau_0)d\nu \tag{31}$$

The integral is the change in $\overline{J}^{blue}_{wing}$ caused by the depth variation of the profile function. This is substituted by $\delta\overline{S}^{blue}$. The monochromatic escape probability is set to zero in the core, and unity in the wing regions along rays pointing towards the outer hemisphere. From eq. 27 one obtains an approximation of the escape probability in one of the wings:

$$P_e(\tau_0) = \frac{1}{2}\int_{\nu_s}^{\infty} \phi_\nu d\nu' \tag{32}$$

The change in escape probability $dP_e^{\dagger blue}$ caused by the change in saturation frequency can then be used in the last term in eq. 31:

$$d\overline{J}^{blue}_{wing} = \delta\overline{S}^{blue} + SdP_e^{\dagger blue} \tag{33}$$

Addition of the two wing contributions give:

$$d\overline{J}_{wing} = \delta\overline{S}^{blue} + \delta\overline{S}^{red} + SdP_e^{\dagger} \tag{34}$$

The profile averaged intensity in the core can be written in terms of the total escape probability by using the saturated value of the intensity:

$$\overline{J}_{core} = S(1-2P_e) \tag{35}$$

Eq. 34 and the derivative of eq. 35 give:

$$d\overline{J} = dS(1-2P_e) - 2SdP_e + SdP_e^{\dagger} + \delta\overline{S}^{blue} + \delta\overline{S}^{red} \tag{36}$$

Differentiation of eq. 24 and using 36 gives a general equation for the differential of S:

$$dS = \epsilon dB + (1-\epsilon)[dS(1-2P_e) - 2SdP_e + SdP_e^{\dagger} + \delta\overline{S}^{blue} + \delta\overline{S}^{red}] + (B-\overline{J})d\epsilon \tag{37}$$

To get a simple analytic solution of an approximate source function, one has to neglect variation of the Planck distribution, variation of the destruction probability and variation of the profile function.

The variation of the profile function leads to the terms $\delta\overline{S}^{blue}$ and $\delta\overline{S}^{red}$. If the sign of the two quantities are opposite, which can be true in the presence of a velocity field of small amplitude, they can have a tendency to cancel each other. When the Doppler-width varies due to changes in temperature and microturbulence, the signs will be equal. The error made in ignoring these terms are of these reasons probably greater when variation of profile broadening dominates the Doppler-shift variation.

The variation of the Planck distribution and destruction probability can be significant in the presence of shocks. Ignoring this will probably lead to an error greater than the

error introduced by neglecting the variation of the profile function. The approximations give:

$$dP_e^{\dagger} = dP_e \tag{38}$$

$$\delta\overline{S}^{blue} = \delta\overline{S}^{red} = 0 \tag{39}$$

A first order differential equation for S is found from eq. 37 by using these approximations:

$$[\epsilon + (1-\epsilon)2P_e]\frac{dS}{dP_e} = (\epsilon - 1)S \tag{40}$$

Which has the familiar "second order" solution:

$$S = [\frac{\epsilon}{\epsilon + (1-\epsilon)2P_e}]^{\frac{1}{2}}B \tag{41}$$

This equation was first given by Ivanov (1973). The Planck distribution B is introduced by the integration limit of zero escape probability. S and P_e are evaluated at τ_0, and ϵ and B are assumed to be constant. As $\tau_0 \to \infty$, $P_e \to 0$, such that $S \to B$. As $\tau_0 \to 0$, $P_e \to 1/2$, such that $S \to \epsilon^{\frac{1}{2}}B$.

The interpretation of this equation when using varying ϵ and B, is that the value of the approximated source function at a specific depth is valid if ϵ and B at this depth are the values in the entire atmosphere. This approach is used later in the thesis where we show that in the general case with varying Planck distribution, varying destruction probability and velocity field, the line source function is controlled by the escape probability and the destruction probability. A discussion for the case of a variable Planck function and destruction probability is given by Frisch & Frisch (1975).

The scale Λ over which the source function approaches B can be estimated as the value of τ_0 that makes the two terms in the denominator of eq. 41 equal. For $\epsilon \ll 1$ this implies:

$$P_e(\Lambda) \approx \epsilon \tag{42}$$

The optical depth Λ defines the *thermalization depth* which acts as an upper boundary for the range of validity for *local thermodynamic equilibrium*. Discussions of thermalization depths can be found in Mihalas (1978) and Kalkofen (1984).

5.4 Departure coefficients in terms of probabilities

By combining eq. 41 and eq. 22, the departure coefficient ratio can be written as:

$$\frac{b_j}{b_i} = [\frac{\epsilon}{\epsilon + (1-\epsilon)2P_e}]^{\frac{1}{2}} \tag{43}$$

The population departures from LTE are mainly controlled by photon transfer in the optically thin wings of the spectral line, while the optically thick core plays a passive role. Photons emitted in the far wings, where the opacity is low, can travel over large distances

in a single step. Some of the photons escape from the atmosphere. The large mean free path compensates for the relatively low probability of wing emission, such that most of the photon flux is carried in the wings. In the core, where the opacity is high, photons are travelling short distances between each interaction event. A scattering event emits the photon in a random direction. The random walk process combined by the short distances gives a small net transportation or photon flux.

When the photon loss from the wings becomes significant well above the thermalization depth, or equivalently that the escape probability exceeds destruction probability, S starts to fall below B. This means that the upper level becomes underpopulated relative to the lower level, and a significant net radiative rate in the direction $j \rightarrow i$ supplies the photon loss. The collisional exitation rate in the transition, and net rates from other transitions into the upper level, will balance the net radiative de-exitation rate. Collisional rates are directed from overpopulated levels to underpopulated levels, and it is this mechanism that tends to compensate the photon losses. Energy is then taken from the thermal pool and converted to escaping photons. This means that the gas is *radiatively cooled.* The contribution to the *flux divergence* from the transition is thus:

$$\nabla \vec{F_{ji}} = h\nu_0(n_j(A_{ji} + B_{ji}\overline{J}) - n_i B_{ij}\overline{J}) = h\nu_0 n_j A_{ji}\rho_{ji} \tag{44}$$

Where $\rho_{ji} = 1 - \frac{\overline{J}}{S_{ij}}$ is the *net radiative bracket.* Some of the photon loss in the wings can be absorbed in the underlying continuum. The total flux divergence is then dependent on this process.

Deeper in the atmosphere, towards the thermalization depth, both departure coefficients approaches unity because of the decreasing escape probability, and the source function is mainly controlled by the Planck distribution. Further down the net rates and the flux divergence will approach zero because of approximate detailed balancing. They will completely vanish in thermodynamic equilibrium.

6 Heating by acoustic waves

6.1 The semiempirical model

In this section we present the semiempirical model of the acoustically heated atmosphere, hereafter model1. The purpose of this semiempirical model is to compare the semiempirical radiative cooling with the time averaged radiative cooling of the dynamic model.

6.1.1 Semiempirical chromospheric temperature rise caused by acoustic waves

The intensity from the dynamic model is averaged over 9 cycles of the fundamental period of 3 minutes, extending from 640 seconds after the initial radiative equilibrium to the end of the simulation at 2250 seconds. The acoustic shocks in the chromosphere produces a radiation temperature of the time averaged intensity that increases from 1500Å to 500Å as can be seen in figure 6. This produces a semiempirical temperature that increases with increasing height (figure 12), since radiation of shorter wavelength is formed at higher altitudes.

6.1.2 Deviations from the reference radiation temperatures

Relatively small temperature corrections of the order of +/- 20K are obtained after 6 iterations. The average deviation between the semiempirical radiation temperature and the radiation temperature of the time averaged intensity is +/-20 K (figure 8).

The radiation temperature deviations above 1500Å are on the average approximately +/- 20K which corresponds to +/-1%. The deviations on wavelengths between 504Å and 1500Å are one the average approximately +/- 50K which corresponds to +/- 1% (figures 6 and 7).

The goal of reproducing the radiation temperature of the time averaged continuum by the semiempirical model can be said to be accomplished.

6.1.3 Accuracy of the temperature structure

We determine the accuracy of the temperature structure by using the response functions to temperature change on radiation temperature. This is described in section 4. The radiation temperature response functions are calculated by perturbing the atmospheric temperature by a 100K step function. The transition depth where the perturbation changes from 0K to 100K is successively moved through the the whole atmosphere in 50 steps. This corresponds to an increase of two depth indices per step. The radiative transfer with hydrogen in NLTE is solved in each perturbed atmosphere to account for NLTE effects in the hydrogen continua. The resulting radiation temperature perturbation at each frequency is then found as a function of transition depth. Derivation of this function gives the response functions we are seeking. The radiation temperature response functions from 300Å to 3000Å are shown in figure 9.

The normalized deviation limits defined in section 4 are then found by using the reciprocal of the maximum valued response functions. The HeI continuum contribution functions

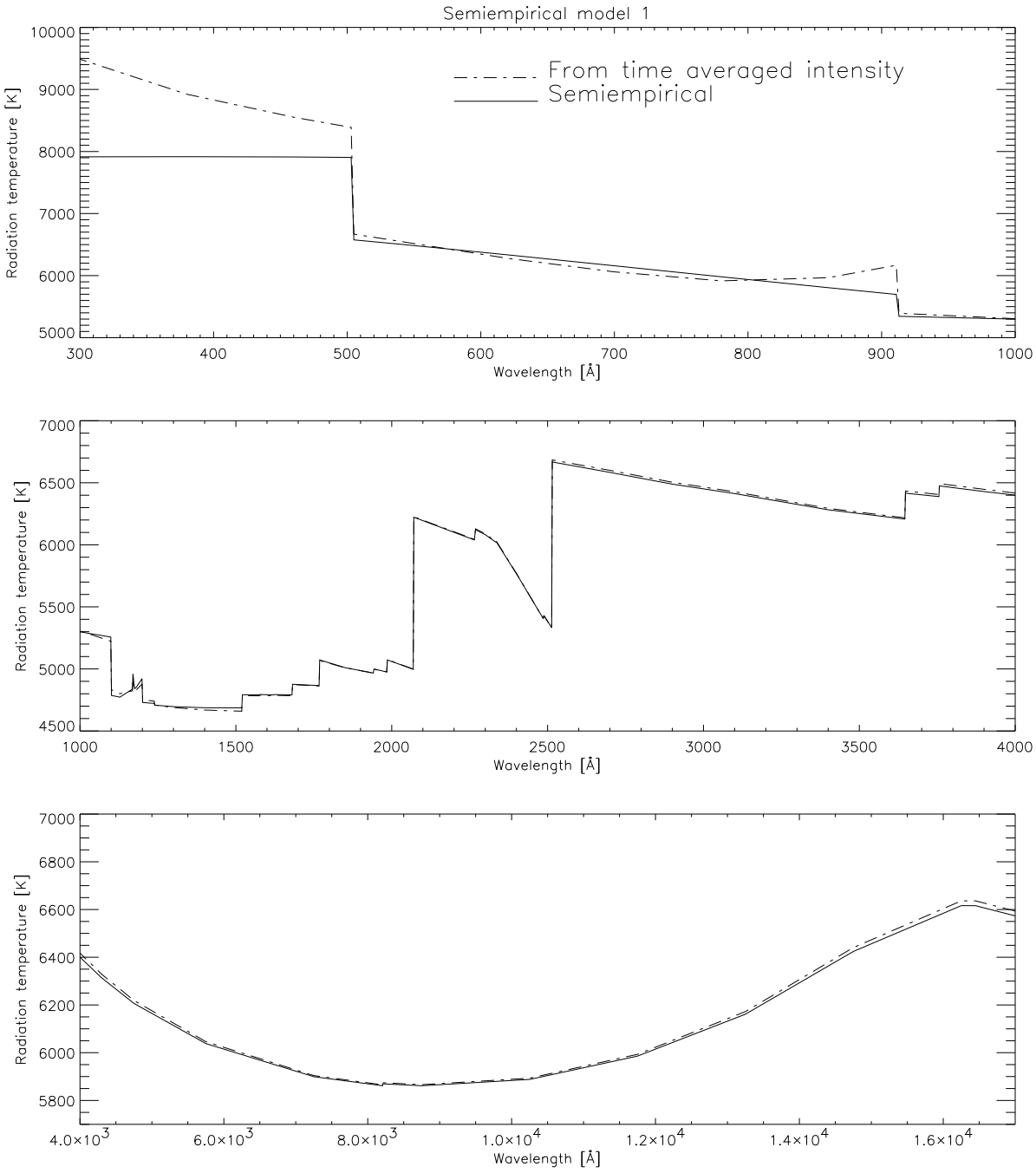

Figure 6: Semiempirical radiation temperature of model1 compared to the radiation temperature of the time averaged continuum spectrum. Wavelengths shorter than 504Å in the HeI continuum were not considered in the calculations of the temperature corrections, and the deviation here is thus relatively great.

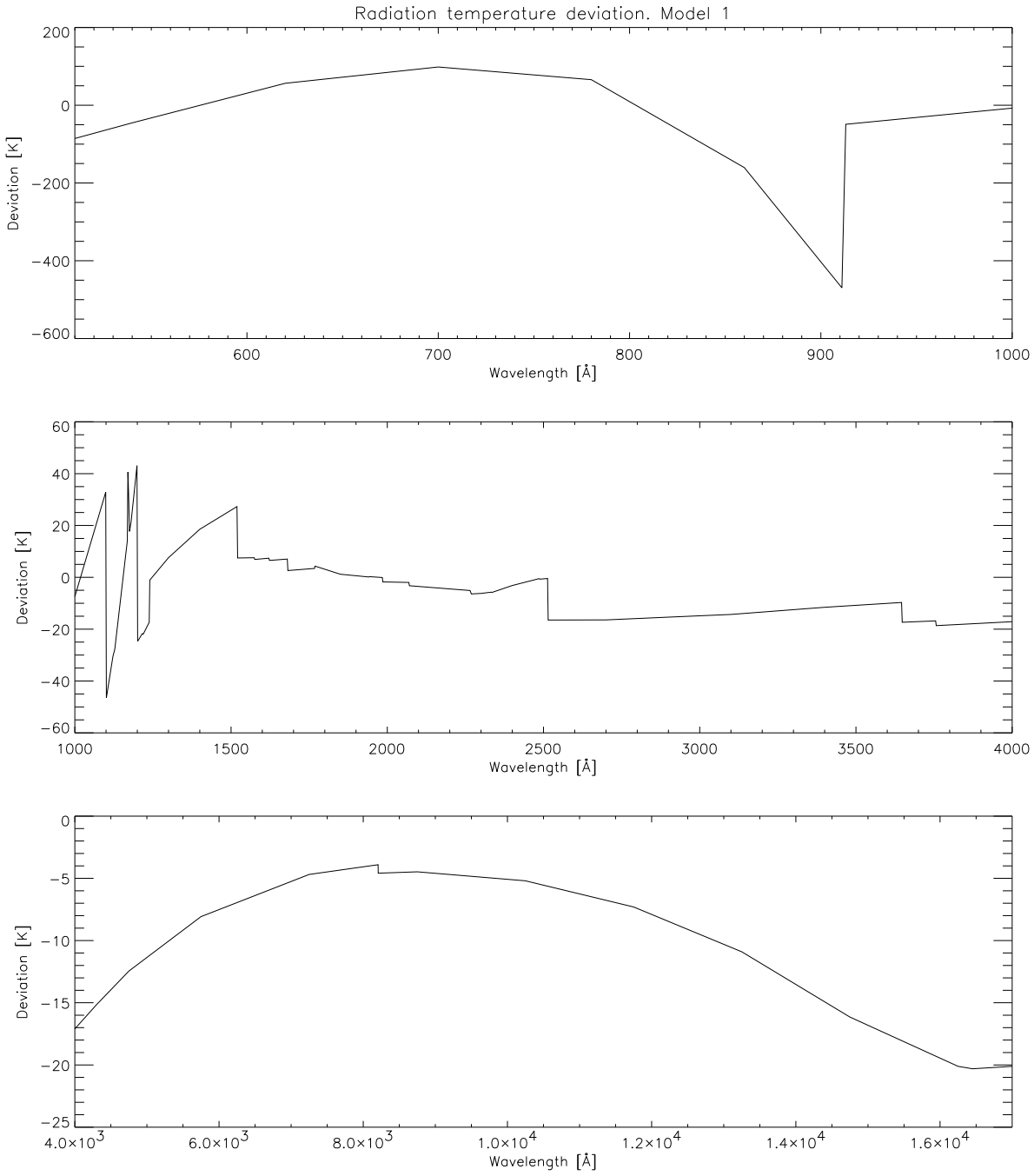

Figure 7: The radiation temperature deviations above 1500Å are on the average approximately +/- 20K which corresponds to +/-1%. The deviations on wavelengths between 504Å and 1500Å are on the average approximately +/- 50K which corresponds to +/- 1%. Positive values correspond to higher semiempirical intensities than time averaged intensities.

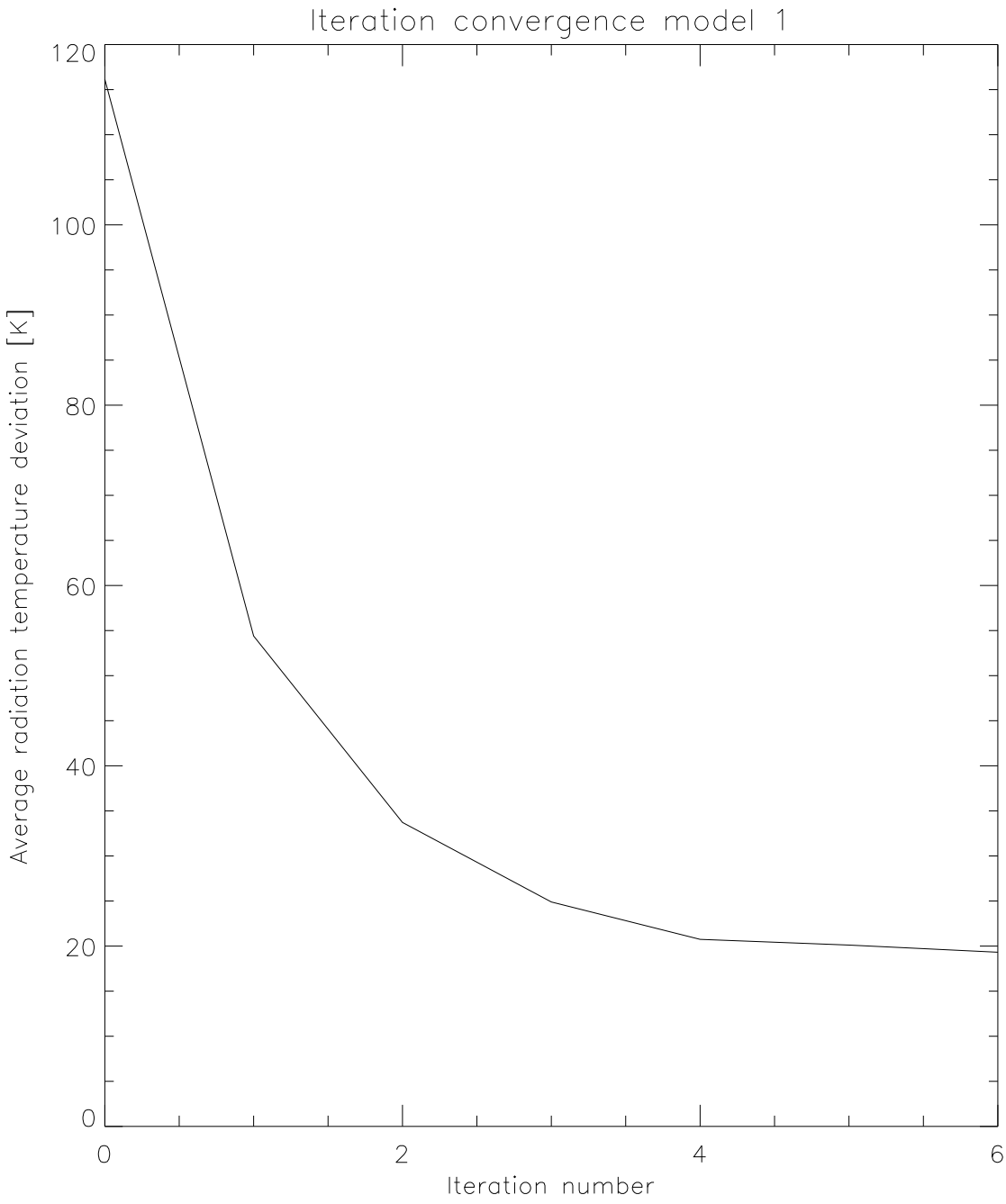

Figure 8: The average radiation temperature deviation seems to converge at approximately 20K. Termination was done after 6 iterations.

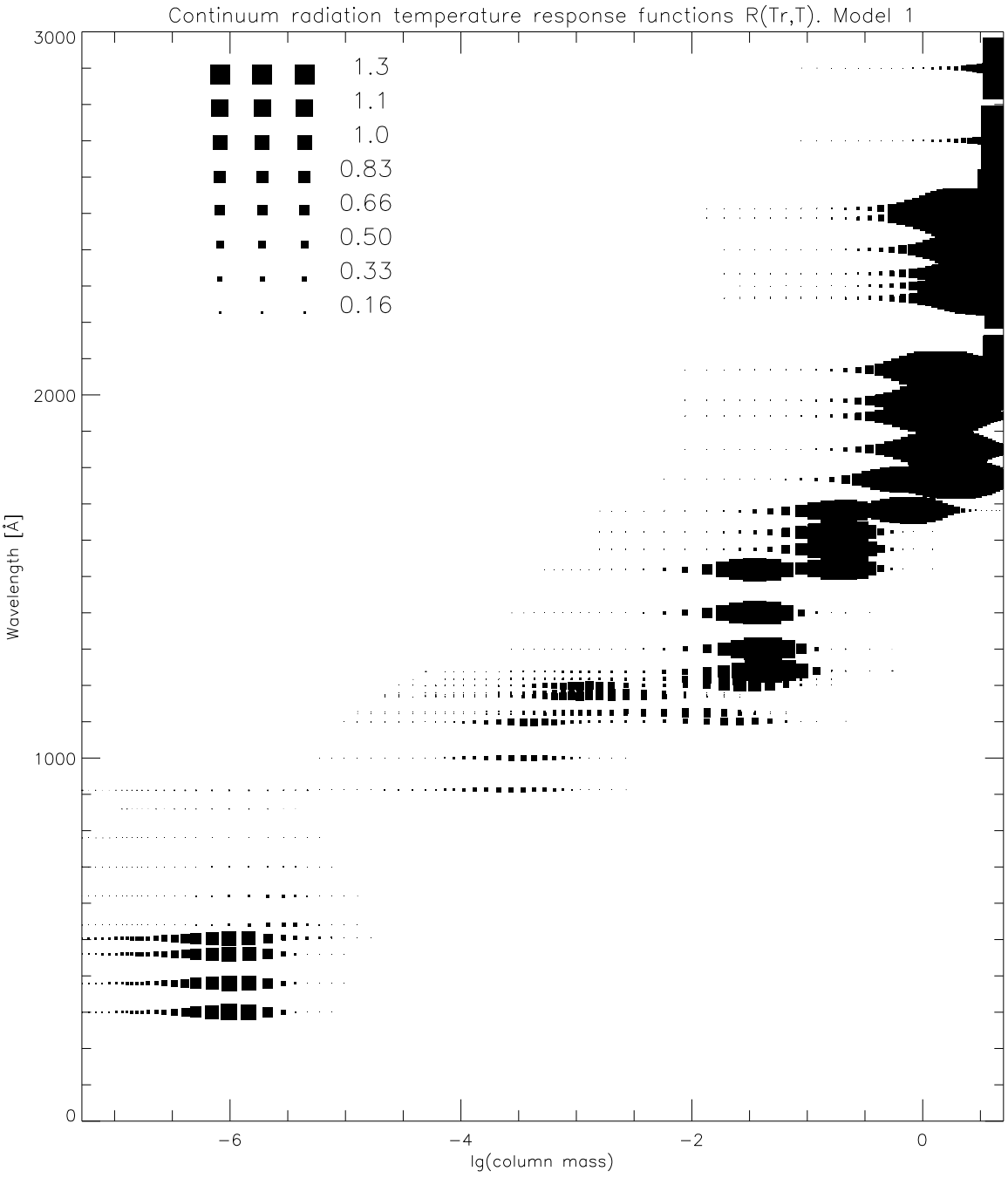

Figure 9: The radiation temperature response functions determine the accuracy of the temperature structure. Small values at a certain depth correspond to an inaccurate determination of the temperature at this depth. Wavelengths below 504Å are not considered in the accuracy calculations because this wavelength interval is excluded from the calculation of the temperature corrections. The accuracy of the uppermost temperature structure is therefore greatly reduced. The values of the response functions are shown in the upper left corner.

are not considered here because they were neglected in the semiempirical modelling. A typical radiation temperature difference between the semiempirical continuum spectrum and the time averaged dynamic spectrum can then be multiplied with this quantity in estimating the temperature interval bounded by the deviation limits where the optimal temperature structure that reproduces the reference spectrum exactly is located.

The normalized deviation limits as a function of depth are shown in figure 10. The semiempirical temperature structure with the deviation limits with an average temperature deviation of 20K is shown in figure 11. The radiation temperature sensitivity to temperature change is relatively small around $lg(column\ mass) = -5$ and above $lg(column\ mass) = -6$. The temperature structure in these intervals can therefore not be determined with high accuracy due to the low valued response functions. The use of a polynomial during the iterations provides a smooth and monotone chromospheric temperature structure between the deviation limits.

6.1.4 Comparisons with other semiempirical models

The temperature structure of model1 is very different compared to the VAL3C model of the average quiet sun (Vernazza et al. 1981) and the FALa (Fontenla et al. 1993) solar model for internetwork regions. The temperature minimum of model1 is located at higher altitudes, and the minimum temperature is approximately 500K higher than for VAL3C and FALa (figure 12). The chromospheric temperature for model1 is overall smaller than for the solar models except at $lg(column\ mass) = -5$ where all the models have approximately equal temperature around 7000K. This is at the base of the transition layer of the solar models. Our model does not have a transition region as in VAL3C or FALa. This is expected since the dynamic model does not include the corona. The temperature in the upper photosphere is higher than for the solar models, and the opposite is true in the lower photosphere.

A comparison of the radiation temperature between model1, VAL3C and FALa is given in figure 13. The opacity is higher at the short wavelength side of the bound-free opacity edges. Increased opacity increases the intensity formation heights. The radiation temperature at the short wavelength side of the opacity edges is then higher if we have an increasing temperature with height as in the chromosphere. The opposite is true in the photosphere where the temperature decreases with height.

The radiation temperature in the ultraviolet range from 300Å to 1200Å originates from the chromosphere for all three models as can be seen in figure 13. Model1 shows lower radiation temperature due to the lower temperature in the chromosphere. The HeI continuum below 504Å is not considered in the semiempirical modelling due to the neglect of helium ionization in the energy equation in the dynamic model.

The radiation from the temperature minimum region is located in the wavelength range around the SiI absorption edge at 1520Å for all models. The radiation temperature varies less here for model1 compared to the solar models. This is explained by the smaller variation of the temperature around the temperature minimum for model1. The radiation temperature varies from high to low at the SiI absorption edge as a function of decreased wavelength, or equivalently increased formation height, for model1. The variation is opposite, e.g. from low to high, for the solar models. The contribution functions at each side of

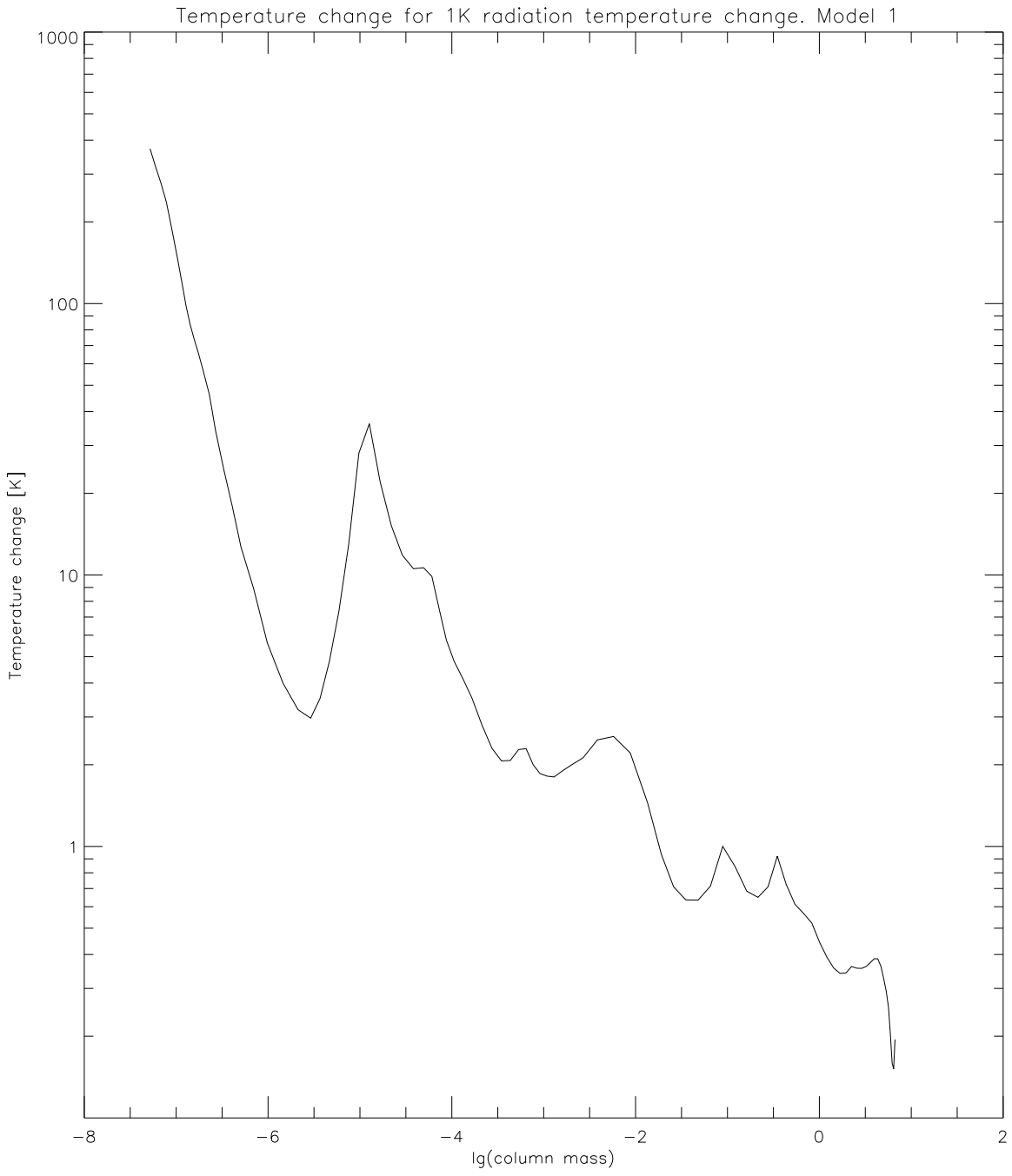

Figure 10: The reciprocal of the maximum valued response functions. This quantity is the normalized deviation limit that gives the atmospheric temperature change in a depth interval of $\Delta lg(column\ mass) = 1$ if a deviation in radiation temperature of 1K over the whole spectrum is to be minimized by the least squares method.

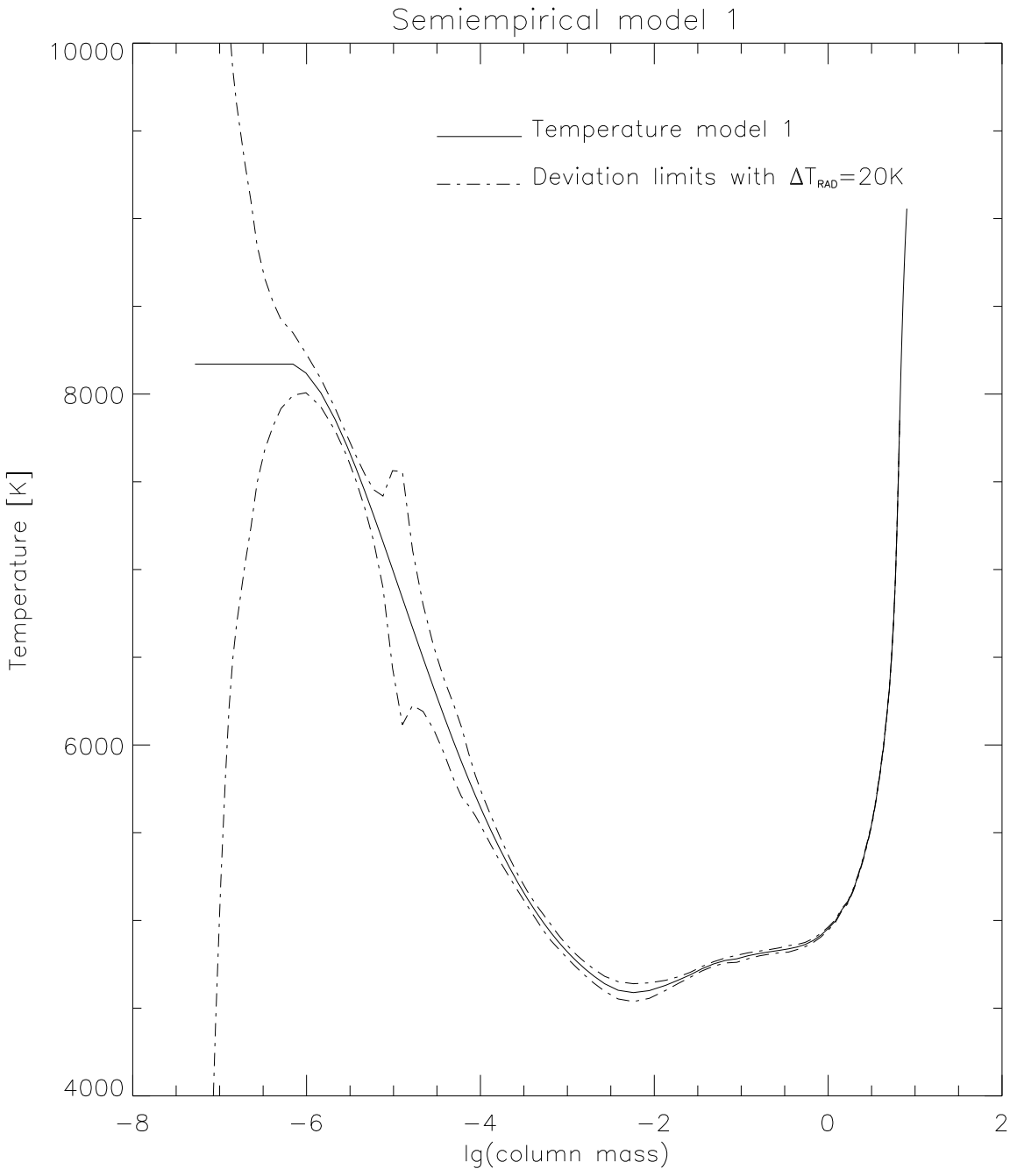

Figure 11: The semiempirical temperature structure (solid) with the deviation limits for a typical radiation temperature deviation of 20K (dotted). The radiation temperature sensitivity to temperature change is relatively small around $lg(column\ mass) = -5$ and above $lg(column\ mass) = -6$. The temperature structure in these intervals can therefore not be determined with high accuracy due to the low valued response functions. The use of a polynomial during the iterations provides a smooth and monotone chromospheric temperature structure between the deviation limits.

this edge lie at the depths where the temperature decreases with height for model1. The long wavelength side of the opacity edge has its contribution function located around the temperature minimum for the solar models. The short wavelength side has its contribution function located at increasing temperature with height. The different intensity variation at 1520Å is therefore explained by the higher altitude of the temperature minimum for model1 relative to the contribution functions to intensity.

The photospheric radiation for all three models is located in the range from 1500Å to 17000Å. The radiation temperature of model1 in the wavelength range between 2100Å and 17000Å is smaller than for the solar models due to the lower temperature in the lower photosphere. Higher radiation temperature for model1 around 1600Å occurs due to the higher temperature towards the temperature minimum in the upper photosphere.

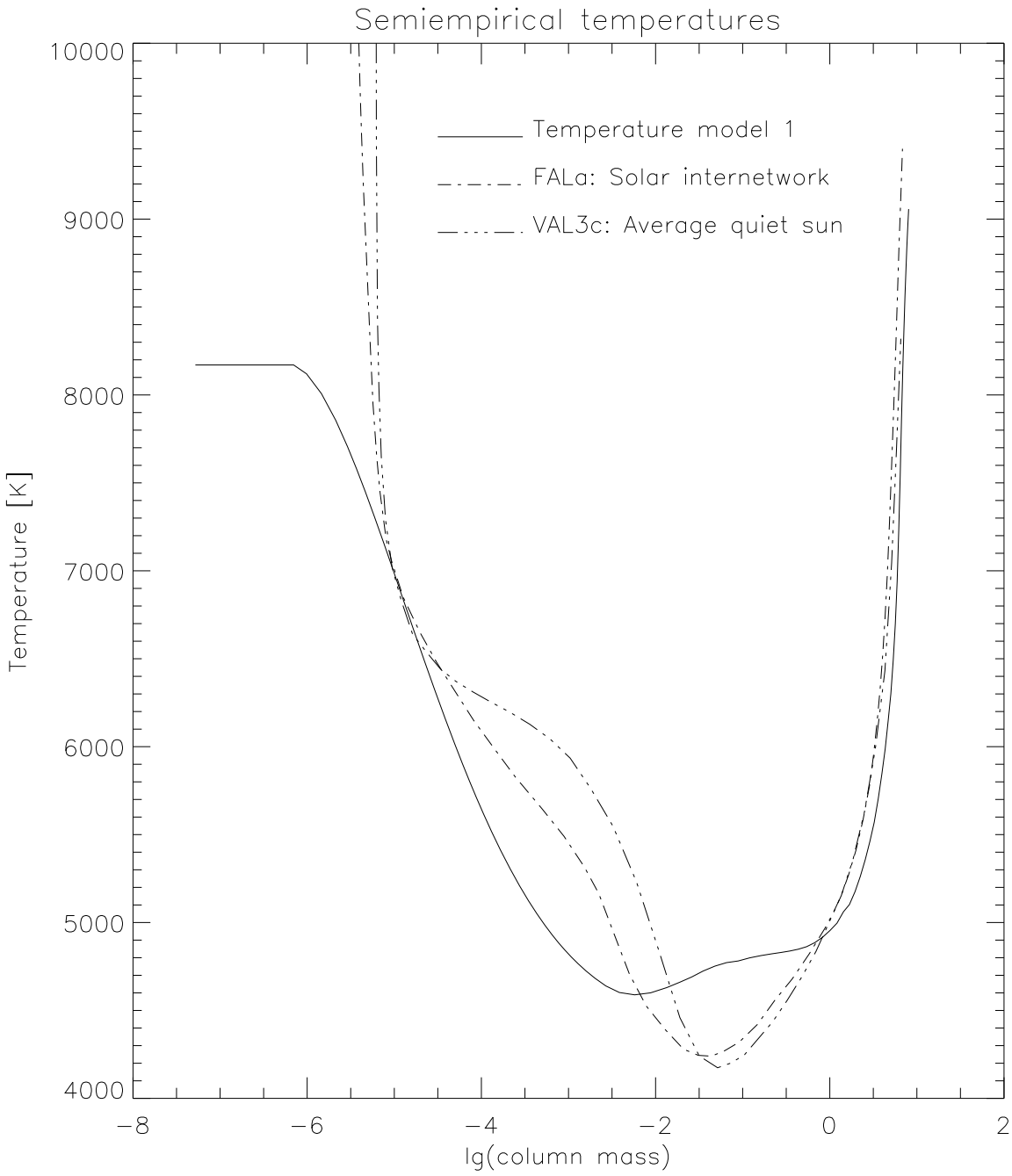

Figure 12: Different semiempirical models. The temperature structure of model1 is very different compared to the VAL3C model of the average quiet sun and the FALa solar model for internetwork regions. The temperature minimum of model1 is located at higher altitude, and the minimum temperature is approximately 500K higher than for VAL3C and FALa. The chromospheric temperature for model1 is overall smaller than for the solar models except at $lg(column\ mass) = -5$ where all the models have approximately equal temperature around 7000K.

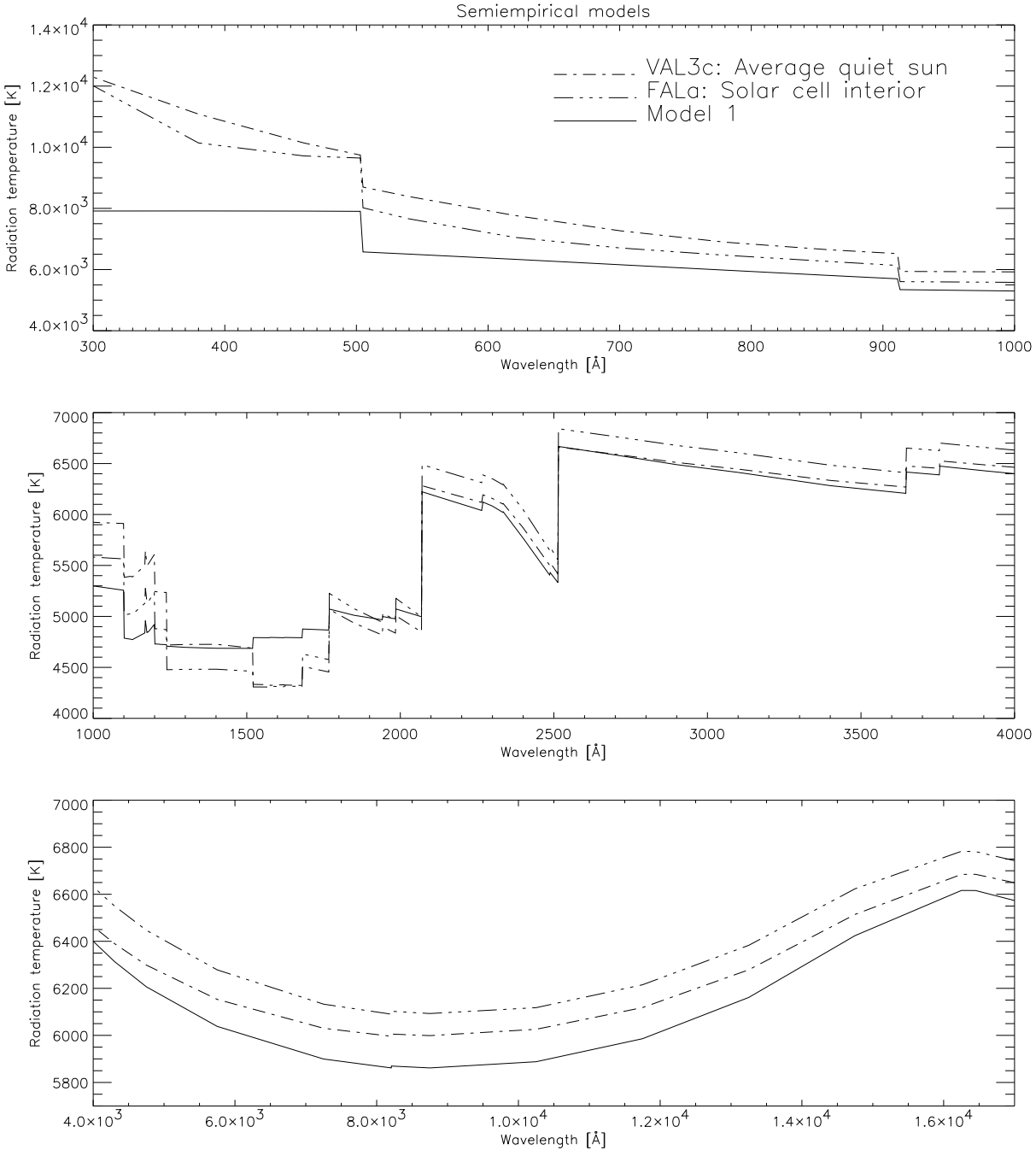

Figure 13: A comparison between different semiempirical radiation temperatures. The chromospheric radiation temperature below 1200Å is lower for model1 compared to the other models due to the lower temperature. The same is true for the radiation that comes from the lower photosphere in the range above 2100Å. The temperature minimum region has higher temperature than the solar models which can be seen around 1500Å. Note the different variation of the radiation temperature at the SiI bound-free edge at 1520Å.

6.2 Dynamic and semiempirical energy balance

Many workers have assumed that the total radiative loss as a function of height in a semiempirical model is equal to the corresponding spatial and temporal average value of the dynamic radiative loss. They have further used the semiempirical radiative loss to constrain the theories for heating mechanisms in the solar atmosphere (e.g. Anderson & Athay 1989), since the dynamic radiative loss is balanced by dynamic heating. The main source of atmospheric heating is the extraction of wave energy. An equality between heating caused by the extraction of wave energy and the dynamic radiative loss is an additional assumption. Conclusions about dynamic heating from static models seems contradictory, and the validity of these assumptions is investigated in this section. Radiative loss is hereafter denoted radiative cooling, or simply cooling. Negative cooling is denoted by heating.

First, we determine the different time averaged heating sources that balance the time averaged radiative cooling in the dynamic model.

Second, we determine the different contributors to radiative cooling in the semiempirical case and in the time averaged dynamic case, and we compare the total time averaged cooling rate with the semiempirical cooling rate.

6.2.1 Time averaged dynamic sources to radiative losses

The radiative cooling in this self-consistently heated dynamic model without magnetic fields is balanced by viscous dissipation, external compression work, thermal conduction and internal energy changes. All these terms have often been referred to as a common heating term or even mechanical heating by several workers who have discussed chromospheric heating mechanisms (e.g. Liu 1974 and Anderson & Athay 1989).

We determine the time averages of these heating terms as a function of height. The different terms are measured on the Lagrangian or co-moving frame, which is equivalent to the column mass scale, since we are interested in what happens in a specific volume element during the simulation. The time averages are then interpolated to a reference column mass scale, and they are taken over the same time interval as for the reference continuum spectrum used to construct the semiempirical model.

The heating terms are given by the internal energy equation. We begin with the stress tensor for a viscous fluid:

$$T_{ij} = -p\delta_{ij} + \sigma_{ij} \tag{45}$$

p is the isotropic thermal pressure and σ_{ij} is the viscous stress tensor. The internal energy equation in the Lagrangian frame can now be written:

$$\rho \frac{De}{Dt} = v_{i,j} T^{ij} - q^{j}_{,j} \tag{46}$$

ρ is the mass density, e is the sum of thermal energy, exitation energy and ionization energy. This quantity is hereafter denoted by internal energy. $v_{i,j}$ is gas velocity component

i derivated with respect to space coordinate j, and $q^j_{,j}$ is the divergence of the radiative and conductive fluxes. The last equation can also be written:

$$\rho\frac{De}{Dt} = -p(\nabla\cdot\vec{v}) - \nabla\cdot\vec{F}_c - \nabla\cdot\vec{F}_{rad} + \Phi_V \tag{47}$$

where the terms on the right side are respectively external compression work, net inflow of heat by conduction, net inflow of radiative energy, and viscous dissipation. Viscous dissipation is always a positive term due to irreversability. For a one dimensional planar flow, which is the case in the dynamic model, the viscous dissipation is given by:

$$\Phi_V = (\frac{4}{3}\mu + \zeta)(\frac{\partial v_z}{\partial z})^2 \tag{48}$$

μ is the coefficient of shear viscosity and ζ is the coefficient of bulk viscosity. v_z is the one dimensional velocity, and z the one dimensional space coordinate. The derivative implies that dissipation will be effective in the presence of shocks where the velocity changes abruptly on small spatial scales. The value of the viscosity coefficients are chosen to be higher than their natural values. This artificial viscosity broadens the shock structure such that it can be resolved on the 100 point adaptive depth grid. It has been shown that artificial viscosity does not alter the energy balance or the level of viscous dissipation significantly. The influence from a broadened shock on the radiative transfer is assumed to be relatively small. The radiative cooling is equal to the radiative flux divergence given by:

$$\Phi_{rad} = \nabla\cdot\vec{F}_{rad} = 4\pi\int_0^\infty(\eta_\nu - \chi_\nu J_\nu)d\nu \tag{49}$$

η_ν is the emissivity, χ_ν is the opacity and J_ν the mean intensity, all at frequency ν. The emissivity and the opacity are here assumed to be isotropic. Radiative cooling is thus the net photon emission from a volume element. Integrating equation 47 with respect to time, and dividing by the corresponding time interval gives the time averaged contributions to radiative cooling:

$$\langle\Phi_{rad}\rangle = \langle\Phi_V\rangle - \langle p(\nabla\cdot\vec{v})\rangle - \langle\rho\frac{De}{Dt}\rangle - \langle\nabla\cdot\vec{F}_c\rangle \tag{50}$$

An atmosphere in quasi-static state implies that the internal energy change averaged over a sufficiently large integer number of cycles of the fundamental period vanishes. This is not true in the time span of the dynamic model. The simulation should be extended considerably for this term to vanish.

There is no reason to believe that the average internal energy change is negligible in the solar chromosphere on small spatial scales and short time intervals lasting only a few oscillation periods. The possibility of internal energy changes must be taken into consideration when chromospheric heating is to be investigated on the basis of observations on small spatial scales and short time intervals.

Two specialized examples of causes of internal energy change are given:

1. Energy can be transferred to a specific volume of the chromosphere from surrounding volumes by wave motion or radiation. The internal energy can then increase in this volume if the rate of energy release is too low to compensate for the energy input.

2. Ionizing post-shock regions increase the ionization energy, and this energy is released by radiative recombinations. The recombination rates are set by the time scales of recombination. The internal energy can then increase if the recombination rates are relatively slow.

Equation 50 shows that viscous dissipation, external compression work, decrease in internal energy, and conductive heat flow into the volume element can contribute to net photon flow out of this volume element. The terms can naturally be negative, except for the dissipation term. The contribution from thermal conduction is found to be negligible compared to the other terms in this model. The time averaged contributions from the dynamic simulation are shown in figure 14. We have calculated the contributions as $ergs/cm^3/s$ which is common in literature of chromospheric energy balance. We refer here to the temperature minimum region and the lower chromosphere as the interval $lg(column\ mass) = [-3, 0]$ and the middle and upper chromosphere as $lg(column\ mass) = [-7, -3]$. The results are summarized as follows:

1. *Temperature minimum region and lower chromosphere in the interval* $lg(column\ mass) = [-1, 0]$, *and the photosphere.*

   The PdV work is negative, which means an increase in wave energy flux. The internal energy decreases, and we have a total radiative cooling. The decrease of internal energy and viscous dissipation balances the increase of wave energy and the radiative cooling. The decrease in internal energy is approximately a factor 100 greater than viscous dissipation. In the photosphere at $lg(colomn\ mass) = 0.5$, the PdV work is positive and it almost balances the radiative cooling.

2. *Temperature minimum region and lower chromosphere in the interval* $lg(column\ mass) = [-3, -1]$.

   PdV work and viscous dissipation balances an increase in internal energy and a total radiative cooling. PdV work is approximately a factor ten greater than viscous dissipation. The total radiative cooling exceeds the internal energy increase with a factor of approximately two below the temperature minimum at $lg(column\ mass) = -2.25$.

3. *Middle and upper chromosphere.*

   PdV work and viscous dissipation balances an increase in internal energy and a total radiative cooling. Viscous dissipation is primarily caused by the chromospheric shocks. PdV work is approximately a factor two greater than viscous dissipation below $lg(column\ mass) = -4$. PdV work is approximately a factor two less than viscous dissipation above $lg(column\ mass) = -4$. The total radiative cooling around $lg(column\ mass) = -4$ and above $lg(column\ mass) = -6$ exceeds the internal energy increase with a factor of approximately two.

Our dynamic model show that external compression work contributes with an approximately equal magnitude of heating as viscous dissipation. The radiative cooling and internal energy increase in the middle and upper chromosphere are roughly of the same magnitude. An assumed equality between the heating terms and radiative cooling will thus be erroneous.

6.2.2 Semiempirical compared with time averaged radiative losses

The continuum- and line cooling are calculated for the same frequency interval and with the same frequency grid for both models. The continuum frequency grid is the same as for the hydrogen continua, and it covers wavelengths from the Lyman continuum ending at 600Å to the Pfundt continuum beginning at 22392Å. We compare the cooling distributions and the total cooling in different layers for the dynamic and static models. The dynamic quantities are time averaged. The distribution of the total cooling among Hydrogen, CaII and the continua can be seen in figures 15 and 16 for dynamic and semiempirical model respectively. Semiempirical and time averaged total cooling are shown in figure 17.

We refer here to the temperature minimum region and the lower chromosphere as the interval $lg(column\ mass) = [-3, 0]$ and the middle and upper chromosphere as $lg(column\ mass) = [-7, -3]$ as in the previous section.

1. *Low chromosphere and temperature minimum region.* The CaII and H line cooling are approximately equal. Continuum heating occurs in the dynamic model.

   Continuum cooling occurs in the static model in the lower parts near $lg(column\ mass) = -0.5$, which leads to a total cooling in the static model of approximately a factor 10 larger than for the dynamic model. There is in fact a total radiative heating in the dynamic model at $lg(column\ mass) = -0.5$.

   The continuum heating rates are approximately equal around $lg(column\ mass) = -2$, and the total cooling rates are thus approximately equal here.

   In the upper parts around $lg(column\ mass) = -2.5$, the static continuum heating is smaller than the dynamic continuum heating, and the static cooling exceeds the dynamic by a factor of ten.

2. *Middle and upper chromosphere.* Hydrogen line cooling and continuum heating tends to cancel each other in the dynamic model. Both contributions in the semiempirical model are from a factor of 10 to 100 smaller. The CaII line cooling rates are approximately the same within a factor of 2, such that the total cooling rates does not deviate more than a factor of 2 from each other.

   The uppermost part around $lg(column\ mass) = -6$ has a total cooling originating from hydrogen in the dynamic model. The static total cooling has only a smaller contribution from continuum, and it decreases faster than the dynamic total cooling with increasing height.

The cooling rate for the same contributor is in general rather different at equal depths in the two models. The continuum cooling rates are very different almost at every depth.

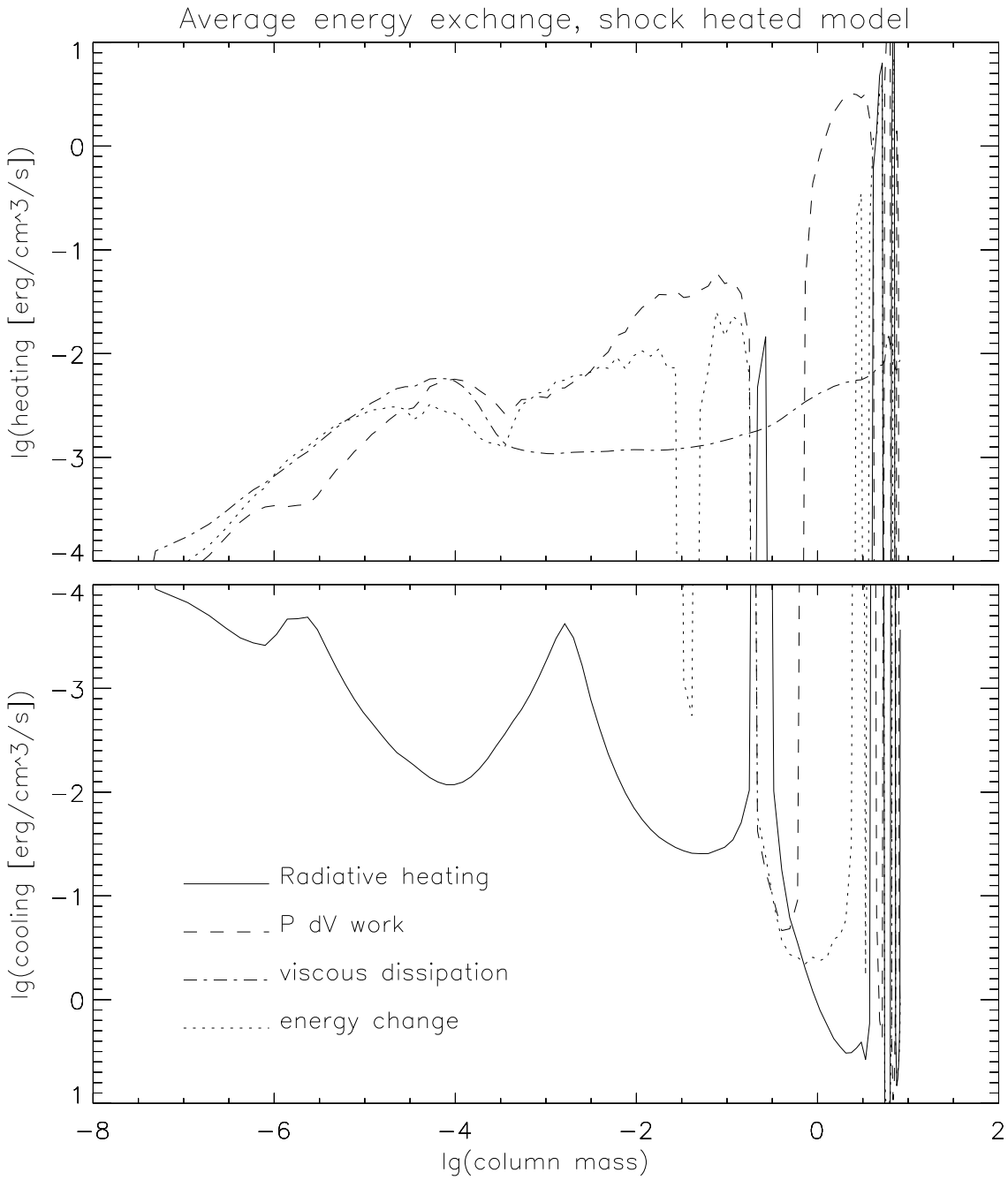

Figure 14: Sources to total cooling in the dynamic model. The chromospheric radiative cooling and internal energy increase above $lg(column\ mass) = -3$ are roughly of the same magnitude, and these sinks are balanced by the sources of viscous dissipation and external compression work.

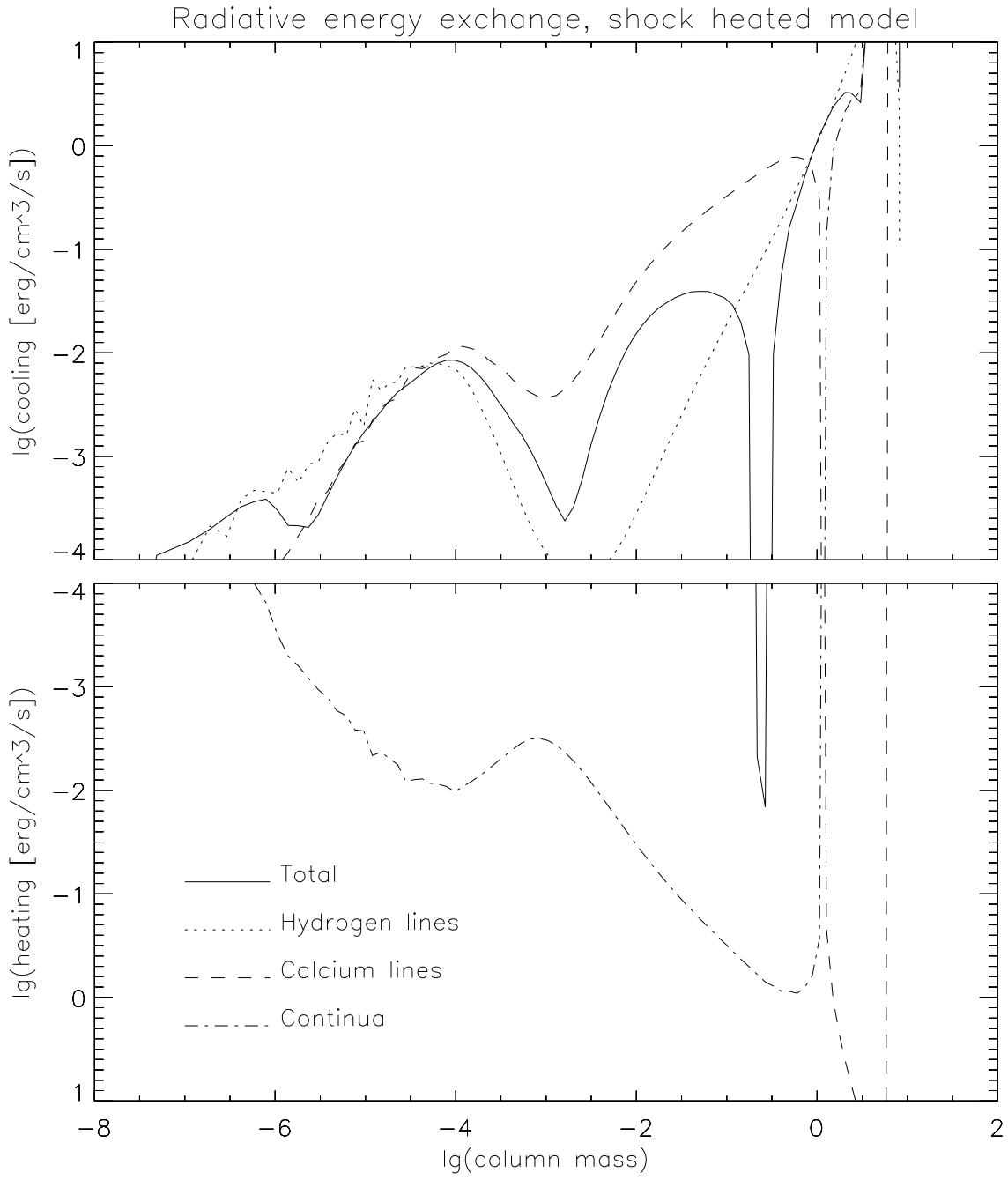

Figure 15: Contributors to total cooling in the dynamic model. The continuum is radiatively heated and the lines of hydrogen and CaII are radiatively cooled in the chromosphere. The line cooling exceeds the continuum heating, and this results in a total radiative cooling of the gas.

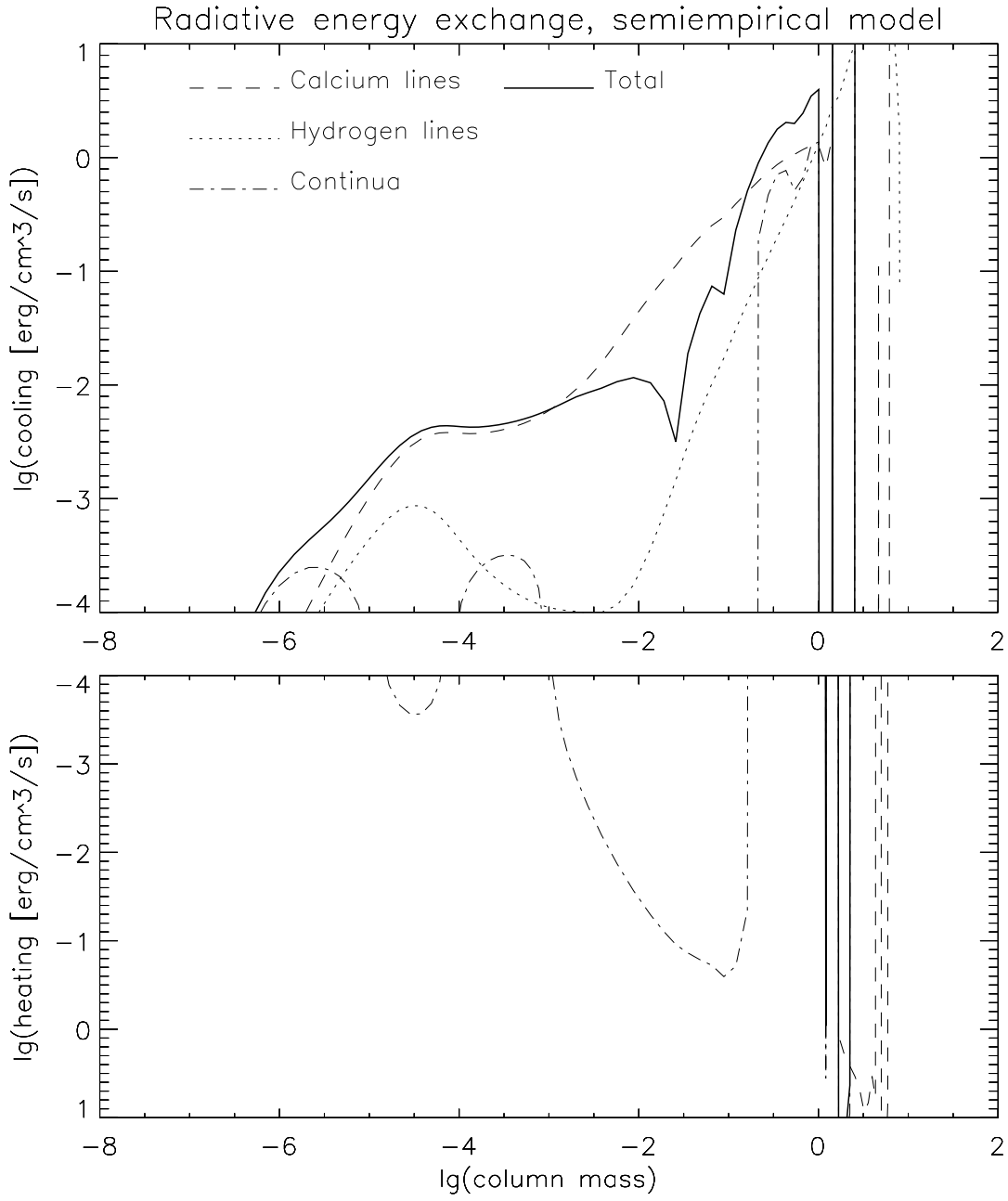

Figure 16: Contributors to total cooling in the semiempirical model. The continuum radiative energy exchange is negligible compared to the cooling of the CaII lines in the chromosphere. The lines of hydrogen contributes to cooling in addition to the lines of CaII which results in a total cooling. The CaII line cooling exceeds the continuum heating in the temperature minimum region around $lg(column\ mass) = -2$, and this results in a total radiative cooling of the gas.

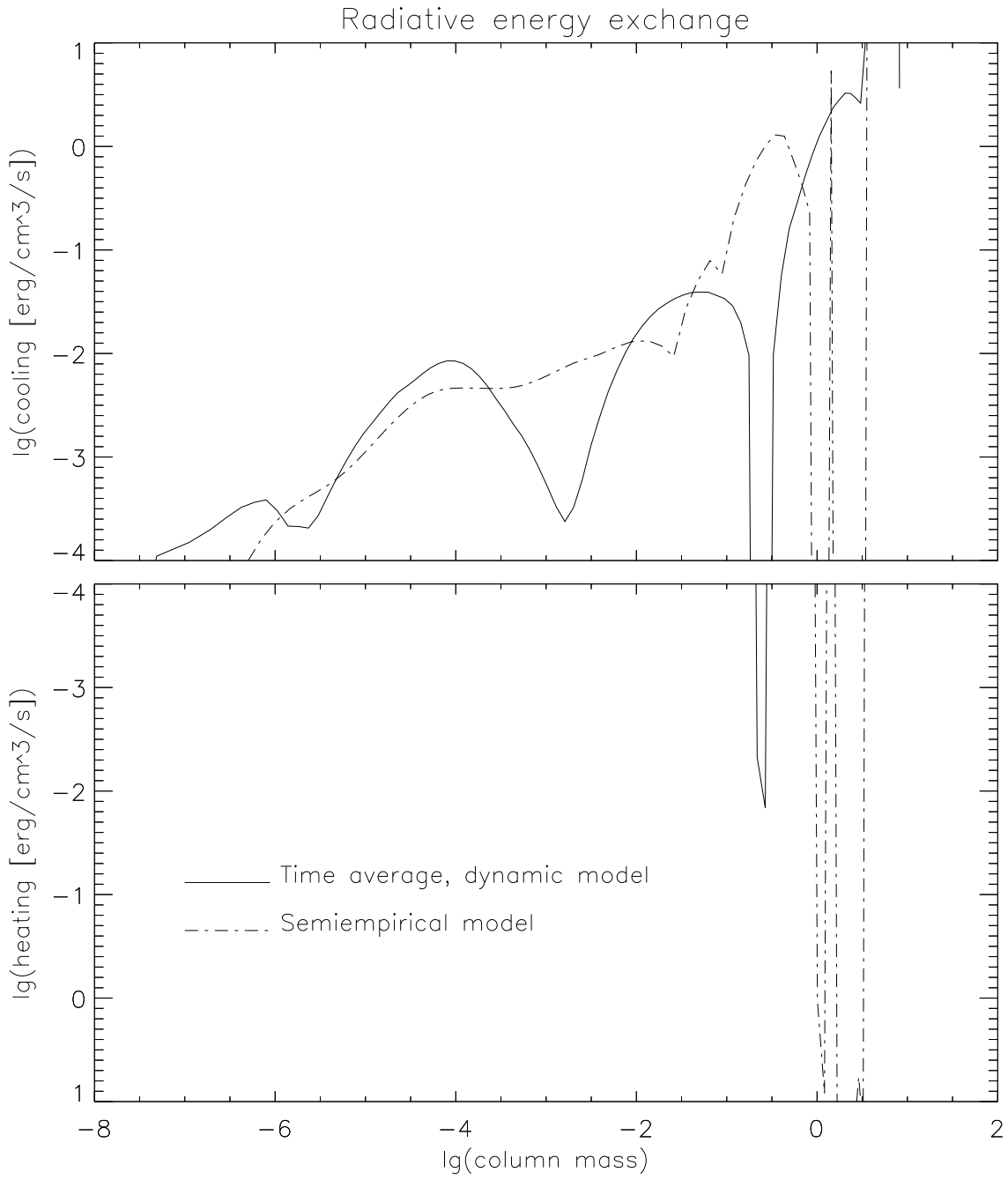

Figure 17: A comparison of total cooling in the dynamic and semiempirical models. The total cooling rates do not deviate more from each other than a factor of two in the middle and upper chromosphere in the interval $lg(column\ mass) = [-7.0, -3.5]$. The deviation is typically a factor of ten on the photospheric side of the temperature minimum region around $lg(column\ mass) = -0.5$, and in the lower chromosphere around $lg(column\ mass) = -2.75$.

The signs can be unequal as well. The hydrogen cooling rates are similar in the low chromosphere and temperature minimum region. The same is true for the CaII line cooling. The hydrogen cooling rate is much lower in the static model compared to the dynamic model in the middle and upper chromosphere. The CaII cooling rates are similar in the middle and upper chromosphere.

The total cooling rates of the dynamic and static model do not deviate more from each other than a factor of two in the middle and upper chromosphere. The difference is typically a factor of ten in the temperature minimum region and the lower chromosphere. The semiempirical model can thus at best be used to estimate the time average of the radiative cooling in the middle and upper chromosphere, but not in lower layers.

The temperature structure uncertainties found in section 6.1 determine the cooling uncertainties for the semiempirical model. These uncertainties are only important in the vicinity of $lg(column\ mass) = -5$ and above $lg(column\ mass) = -6$, such that the overall disparities between semiempirical and dynamic cooling rates are not significantly affected.

It seems very difficult or perhaps impossible to conclude which mechanisms that heat the dynamic atmosphere from a semiempirical model since the detailed dynamic energy budget is unknown. The internal energy change during the observation of the semiempirical reference spectrum must also be taken into consideration.

7 Shock perturbation on constant heating

7.1 Observed and computed temporal behavior of CaII H and K line profiles

The characteristic time-evolution of the H-line is reviewed. Comparisons are done with the simulated profile of the pre-heated atmosphere where we find many similarities. Connections between the line profile appearance and the dynamic state in the model atmosphere are discussed.

Following Hale & Ellerman (1904) we denote the absorption at line center H3, the emission peak on the violet side of the line center H2V, and the emission peak on the red side H2R. The absorption troughs between the line wings and the emission peaks are denoted H1V and H1R. Similar labels are used for the K line. The H2V or K2V emission peaks can be seen as round bright grains of 1-2Mm in diameter that covers the entire solar image in spectroheliograms. See figure 18. These emissions are therefore also denoted by "bright grains".

7.1.1 Observed behavior

The extensive observational literature of the H and K lines of CaII is reviewed by Rutten & Uitenbroek (1991). Cram & Damé (1983) discuss the time resolved H-line. The observations were done by D.R. Brown and H.A. Mauter on 1976 November 9, using the Vacuum Tower Telescope at Sacramento Peak Observatory. Since the H and K lines have similar evolution patterns in time, we will only summarize their discussions of the H-line by listing the most important signatures. Only internetwork regions are considered, since the dynamic model represents these areas.

1. Spatial and temporal analysis show that bright grains are much less prominent in H2R than they are in H2V. About 75% of the grains visible in H2V are visible in H2R. Some regions are bright in H2R and dark in H2V.

2. Temporal analysis of the H line profile shows an enormous variety of patterns. A typical evolution pattern is described as follows. First, a brightening appears symmetrically in the far wings, and sweeps toward the line center with decreasing spectral velocity. At the same time, H3 gradually shifts to red. The brightenings outline the "dark whiskers" seen in the wavelength-time diagrams.

   When the brightenings reach the H1 regions, the core becomes strongly asymmetric, with a stronger H2V peak than H2R peak and maximum redshifted H3 absorption. As the H2V peak fades, H3 shifts sharply to the the violet.

   The H2R intensity is higher than the H2V intensity immediately after the H3 shift, although a prominent H2R peak is seen only rarely at this specific phase.

   In many cases, the wing brightening starts to fade before the H2V bright grain reaches its maximum intensity. A sudden shift of H3 to the violet usually coincides with the disappearance of the wing brightening, which outlines the next dark whisker.

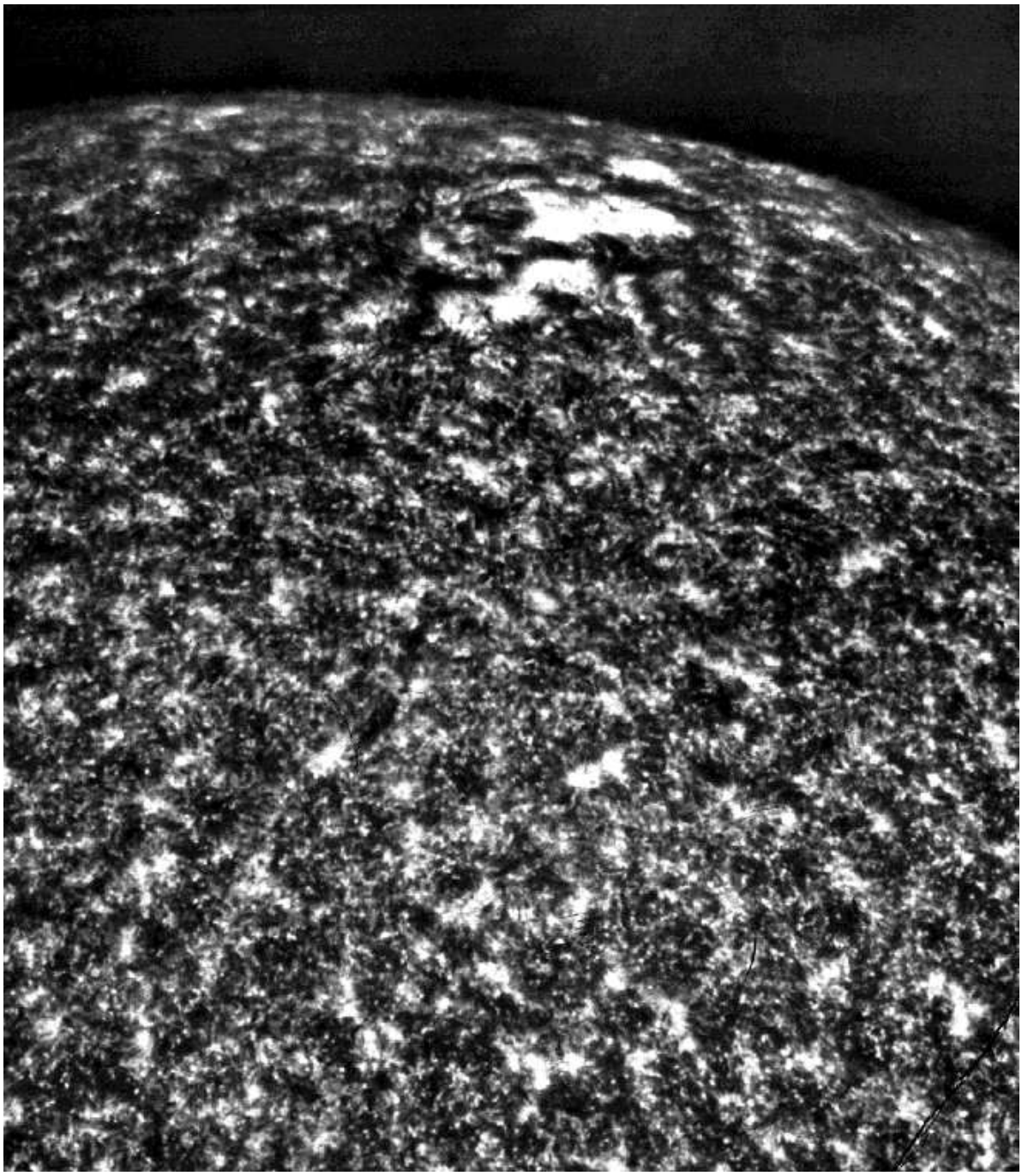

Figure 18: This spectroheliogram in the wavelength interval around K2V shows clearly the bright grains as small dots between bright network regions. It was taken by Bruce Gillespie with the east auxiliary of the McMath Solar Telescope, National Solar Observatory.

3. Although most of the internetwork grains seem to arise from bright wing contractions, there are cases where either one of these features appears without the other. The full range of behavior is thus tremendously diverse. The absence of regular patterns reflects the fact that the chromospheric oscillation is a nonlinear phenomenon involving interactions between several wave packets simultaneously.

4. The location of maximum intensity of the H2V grains is approximately 10 pm or 0.1Å to the violet side of the center rest center wavelength. The grain diameter is in the range 1-2 Mm, or slightly less than the thickness of the solar atmosphere including the photosphere and the chromosphere.

5. The maximum H3 redshift is in the range of 5-10 km/s. The maximum blueshift is smaller than the maximum redshift.

6. 2-5 grains are occurring at the same spatial location with a period close to 180 seconds between longer time intervals of no grains.

7.1.2 Computed behavior of the line profile related to the atmospheric state.

The simulations with the additional heating term on a column mass scale reproduces almost all of the features described above. The "dark whisker" pattern in the line wings, the Doppler excursions in the line core, the H2V/H2R intensity asymmetry and the pulsation period of approximately 3 minutes agrees very well with the observed profile. The wavelength displacement of the bright grains of approximately 0.1Å agrees with the simulation when a microturbulence of 2km/s is applied. The main difference is that there is one grain almost every 180 seconds in the simulations.

A comparison between the simulated profile and an observed sequence (Lites et al. 1993) is shown in figure 19. The velocity field at the lower boundary is taken from the Doppler shifts in the line core of a photospheric FeI line observed at the same slit position as the H-line observations. Comparisons between observed and computed profiles are therefore possible.

Connections between modelled atmospheric dynamics and the line profile evolution for a typical sequence can be summarized as follows:

1. The H3 intensity is formed at the highest layers of the line formation depths. Maximum H3 blueshift occurs at the same time as the onset of wing brightening in the far wings. The H3 blueshift is due to outward moving layers of high velocity in post-shock regions of the shock that just passed the H3 formation depth.

   The following gradual H3 shift from the blue side of the line core to the red reflects that outward motion of the H3 forming layer changes to downward motion.

   Observed and computed Doppler-shift evolution of this phase is linear in time. We thus have a parabolic trajectory or ballistic motion between the upthrusts caused by the shocks.

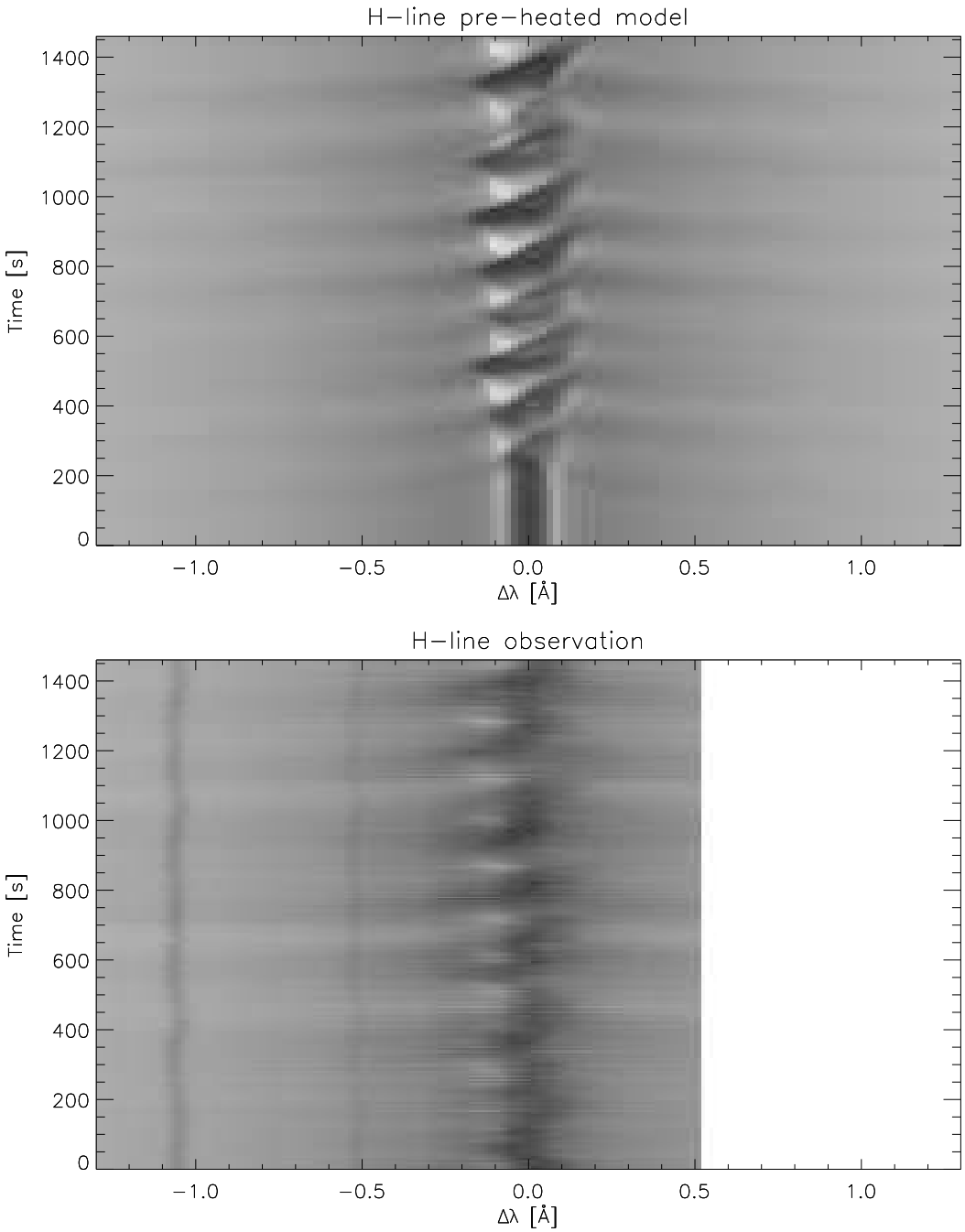

Figure 19: A comparison between the simulated profile of the pre-heated atmosphere and an observed sequence (Lites et.al. 1993a). The velocity field at the lower boundary is taken from the observed slit position from a photospheric FeI line such that observed and computed profiles can be compared at equal times. The dark whiskers, the position of the bright grains and the oscillation period close to 180 seconds agrees very well to the observation. There is some disparity between the locations of the bright grains along the time axis due to different atmospheric oscillation patterns. This can partially be explained by the transients occurring after the lower boundary piston is set into action.

2. The symmetric wing brightening that propagates towards the line center originates from an outward propagating perturbation of increased temperature set up by the outward propagating wave. Increased temperature is associated with increased density.

   Unity optical depth reaches higher altitudes towards the line core, such that the inner wings probes higher layers than the outer wings. When the increased temperature propagates outwards, the wing brightening propagates towards line center. The decreasing spectral velocity toward line center reflects the increased gradient of unity optical depth with respect to height.

3. Gas motion in outwards direction occurs at grain forming depths when the wing brightening reaches H1. Downdraft from layers above, and upward motion below creates a shock front that reaches a strength of approximately 10 km/s at the time of maximum H3 redshift. This corresponds to high atmospheric compression of the upper layers. A source function peak is formed in the post-shock region. The opacity pattern is now determined by the shape of the velocity field. This determines the appearance of the emission peaks originating from the source function peak. The H2V intensity is now maximum.

4. The sudden H3-blueshift occurs when the shock passes the H3 forming layer. Blueshifted opacity due to upward motion in post-shock regions increases the formation height at the position of the H2V bright grain. The source function has a lower value here, such that the violet emission peak fades. The red emission peak can now originate from the source function peak further down, revealed by the blueshifted opacity due to upward motion in post-shock regions.

   This leads to a H2V/H2R intensity ratio less than one after the sudden H3 transition. The cycle is completed by starting at point 1 again.

5. A source function peak occurs at all times. The peak is located in the interval $\tau_{5000} = [-5.5, -5]$. These are depths where non-linear wave steepening sets in and shocks are formed. The value of the source function peak at these depths is increased when a shock is present due to the high post-shock temperatures. High temperatures will also increase the thermal coupling parameter and thus the coupling to the Planck distribution. The source function decreases where the escape probability exceeds the thermal coupling parameter due to optically thinner layers.

The majority of observed features can thus be explained by photospheric piston exitation and a pre-heated chromosphere.

7.2 Physics of the K2V and the H2V grains

The physics of the *calcium grains* of the pre-heated model with microturbulence of 2km/s are studied in this section. Since the dynamic behavior seen both in observations and simulations are similar for the H and K lines, only the H line is analyzed in detail.

The state of the atmosphere when the H2V bright grain has its maximum intensity is studied. This is done at two different occasions, at t=1250s where the H2R emission is present and at t=1590s where it is absent. It must be noted that the atmospheric state described here is sufficient but not necessary for grain formation, since only one simulation model is investigated.

First, the opacity pattern and its connection to velocity and density is explained. Second, the source function that produces the bright grains is explained qualitatively in a probabilistic view. Third, we explain the H2R and H2V emission peaks and their intensity difference. Fourth, we compare our results with previous work by other authors. Finally we discuss the grain intensity response and the grain frequency response to atmospheric dynamics.

7.2.1 The opacity

The opacity is the quantity that determines how and where the source function is probed. It is therefore necessary to examine its behavior in the depth-frequency plane to explain the line profile at the time of grain formation. The opacity for a line transition can, when the emission profile equals the absorption profile, be written:

$$\chi_\nu = (n_i B_{ij} - n_j B_{ji})\phi_\nu \frac{h\nu_{ij}}{4\pi} \tag{51}$$

n_i and n_j are respectively the population densities in the lower and upper level of the line transition. ϕ_ν is the normalized absorption profile. B_{ij} is the Einstein absorption coefficient, and B_{ji} is the Einstein coefficient for stimulated emission. ν_{ij} is the transition frequency. Stimulated emission and thus the downward transition rate $n_j B_{ji}$ can be neglected in the case for the H and K lines.

The ground level population is approximately equal to the particle density of CaII, since the sum of the populations for all other levels is much smaller compared to the ground level population. The CaII density is approximately equal to the Ca density in the chromosphere, but this assumption can lead to errors when CaII ionizes to CaIII in the post-shock region. The opacity expressed by the Ca abundance relative to hydrogen A_{Ca} becomes when these approximations are used:

$$\chi_\nu = \frac{\rho A_{Ca}}{GRPH} B_{ij}\phi_\nu(V,T,\xi)\frac{h\nu_{ij}}{4\pi} \tag{52}$$

$GRPH$ is the total density divided by the hydrogen particle density, i.e. total mass per hydrogen atom. This constant has the value $2.38 \cdot 10^{-23}$ grams/hydrogen atom for solar abundances.

The profile function depends on macroscopic velocity V, microturbulence ξ and temperature T. The assumptions of a Voigt profile and CRD (complete re-distribution) are

used in the simulations. The Voigt profile takes into account the thermal and microturbulent motions of the gas, and the natural broadening of the energy levels in accordance to the uncertainty principle. Other broadening mechanisms such as collisional broadening are non-dominant in the low density layers of the chromosphere we are primarily concerned with. In the cases of interest here, the Voigt damping parameter will satisfy the condition $a \ll 1$. If we are considering the line center frequency in the frame of the macroscopic motions of the gas, the value of the Voigt profile at line center ν_0 can be written:

$$\phi_{\nu_0} = \frac{1}{\pi^{\frac{1}{2}} \Delta\nu_D} \tag{53}$$

$\Delta\nu_D$ is the Doppler-width of the profile, which is determined by the most probable thermal velocity and the parameter for microturbulence:

$$\Delta\nu_D = \frac{[\frac{2kT}{m_{ion}} + \xi^2]^{\frac{1}{2}} \nu_0}{c} \tag{54}$$

Substituting eq. 53 into eq. 52 gives:

$$\chi_{\nu_0} = \frac{A_{Ca} B_{ij} h\nu_{ij}}{GRPH4\pi^{\frac{3}{2}}} \frac{\rho}{\Delta\nu_D} \tag{55}$$

This equation will be used to discuss the opacity at the center of the profile following the macroscopic motion of the gas. The wing opacity will be discussed qualitatively by using the facts that the opacity in the whole profile is proportional to the density, and that broadening increase by microturbulence and thermal motions of the gas decreases the core opacity and increases the wing opacity. The opacity for t=1590s are characterized by the following atmospheric properties (figures 20 and 21):

1. There is one shock front at $lg(\tau_{5000}) = -6$ where down-falling matter at -9 km/s breaks to -1 km/s (figure 20). The post-shock region contains an outward moving layer with a maximum velocity of approximately 2 km/s.

2. The opacity at line center in the Lagrangian frame in figure 21 falls off rapidly in the outward direction. This is caused primarily by the density decrease. The influence from variations in Doppler-width is not significant at any heights. The density jump at the shock causes a relatively small opacity jump.

3. The opacity in the wings below and above the shock in figure 20, is also dominantly influenced by the decreasing density.

4. In the contour plot (figure 20), one can see that the velocity curve traces out the "opacity ridge". Thus the velocity controls the shift of the opacity profile as expected. The down-falling matter above the shock causes a redshift that decreases the line of sight opacity on the blue side of the rest center wavelength and increases the line of sight opacity on the red side compared to unshifted profiles. Below the shock on the blue side, the velocity is slightly positive, causing increased opacity at approximately the frequency and depth for bright grain formation.

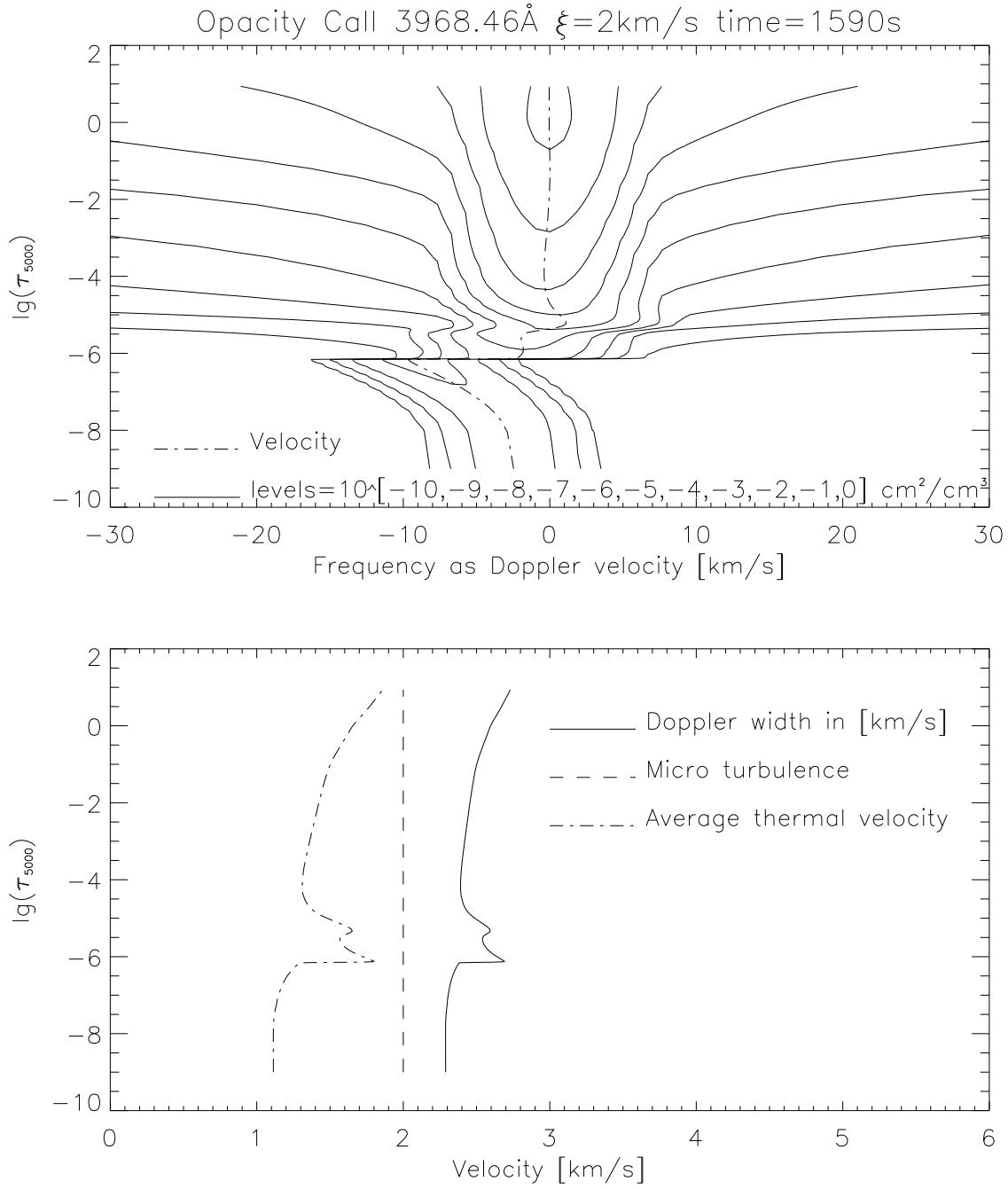

Figure 20: *Upper panel.* Total opacity at t=1590s. The down-falling matter above the shock causes a redshift that decreases the line of sight opacity at positive frequencies corresponding to positive velocities. The line of sight opacity increases at negative frequencies corresponding to negative velocities. Below the shock at positive frequencies, the velocity is slightly positive, causing increased opacity at approximately the frequency and depth for bright grain formation. *Lower panel.* Contributions to Doppler width. High post-shock temperatures increases the broadening of the profile function.

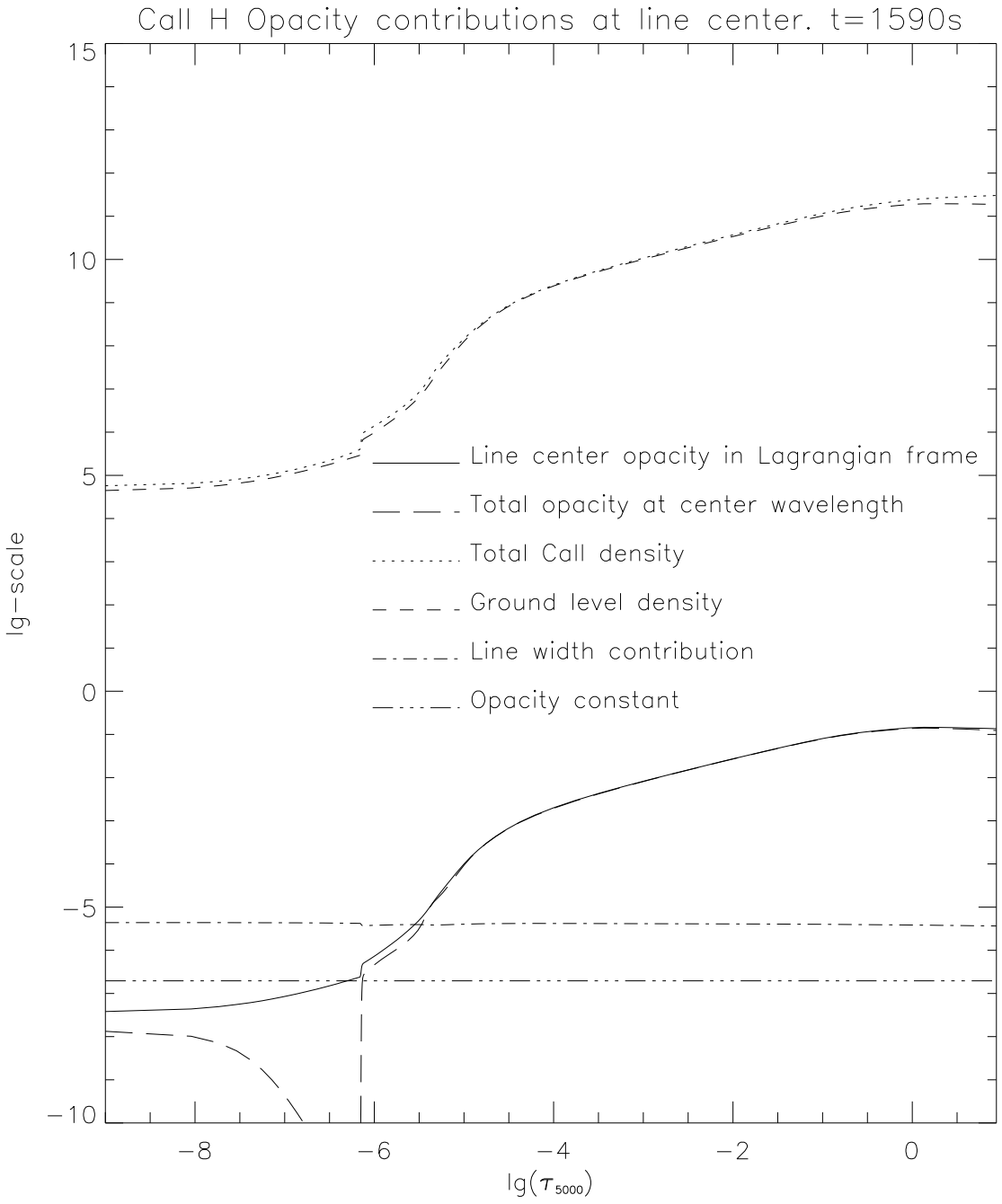

Figure 21: The opacity at line center in the Lagrangian frame falls off rapidly in the outward direction. This is caused primarily by the density decrease. The opacity at the rest center wavelength in the Eulerian frame (long dashes) is always smaller than the opacity at the center of the profile function in the Lagrangian frame (solid) due to the Doppler shifts. The different contributions to opacity are shown on a logarithmic scale, and they can be summed to give the line center opacity in the Lagrangian frame.

The opacity for t=1250s are characterized by the following atmospheric properties: (Figures 22 and 23.)

1. There is one shock front at $lg(\tau_{5000}) = -8$ where down-falling matter at -8 km/s is accelerated upwards to a velocity of 5 km/s (figure 22). Another shock front is just about to form at $lg(\tau_{5000}) = -5.5$ where down-falling matter at -5 km/s hits an outward moving layer with a velocity of 1 km/s. I will also refer to this as a shock, since similar situations occur where a low amplitude shock has formed approximately at the same location. We thus have a double-shock situation.

2. The opacity at line center in the Lagrangian frame in figure 23 falls off rapidly in the outward direction. This is caused primarily by the density decrease. A slight opacity decrease caused by the increase in thermal broadening can be seen below the upper shock.

3. The opacity in the wings below the shocks in figure 22 is also dominantly influenced by the decreasing density. The opacity above the upper shock is smaller than for t=1590s due to a shock location at lower column mass.

4. The opacity shifts occurring at the lowest shock determines the relevant opacity pattern for the line center regions (figure 22). Down-falling matter above the shock causes a redshift that reveals the blueshifted opacity below at approximately the frequency and depth for bright grain formation. Redshifted opacity at negative velocities increases the line of sight opacity on the red side of the rest center wavelength.

7.2.2 Grain source function

The two situations in the previous section are considered where we have a high amplitude shock at t=1590s, and a wave crest that is about to form a low amplitude shock at t=1250s. I label the two situations as high and low amplitude shock scenarios.

The thermal properties of the shock is entirely set by hydrogen. The temperature increases abruptly when the gas enters the shock front due to viscous work and external compression work. The temperature falls off behind the shock front when electrons with high thermal energy starts to collisionally ionize the hydrogen atoms (Carlsson & Stein 1992b). The temperature profile behind the shock is thus set by the time scales of ionization. The post-shock source function is controlled through the Planck distribution by the temperature if the thermal coupling parameter is greater than the escape probability. Increasing post-shock temperature will then lead to an increasing source function with height. The escape probability increases towards the shock front, and the source function will decrease when the escape probability exceeds the destruction probability. A source function peak is thus created in the grain forming layers in post-shock regions.

Downward motion in pre-shock regions increases the saturation depth (cf. section 5) on the blue side of the Doppler-core in post-shock regions. See figures 24 and 26. The escape probability integral on the blue side of the Doppler-core increases if the saturation frequency

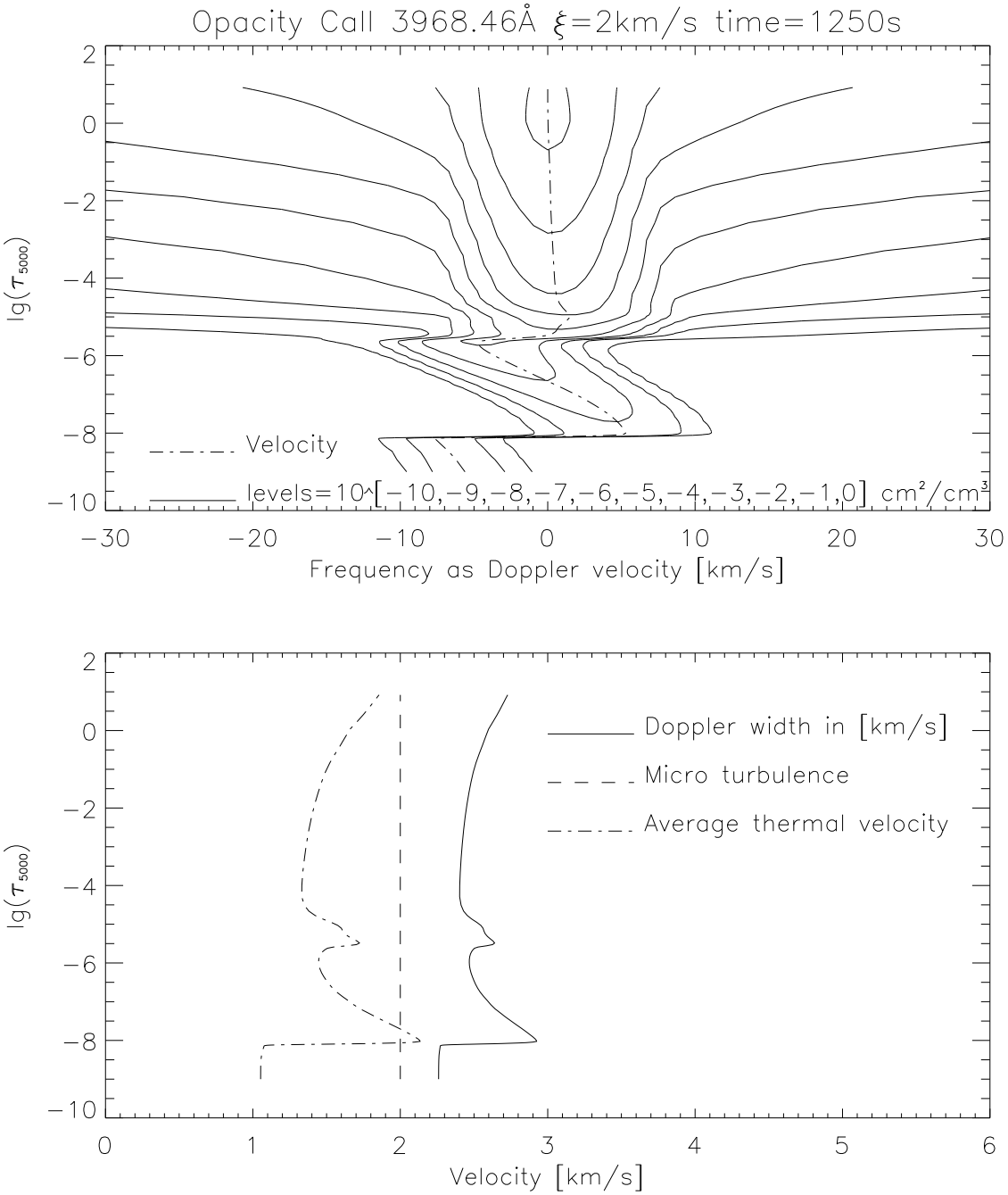

Figure 22: *Upper panel.* Total opacity at t=1250s. The down-falling matter above the shock causes a redshift that decreases the line of sight opacity at positive frequencies corresponding to positive velocities. The line of sight opacity increases at negative frequencies corresponding to negative velocities. Below the shock at positive frequencies, the velocity is slightly positive, causing increased opacity at approximately the frequency and depth for bright grain formation. *Lower panel.* Contributions to Doppler width. High post-shock temperatures increases the broadening of the profile function.

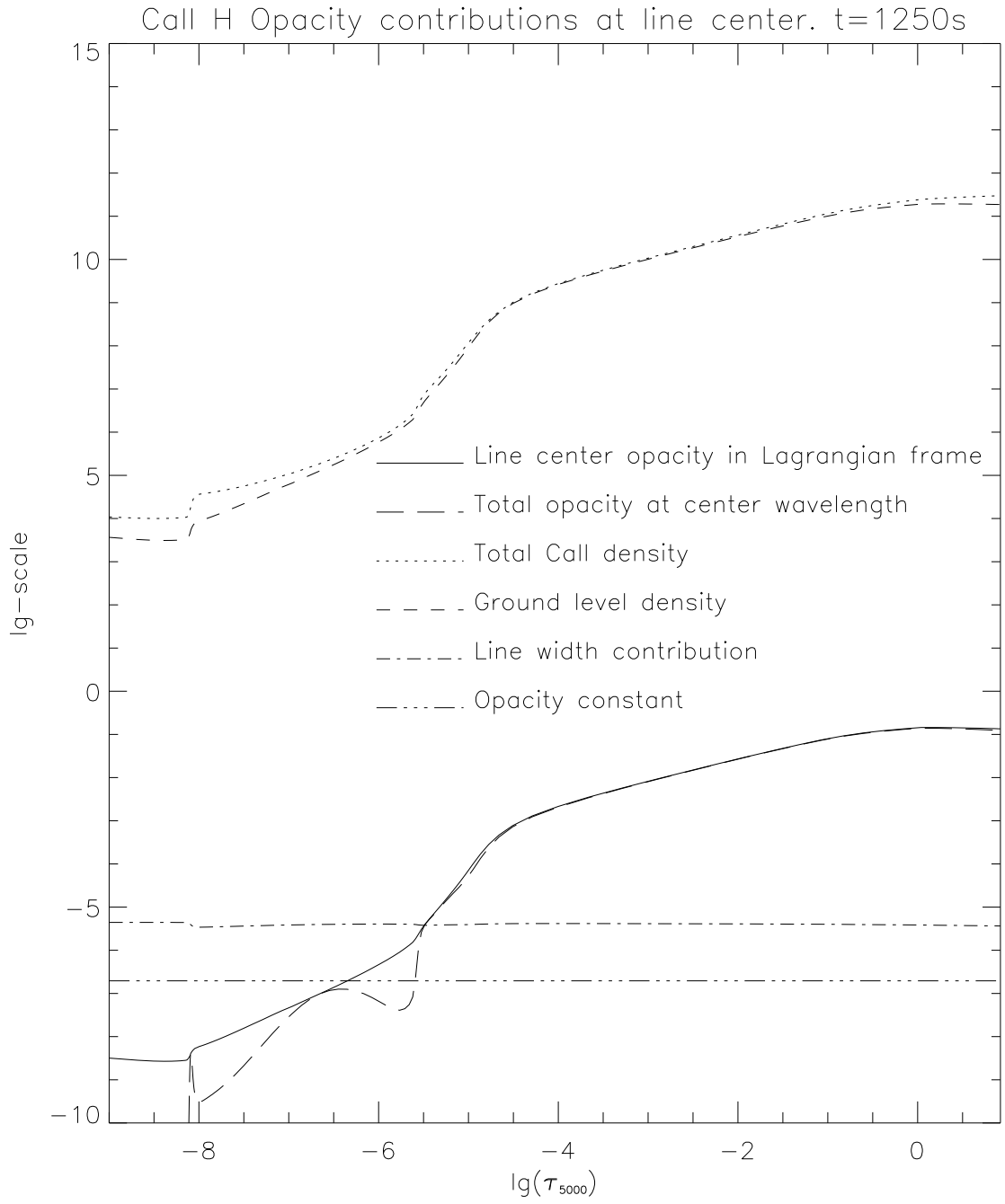

Figure 23: The opacity at line center in the Lagrangian frame falls off rapidly in the outward direction. This is caused primarily by the density decrease. The opacity at the rest center wavelength in the Eulerian frame (long dashes) is always smaller than the opacity at the center of the profile function in the Lagrangian frame (solid) due to the Doppler shifts. The different contributions to opacity are shown on a logarithmic scale, and they can be summed to give the line center opacity in the Lagrangian frame.

decreases, which corresponds to increased saturation depth. The escape probability will also increase if the opacity profile is blueshifted.

Upward motion (blueshift) combined with increased saturation depth leads thus to much higher escape probability on the blue side of the Doppler-core compared to the red side in the grain forming layers. This is true for both time steps. See figures 25 and 27.

Thus *the escape probability on the blue side of the Doppler-core controls the escape probability in the grain forming layers.*

Negative velocity makes the escape probability on the red side of the Doppler-core to exceed the escape probability on the blue side of the Doppler-core in the pre-shock region. See figures 24 and 26. The pre-shock part of the source function peak is thus controlled by the "red" escape probability in both cases.

Immediately above the shock at t=1590s, the source function has a discontinuous jump to a slightly higher value. If the velocity amplitude is high enough, typically 10 km/s, the absorption profile is shifted into higher wing intensity that comes from a layer further down in the atmosphere, and the source function is increased due to the scattering term. Scattering dominates due to the relatively low value of the destruction probability at this level, typically 10^{-4}. This is negligible compared to the escape probability which has almost reached a maximum value of $\frac{1}{2}$.

Mechanisms that take part in forming the source function at the time of grain formation can be summarized as follows:

1. Temperature changes are controlled by shocks or nonlinear waves just before they shock.

2. Low escape probability relative to the destruction probability ϵ, leads to an increase in the source function when the temperature rise towards the shock in the post-shock region.

3. The source function decreases when the escape probability increases due to increased escape from the blue side of the Doppler-core. The local source function maximum is thus created. Outward motion is associated with the increase in escape probability.

4. Differences in escape probabilities for blue and red wings are controlled by the velocity field.

7.2.3 H-core intensity formation

This section explains where the intensity in the frequency interval from H1R to H1V is formed when the H2V bright grain occurs. The two situations for t=1250s where a relatively small H2R intensity peak occurs, and for t=1590s where the H2R peak is absent are discussed.

Observations of the sun and the simulation results show that the intensity of H2V bright grains exceeds the intensity at H2R by typically a factor of 5. The same holds for the K-line.

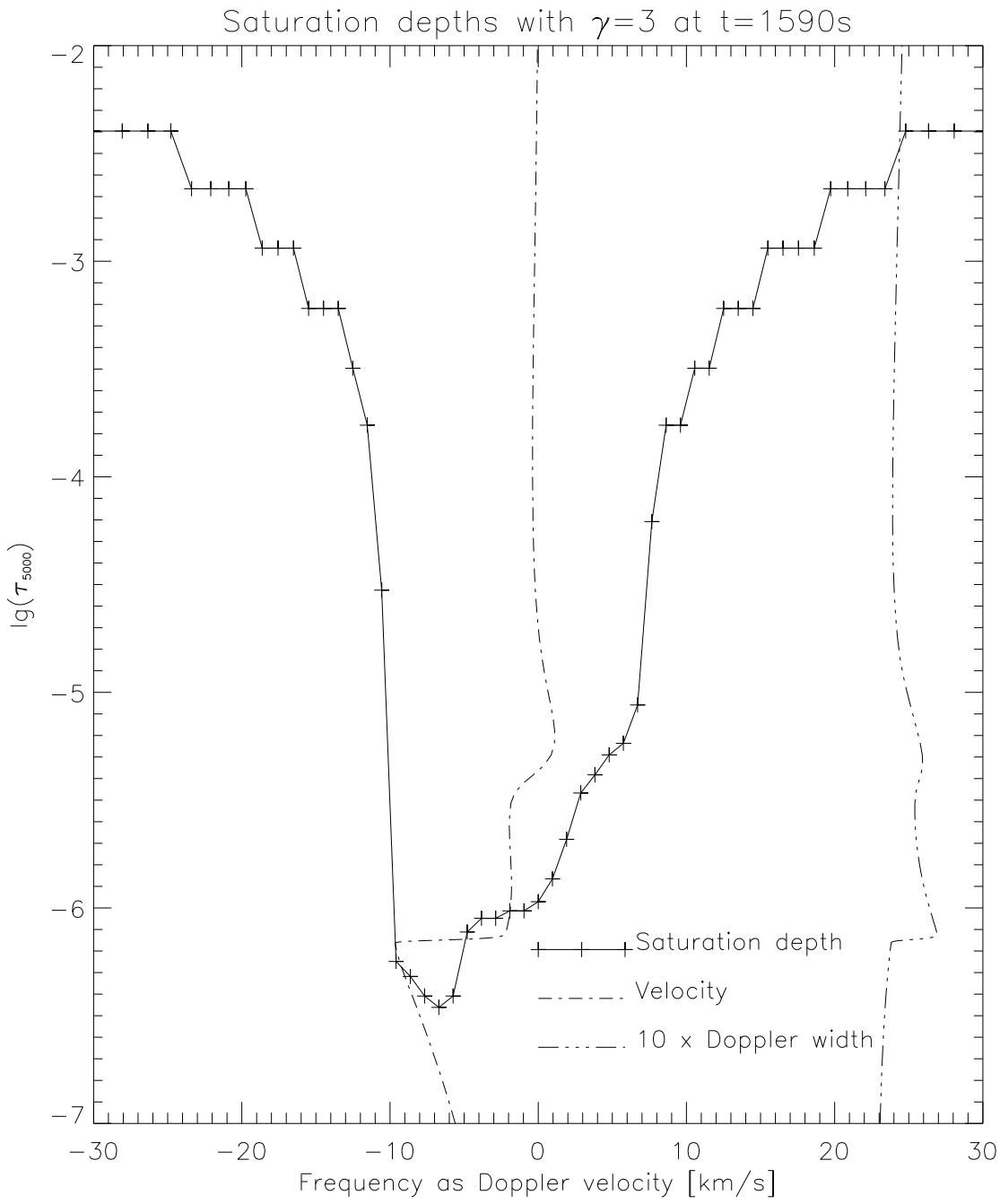

Figure 24: Saturation depths at t=1590s. Optical depth for saturation is chosen as $\gamma = 3$. Redshifted pre-shock opacity increases the saturation depth in post-shock regions. Upward motion combined with increased saturation depth in pre-shock regions increases the escape probability integral.

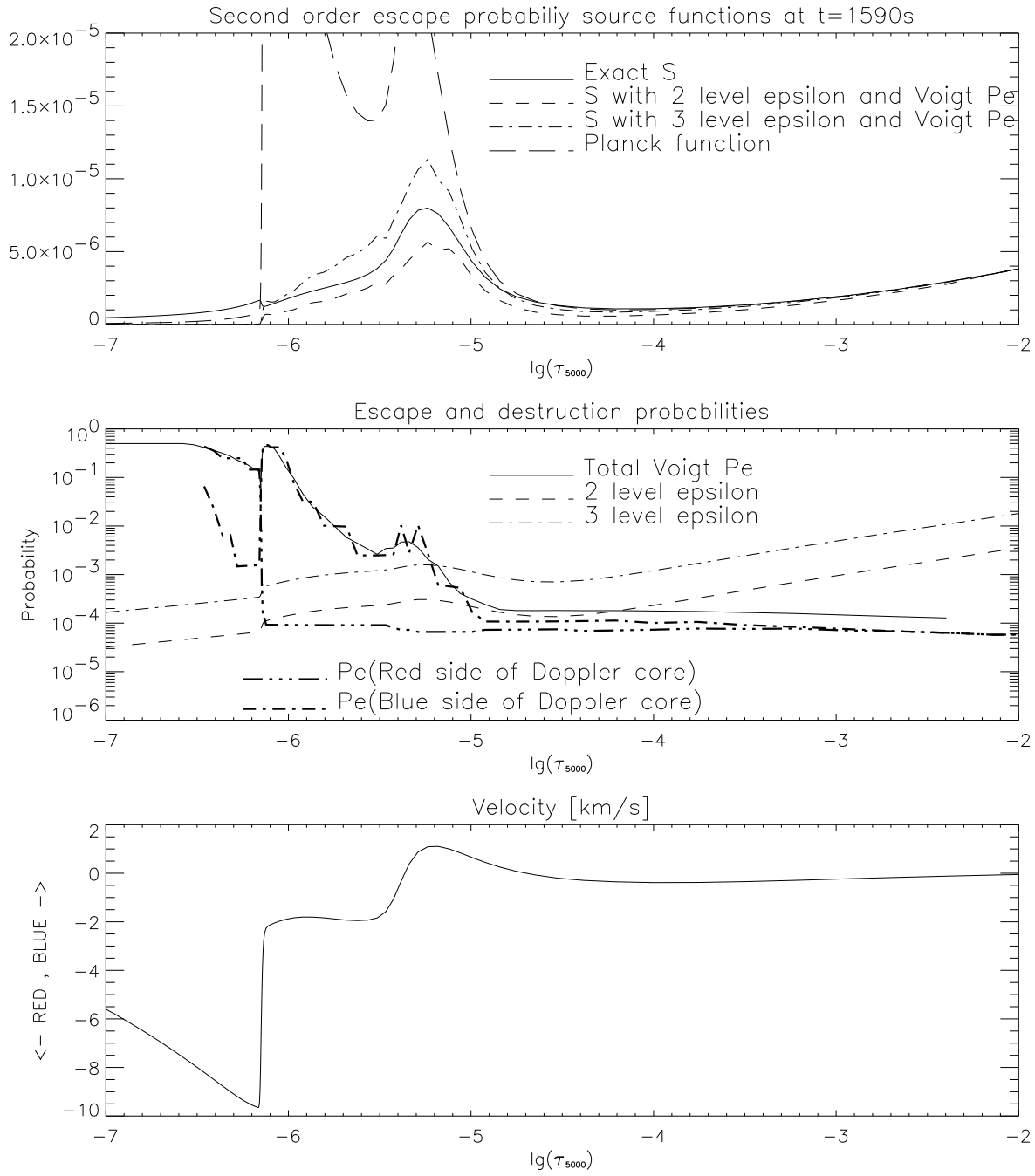

Figure 25: *Upper panel.* The exact source function is compared with the approximated source function. The escape probability is computed from the Voigt profile and saturation depths. The destruction probability ϵ is computed from 2 and 3 level approximations. *Middle panel.* The escape probability on the blue side of the Doppler-core controls the variation of the source function when the destruction probability is less than the escape probability. *Lower panel.* The velocity field controls the location of the opacity profiles, and thus the different escape probabilities for the blue and red side of the Doppler-core.

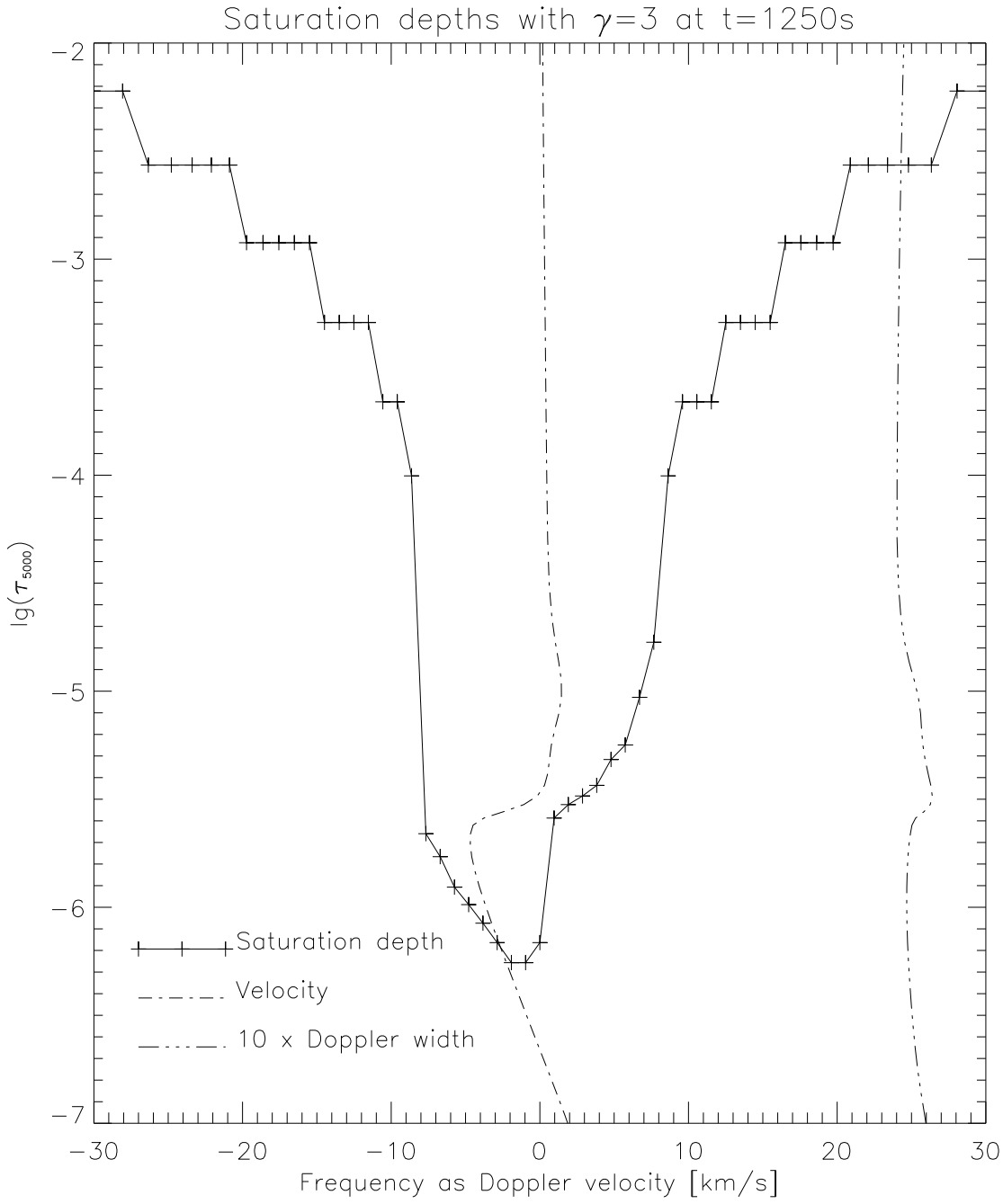

Figure 26: Saturation depths at t=1250s. Optical depth for saturation is chosen as $\gamma = 3$. Redshifted pre-shock opacity increases the saturation depth in post-shock regions. Upward motion combined with increased saturation depth in pre-shock regions increases the escape probability integral.

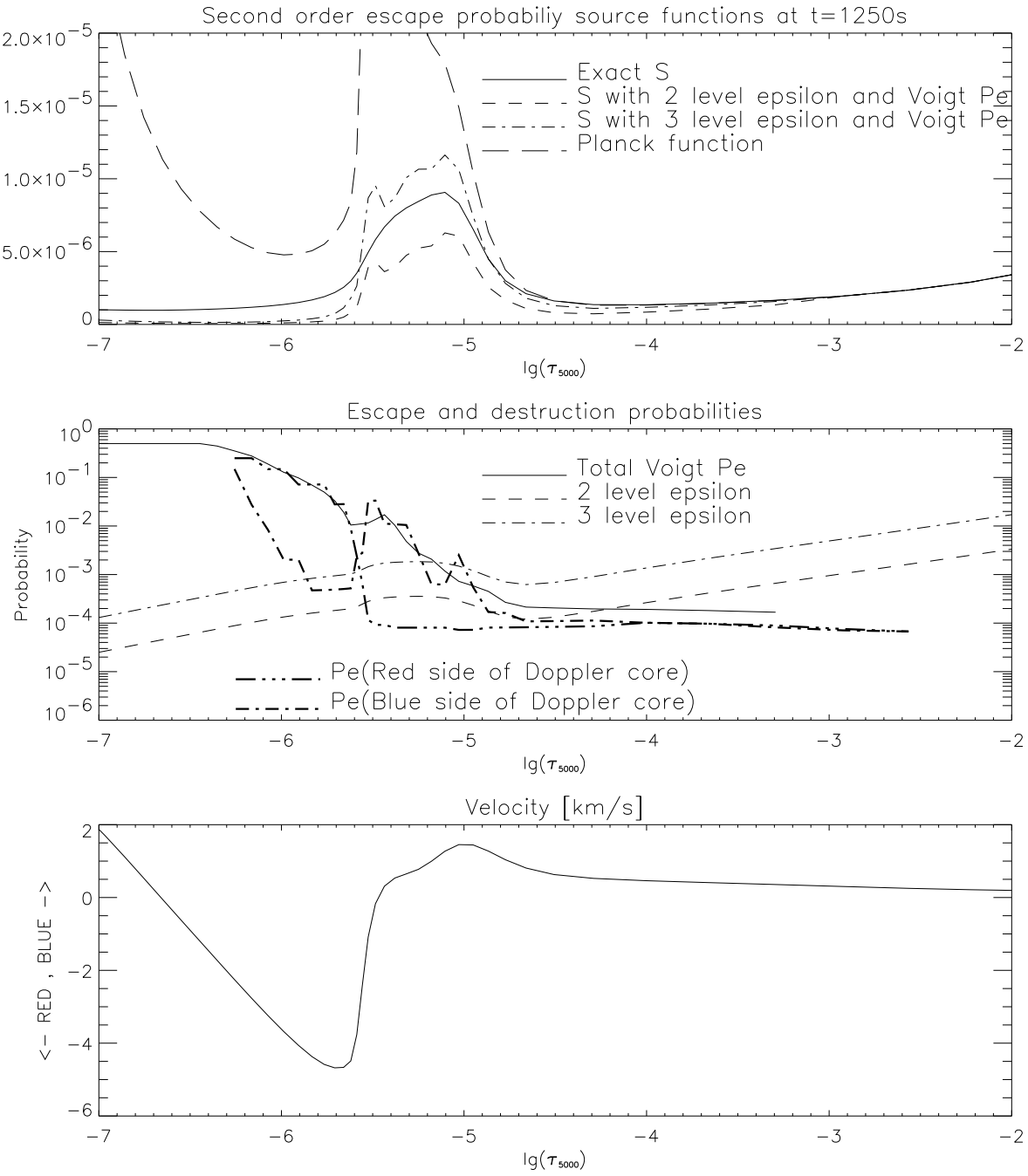

Figure 27: *Upper panel.* The exact source function is compared with the approximated source function. The escape probability is computed from the Voigt profile and saturation depths. The destruction probability ϵ is computed from 2 and 3 level approximations. *Middle panel.* The escape probability on the blue side of the Doppler-core controls the variation of the source function when the destruction probability is less than the escape probability. *Lower panel.* The velocity field controls the location of the opacity profiles, and thus the different escape probabilities for the blue and red side of the Doppler-core.

The Eddington-Barbier relation states that the emergent intensity is equal to the source function at an optical depth equal to the cosine of the viewing angle. This implies equal intensities for H2V and H2R at frequencies where the chromospheric source function maximum is reached. The Eddington-Barbier relation can therefore not be used in explaining the physics of the observed emission peaks. Another theoretical approach has to be developed in order to reveal the dominating causes of the different H2V and H2R intensities. Two approximations are done here in doing this:

1. The chromospheric source function peak is approximated by a box-function centered on τ_{0c} with a constant value S in the interval $\Delta\tau_0$ and zero value elsewhere. τ_0 is the reference optical depth scale.

2. The opacity ratio $\frac{\chi_\nu}{\chi_0}$ or equivalently the gradient in monochromatic optical depth on the reference scale is taken to be constant in the interval $\Delta\tau_0$.

The intensities originating from the approximated source function at an arbitrary pair of frequencies can be found. Let an arbitrary monochromatic optical depth γ at these frequencies coincide with τ_{0C}. The frequencies at each side of the Doppler-core are then given by $\tau_\nu(\tau_{0c}) = \gamma$. γ will be close to unity at emission peak frequencies.

The definitions and approximations given above leads to:

$$\tau_\nu = (\gamma - \frac{\chi_\nu}{\chi_0}\tau_{0c}) + \frac{\chi_\nu}{\chi_0}\tau_0 \tag{56}$$

The contribution to intensity from the approximated source function gives:

$$I_\nu^+(\tau_0 = 0, \mu = 1) = S\frac{\chi_\nu}{\chi_0}\int_{\Delta\tau_0} e^{-\tau_\nu} d\tau_0 \tag{57}$$

Eq. 56 and 57 then gives:

$$I_\nu^+(\tau_0 = 0, \mu = 1) = Se^{-\gamma}(e^{\frac{1}{2}\frac{\chi_\nu}{\chi_0}\Delta\tau_0} - e^{-\frac{1}{2}\frac{\chi_\nu}{\chi_0}\Delta\tau_0}) \tag{58}$$

In the line core region the relation $\frac{\chi_\nu}{\chi_0} \gg 1$ holds. The optical depth interval bounding the source function is of order 10^{-5}. It is thus necessary to investigate both limits of small and great exponential terms compared to unity. $\frac{1}{2}\frac{\chi_\nu}{\chi_0}\Delta\tau_0 \gg 1$ gives:

$$I_\nu^+(\tau_0 = 0, \mu = 1) = Se^{-\gamma}e^{\frac{1}{2}\frac{\chi_\nu}{\chi_0}\Delta\tau_0} \tag{59}$$

$\frac{1}{2}\frac{\chi_\nu}{\chi_0}\Delta\tau_0 \ll 1$ gives:

$$I_\nu^+(\tau_0 = 0, \mu = 1) = Se^{-\gamma}\frac{\chi_\nu}{\chi_0}\Delta\tau_0 \tag{60}$$

All three equations 58, 59, 60 show that:

1. The intensity is increased if the opacity or gradient in optical depth is increased. This is due to the increased emissivity $\eta_\nu = S\chi_\nu$.

2. The intensity is increased if the source function increases.

3. The intensity is increased if the width of the source function peak increases.

4. The intensity is decreased if γ increases.

γ increases by selecting frequencies close to the Doppler-core. The core opacity above the source function peak will then reduce the emergent intensity. γ decreases by selecting frequencies far from the Doppler-core. The reduced opacity will then reduce the emergent intensity. Maximum intensity occurs at the frequency where the opacity is high enough for significant emission, but low enough such that the exponential damping does not dominate.

Figures 28 and 29 show the H-line profiles at t=1590s and t=1250s with the contribution function to intensity and the integrand to optical depth presented as a contour plot. Curves of equal optical depth are plotted together with the velocity and the line source function. Figures 20 and 22 show the opacity as a contour plot. These figures are highly informative, and they are used in discussing which features dominate the formation of the H-profiles. Frequency is in the following denoted by the corresponding Doppler-velocity to be used in comparison with the macroscopic velocity field.

The atmospheric properties during grain formation at t=1590s when the H2R emission peak is absent are (figure 28):

1. *K3 intensity.* Down-falling matter above the shock front shifts the contribution functions near the line core to the region -15 km/s to -2 km/s due to the opacity shift. The pre-shock velocity is approximately -9 km/s. The relatively low value of the source function above the shock provides low intensity in the core.

2. *H2R intensity.* The pre-shock opacity is not high enough to keep the optical depth at unity in the pre-shock region at -12 km/s. There is relatively low opacity in the post-shock region at this frequency since the pre-shock opacity profile is redshifted relative to the post-shock opacity. Optical depth unity is thus reached further down at higher densities relatively far from the shock. This is approximately at the source function minimum. Sudden jumps for the curves of equal optical depth, indicates the low gradient in monochromatic optical depth or low opacity in the post-shock region. The source function has a peak where the opacity is low. *The velocity difference at the shock is sufficiently high such that the pre-shock opacity at the source function peak is too small to create the emission peak.*

3. *H2V intensity.* The opacity shift caused by the down-falling matter reveals the post shock region of high opacity where the source function peaks. The steep gradient in monochromatic optical depth can be seen in the figure as small spacing between the opacity curves. The high opacity at the emission peak frequency is caused by a positive velocity of approximately 1 km/s at the depth of the source function maximum. *The relatively high H2V intensity (compared to the red side) occurs due to high opacity at the source function peak.*

4. *K1 intensities.* The intensity in the region above 10 km/s is formed around the source function minimum, creating the intensity minimum around 15 km/s. The

opacity pattern is controlled by the density and not the velocity. The intensity below -15 km/s is formed below the source function minimum. The intensity minimum is thus absent.

The atmospheric properties during grain formation at t=1250s when the H2R emission peak is present are (Figure 29):

1. *K3 intensity.* Down-falling matter above the shock front shifts the contribution functions near the line core to the region -10 km/s to 5 km/s due to the opacity shift. The pre-shock velocity is approximately -4 km/s. The relatively low value of the source function above the shock provides low intensity in the core.

2. *H2R intensity.* The H2R emission peak occurs at -9km/s. The opacity in the post-shock region at this frequency is now higher since the pre-shock opacity profile is less redshifted relative to the post-shock opacity profile. The jumps for the curves of equal optical depth is now smaller, indicating a higher gradient in monochromatic optical depth. *The velocity difference at the shock is sufficiently low such that the pre-shock opacity at the source function peak is sufficient to create the emission peak.*

3. *H2V intensity.* The opacity shift caused by the down-falling matter reveals the post shock region of high opacity where the source function peaks. The steep gradient in monochromatic optical depth can be seen in the figure as small spacing between the opacity curves. The high opacity at the emission peak frequency is caused by a positive velocity of approximately 2 km/s at the depth of the source function maximum. *The relatively high H2V intensity (compared to the red side) occurs due to high opacity at the source function peak.*

4. *K1 intensities.* The intensity in the region above 10 km/s and below -15km/s is formed around the source function minimum, creating the intensity minima. The opacity pattern is controlled by the density and not the velocity.

The main reasons for the intensity differences between H2V and H2R emission peaks and the absence or presence of the H2R emission peak are summarized as follows:

Consider a velocity difference due to a shock between two neighboring slabs where the upper slab has an opacity profile redshifted relative to the underlying profile. The lower slab contains the source function maximum. Unity optical depth reaches the post-shock region where the source function peaks at the H2V and H2R frequencies. The opacity at the source function peak will thus be higher at H2V frequencies compared H2R frequencies. The H2V intensity will thus be higher than the H2R intensity (equation 58), and the H2V/H2R intensity ratio will be greater than one.

The opacity difference in the post-shock region at emission peak frequencies is the main reason for the differences between H2V and H2R intensities.

The opacity difference and the H2V/H2R intensity ratio increases if the shock strength or Mach-number increases. The H2R peak vanishes if the Mach-number is sufficiently high.

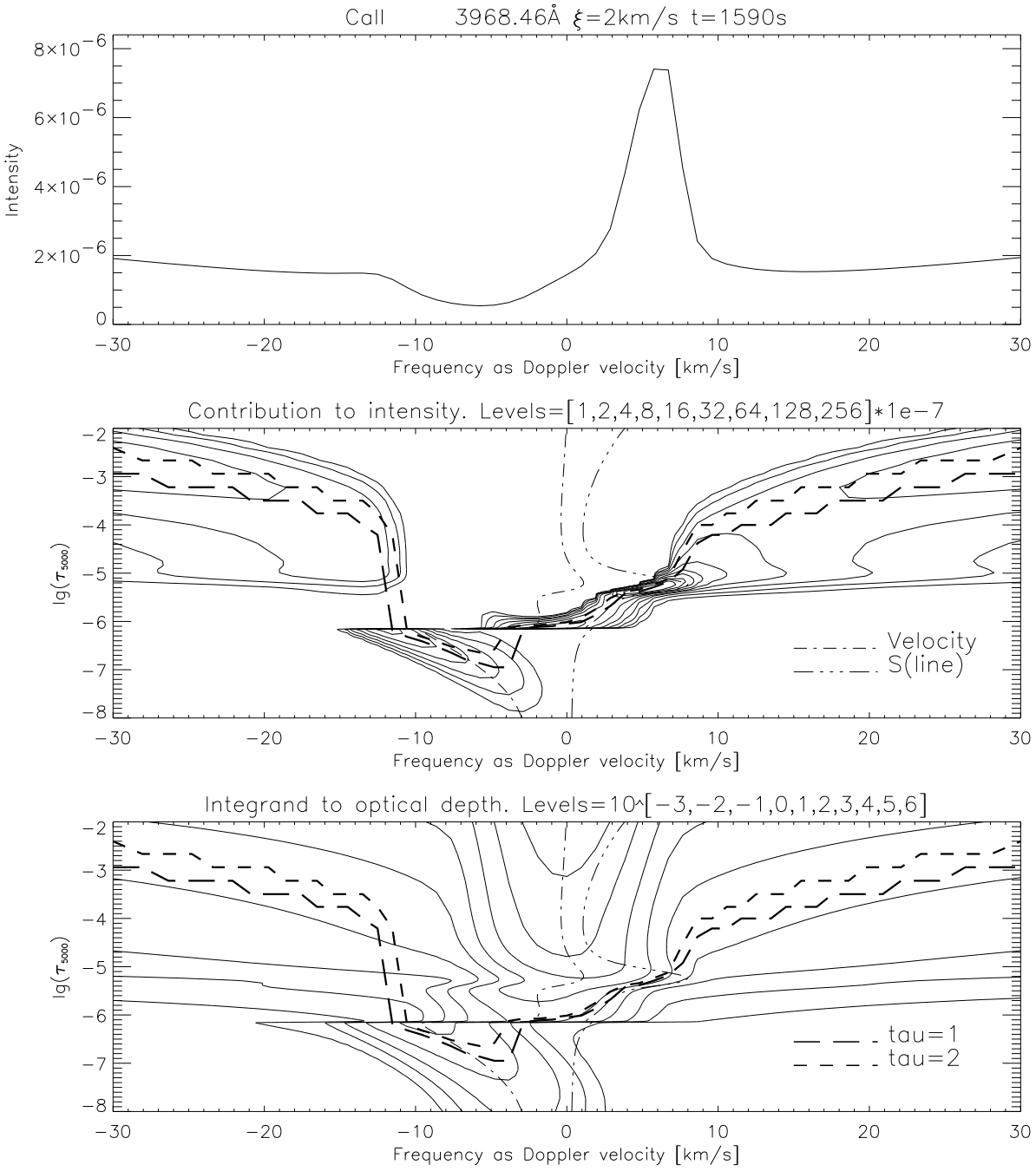

Figure 28: *Upper panel.* Intensity profile in the H-core region. The H2V emission peak is present and the H2R emission peak is absent. Blueshift corresponds to positive velocities. Frequency is given as the corresponding Doppler-velocity. *Middle panel.* Contribution functions to intensity as a contour plot in the depth-frequency plane. Curves of equal monochromatic optical depth are given together with the velocity and the the source function (arbitrary scaled). *Lower panel.* The integrands to monochromatic optical depth on a $lg(\tau_{5000})$ are given to show which layers control the curves of equal optical depth. Small spacing between these curves indicates relatively high opacity and high sensitivity to the source function.

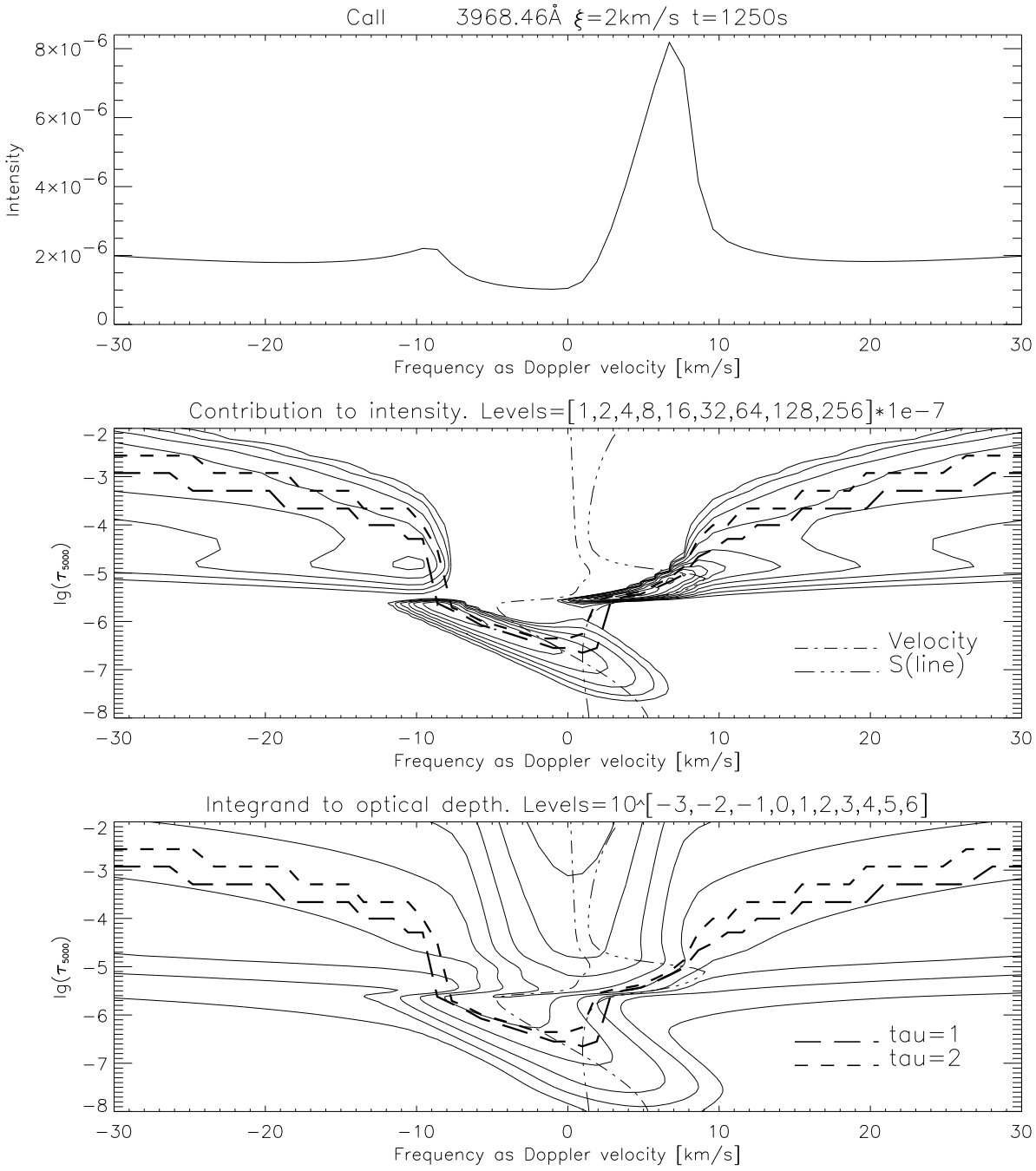

Figure 29: *Upper panel.* Intensity profile in the H-core region. Both emission peaks are present. Blueshift corresponds to positive velocities. Frequency is given as the corresponding Doppler-velocity. *Middle panel.* Contribution functions to intensity as a contour plot in the depth-frequency plane. Curves of equal monochromatic optical depth are given together with the velocity and the the source function (arbitrary scaled). *Lower panel.* The integrands to monochromatic optical depth on a $lg(\tau_{5000})$ are given to show which layers control the curves of equal optical depth. Small spacing between these curves indicates relatively high opacity and high sensitivity to the source function.

Both H2R and H2V emission peaks occur if a low amplitude shock of typically 5 km/s is present. Only the H2V emission peak occur if a high amplitude shock of typically 10 km/s is present.

It must be noted that a steep velocity gradient is sufficient to create a grain, and that a shock is not required. It must also be noted that there is a significant contribution to intensity from pre-shock regions as can be seen in figures 28 and 29.

7.2.4 Comparisons with previous work

In a simulation of Rammacher & Ulmschneider (1992), a short period P=45s sinusoidal piston at the lower boundary drives the 3 min. shock waves in the chromosphere by shock-overtaking. Their K2V/K2R intensity ratio is too small in the K-line. Their explanation for this is that CRD redistributes photons from the violet peak such that the red peak is enhanced. This can also be true in our simulation, but there is nevertheless occasions where H2R is absent when a strong H2V is present.

Their relatively small shock strength of about 6 km/s at grain formation heights can also be a partial explanation of the enhanced red peak. There is in addition several shocks in the chromosphere which influences the radiative transfer. The grain forming heights contain two shocks in their figure 2. The upper post-shock region shifts opacity into the violet peak intensity which reduces its magnitude.

Their main reason for intensity asymmetry is the same as ours: opacity differences at the emission frequencies in post-shock regions where the source function has its local maximum. They formulate it in another way: "Velocity-temperature correlation in the post-shock region combined with the removal of violet opacity in the pre-shock region."

It must be noted that the simulation of Rammacher & Ulmschneider (1992) assumes hydrogen in LTE, a CaII model of two levels, and that the advection- and time derivatives in the rate equations are neglected.

7.2.5 Further connections to dynamics

I will list some observable grain features in the line profile that are likely to occur if the only atmospheric change is the one described in each point.

1. Higher pre-shock velocities cause an intensity increase and redshift of H2V. The increased pre-shock redshift decreases the line of sight opacity on the blue side of the rest center wavelength. The wavelength of unity optical depth (on the blue side) that reaches local source function maximum will then increase. The opacity at the post shock source function maximum at this wavelength is higher and thus the intensity increases.

2. Higher positive post-shock velocity causes a blueshift of H2V because of unity optical depth at the local source function maximum at a shorter wavelength.

3. Higher post-shock temperature increases the thermal coupling parameter through collisions. Both increased coupling to the Planck distribution and increased temper-

ature behind the shock leads to an increased source function towards the shock. This causes higher intensity at the H2V and H2R peaks.

4. The temperature can probably be estimated by the intensity level of the line core since this probes source function above its local maximum value. It must be noted that the scattering term will control the source function at these layers, such that only indirect measurements are possible.

7.3 Physics of the Ca II V-I and V-V phase relations

The CaII lines have been used extensively by several authors (e.g. Fleck & Deubner 1989, Deubner & Fleck 1990, Kulaczewski 1992, Lites et al. 1993) to determine chromospheric dynamics of the sun. All the authors have used linear theory to arrive at their conclusions about wave modes or velocity response heights. In this section we investigate the diagnostic potential of Fourier domain analysis of the time variable CaII spectral lines by using the pre-heated dynamic model atmosphere. We point out that linear wave theory can not be applied in the upper chromosphere to explain the observed features.

First, we review the relevant tools in the Fourier domain. Second, we investigate the validity of linear theory on acoustic waves to determine height differences. Third, we determine the accuracy of linear theory at the heights where it is valid. Fourth, we find time variable velocity response heights of the line core Doppler shifts that fluctuates a few hundred kilometers, in contradiction to previously assumed constant heights. Fifth, we compare observed phase relations to the simulation results, were we find many similarities. Finally we connect the Fourier domain signatures to chromospheric dynamics and heating.

7.3.1 Tools in the Fourier-domain

Fourier-domain analysis of the time development of spectral lines is useful to determine dynamic properties of the atmosphere. Several tools have been used by previous workers (e.g. Lites et al. 1993). These are phase differences between Doppler-shifts of two spectral lines to determine differences in heights of formation, power spectra to determine atmospheric damping properties as a function of frequency, and phase coherence to determine the degree of correlation between motions in different atmospheric layers.

We will use these tools on our simulations such that comparisons with previous observational work can be done (Fleck & Deubner 1989, Deubner & Fleck 1990, Kulaczewski 1992, Lites et al. 1993).

1. *Power spectra.* The power spectrum $P(\omega)$ of a signal as a function of frequency ω is defined as the squared amplitude A^2 of the Fourier-components Z:

$$Z(\omega) = Ae^{i\theta} \Rightarrow P(\omega) = ZZ^* = A^2 \tag{61}$$

   where $\theta = \theta(\omega)$ is the phase of the Fourier components.

2. *Phase difference spectra.* The phase difference $\Delta\theta(\omega)$ between two signals ($k = 1, 2$) as a function of frequency ω is defined as the angle difference between their Fourier components Z_k in the complex plane:

$$Z_k(\omega) = A_k e^{i\theta_k} \Rightarrow \Delta\theta(\omega) = \theta_1 - \theta_2 \tag{62}$$

3. *Phase coherence spectra.* Consider two different discrete sequences v_1 and v_2. Let Z_1 and Z_2 denote their discrete Fourier transforms. We wish to determine the degree of phase coherence, C between the signals. Let C=1 express maximum phase coherence and C=0 minimum phase coherence.

   In general, there will be a phase difference between the signals at each frequency determined by the angle between the complex vectors. There will also be an amplitude difference between the two signals at each frequency. If the phase differences in a chosen frequency interval deviates much from each other, the phase coherence will be low. If the phase differences are equal, the coherence will be higher. If in addition the two power spectra are proportional to each other, the coherence will be equal to one. High phase coherence will in general occur in a situation of small phase difference deviation between neighboring frequency points and when the two power spectra are approximately proportional to each other.

   If one of the signals is input to an arbitrary physical system, and the other is the output, high coherence in a given frequency interval corresponds to conservation of the Fourier components in this interval, apart from a uniform phase shift and a frequency independent scaling of the amplitudes.

   One equation that satisfies these properties of phase coherence is written (Edmonds & Webb 1972):

$$C^2(\omega) = \frac{< Z_1 Z_2^* > [< Z_1 Z_2^* >]^*}{< Z_1 Z_1^* >< Z_2 Z_2^* >} = \frac{< A_1 A_2 e^{i\Delta\theta} > [< A_1 A_2 e^{i\Delta\theta} >]^*}{< (A_1)^2 >< (A_2)^2 >} \qquad (63)$$

   where angle brackets represent averaging over frequency, Z^* the complex conjugate, A amplitude, and $\Delta\theta$ the phase difference. Without the averaging, the coherence is unity. We have adopted a running averaging interval of 9 frequency points as in the paper of Lites et al. (1993) to make comparisons possible. We have also used their convention of plotting the squared quantity of C rather than C itself.

One has to be aware of some fundamental properties of the Fourier transform in order to use it correctly. Sampling causes a replication of the basic transform of the original continuous data at intervals of $\Delta f = f_s$ in the transform domain, where f_s is the sampling frequency. When the contributions of the successive replicas are added together, the result is a periodic transform. Unreliable transforms occur if the replicas overlap. In the case of undersampling, an overlap occurs at each side of the Nyquist frequency $f_N = \frac{1}{2} f_s$. (The Nyquist frequency is located midway between the centers of the repeated transforms.) The transform is then said to be aliased. To eliminate this effect the sampling rate has to be increased, or the original signal has to be band limited such that $f_s = 2f_{max}$, where f_{max} is the highest frequency contained in the original signal. This will separate the replicas enough to prevent their mutual distortion or folding. *This is satisfied as long as the band width is less than the Nyquist frequency.* The simulations has a sampling rate of 0.1 Hz. Since this rate can not be altered, the high frequency parts of the spectra has to be rejected if aliasing tendencies are present near the Nyquist frequency.

Only a short segment of a signal of infinite duration can be considered in a real measurement. This is equivalent to multiplying the infinite sampled sequence by a rectangular window of unit height and arbitrary width. This introduces high frequency components due to the discontinuous ends of the sequence. The resulting signal will then be undersampeled and aliased. This effect is reduced by applying a *window with smooth ends such as a cosine bell*, which is used in this thesis.

Multiplication by a window on the signal in time domain is equivalent to an inverse transform of a convolution between the transform of the signal and the transform of the window. This convolution results in a smearing of the Fourier components. To reduce this effect, the lowest frequency components, or at least *the DC-component has to be removed* by subtracting the average value of the measured sequence.

Noise from seeing and detectors such as CCD's is introduced in observations. This must be filtered out by applying a noise filter such as a Wiener filter in the transform domain. This was unnecessary on the noiseless simulation results.

7.3.2 V-V phase differences.

An approximate analytic expression for velocity phase differences between two different heights can be given if small perturbations in an isothermal atmosphere are assumed. We investigate the applicability of this expression by a comparison with direct measurements of the velocity phase differences between two heights in the model.

We neglect magnetic fields since we only compare with observations of regions with weak magnetic fields, and since our simulations do not include magnetic fields. The relevant waves are thus acoustic-gravity waves. The linearized hydrodynamic wave equation for plane waves in an *isothermal* gravitationally stratified stellar atmosphere give the dispersion relation (Mihalas & Mihalas 1984):

$$\omega^4 - [C_s^2(k_x^2 + K_z^2) + i\gamma g K_z]\omega^2 + (\gamma - 1)g^2 k_x^2 = 0 \tag{64}$$

ω is the frequency for one Fourier-component, C_s is the sound speed, k_x is the horizontal real component of the wave vector, K_z is the vertical complex component of the wave vector, and g is the acceleration of gravitation. We have assumed constant ratio of specific heats γ. This equation does not include radiation effects such as radiative damping. Only one horizontal component of the wave vector is necessary since no preferred horizontal direction exist due to horizontal homogeneity. The horizontal component is also real because waves should neither grow nor decay in the homogeneous direction. The vertical component is in general complex due to the stratified medium. We have:

$$K_z = k_z + \frac{i}{2H} \tag{65}$$

$$\vec{x}_1 = \vec{X} e^{i(\omega t - \vec{k}\cdot\vec{x})} \quad \vec{v}_1 = \vec{V} e^{i(\omega t - \vec{k}\cdot\vec{x})} \quad \vec{k} = (k_x, 0, K_z) \tag{66}$$

This implies that the displacement perturbation $\vec{x}_1$ and velocity perturbation $\vec{v}_1$ grow as $e^{\frac{z}{2H}}$, where H is the isothermal scale height. Equation 64 can now be written:

$$\omega^4 - [\omega_a^2 + C_s^2(k_x^2 + k_z^2)]\omega^2 + \omega_{BV}^2 C_s^2 k_x^2 = 0 \tag{67}$$

ω_a is the acoustic cut-off frequency and ω_{BV} the Brunt-Väisälä frequency or buoyancy frequency. These quantities are to be evaluated for the ambient or unperturbed medium. Only vertical propagation of gravity modified acoustic waves can be studied, since the simulations are one-dimensional in the z-direction. Buoyancy waves require horizontal components of the wave vector. They can therefore not exist in the model. This modifies equation 67 to:

$$\omega^4 - [\omega_a^2 + C_s^2 k_z^2]\omega^2 = 0 \tag{68}$$

Index z is hereafter dropped. The vertical wave number is thus:

$$k = \frac{[\omega^2 - \omega_a^2]^{\frac{1}{2}}}{C_s} \tag{69}$$

This shows that damped standing waves occur if the frequency is less than the cut-off frequency. The phase velocity can be written using equation 68:

$$v_{ph} = C_s[1 - (\frac{\omega_a}{\omega})^2]^{-\frac{1}{2}} \tag{70}$$

where in general the cut-off frequency and sound speed vary as a function of height in a realistic stellar atmosphere. The phase difference occurring after the wave has propagated the distance Δz can be approximated by using an averaged wave number in this interval:

$$\Delta\theta(\omega) = \langle k \rangle \Delta z = \int_{\Delta z} k dz = \omega \int_{\Delta z} \frac{[1 - (\frac{\omega_a}{\omega})^2]^{\frac{1}{2}}}{C_s} dz \tag{71}$$

The phase difference will be zero if standing waves are present. The assumption of an isothermal atmosphere, and thus constant cut-off frequency and sound speed, will hold if the ambient temperature change in the interval Δz is relatively small, and if the wavelengths considered are smaller than this interval. It must be noted that the equations above are only valid in the linear regime where the perturbations are relatively small.

Assume that we are able to measure the velocity field at an arbitrary fixed point in a stellar atmosphere by using the Doppler-shift in the line core. We denote this as fixed velocity response heights. The phase differences between two line cores can be determined as a function of frequency. Equation 71 can then be used to determine the difference in heights of formation of the two line cores by curve fitting if the variation in cut-off frequency and sound speed as a function of height is known.

In the high frequency limit where $(\frac{\omega_a}{\omega})^2 \ll 1$, and if $C_s(z)$ is approximately constant, equation 71 reduces to:

$$\Delta\theta(\omega) = \omega \langle \frac{1}{C_s} \rangle \Delta z \tag{72}$$

A linear relation for high frequencies is thus expected in observed phase differences with the assumption of fixed velocity response heights and linear wave theory as pointed out by

Lites et al. (1993). Fixed velocity response heights and linear wave theory have also been used by Fleck & Deubner (1989) to find types of wave modes between two response heights that are assumed to be known.

It is possible to directly measure the velocity at two different fixed heights in the simulation. We compare the phase differences from the measured velocities with the ones predicted from equation 71. The height range of validity of the linear theory can then be determined. The equation is evaluated from the cut-off frequency and sound speed in the initial dynamic atmosphere which is similar to the VAL3C semiempirical model (Vernazza et al. 1981). We denote this initial atmosphere by VAL. The results are shown in figures 30-35, and they can be summarized as follows:

1. Standing waves below 1000km are present below the acoustic cut-off frequency of 5.5mHz (Fig.32). Relatively low phase coherence occurs between the acoustic cut-off frequency and 10 mHz below 500km (Fig.30). This can be due to a variation of the actual transition frequency between standing and propagating waves as a function of height which leads to phase scattering between neighboring frequencies.

2. Phase differences up to 20mHz can be estimated by the unperturbed VAL model with typical errors of less than +/- 50 degrees in the height range from 0km to approximately 1000km, even if nonlinear perturbations occur in the range from 500km to 1000km (Fig.32). A decreasing phase coherence above 10mHz towards 800 km indicates phase shifts introduced by a transition from linear to nonlinear perturbations.

3. The phase coherence increases again from 1600km to 2000km due to the development of pure shock wave velocity profiles (Fig.35). The range from 1600km to 2000km show reduced phase difference compared to equation 71. This can be understood if the shock waves are approximated as a propagating train of constant shaped sawtooth velocity profiles. The phase differences in this limit will be constant as a function of frequency due to a pure displacement in time of the velocity profile. A tendency of constant phase can be seen for the height interval from 1800km to 2000km between 15mHz and 25mHz, where the phase coherence is about 0.85.

4. A general tendency of damping of amplitudes below the acoustic cut-off frequency, and amplification of frequencies above, can be seen from the power spectra ratios in the lower atmosphere (Fig.31). Harmonics of a periodic N-wave train can be seen from the power spectra in the chromosphere (Fig.34). Frequencies around 4mHz dominate in photospheric layers, and frequencies around 5.5mHz dominate in chromospheric layers.

This analysis show that linear theory of phase differences becomes inaccurate above approximately 500km due to reduced phase coherence above 10mHz. This can be explained by non-linear wave steepening, where high velocity parts have greater phase velocity than low velocity parts.

Formation height differences can at best be estimated up to 1000km with curve fitting between observations and equation 71 for frequencies above the acoustic cut-off of 5.5mHz

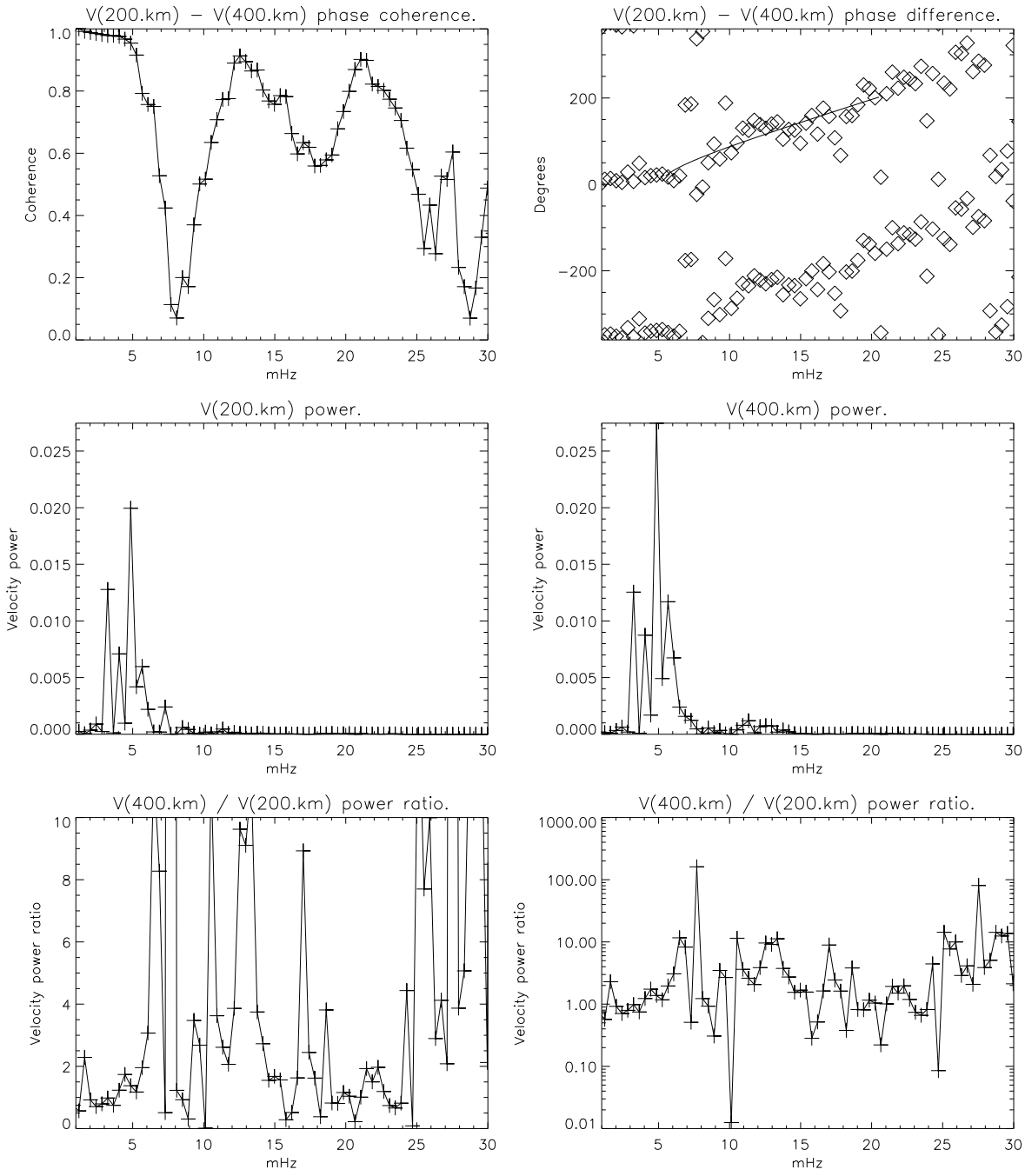

Figure 30: Photosphere. Predicted phase differences from linear theory (solid) are plotted together with the actual phase differences (diamonds). High coherence is evident between the photospheric altitudes of 200km and 400km. Low coherence at 8 mHz occurs just above the cut-off frequency due to the transition from standing to propagating waves. There is good agreement with the predicted phase differences from the unperturbed VAL model. A velocity amplitude amplification with increasing height can be seen from the power spectra. The power concentrates towards 3 minute oscillations with increasing height which can be seen from the power ratio.

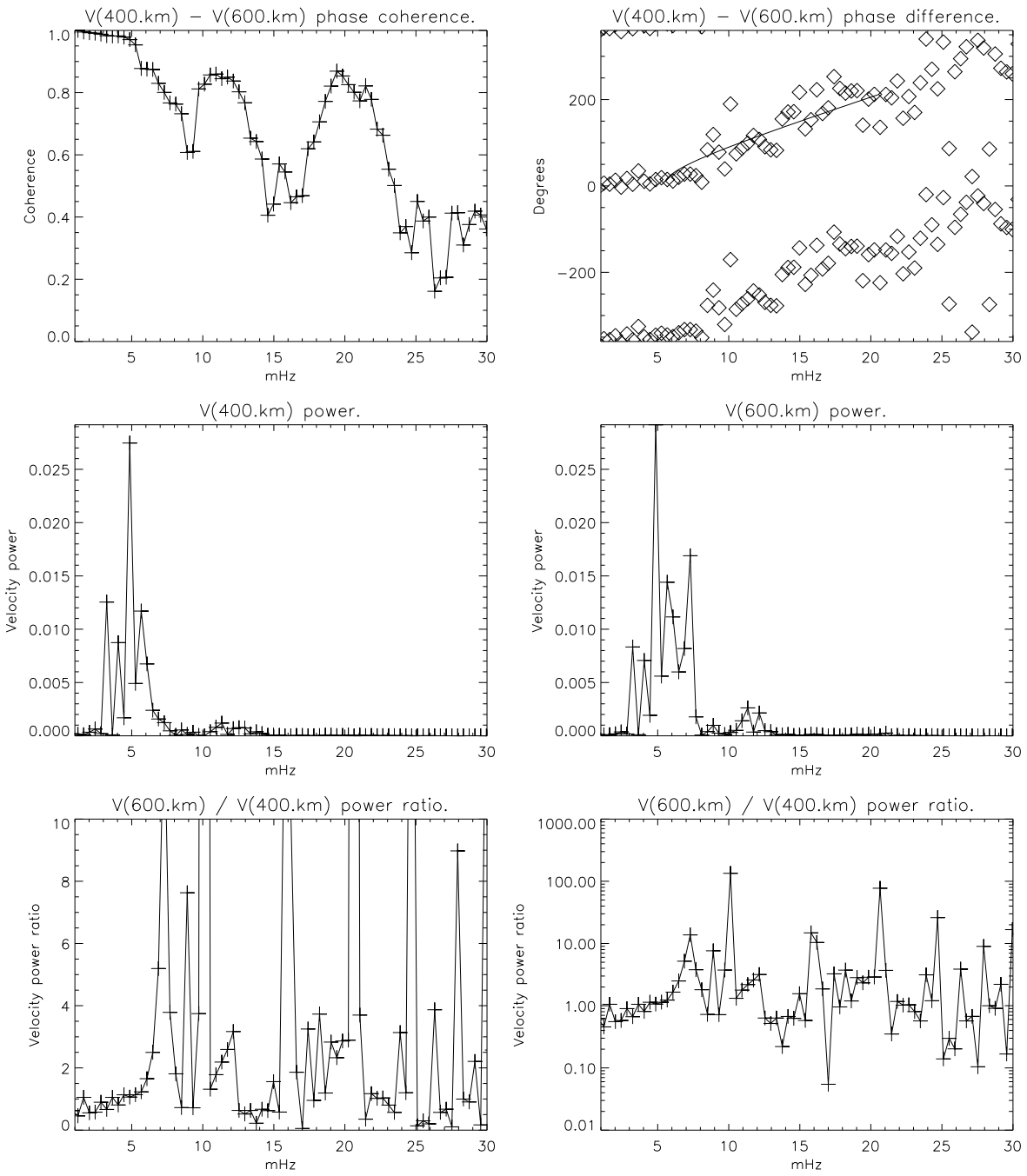

Figure 31: Temperature minimum region. Predicted phase differences from linear theory (solid) are plotted together with the actual phase differences (diamonds). Slightly decreased coherence at high frequencies can be seen compared to the 200-400km relation. Standing waves are still present at low frequencies. There is good agreement with the predicted phase differences from the unperturbed VAL model. A velocity amplitude amplification with increasing height can be seen from the power spectra. An amplitude increase at 7mHz and 10mHz can be seen from the power ratio.

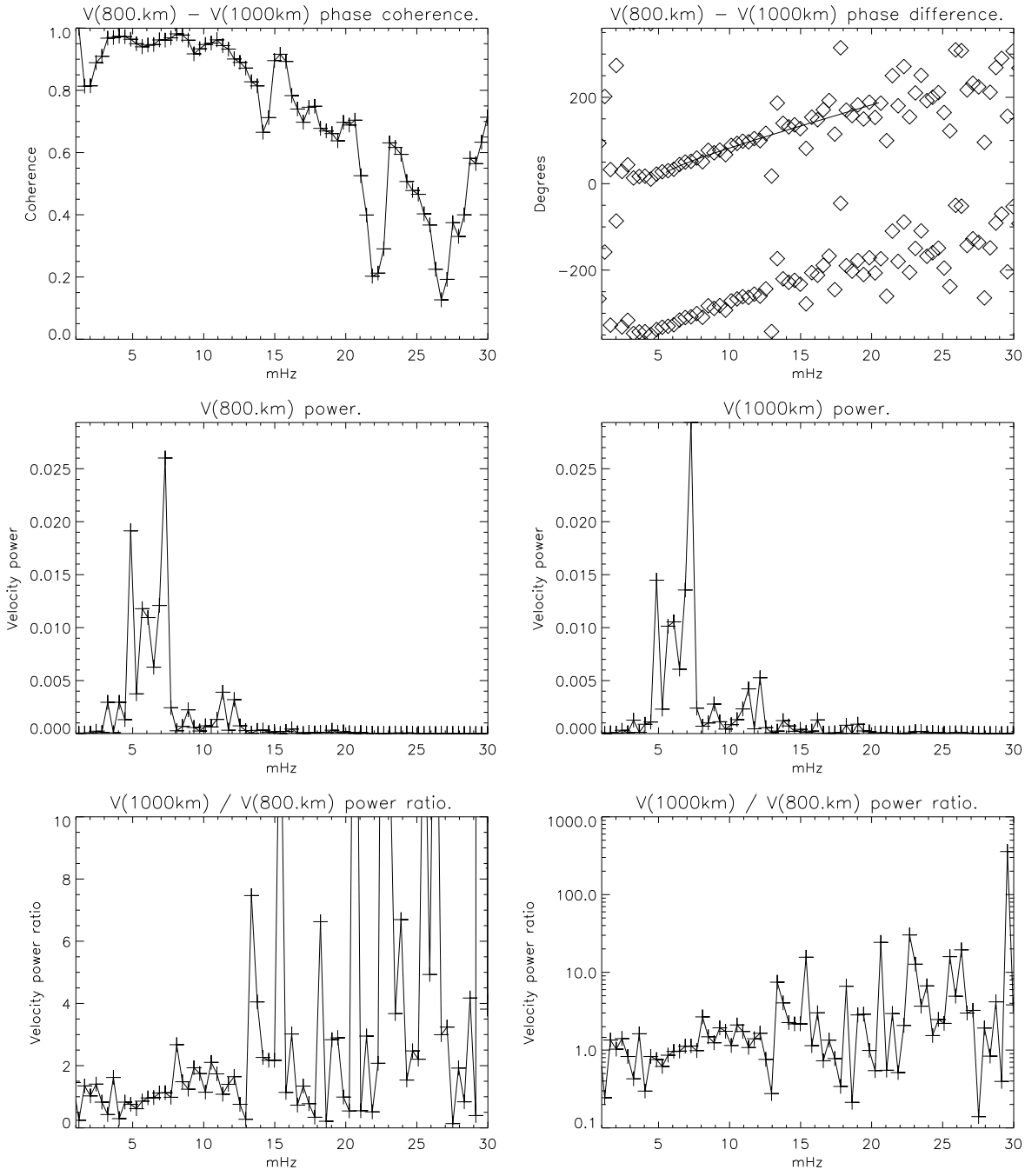

Figure 32: Low chromosphere. Predicted phase differences from linear theory (solid) are plotted together with the actual phase differences (diamonds). Standing waves are less evident compared to the 400-600 km relation. There is still good agreement with the predicted phase differences from the unperturbed VAL model. A velocity amplitude amplification at frequencies above the acoustic cut-off with increasing height can be seen from the power ratio.

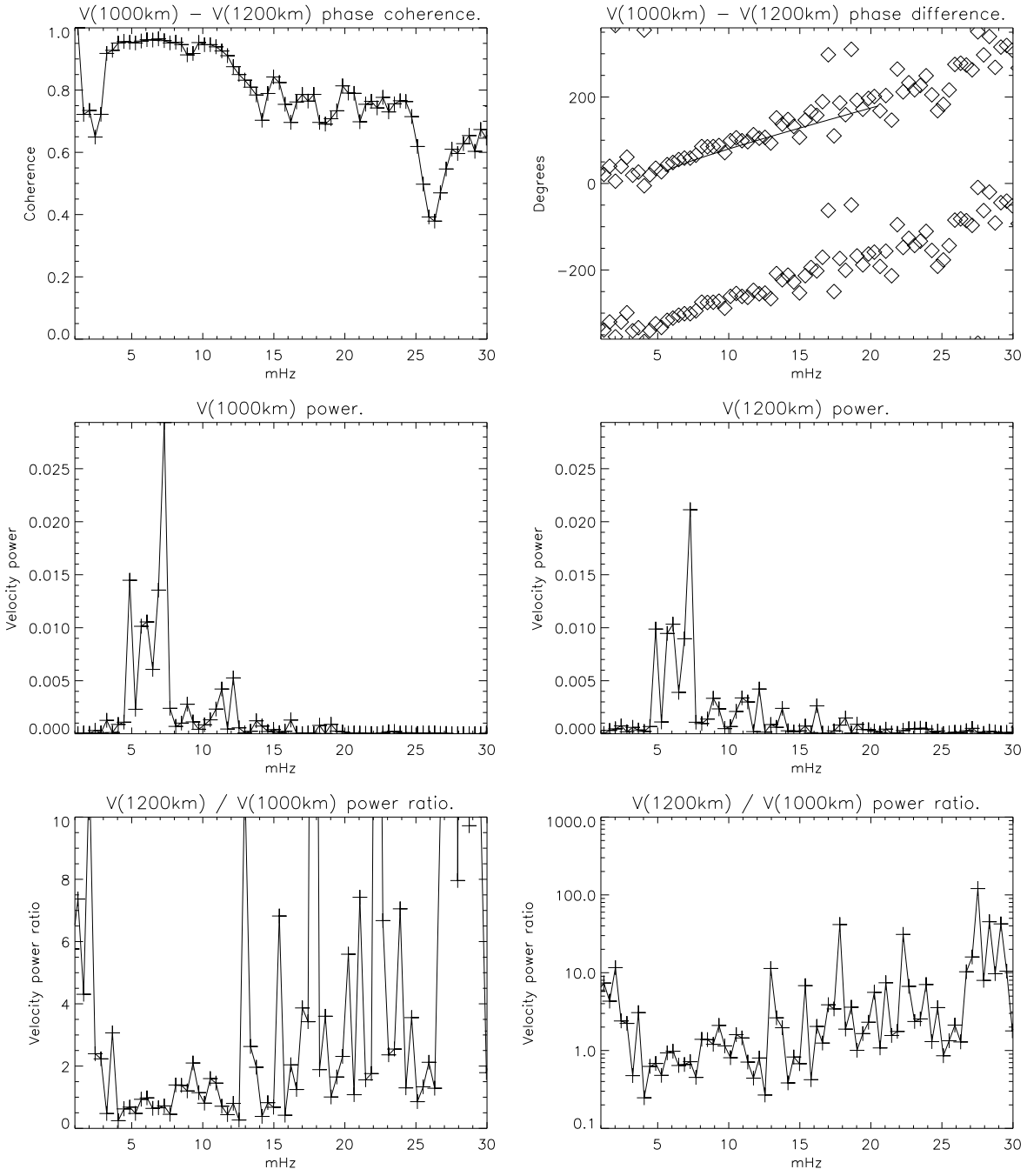

Figure 33: Middle chromosphere. Predicted phase differences from linear theory (solid) are plotted together with the actual phase differences (diamonds). Standing waves are not present since phase differences can be seen at low frequencies. There is too much phase scattering at high frequencies to get a good agreement with the predicted phase differences from the unperturbed VAL model. This is due to the shock formation which introduces phase modifications. The velocity amplitudes at frequencies above the acoustic cut-off are approximately the same, except some amplification of discrete frequencies.

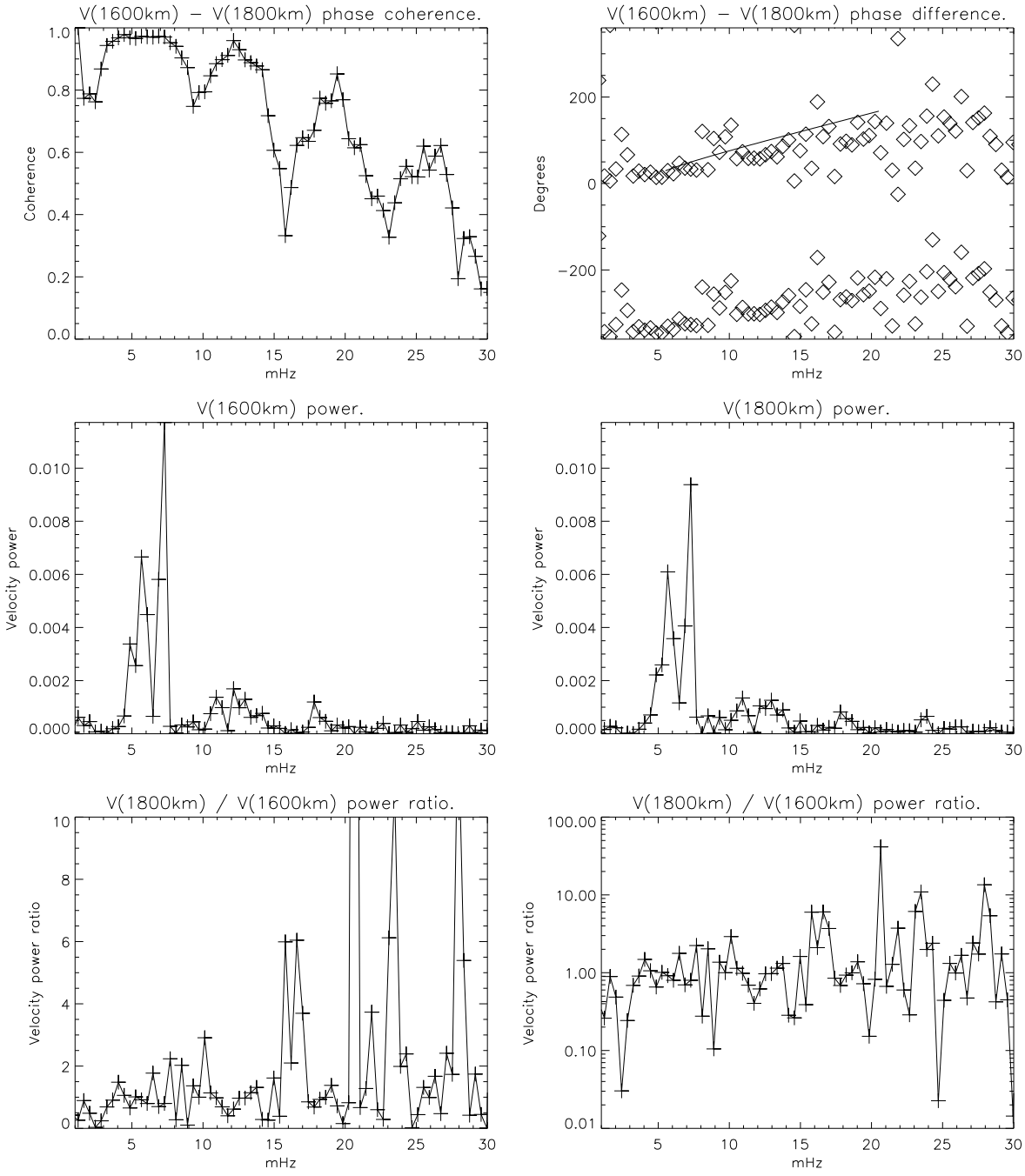

Figure 34: High chromosphere. Predicted phase differences from linear theory (solid) are plotted together with the actual phase differences (diamonds). Standing waves are not present since phase differences can be seen at low frequencies. There is much phase scattering in the entire frequency range due to the shocks that are developing. Comparisons with the predicted phase differences from the unperturbed VAL model become meaningless because of the non-linearities. High velocity amplitudes in distinct frequency intervals at high frequencies due to the N-wave harmonics can be seen from the power spectra.

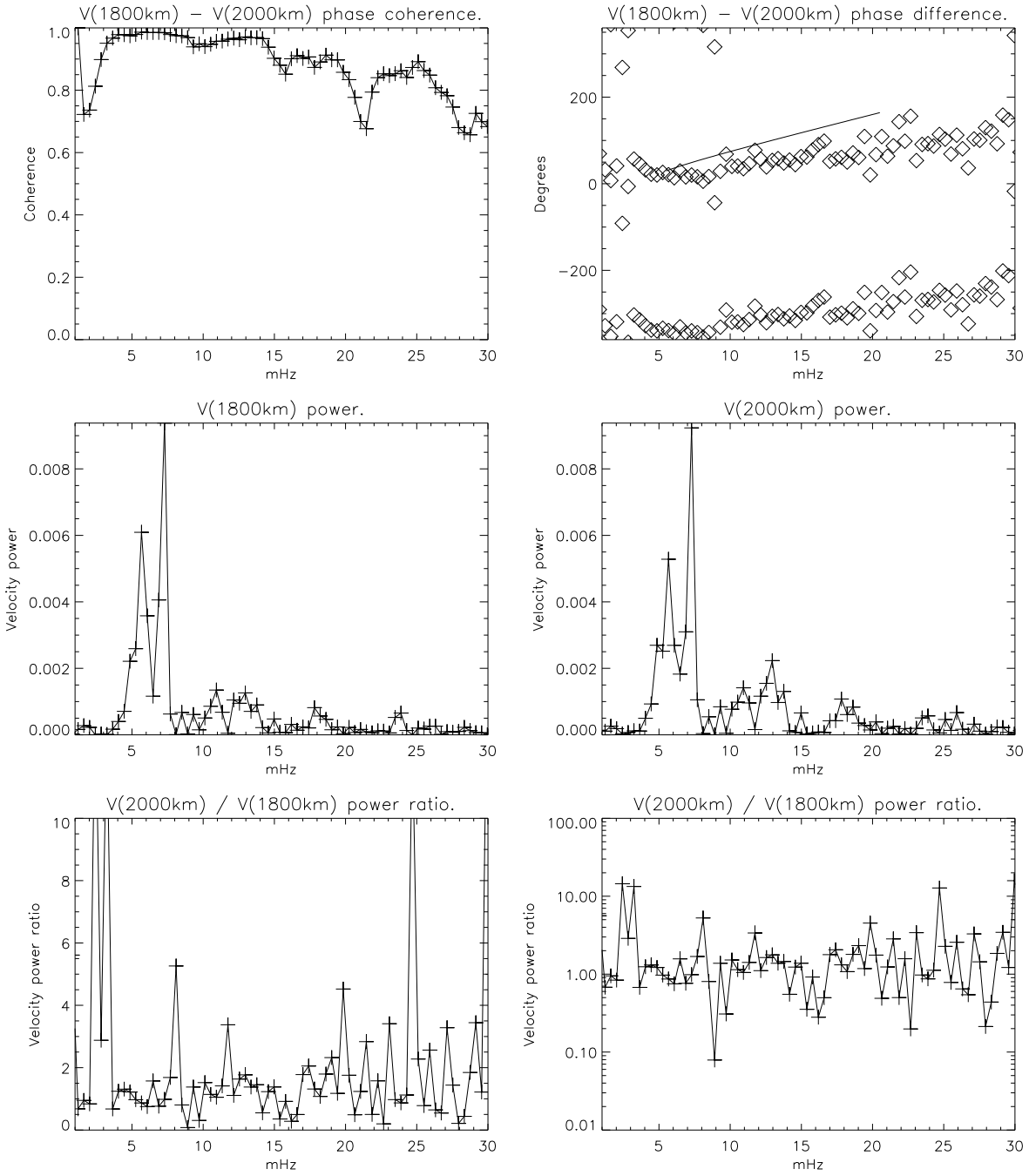

Figure 35: Upper chromosphere. Predicted phase differences from linear theory (solid) are plotted together with the actual phase differences (diamonds). Phase scattering is less prominent in the entire frequency range due to the fully developed shocks. The phase coherence is thus high above the acoustic cut-off frequency. Phase differences tend to be more constant as a function of frequency compared to lower altitudes. This is due to less modification of the N-wave shape. Frequencies around 5.5mHz and 7mHz dominate completely.

and up to approximately 20mHz. Equation 72 for the high frequency limit based on few frequency points, becomes more inaccurate than using equation 71 due to the increased phase difference scattering with increased frequency.

Linear theory breaks down in the chromosphere above 1000km where shocks form, and the method becomes useless. Another approach for this height range should be seeked. This can be identification of parts in the phase difference spectra of constant phase difference. The distance of propagation between two points can then be deduced from this phase difference if the shock speed is known. Difficulties will certainly occur in determining a typical shock speed because of strong back reactions from the shock waves on the atmosphere.

7.3.3 Accuracy of linear V-V phase difference theory

We turn to the question of how accurately linear theory can predict depth differences between two points at heights where linear theory is more or less valid. Theoretical curves (equation 71) are adjusted to give a best fit to the measured phase differences between two points with a height difference of 200km. The sound speed and cut-off frequency needed in this equation are taken from the unperturbed initial solution similar to the VAL3C atmosphere denoted by VAL. The fit is done by adjusting the highest altitude while the lowest altitude was held constant at the actual height. This procedure is carried out for 10 different heights. Deviations from the actual height difference of 200km is found as a function of the lowest altitude (Fig. 36).

Linear theory can at best predict height differences within a typical deviation of 20 km below 1000km. This is equal to a relative deviation of 10%. Above this height, the shocks become fully developed, and the predictions from the VAL model become erroneous.

Greater height differences between altitudes from 0-1000km are predicted from the VAL model compared to the actual ones. The actual phase differences are thus greater than for the ones predicted from the VAL model with the actual height difference. The actual phase speed from 0 to 1000km is thus less than for the VAL model (equation 71). The acoustic cut-off frequency and the sound speed determines the phase speed. It is only dependent on the sound speed in the high frequency limit (equation 72). A lower sound speed in the dynamic model will thus cause lower phase speed and higher phase differences compared to the VAL-model. For an adiabatic perfect gas in the linear regime we have for the sound speed:

$$C_s = [\frac{\gamma P_0}{\rho_0}]^{\frac{1}{2}} = [\gamma R T_0]^{\frac{1}{2}} \tag{73}$$

γ is the ratio of the specific heats, P_0 the ambient pressure, ρ_0 the ambient mass density, R a gas constant for the particular gas studied and T_0 the ambient temperature. In this case, the sound speed C_s is a function of temperature and the ratio of the specific heats only. The lower sound speed in the dynamic model can be explained by a lower ambient temperature or lower ratio of specific heats compared to the VAL-model.

Ionization leads to a lower ratio of specific heats and this effect should be included in the calculation of the analytic phase differences. Further inaccuracies will be introduced

by radiative energy exchange that invalidates the assumption of an adiabatic gas.

7.3.4 Dynamic velocity response heights

It is impossible to observe vertical mass motion at a specific height in a stellar atmosphere. The related observable quantity is the Doppler-shift displacement in the cores and wings of spectral lines. This Doppler-shift is an accumulated effect of absorption profile Doppler-shifts in different layers. The velocity response functions will thus extend over depths with different velocities. The mean velocity response height for line core displacements will in general be time dependent. Methods have nevertheless been used by several authors to determine chromospheric velocity fields by the assumption of fixed velocity response heights:

1. Fleck & Deubner (1989) determined wave mode types such as standing or propagating waves by the use of CaII line core velocity phase differences and phase differences between intensity and velocity. They adopted fixed response heights and they used linear phase difference theory. Frequency variable response heights for intensity and velocity fluctuations in CaII line cores (Mein & Mein 1980, Provost & Mein 1979) have been proposed as an improvement.

2. Lites et al. (1993) used velocity phase differences in the high frequency limit (equation 72) to deduce *differences* between fixed response heights for two spectral lines. These authors assumed a phase speed equal to the sound speed in a semiempirical model.

Here we investigate the validity of the assumption of fixed velocity response heights to line core displacements, and the connection between atmospheric velocity fields and line core Doppler-shifts by using the pre-heated model. The point of minimum intensity is taken as the line core. The response function for the line core displacement is given by (Magain 1986):

$$\delta\lambda(t) = \int_{-\infty}^{\infty} R_{\delta\lambda,v}(x,t)v(x,t)dx \tag{74}$$

where $R_{\delta\lambda,v}(x,t)$ is the response function, hereafter RF, and $v(x,t)$ the velocity at position x on an arbitrary height scale. We find that using this equation with the contribution function to line depression $C_R(x,t)$ (Magain 1986) as a response function reproduces the measured line core fluctuations very well for the H, K, 8542 and 8662 lines. See figure 37. We will therefore use:

$$R_{\delta\lambda,v}(x,t) = C_R(x,t) \tag{75}$$

The deduced line core displacement for the weakest infrared line 8498 has a severe deviation from the actual line core displacement. The 8498 line center is formed at a local maximum of the source function, and the point of minimum intensity is therefore not a measure of bulk velocity, but is influenced by the offset from line center opacity needed to reach a local source function minimum. This can be the explanation of the poor correspondence.

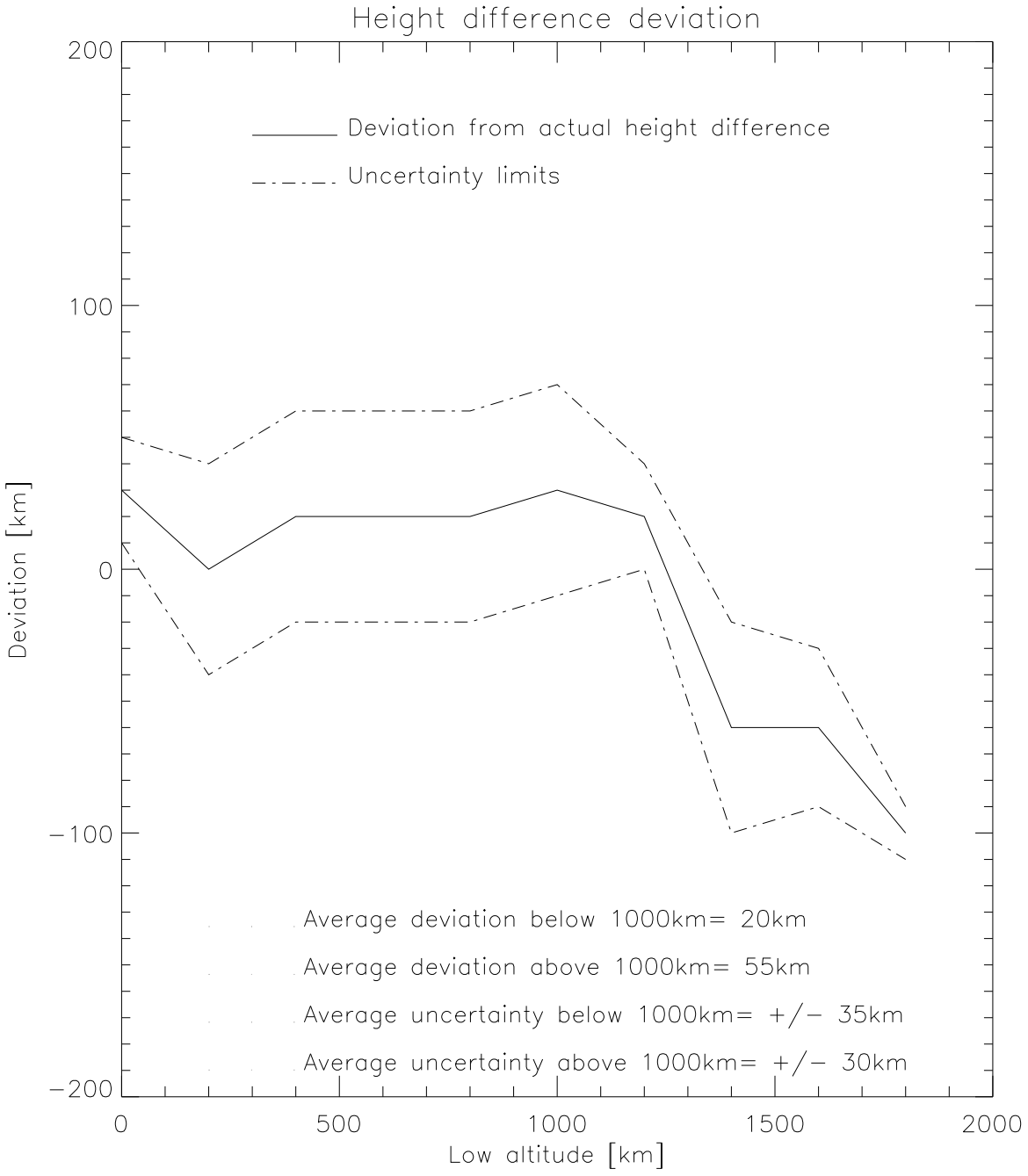

Figure 36: Height difference predictions from linear theory using the initial dynamic model similar to the VAL3C model. The predictions are determined by a best fit to the actual phase differences occurring between height intervals of 200km. The fit was done by adjusting the highest altitude while the lowest altitude was held constant. The deviations from the actual height differences are plotted against low altitude. The uncertainty limits are set by the typical range of phase scattering. Increased phase scattering reduces the accuracy of the best fit. Linear theory can at best predict height differences within a typical error of 10% below 1000km.

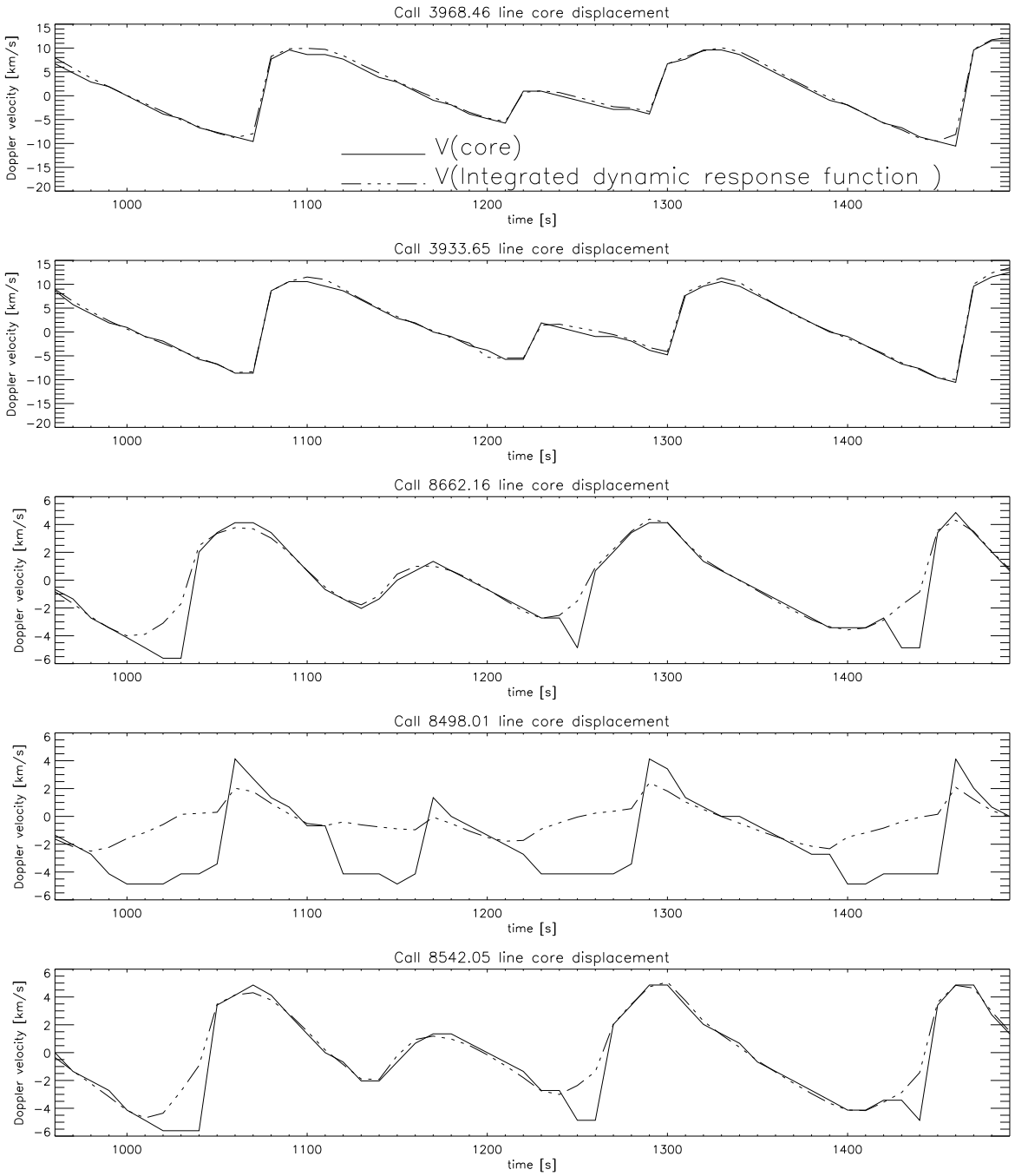

Figure 37: The actual Doppler shift (solid) is compared to the same quantity computed from the response function to velocity, or in this case the contribution function to relative absorption (dot-dashed). It is seen that the curves are almost identical, except for the 8498-line, where an erroneous line core determination has occurred. Some deviation occurs for the 8662 and 8542 lines where the redshift is maximum (negative velocities). This can occur if the point of minimum intensity at maximum redshift is not a measure of bulk velocity, but an additional displacement needed in order to reach the source function minimum.

The agreement between the other curves in figure 37 confirms the high accuracy of equation 75. The Doppler shift is thus physically connected to the velocity field through the absorption properties of the plasma in different layers. Increased absorption gives increased RF. The RF's have widths of typically 500km. The state of the chromosphere determines the shape and location of the RF's. High amplitude disturbances propagates and the RF's will thus be time dependent.

Let the mean height of formation of line depression (Magain 1986) on a $x = lg(\tau_{5000})$ scale define the mean response height of the Doppler shift:

$$\langle x \rangle(t) = \frac{\int_{-\infty}^{\infty} x C_R(x,t) dx}{\int_{-\infty}^{\infty} C_R(x,t) dx} \tag{76}$$

Let the mean response height on a geometric scale $\langle z \rangle(t)$ be located at the same atmospheric point as $\langle lg(\tau_{5000}) \rangle(t)$. We define the mean response height on a column mass scale and the optical depth scale in the same manner. The time dependent mean response heights on a height scale, optical depth scale and a column mass scale are shown in figures 38, 39 and 40.

$\langle z \rangle(t)$ vary between 1.3Mm and 2.0Mm for the H and K lines, and between 0.5Mm and 1.4Mm for the infrared lines. The assumption of fixed response heights will therefore be erroneous. The H and K lines have single peaked RF's. The IR lines can have doubly peaked RF's, and this can lead to spurious mean response heights located between the peaks where the RF is relatively small. The dynamic mean velocity response heights can be explained by:

1. *The H and K line.* These are formed at approximately the same variable mean response heights. The height scale show a ballistic trajectory. The column mass scale show an approximately constant value. This indicates that the opacity responsible for the line core depression can be assigned to the same gas volume. This volume is accelerated upwards for a short moment when the shock passes. The gravitational force will then provide a ballistic trajectory with maximum height at 2.0Mm and minimum height at approximately 1.5Mm.

2. *The 8662 and 8542 line.* These IR (infrared) lines have also approximately the same mean response heights in regions of shock formation. See figure 41 as an example.

   Outward moving matter in post-shock regions brakes and fall back (see t=1320s and t=1380s in figure 41 and figure 38) while the RF's are located at approximately the same depths.

   The RFs follows the down-falling matter (redshift) at t=1410s. As the the upward propagating steepening shock enters the RFs, they change position from pre-shock regions to post-shock regions. The RFs tends to follow relatively close to the upward propagating shock front. This results in an upward propagating response height, and a change from redshift to blueshift (see t=1450s and t=1470s in figure 41 and figure 38).

   The cycle starts again after this phase. It must be noted that deviations from this description can occur.

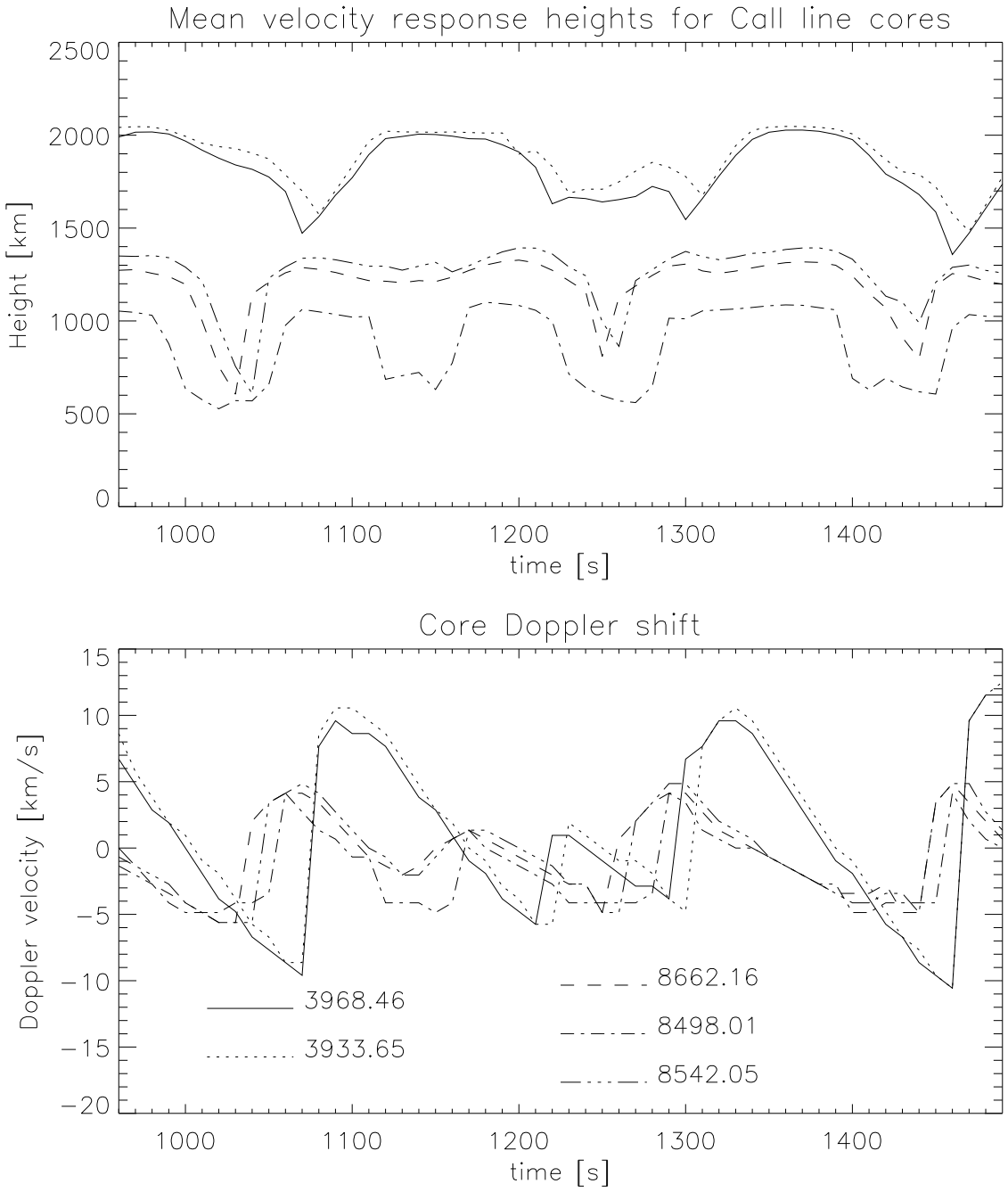

Figure 38: *Upper panel.* The time dependent mean response heights for the H and K line cores on a geometric height scale follows a ballistic trajectory. Since the column mass is approximately constant at these heights, the line core absorption occurs in the same plasma parcel. The two strongest IR-line cores are formed at approximately the same time dependent depths. The weakest line is formed somewhat deeper. The errors introduced by the anomal behavior of the core intensity makes the core determination uncertain for this line. *Lower panel.* A correlation between blueshift and upward movement of the mean formation heights can be seen from the Doppler shifts.

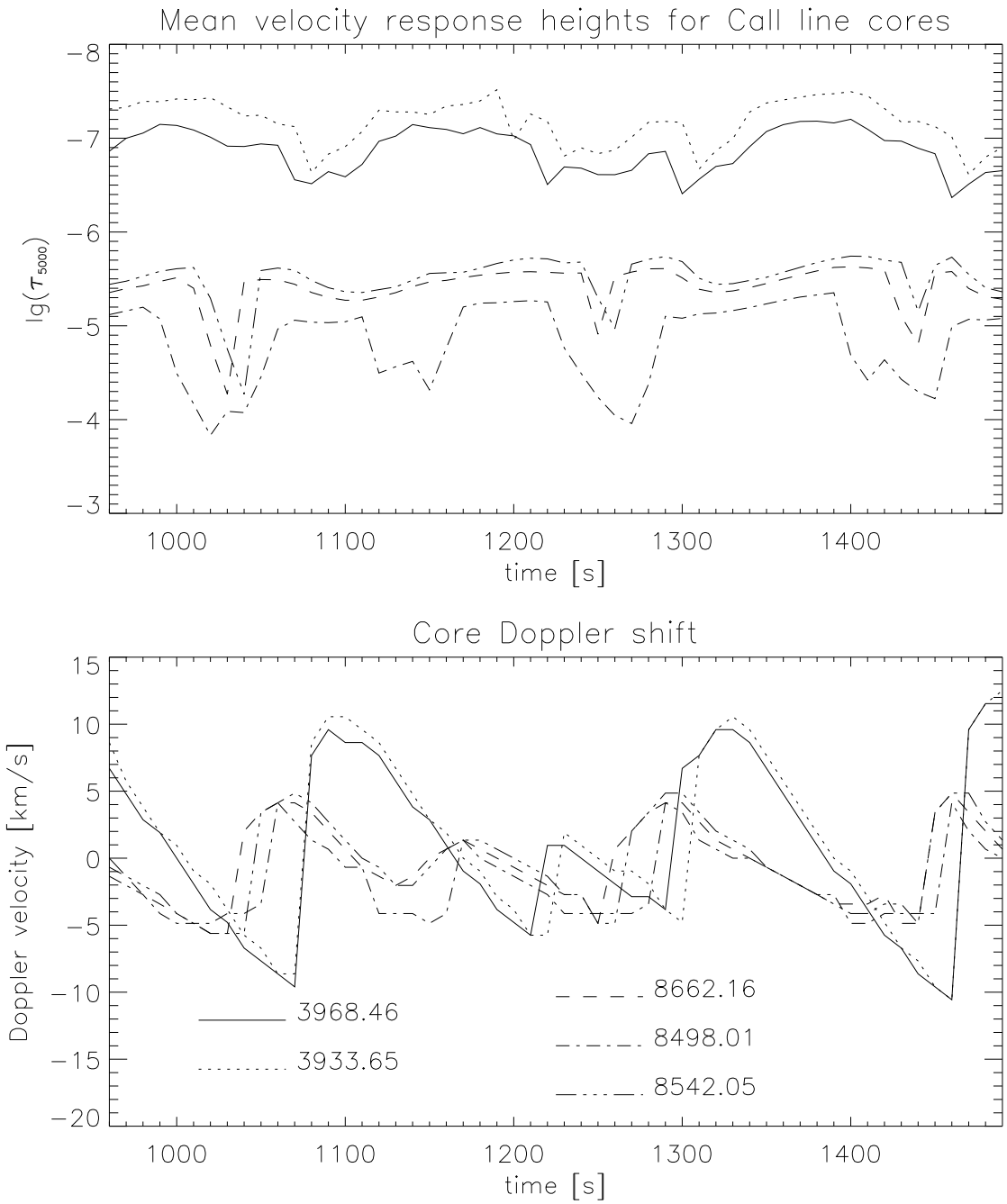

Figure 39: *Upper panel.* The time dependent mean response heights for the H and K line cores on an optical depth scale is approximately constant. The two strongest IR-line cores are formed at approximately the same time dependent depths. The weakest line is formed on somewhat deeper. The errors introduced by the anomal behavior of the core intensity makes the core determination uncertain for this line. *Lower panel.* A correlation between blueshift and upward movement of the mean formation depths of the two strongest IR lines can be seen from the Doppler shifts.

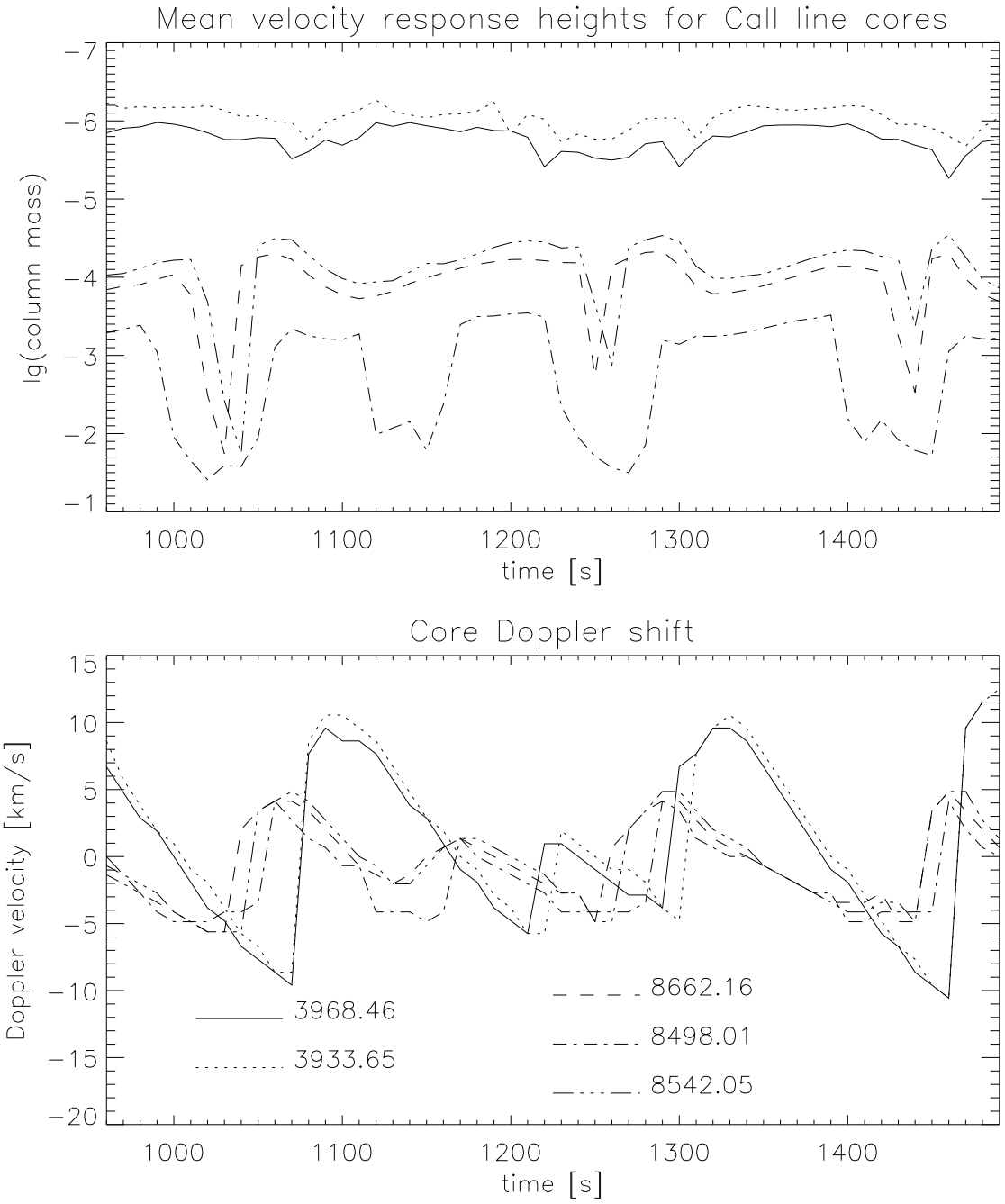

Figure 40: *Upper panel.* The time dependent mean response heights for the H and K line cores on a column mass scale are approximately constant, indicating line core formation in approximately the same plasma parcels as the medium bounces up and down due to the shock waves. The two strongest IR-line cores are formed at approximately the same time dependent depths. The weakest line is formed somewhat deeper. The errors introduced by the anomal behavior of the core intensity makes the core determination uncertain for this line. *Lower panel.* A correlation between blueshift and upward movement of the mean formation depth of the two strongest IR lines can be seen from the Doppler shifts.

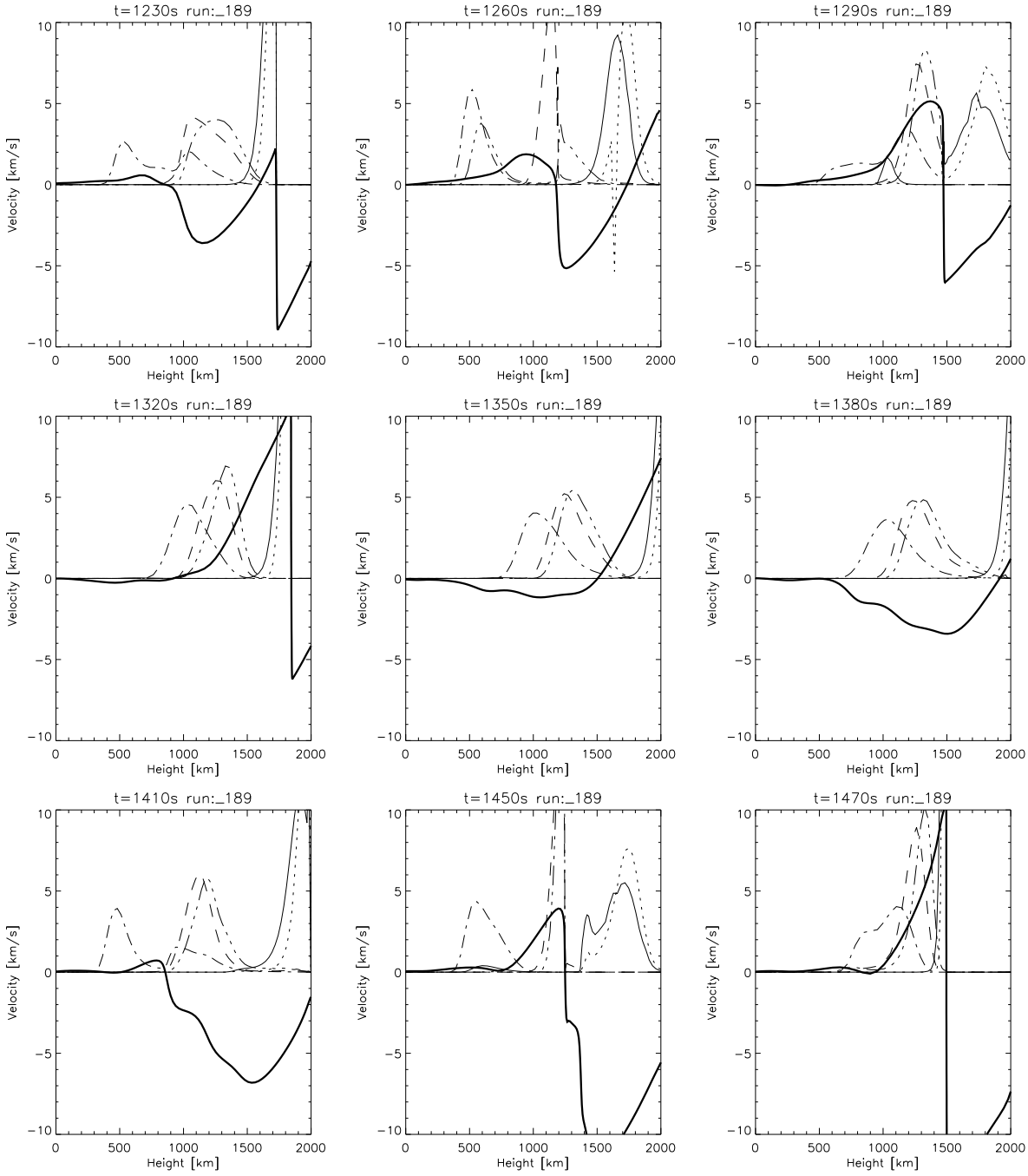

Figure 41: The response functions (RF) to Doppler shift, or here the contribution functions to relative absorption are plotted for the five CaII lines, together with the velocity field (bold) for some time steps. The response functions are equally scaled with an arbitrary factor. The RF coding: 3968 (solid), 3933 (dotted), 8662 (dashed), 8498 (dot-dashed) and 8542 (triple dot-dashed). The influence from dynamics on RF locations are evident, showing the highly non-linear conditions.

3. *The 8498 line.* The mean response height is on the average located in deeper layers than the other lines, and its RF behavior is quite complicated. It must again be pointed out that errors in line core determination lead to an inaccurate RF.

   This RF has two peaks, one above a steepening crest and one below at t=1230s and t=1410s (see figure 41). The contribution from down-falling matter dominates, such that a redshift occurs (figure 38. As the wave crest steepens, the RF become single peaked at the lowest altitude at zero velocity. The Doppler shift is then zero at t=1450s.

   The shock develop, and the RF starts to propagate up the post shock region at t=1470s and t=1320s (figure 41), and a blueshift occurs (figure 38). The material falls down again until a new steepening crest forms a shock. When the matter falls back, an increasing redshift occurs while the RF stays at approximately the same depth (figures 38 and 41 at t=1380s).

   The cycle starts again after this phase. It must be noted that deviations from this description can occur.

The H and K line core Doppler shifts reflects the constant acceleration downwards by gravity. The observed Doppler excursions in these lines are very similar to the synthetic ones, such that ballistic downfall and upthrusts by shock trains can explain the observed features.

Both the 8662 and 8542 lines have Doppler excursions approximately in phase since their time variable RFs have approximately the same location. Almost the same velocities are thus measured by the two Doppler shift sequences.

Difficulties in determining the correct 8498 RF due to the emission peak in the line core, makes the Doppler-shift interpretations difficult for this line. It has not been reported any observations of such an emission peak.

A comparison between the Doppler shift for the lines and the atmospheric velocity at the mean response heights can be found in figure 42. The deviations are somewhat greater than the computed line core displacements by using the RF's. Since the correspondence is relatively good, the Doppler shift measures approximately the atmospheric velocity at the mean response heights or in this case the mean formation depth of line depression. Great deviations for the 8498-line are again due to measurement errors introduced by the emission peak found in the simulations.

7.3.5 Observed and simulated V-I and V-V phase relations

Power spectra, phase difference spectra and phase coherence spectra for the CaII line cores in the pre-heated model atmosphere are here presented and compared with the observations of Fleck & Deubner (1989), Deubner & Fleck (1990), Lites et al. (1993) and Kulaczewski (1992). We find that the simulations reproduce many of the observed spectral signatures with a high degree of accuracy. We are therefore able to connect atmospheric dynamics to the intensity and velocity fluctuations observed in CaII line cores.

Power spectra of V (velocity) and I (intensity) are computed. Phase differences and the corresponding phase coherence are computed for velocity signals (V-V) or one velocity

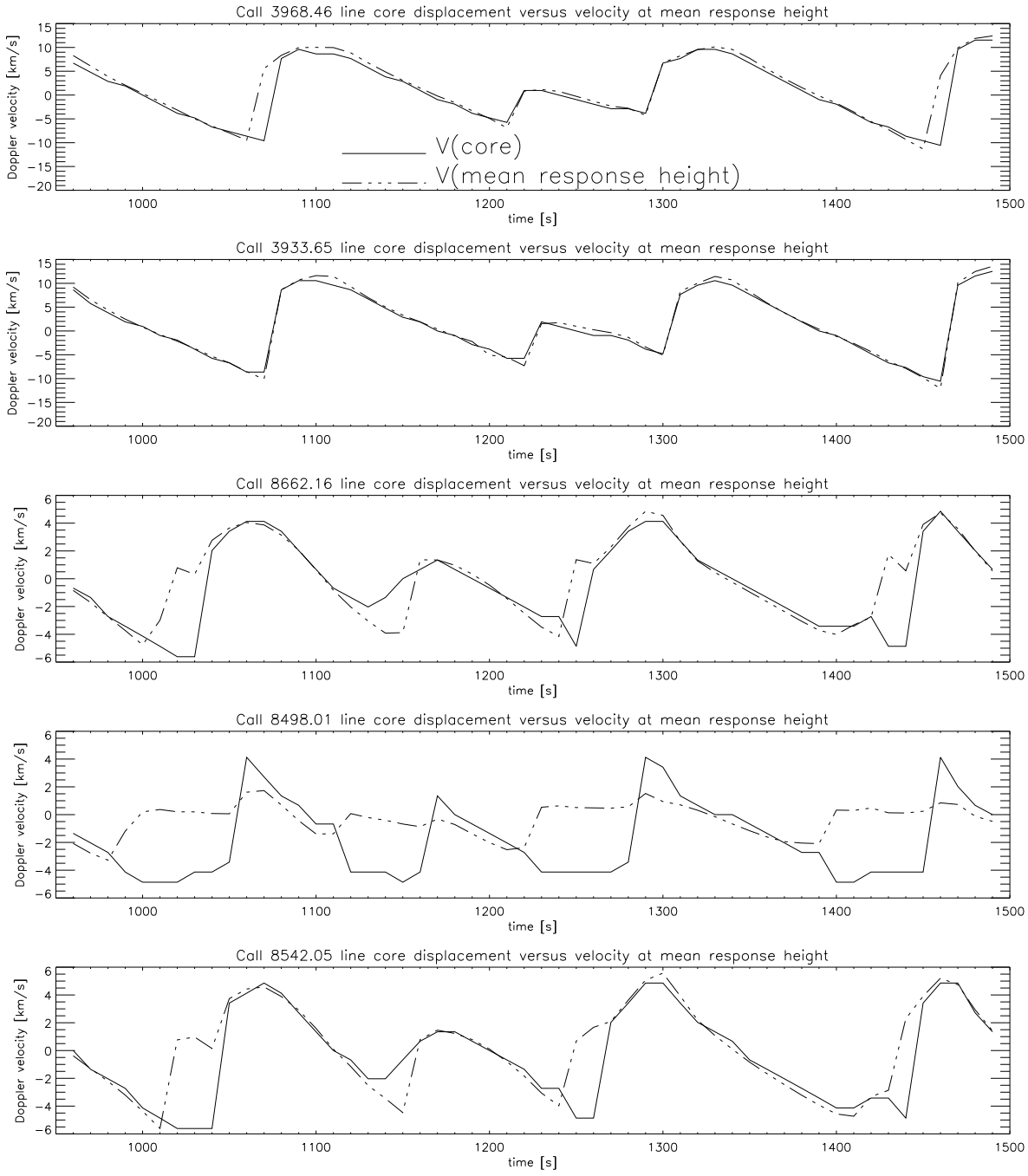

Figure 42: Doppler shift for the line cores (solid) and the atmospheric velocity at the mean response height (dot-dashed) are shown. Since the correspondence is relatively good, the Doppler shift measures approximately the atmospheric velocity at the mean response heights. Great deviations for the 8498-line are due to measurement errors introduced by the emission peaks found in the simulations. Some deviation occurs for the 8662 and 8542 lines where the redshift is maximum (negative velocities).

signal and one intensity signal (V-I), in general A-B. This means that if the signal A leads the signal B at a certain frequency, the phase difference is positive.

The two discrete signals are in the V-V phase difference relation substituted by V1 and V2 for velocity fluctuations in two line cores. We use the V-V phase sign convention of Fleck & Deubner (1989) and Deubner & Fleck (1990) which states the phase difference is positive when the Doppler shift of the line formed deepest in the atmosphere lags the same quantity for the line formed at the highest altitude. In other terms: The signs are such that upward propagating waves correspond to negative phase differences.

The two discrete signals are in the V-I phase difference relation substituted by velocity (V) and intensity (I) fluctuations in one line core. We use the V-I sign convention of Fleck & Deubner (1989), Deubner & Fleck (1990), Lites et al. (1993). Positive velocity is defined to be motion towards the observer (blueshift). The V-I phase difference is positive if positive velocity leads the intensity signal.

Note that Kulaczewski (1992) uses the I-V phase relation and positive velocity for downward motion (redshift).

We concentrate particularly on V-I and V-V relations between the 8542 and 8498 IR lines, and the V-I relation for the 3968 and 3933 line, since much attention has been given to these lines in determining chromospheric dynamics.

Observed phase relations and power spectra

Fleck & Deubner (1989) concluded that waves were propagating in the photosphere and the lower chromosphere. Between 800 and 1000km they argued for strong damping that reduced the wave energy. Above this zone, upward and downward wave propagation created a standing wave pattern in the cavity produced by the reflecting transition region. They argued that standing waves are contradicting to chromospheric heating by acoustic waves. In this paper they made no distinction between network and internetwork. They made this distinction in Deubner & Fleck (1990) where they found significant differences in the network compared to internetwork regions. Their curves for internetwork regions do not deviate much from their average sun measurements. The approximately non-magnetic internetwork regions can be compared to our simulations since we have not included magnetic fields. They found these relations that are relevant to our simulations:

1. *8542-8498 V-V phase relation.* They assumed constant line core formation heights, at 1500 km for the 8542 line, and at 1200km for the 8498 line. From this assumption they concluded that a standing wave pattern is present in the chromosphere due to very small velocity phase differences. There were also signs of downward propagation in the range from 3mHz to 5mHz due to positive phase difference of about +5 degrees and upward propagation elsewhere due to negative phase differences of typically -3 to -5 degrees. They noted the absence of 180 degree phase jumps which should occur at the nodal planes of standing waves at certain frequencies. High coherence of 0.95 were found between 3mHz and 7mHz. The coherence had a relatively slow decrease at each side of this interval.

2. *8542 V-I phase relation.* Above the acoustic cut-off frequency they found a phase difference of about -70 degrees. Below this frequency, they found increasing negative values towards -180 degrees at the lowest frequencies. The coherence was increasing abruptly at approximately 3mHz to a value of about 0.9 at 7mHz. A slowly decreasing value were found towards higher frequencies.

3. *8498 V-I phase relation.* Above the acoustic cut-off frequency they found a phase difference of about -90 degrees which changed toward -110 degrees at higher frequencies. They associated this with an expected standing wave phase difference of -90 degrees between velocity and intensity. Below the acoustic cut-off frequency, they found increasing negative values towards -180 degrees at the lowest frequencies. The coherence was increasing abruptly at approximately 3mHz to a value of about 0.9 at 7mHz. A slowly decreasing value was found towards higher frequencies.

4. *8542 velocity and intensity power spectra.* Both spectra had dominating amplitudes between 3mHz and 9mHz. The highest amplitude was found at approximately 5.5mHz, i.e. 3 minute oscillations.

5. *8498 velocity and intensity power spectra.* The intensity spectrum was very similar to the 8542 intensity spectrum. The velocity spectrum had also dominating amplitudes between 3mHz and 9mHz, but the highest amplitude was found at approximately 3.5mHz.

Lites et al. (1993) also separated network and internetwork regions. Their observed V-I phase difference (figure 43), coherence (figure 44) and power spectra for the 3968-line in the internetwork are used here to compare with the simulations, since we require non-magnetic regions. They did not give any explanations for these relations, but they encouraged the reader to study detailed numerical simulations of chromospheric dynamics, before any interpretations could be done. Their findings relevant to our simulations are:

1. *3968 V-I phase relation.* Brightening leads upward velocity by approximately 100 degrees at the acoustic cut-off frequency. The phase difference is thus -100 degrees. There is an increasing negative value to about -130 degrees towards 10mHz. A coherence of approximately 0.65 occurs between 3mHz and 8mHz, and it is approximately 0.2 outside this range.

2. *3968 velocity and intensity power spectra.* They found much less high frequency intensity power compared to velocity power, which they found to be an internetwork property. Dominating velocity amplitudes were found from 3.5mHz to 7.5mHz. Dominating intensity amplitudes were found in the same frequency range.

Kulaczewski (1992) found similar behavior for the 3933 line V-I phase differences and coherence relations as Lites et al. (1993) did for the 3968 line. He also found similar behavior for the 8542 V-I phase differences and coherence relations as Fleck & Deubner (1989) and Deubner & Fleck (1990) did for the same line.

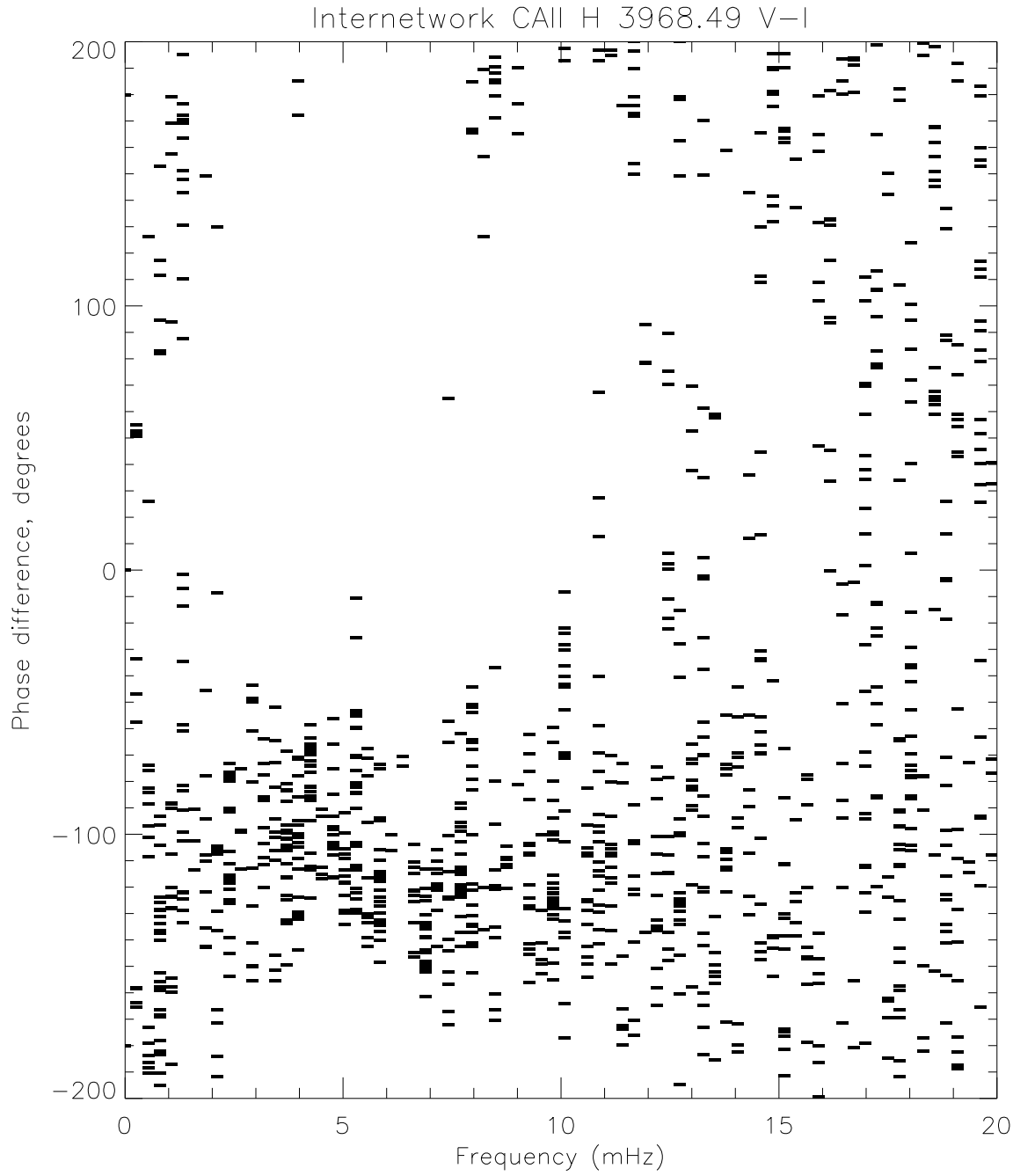

Figure 43: Observed phase differences in internetwork regions of the quiet sun. Brightening leads upward velocity by approximately 100 degrees at the acoustic cut-off frequency of 5.5mHz. The phase difference is thus -100 degrees. There is an increasing negative value to about -130 degrees towards 10mHz. The figure is reproduced by using the sequence of digital spectrograms from observations done with the Vacuum Tower Telescope at Sacramento Peak on 1984 April 12 (Lites et al. 1993). The amplitudes of the V and I signals are geometrically averaged. The phase difference at a certain frequency originating from a certain slit position is plotted if the average amplitude exceeds a given threshold.

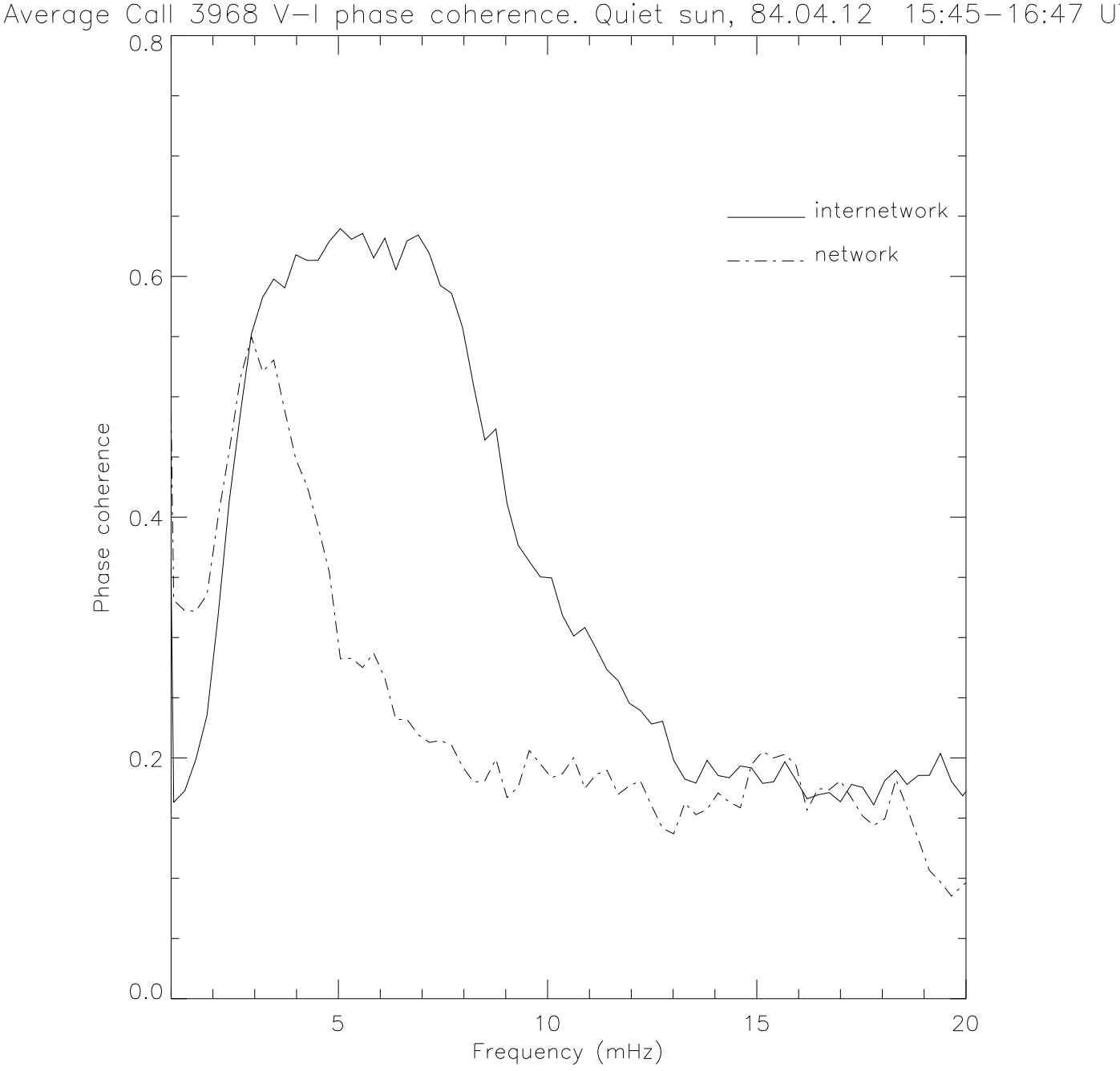

Figure 44: Observed V-I phase coherence for the 3968 line show different behavior in network and internetwork regions of the quiet sun. The phase coherence from different slit positions are arithmetically averaged. A higher correlation between the two signals is evident in internetwork regions. Internetwork regions have weak magnetic fields compared to the network areas. Only internetwork data can then be compared to the simulations. The figure was reproduced by using the sequence of digital spectrograms from observations done with the Vacuum Tower Telescope at Sacramento Peak on 1984 April 12 (Lites et al. 1993).

Simulated phase relations and power spectra compared to observations

1. *8542-8498 V-V phase relation.* Figure 45. The reader should be reminded about 8498 line core emission peaks which gave spurious estimates of the atmospheric velocity when this peak occurred. This can influence the spectral signatures significantly.

   There is nevertheless good phase difference correspondence to observations with small positive phases around 5mHz, and negative small phases at higher frequencies up to 12mHz. Standing waves are thus not required to produce the observed small phase differences. The phase differences are scattered between +/- 50 degrees above 12mHz. High coherence occurs between 4mHz and 9mHz which agrees with the observed range of the coherence peak. The coherence is about 0.95 in this interval which agrees with observations.

2. *8542 V-I phase relation.* Figure 46. Above 4mHz, the phase difference is approximately -100 degrees in good correspondence with the observed -70 degrees. Below 4mHz, it is increasing to about -180 degrees for frequency components with the highest amplitudes. This is also in correspondence with observations. The coherence curve agrees with observations, with a sharp increase to 0.95 at 4mHz and a maximum value of 0.98 at about 7mHz.

3. *8498 V-I phase relation.* Figure 47. Above 5mHz, the phase difference is approximately -130 degrees which changes to -170 degrees at 10mHz. Increasing negative values was also found in the observations, but at overall smaller negative values from -90 to -110 degrees. The coherence curve agrees with observations, with a sharp increase to 0.85 at 4mHz and a maximum value of 0.95 at 8mHz. The phase difference deviations from the observed values can be due to the ill defined line core.

4. *8542 velocity and intensity spectra.* Figure 46. Both spectra have dominating amplitudes between 4mHz and 10mHz which agrees with the observations. The highest amplitudes are located around 5.5mHz which is the same as for the observations. The high frequency intensity power above 10mHz is damped relative to the velocity power. This tendency can also be seen in the observations.

5. *8498 velocity and intensity spectra.* Figure 47. Comparisons are again difficult due to the emission peaks. There are again dominating amplitudes between 4mHz and 10mHz consistent with observations.

6. *3968 V-I phase relation.* Figure 48. The high coherence range from 3mHz and 8mHz is consistent with observations. The coherence reaches a maximum value of approximately 0.7 at 5mHz which agrees very well with the observed value of 0.65. Above 10 mHz, the coherence has a fluctuating value around 0.6 which do not agree with the corresponding observed value of 0.2. It most be noted that seeing and noise in observations reduces the high frequency coherence such that a direct comparison with simulations becomes difficult.

The phases in the high coherence range and at the cut-off frequency of 5.5mHz lies at approximately -100 degrees. This is almost the same as for the observations. There is a further decrease to -130 degrees towards 10mHz, again consistent with observations.

7. *3968 velocity and intensity spectra.* Figure 48. As for the observations, there is less intensity power above 10mHz compared to velocity power above 10mHz. Dominating intensity and velocity amplitudes are found between 3.5mHz and 7.5mHz as for the observations. The 3933 line show very similar phase relations and power spectra.

8. *3968-8542 V-V phase relation.* Figure 49. This relation has not been shown by the authors we have referred to. It is included to cover V-V phase relations between two lines with a greater difference in response heights compared to the 8542 and 8498 line pair. Simulated phase relations can also be useful for future analysis of observational data. The phase differences show clearly increasing negative values from about -25 degrees at 4mHz to about -150 degrees at 10mHz. This indicates propagating waves if the standard interpretation is used. This is in fact true since propagating waves are measured in the model. High coherence of 0.85 is found between 4mHz and 9mHz.

It must be noted that the observed values are averages over several internetwork slit-positions. The model atmosphere is exited by a moving piston with a velocity spectrum taken from a photospheric Fe-line at a single slit position from the observations by Lites et al. (1993). Deviations from observed values are thus expected since our model is exited by a local sub-photospheric velocity field. The simulations must be said to agree very well with observed values of phase differences, coherence, and power spectra with the local exitation limitation in mind. The only clear deviation occurs for the V-V relations or V-I relations where the 8498 line is involved, due to difficulties in determining the 8498 line-core position. We thus feel justified to explain some of the observed spectral features where the 8498 line is not involved.

7.3.6 Sensitivity to chromospheric heating

Phase difference, phase coherence, and power spectra were also computed for the acoustically heated model. These quantities deviate much from those found in the pre-heated model, and thus from the observed values. This suggests that an additional heating term is needed in order to obtain a close agreement with solar chromospheric dynamics. Both models had constant microturbulence on a height scale.

7.3.7 Phase relation interpretations

In the previous sections we found that linear theory can not be used to determine height differences between fixed heights if one or both of the measuring points were located above the typical shock formation height at 1000km. Inaccurate measurements occurred already between 500km and 1000km. The mean response heights for CaII line core Doppler shifts fluctuated several hundred kilometers on time scales equal to the typical fluctuation period of the waves. Such response height fluctuations makes it impossible to conclude about

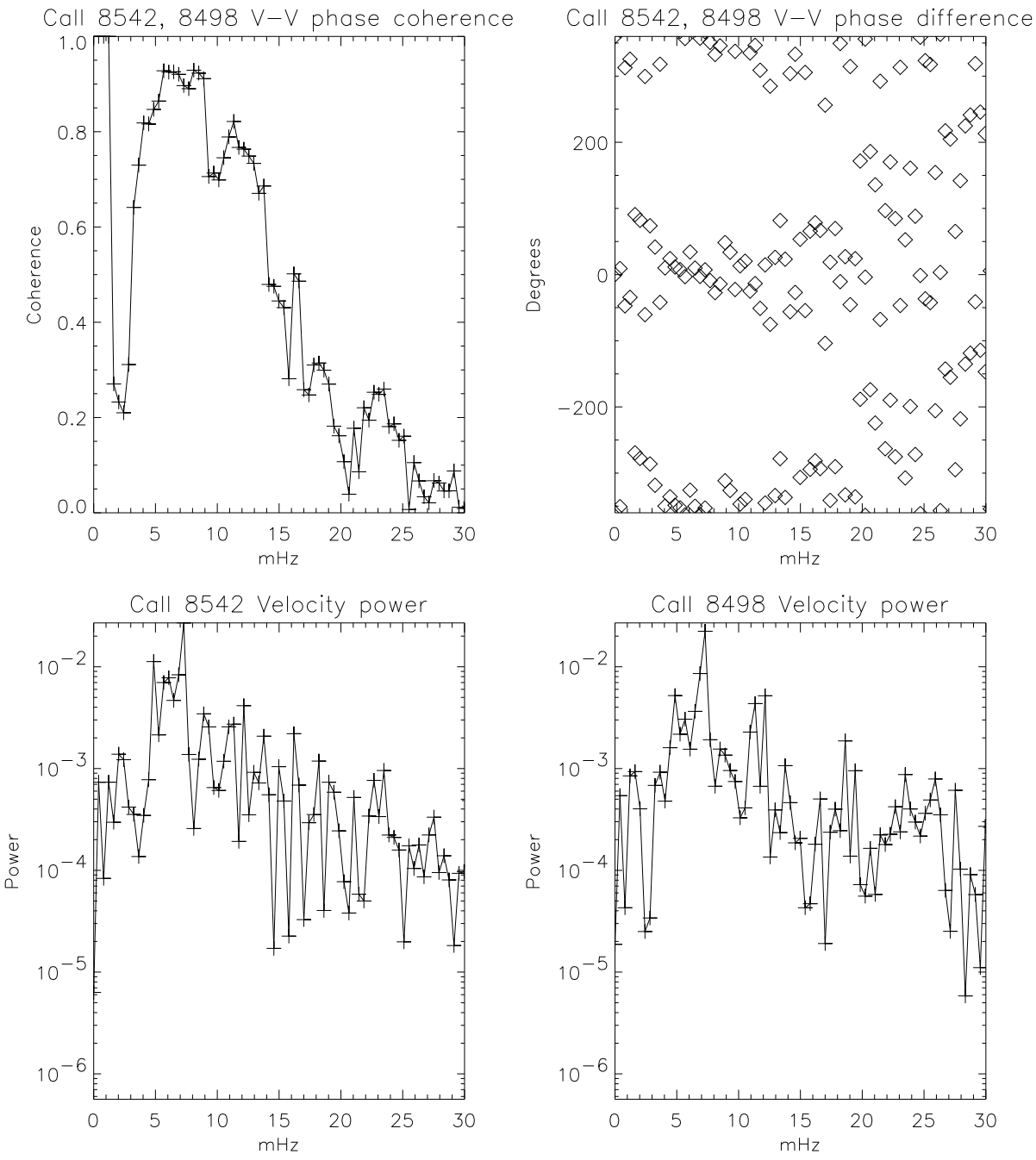

Figure 45: V(8542)-V(8498) phase difference and phase coherence for the infrared CaII lines 8542 and 8498. The phase coherence was computed by a 9 point running average. The phase differences are periodic with a period of 360 degrees. The corresponding power spectra are shown. The sampling frequency was 100mHz. The Nyquist frequency is thus located at 50mHz.

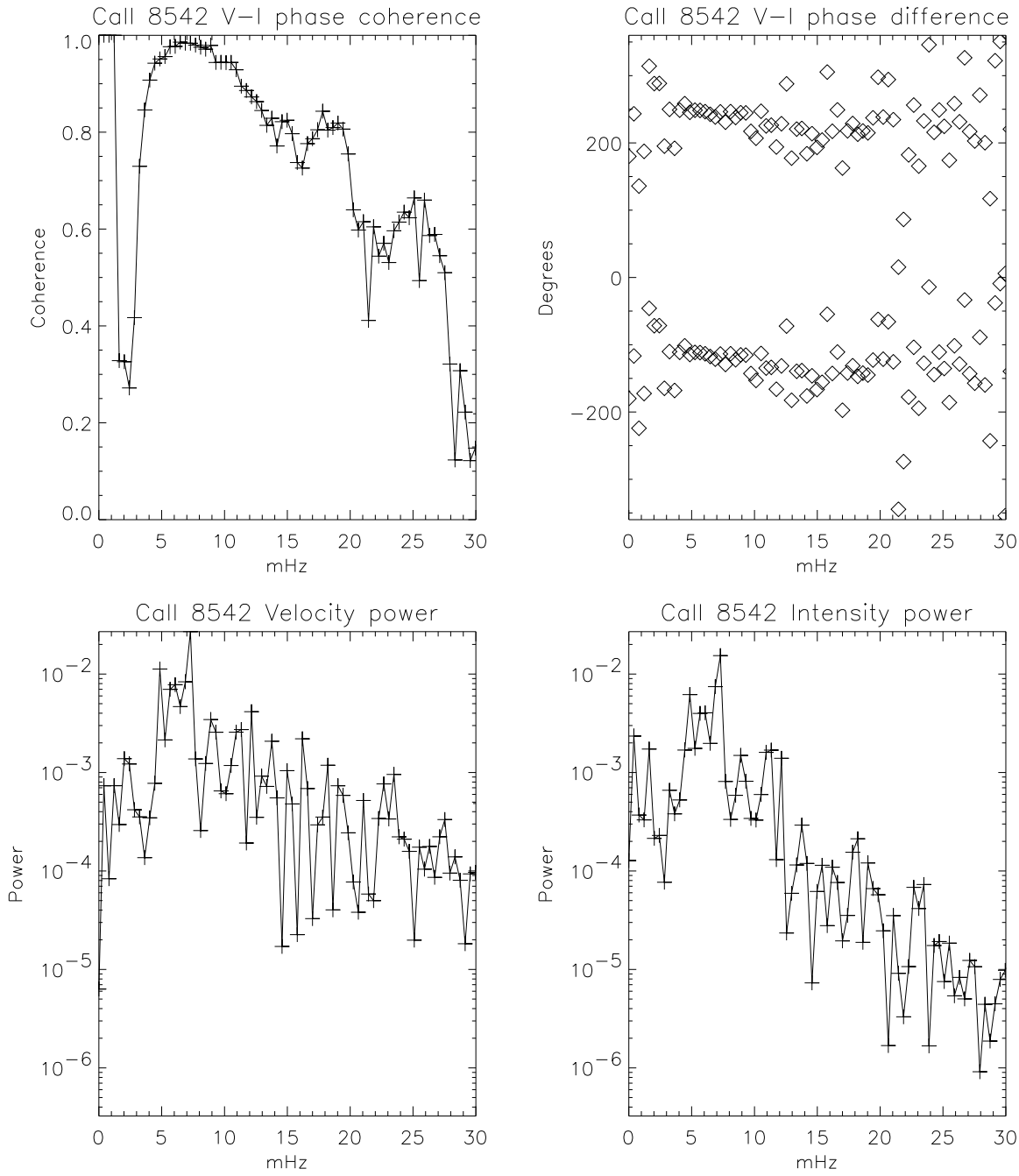

Figure 46: V(8542)-I(8542) phase difference and phase coherence for the infrared CaII line. The phase coherence was computed by a 9 point running average. The phase differences are periodic with a period of 360 degrees. The corresponding power spectra are shown. The sampling frequency was 100mHz. The Nyquist frequency is thus located at 50mHz.

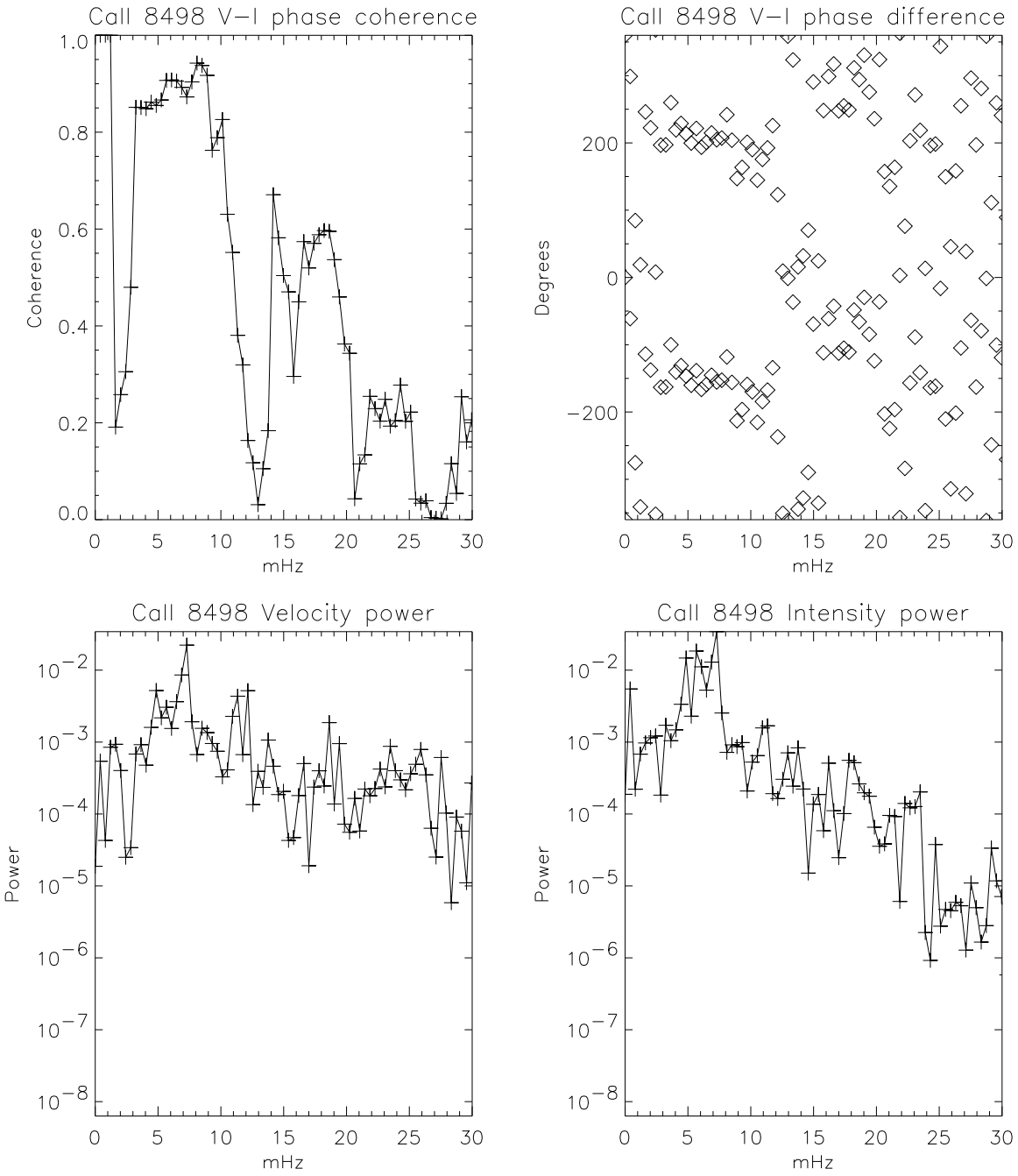

Figure 47: V(8498)-I(8498) phase difference and phase coherence for the infrared CaII line. The phase coherence was computed by a 9 point running average. The phase differences are periodic with a period of 360 degrees. The corresponding power spectra are shown. The sampling frequency was 100mHz. The Nyquist frequency is thus located at 50mHz.

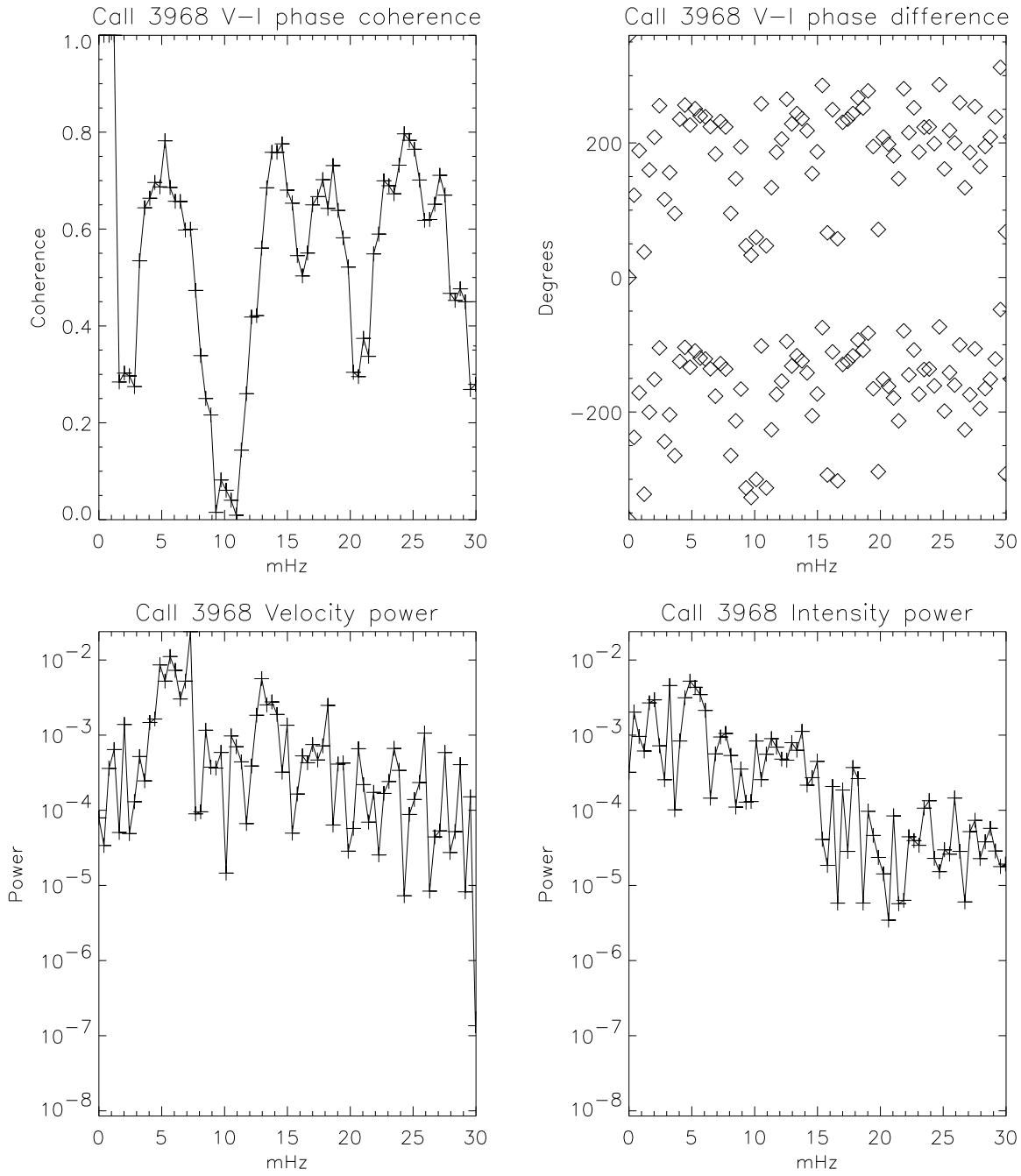

Figure 48: V(3968)-I(3968) phase difference and phase coherence for the violet CaII line. The phase coherence was computed by a 9 point running average. The phase differences are periodic with a period of 360 degrees. The corresponding power spectra are shown. The sampling frequency was 100mHz. The Nyquist frequency is thus located at 50mHz.

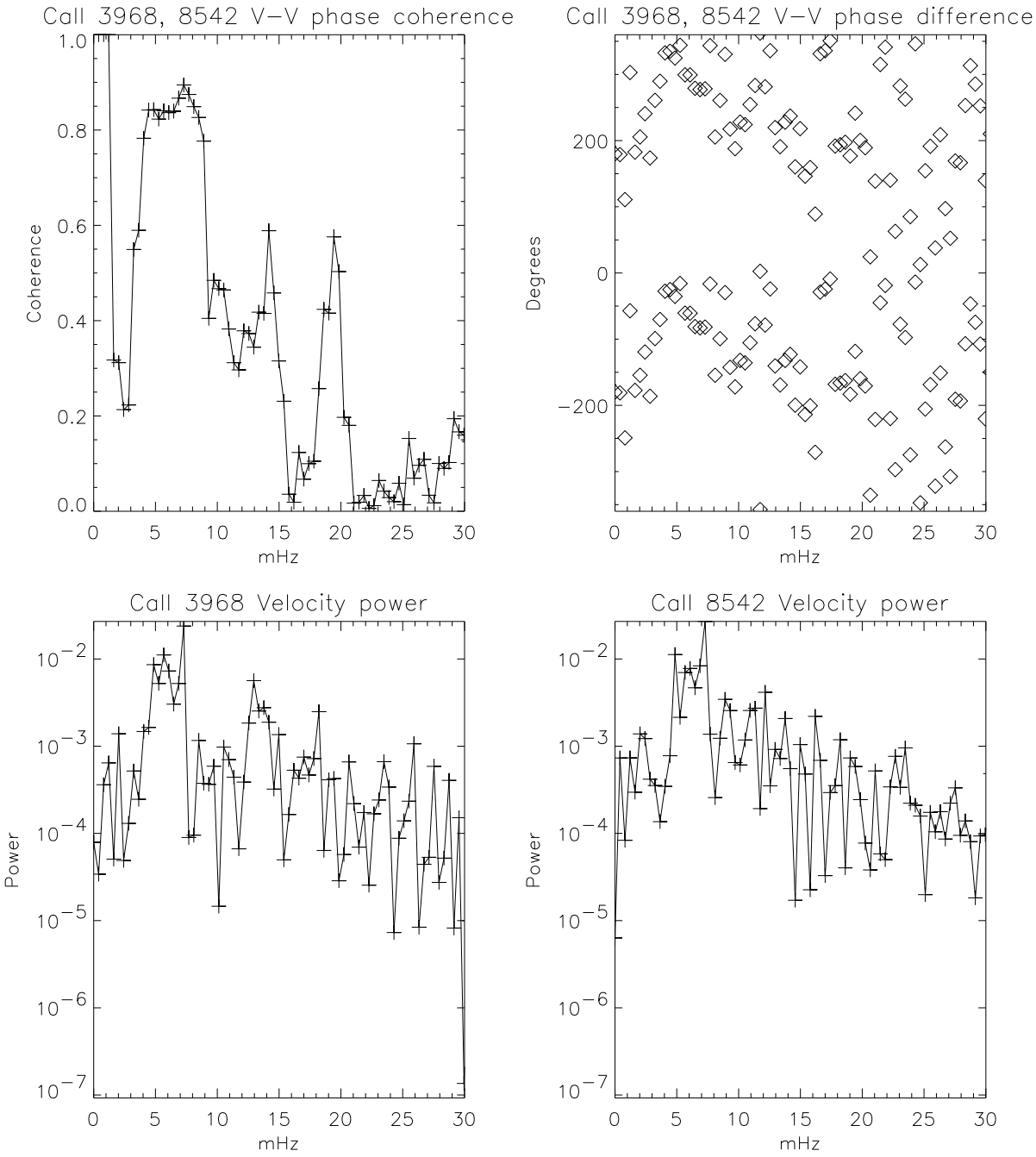

Figure 49: V(3968)-V(8542) phase difference and phase coherence. The phase coherence was computed by a 9 point running average. The phase differences are periodic with a period of 360 degrees. The corresponding power spectra are shown. The sampling frequency was 100mHz. The Nyquist frequency is thus located at 50mHz.

types of wave modes such as propagating or standing waves from line core fluctuations (Fleck & Deubner 1989). The additional invalidity of linear theory in the chromosphere where these line core shifts originate, make such interpretations of V-V and V-I phase relations impossible.

As far as we know, the only solution to proper interpretations is to solve the radiation hydrodynamic equations, and thereafter look for connections between physics and V-V relations and V-I relations.

We choose to explain the physics of the 3968 V-I phase differences and the 8542 V-I phase differences, since these agree well with observations. The 3968-8542 V-V phase differences are explained in order to include a V-V relation between chromospheric lines which have their mean response heights on the average far apart. This last relation should also be interesting in order to test our model by a comparison with future observations. The phase differences around 5.5 mHz are discussed, since these Fourier components dominate the shape and phase shifts of the V and I curves due to their high amplitudes and phase coherence.

The V-I relation is explained with the aid of the contribution function contour plots in the depth-frequency plane. There is one figure for every 40 seconds. A total interval of 160 seconds is considered, giving 5 different snap-shots. Each figure contains three panels (figure 53). The upper panel shows the intensity in the line core. The middle panel shows the contribution function to intensity in the depth-frequency plane. The bottom panel shows the contribution function to relative absorption or response function to Doppler shift. A slice parallel to the depth-axis through the contour plots at the line core position gives the contribution functions we are interested in. The intensity formation depths and Doppler shift response heights in the line core can then be found.

1. *3968 V-I phase difference.*

   A phase difference of -100 degrees around 5.5mHz was found in the simulations. Figure 50 shows that intensity leads velocity by approximately 100 degrees. Figures 53-57 illustrates the typical atmospheric properties responsible for the 100 degree phase shift.

   At 2200s (figure 53), a blueshifted line core occurs because the RF is located in a region with positive velocities. The intensity is formed at low source function values above the local maximum, producing minimum intensity.

   At 2240s (figure 54), an almost un-displaced line core occurs because the RF is located in regions with both positive and negative velocities. The intensity is formed above the local maximum which has gained an increased value due to the shock formation, leading to increased intensity.

   At 2280s (figure 55) , a maximum redshifted line core occurs because the RF is located in the pre-shock region close to the shock with high negative velocities. The intensity is now formed close to the source function peak in the post-shock region, leading to maximum intensity.

   At 2320s (figure 56), a maximum blueshifted line core occurs because the RF is located in the high velocity post-shock region. The intensity is now formed at the

low source function values in the post-shock region, making the intensity relatively low. Maximum intensity occurred at 2280 seconds. A time delay of 40 seconds between maximum intensity and maximum blueshift is consistent with a 100 degree phase shift. 40 seconds corresponds to 80 degrees for a 180 second oscillation period.

At 2360s (figure 57), the line core is just about to become redshifted again because the RF is located where the plasma begins to move down again. The intensity is still formed above the source function peak, and it will thus stay relatively low until the formation depth approaches the shock that will eventually form again. The cycle is thus completed.

This atmospheric behavior is thus sufficient to explain the -100 degree V-I phase shift at the "fundamental" period of 3 minutes.

2. *8542 V-I phase difference.*

A phase difference of -100 degrees around 5mHz was found in the simulations. Figure 51 shows that intensity leads velocity by approximately 100 degrees.

Figures 58-62 illustrates the typical atmospheric properties responsible for the 100 degree phase shift.

At 2220s, (figure 58) the line core is just about to become redshifted because the RF is located where downward motion will dominate. The intensity is formed above the source function peak, and it will be relatively low until the formation depth approaches the shock that will eventually form.

At 2240s, (figure 59) maximum redshift occurs because the RF is located in a trough with downward motion. The intensity is now formed partially on the source function peak, making a relatively higher intensity.

At 2280s, (figure 60) an almost un-displaced line core occurs because the RF has moved to the recently formed post-shock region with low positive velocities. The intensity is formed in the post-shock region where the source function peaks, making the intensity maximum.

At 2320s, (figure 61) a maximum blueshifted line core occurs because the RF is located in the post-shock region with relatively high positive velocities. It is thus a 40s time delay between maximum intensity and maximum blueshift corresponding to 80 degrees for a 180s period. This is consistent with a 100 degree phase shift. The intensity is now formed at a decreased source function, making a decreased intensity.

At 2360s, (figure 62) zero displacement occurs because the RF is located in the far post-shock region with relatively low positive and negative velocities. The source function value has now decreased to a minimum at the formation depth, making minimum intensity. There is thus a 120s time delay between maximum redshift and minimum intensity. This corresponds to a 120 degree phase shift for a 180s period where the intensity leads velocity. The previous value of the phase shift was 80 degrees. The average between these two values is thus 100 degrees. The cycle is thus completed.

This atmospheric behavior is thus sufficient to explain the -100 degree V-I phase shift at the "fundamental" period of 3 minutes.

3. *3968-8542 V-V phase difference.*

   The highest amplitude and coherence is located at 7mHz where the phase difference is approximately -90 degrees. It is thus easily seen in figure 52 that the velocity signal of 8542 leads the upward velocity signal of 3968 by approximately 90 degrees. Figure 63 illustrates the typical atmospheric properties responsible for the 90 degree phase shift.

   At 1290s, blueshift occurs for 8542 where the RF is located in a post-shock region with upward motion. 3968 is maximum redshifted due to the RF location in pre-shock regions with downward motion.

   40 seconds later at 1330s, a velocity gradient and overall smaller velocities make the 8542 blueshift smaller. The RF has remained at the same height, but it is now wider. The 3968 core has now maximum blueshift due to the RF in the post-shock region. Higher maximum blueshift for 3968 compared to 8542 is due to the increased shock strength at higher altitudes.

   60 seconds later at 1390s, the 8542 RF is located at the trough above the next shock that is about to form. The 8542 is now maximum redshifted because of downward moving matter at the trough. The 3968 RF now probes a layer that is almost at rest, such that the Doppler shift is approximately zero.

   60 seconds later at 1450s, the 8542 RF is located in the post-shock region again but now for the next shock that is fully developed. Upward motion leads to a a blueshifted 8542 line core. The 3968 RF is now located at high negative velocities and the core is redshifted again. The cycle is now completed.

   This atmospheric behavior is sufficient to explain the -90 degree phase shift between the two line cores at the "fundamental" period of 3 minutes.

4. *Some general considerations*

   A few important and general relations that are valid for the 8542 and 3968 lines are evident from the contour plots.

   The formation depths of minimum intensity and the response depths to line core displacements are approximately equal, even if these depths or heights vary strongly with time. The line core intensity is formed above the local source function maximum where high escape probability relative to destruction probability makes the source function less dependent on local temperature. Scattering dominates and NLTE effects are important. The core intensity can therefore *not* be associated with local temperatures.

   The velocity at the mean response height gave a good estimate of the averaged velocity. The only observed quantity that has a direct interpretation is therefore a Doppler velocity signal from one of the CaII lines. It will of course be difficult to

connect this quantity to the velocity field in the solar chromosphere, if the mean response height fluctuates several hundred kilometers.

The CaII V-I relations should thus not be considered as velocity-temperature relations for the purpose of investigating chromospheric wave dynamics.

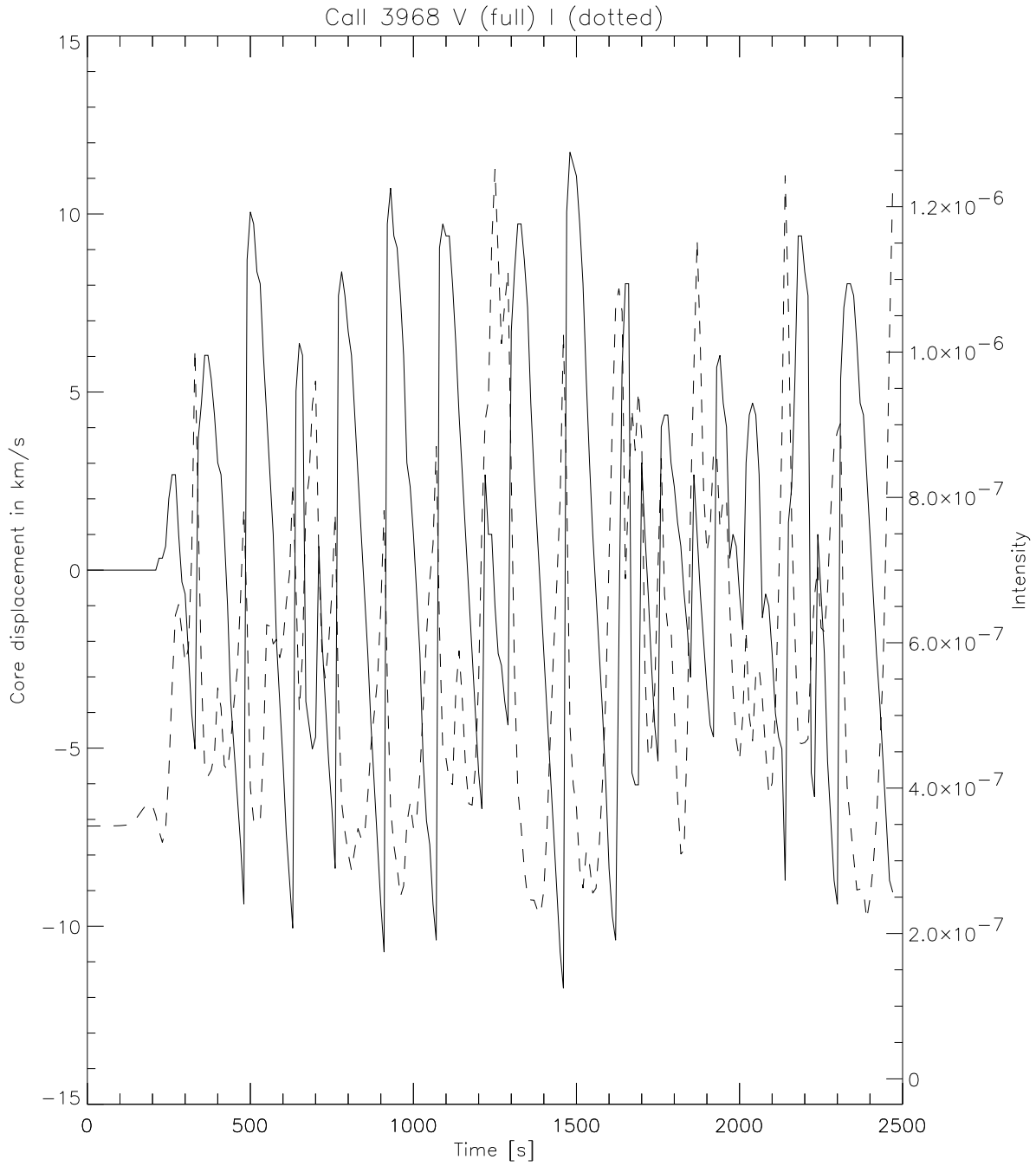

Figure 50: Intensity and velocity fluctuations for the 3968 line core during the total sequence of 40 minutes. The "fundamental" oscillation period of 3 minutes dominate the shape of the signals. Intensity leads velocity by approximately 100 degrees.

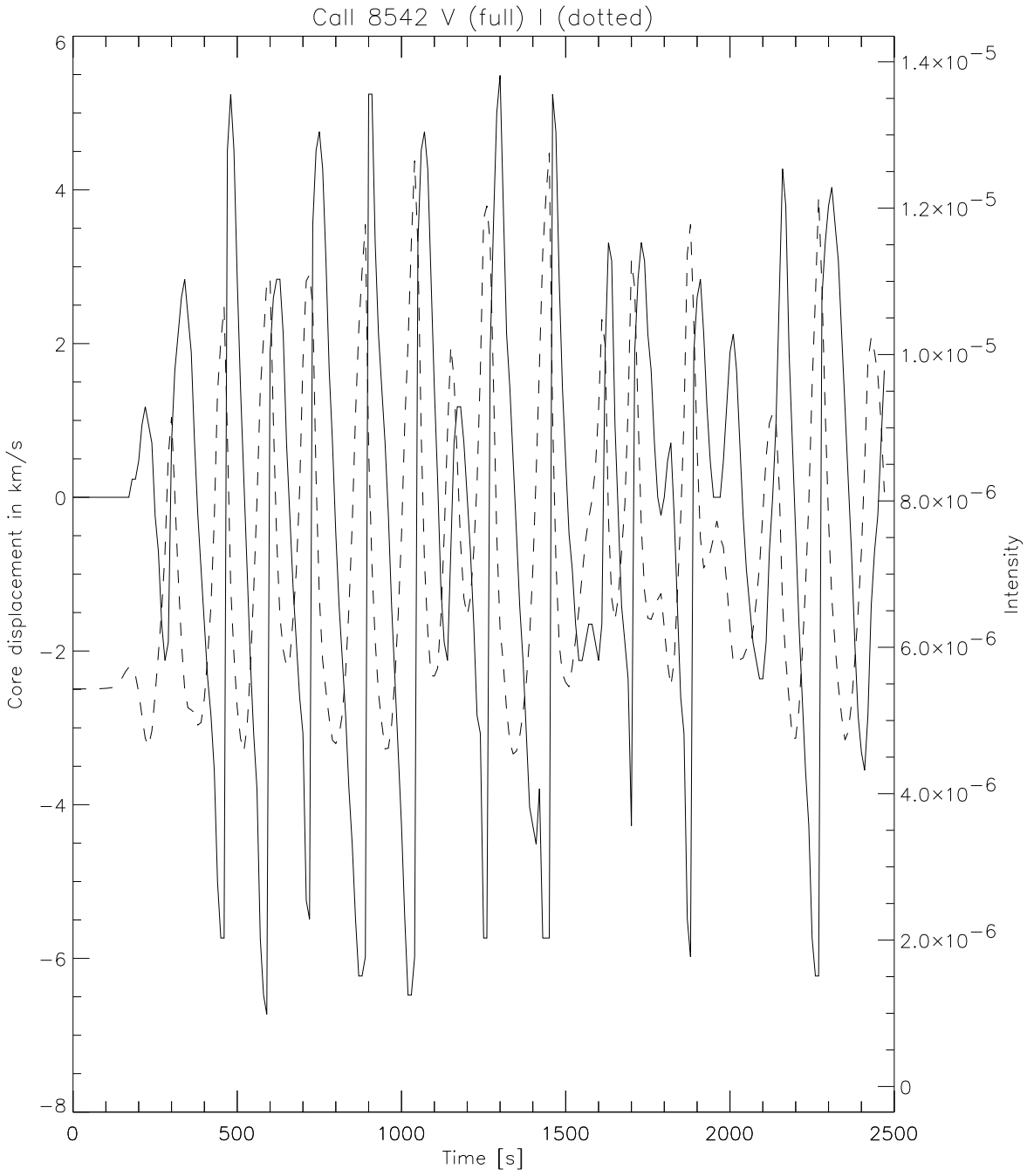

Figure 51: Intensity and velocity fluctuations for the 8542 line core during the total sequence of 40 minutes. The "fundamental" oscillation period of 3 minutes dominate the shape of the signals. Intensity leads velocity by approximately 100 degrees.

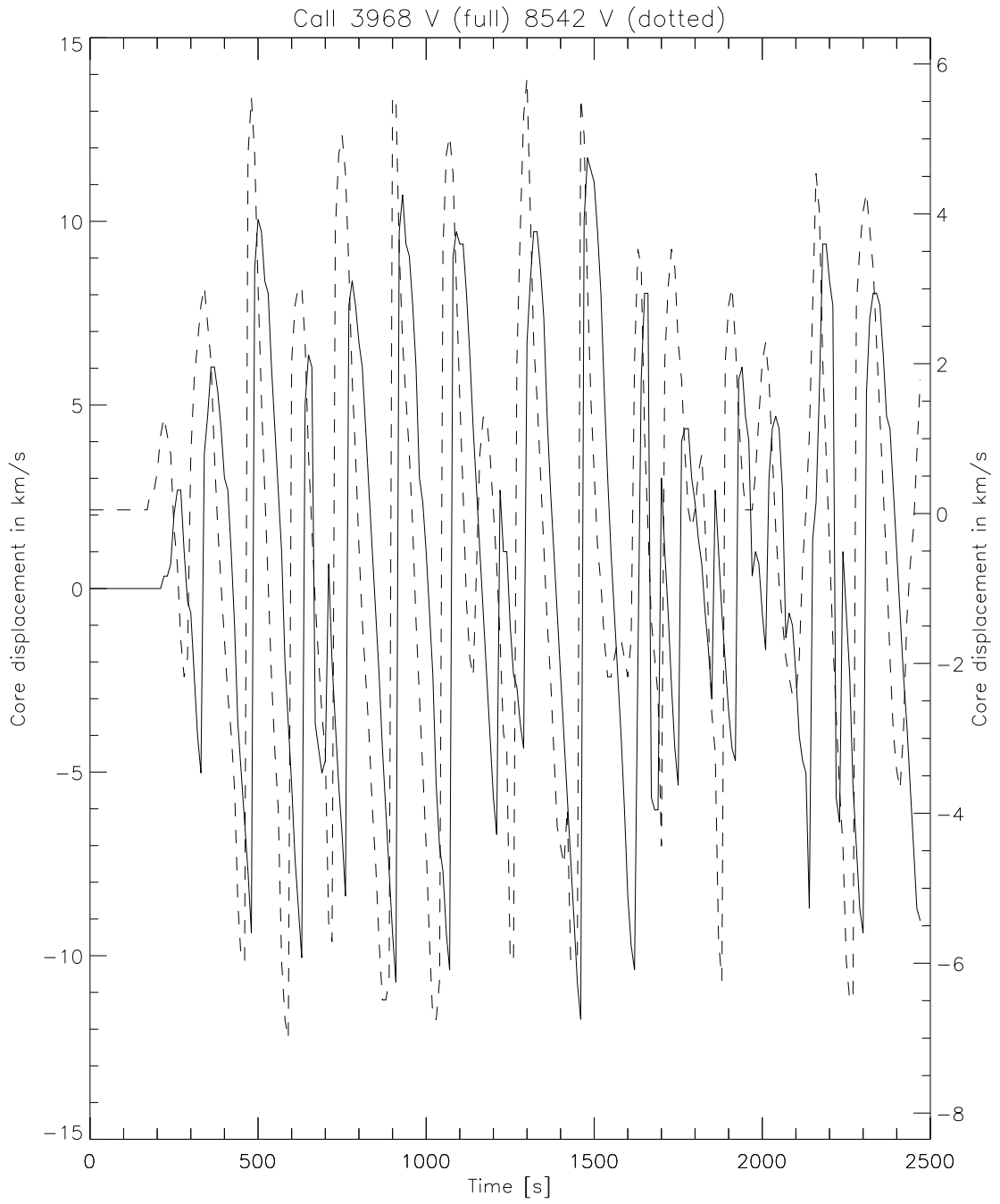

Figure 52: Velocity fluctuations for the 8542 and 3968 line cores during the total sequence of 40 minutes. The velocity axis on the left side belongs to the 3968 line. The "fundamental" oscillation period of 3 minutes dominate the shape of the signals. The 8542 signal leads the 3968 signal by approximately 90 degrees, due to upward wave propagation.

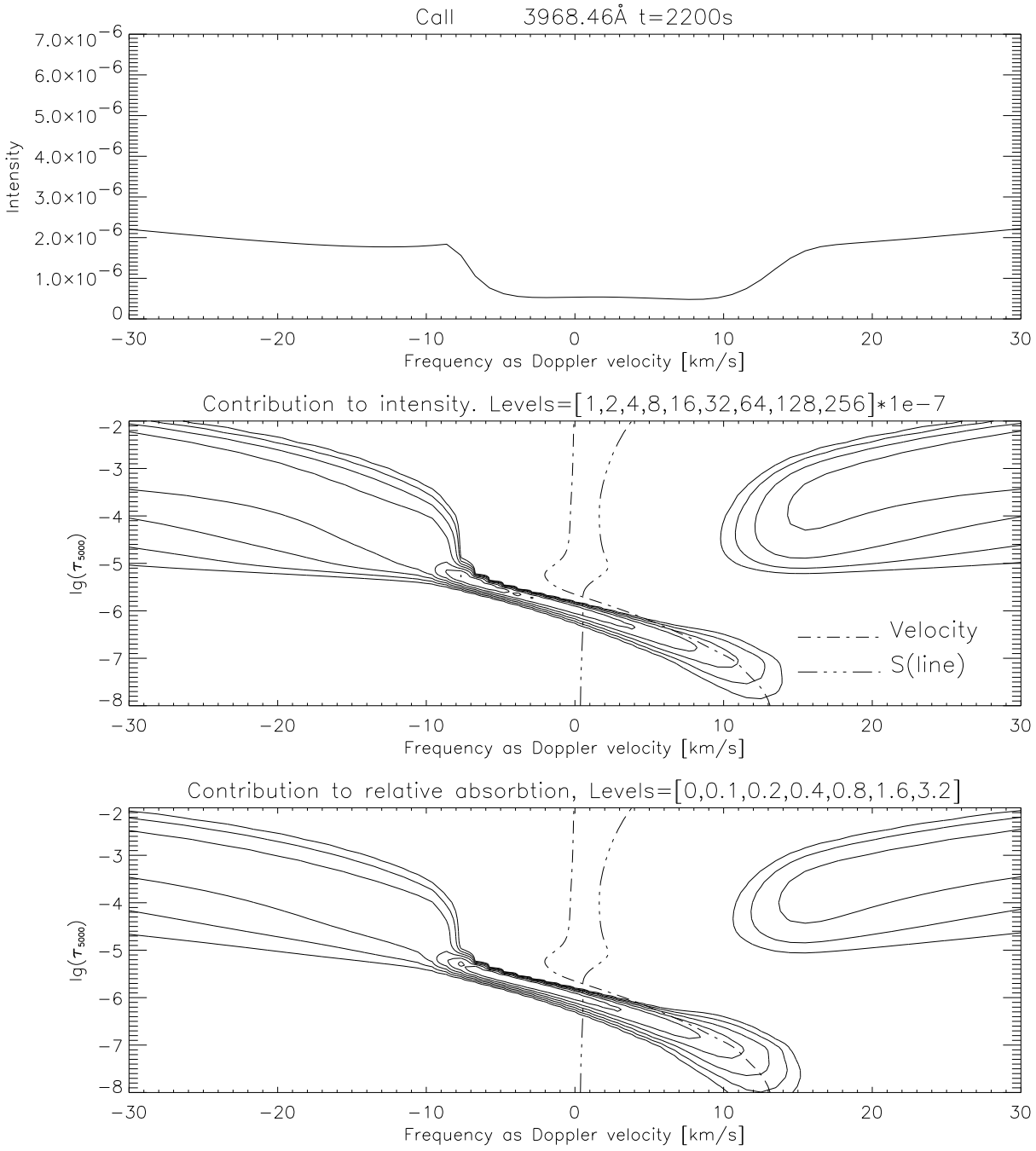

Figure 53: *Upper panel.* Line core region intensity. The frequency difference relative to line center is shown as the corresponding Doppler-velocity. Blueshift corresponds to positive velocity values. *Middle panel.* The contribution function to intensity is shown in the depth-frequency plane as a contour plot. *Bottom panel.* The contribution function to relative absorption or response function to Doppler shift is shown as a contour plot. A slice parallel to the depth-axis through the contour plots at the line core position gives the contribution function to intensity and relative absorption at this frequency. The formation depths to intensity and velocity response depths at the line core are then found. The atmospheric velocity field, and the run of the line source function are also shown.

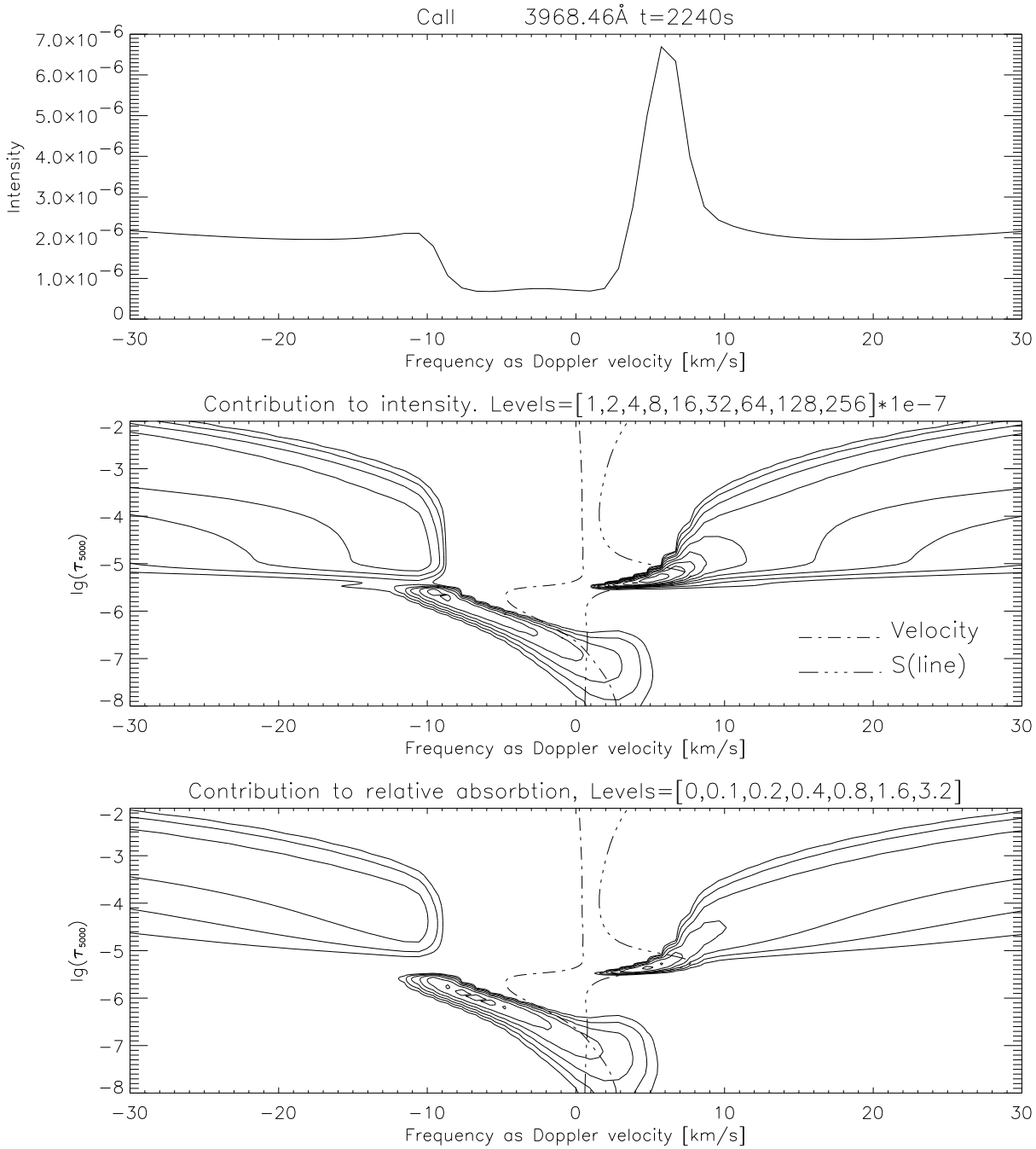

Figure 54: *Upper panel.* Line core region intensity. The frequency difference relative to line center is shown as the corresponding Doppler-velocity. Blueshift corresponds to positive velocity values. *Middle panel.* The contribution function to intensity is shown in the depth-frequency plane as a contour plot. *Bottom panel.* The contribution function to relative absorption or response function to Doppler shift is shown as a contour plot. A slice parallel to the depth-axis through the contour plots at the line core position gives the contribution function to intensity and relative absorption at this frequency. The formation depths to intensity and velocity response depths at the line core are then found. The atmospheric velocity field, and the run of the line source function are also shown.

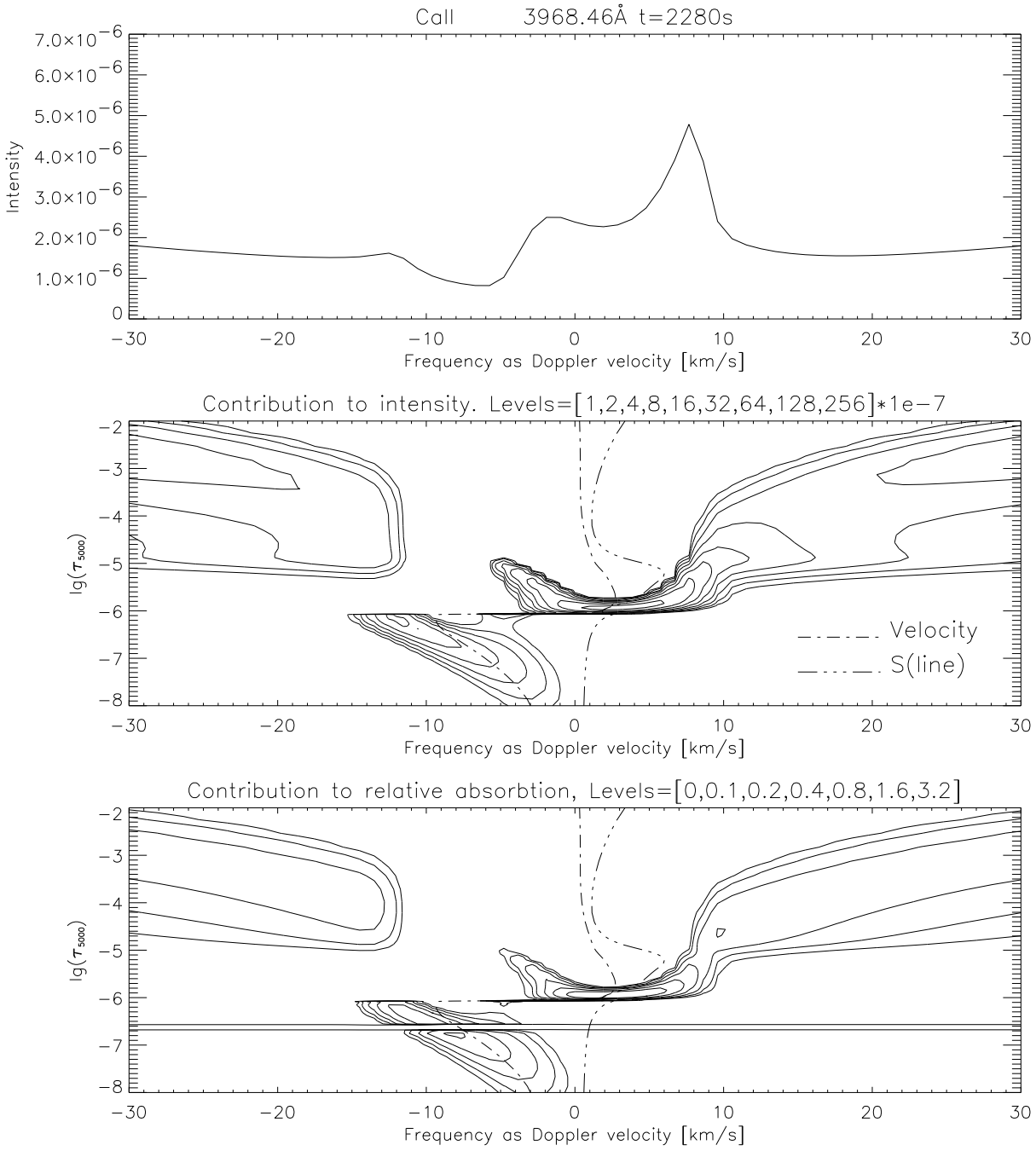

Figure 55: *Upper panel.* Line core region intensity. The frequency difference relative to line center is shown as the corresponding Doppler-velocity. Blueshift corresponds to positive velocity values. *Middle panel.* The contribution function to intensity is shown in the depth-frequency plane as a contour plot. *Bottom panel.* The contribution function to relative absorption or response function to Doppler shift is shown as a contour plot. A slice parallel to the depth-axis through the contour plots at the line core position gives the contribution function to intensity and relative absorption at this frequency. The formation depths to intensity and velocity response depths at the line core are then found. The atmospheric velocity field, and the run of the line source function are also shown.

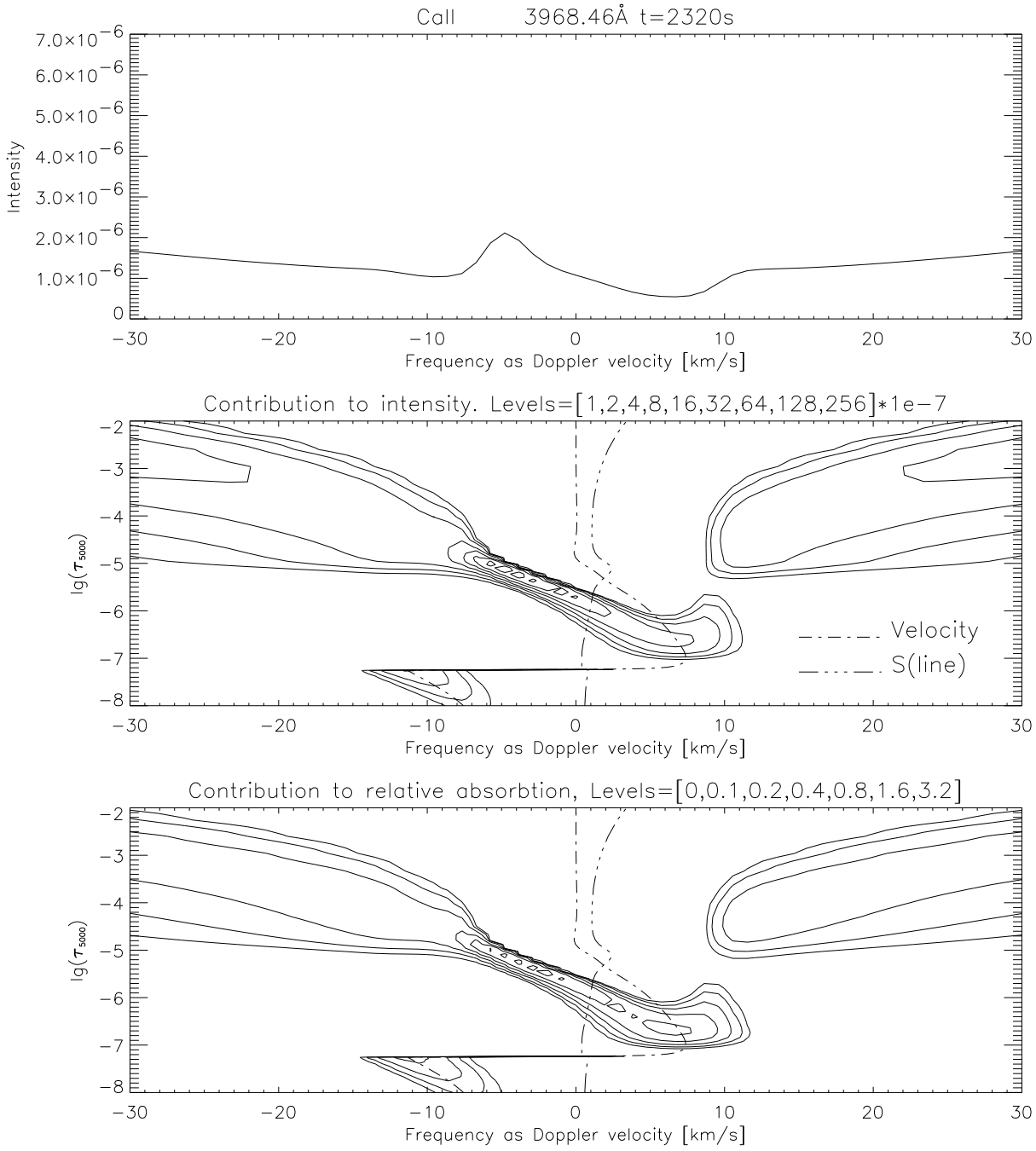

Figure 56: *Upper panel.* Line core region intensity. The frequency difference relative to line center is shown as the corresponding Doppler-velocity. Blueshift corresponds to positive velocity values. *Middle panel.* The contribution function to intensity is shown in the depth-frequency plane as a contour plot. *Bottom panel.* The contribution function to relative absorption or response function to Doppler shift is shown as a contour plot. A slice parallel to the depth-axis through the contour plots at the line core position gives the contribution function to intensity and relative absorption at this frequency. The formation depths to intensity and velocity response depths at the line core are then found. The atmospheric velocity field, and the run of the line source function are also shown.

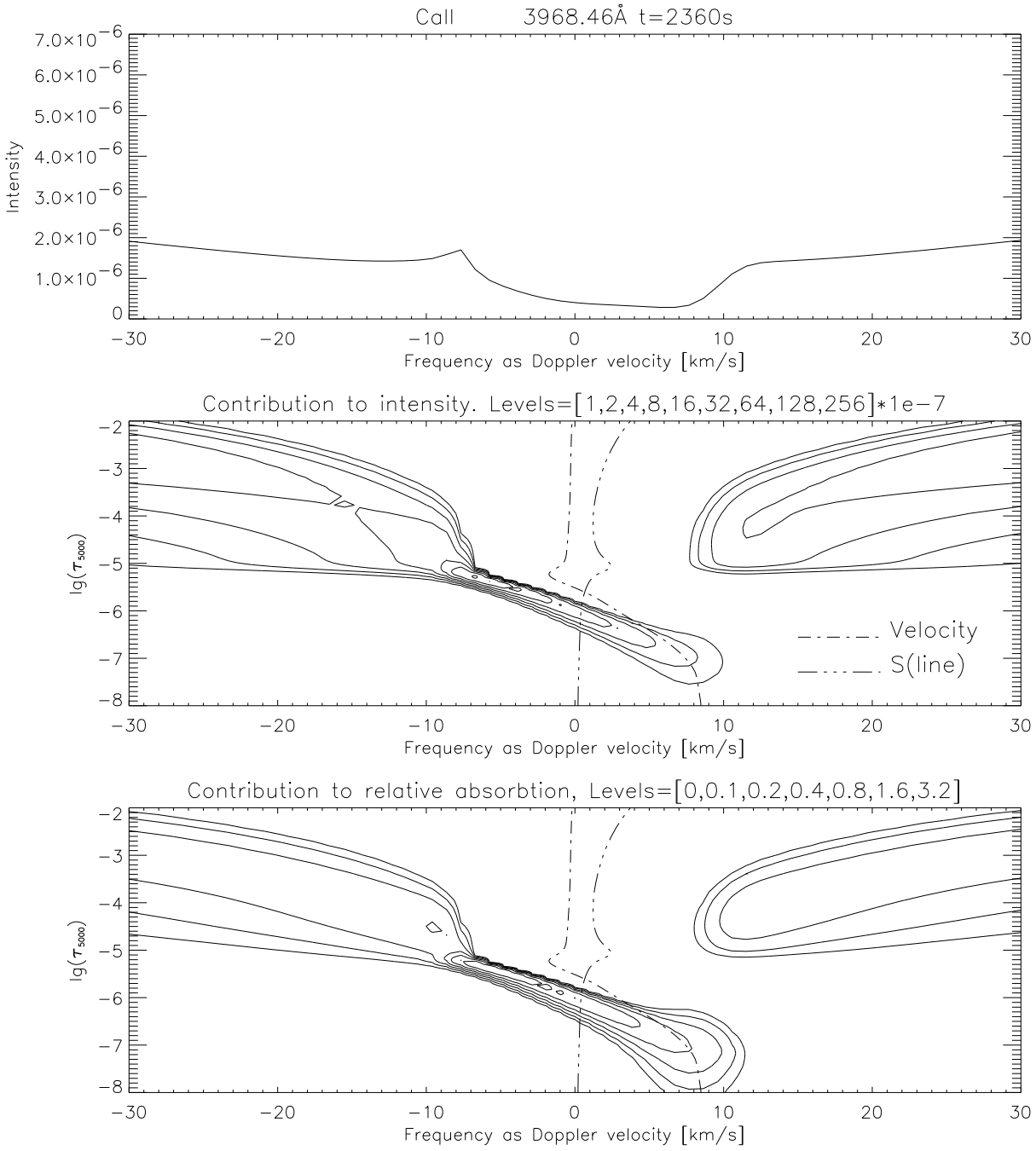

Figure 57: *Upper panel.* Line core region intensity. The frequency difference relative to line center is shown as the corresponding Doppler-velocity. Blueshift corresponds to positive velocity values. *Middle panel.* The contribution function to intensity is shown in the depth-frequency plane as a contour plot. *Bottom panel.* The contribution function to relative absorption or response function to Doppler shift is shown as a contour plot. A slice parallel to the depth-axis through the contour plots at the line core position gives the contribution function to intensity and relative absorption at this frequency. The formation depths to intensity and velocity response depths at the line core are then found. The atmospheric velocity field, and the run of the line source function are also shown.

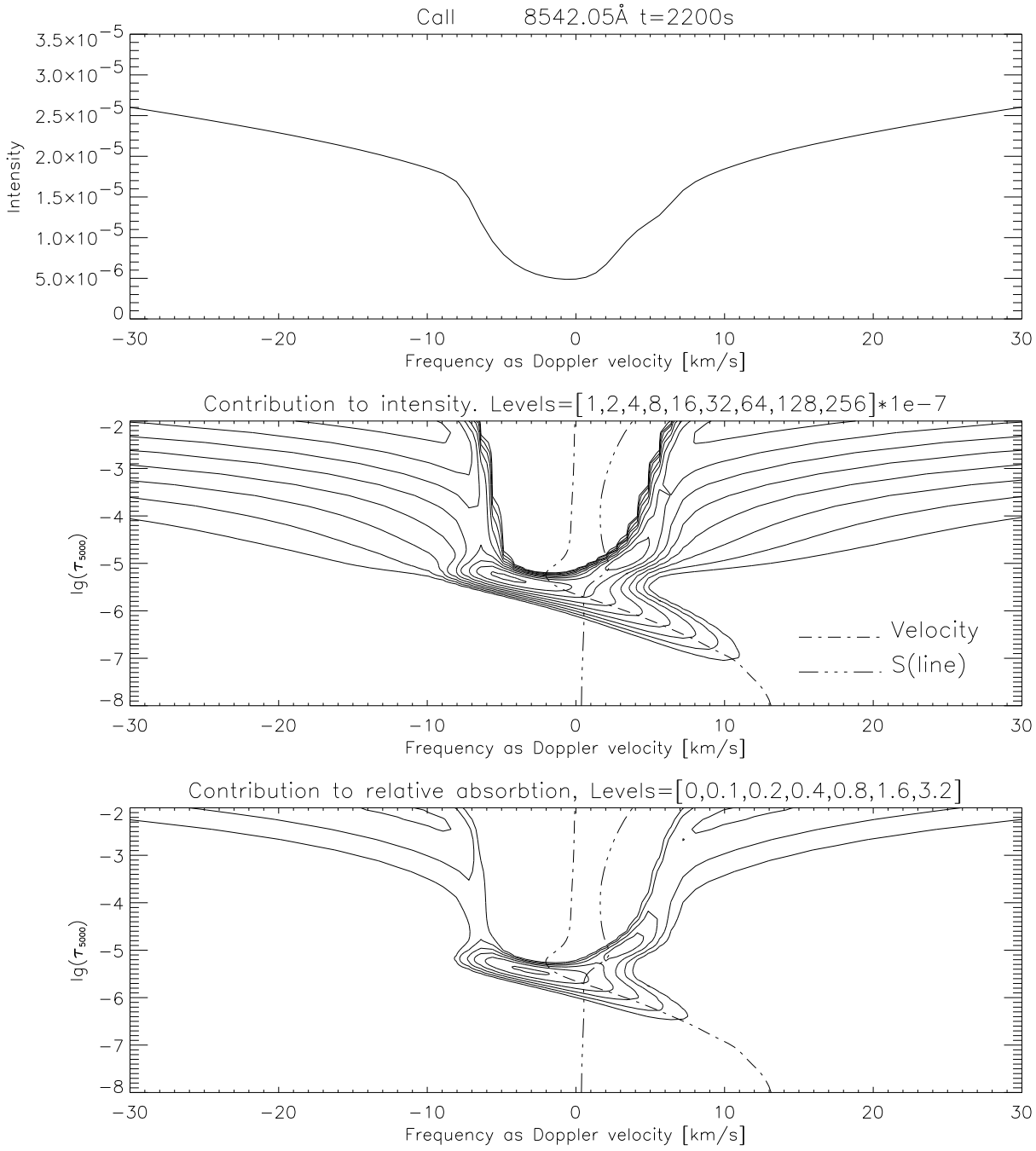

Figure 58: *Upper panel.* Line core region intensity. The frequency difference relative to line center is shown as the corresponding Doppler-velocity. Blueshift corresponds to positive velocity values. *Middle panel.* The contribution function to intensity is shown in the depth-frequency plane as a contour plot. *Bottom panel.* The contribution function to relative absorption or response function to Doppler shift is shown as a contour plot. A slice parallel to the depth-axis through the contour plots at the line core position gives the contribution function to intensity and relative absorption at this frequency. The formation depths to intensity and velocity response depths at the line core are then found. The atmospheric velocity field, and the run of the line source function are also shown.

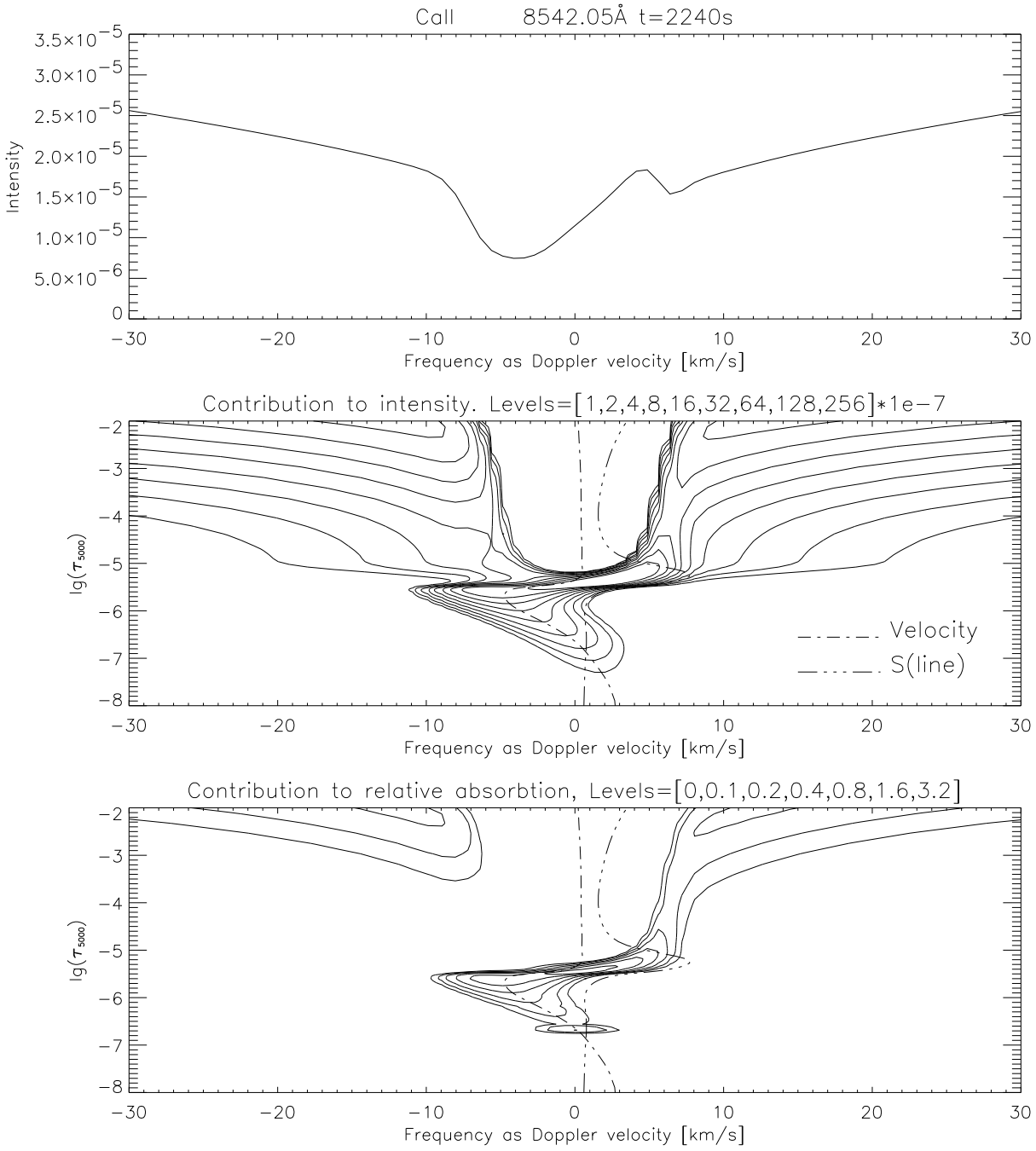

Figure 59: *Upper panel.* Line core region intensity. The frequency difference relative to line center is shown as the corresponding Doppler-velocity. Blueshift corresponds to positive velocity values. *Middle panel.* The contribution function to intensity is shown in the depth-frequency plane as a contour plot. *Bottom panel.* The contribution function to relative absorption or response function to Doppler shift is shown as a contour plot. A slice parallel to the depth-axis through the contour plots at the line core position gives the contribution function to intensity and relative absorption at this frequency. The formation depths to intensity and velocity response depths at the line core are then found. The atmospheric velocity field, and the run of the line source function are also shown.

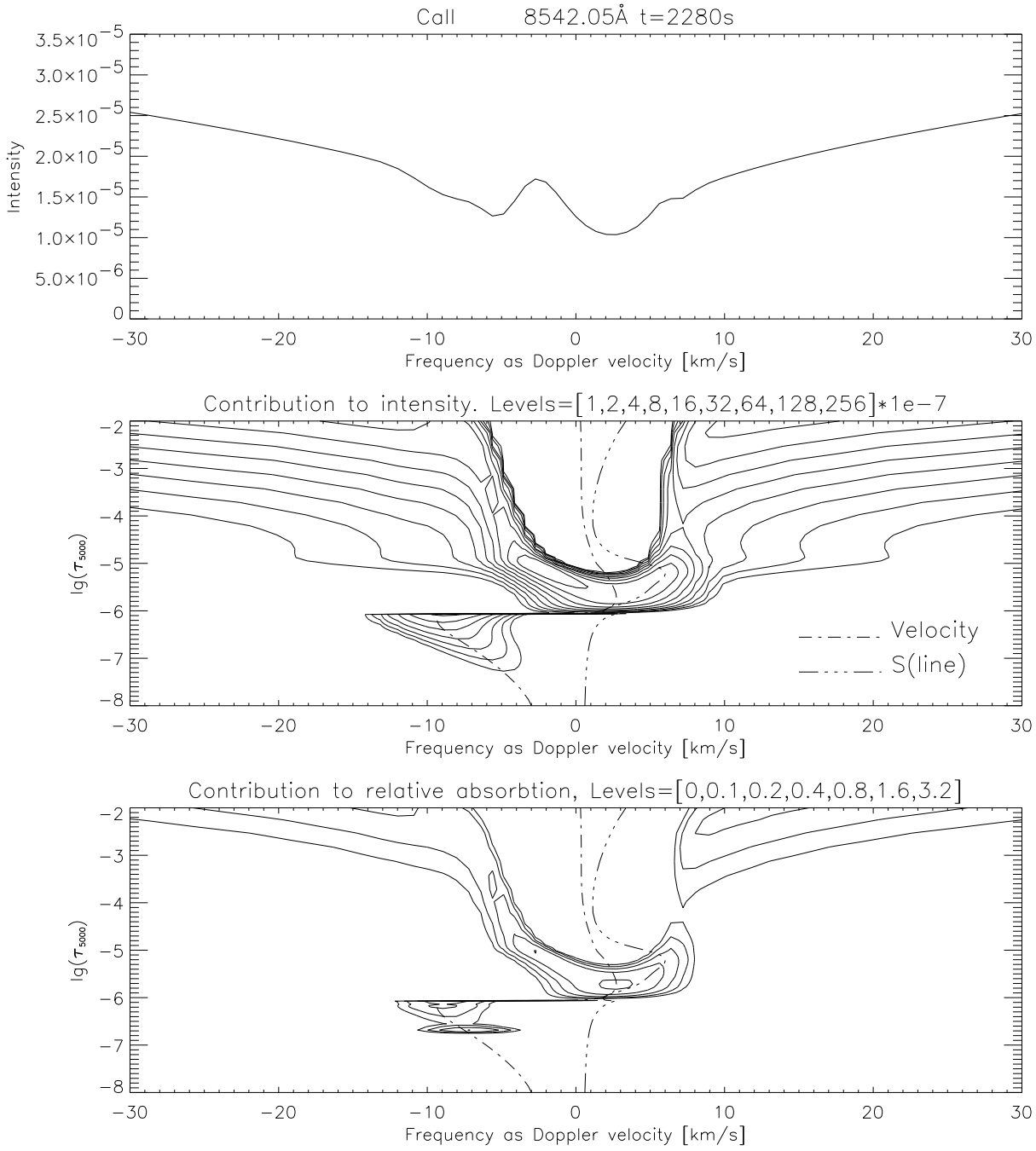

Figure 60: *Upper panel.* Line core region intensity. The frequency difference relative to line center is shown as the corresponding Doppler-velocity. Blueshift corresponds to positive velocity values. *Middle panel.* The contribution function to intensity is shown in the depth-frequency plane as a contour plot. *Bottom panel.* The contribution function to relative absorption or response function to Doppler shift is shown as a contour plot. A slice parallel to the depth-axis through the contour plots at the line core position gives the contribution function to intensity and relative absorption at this frequency. The formation depths to intensity and velocity response depths at the line core are then found. The atmospheric velocity field, and the run of the line source function are also shown.

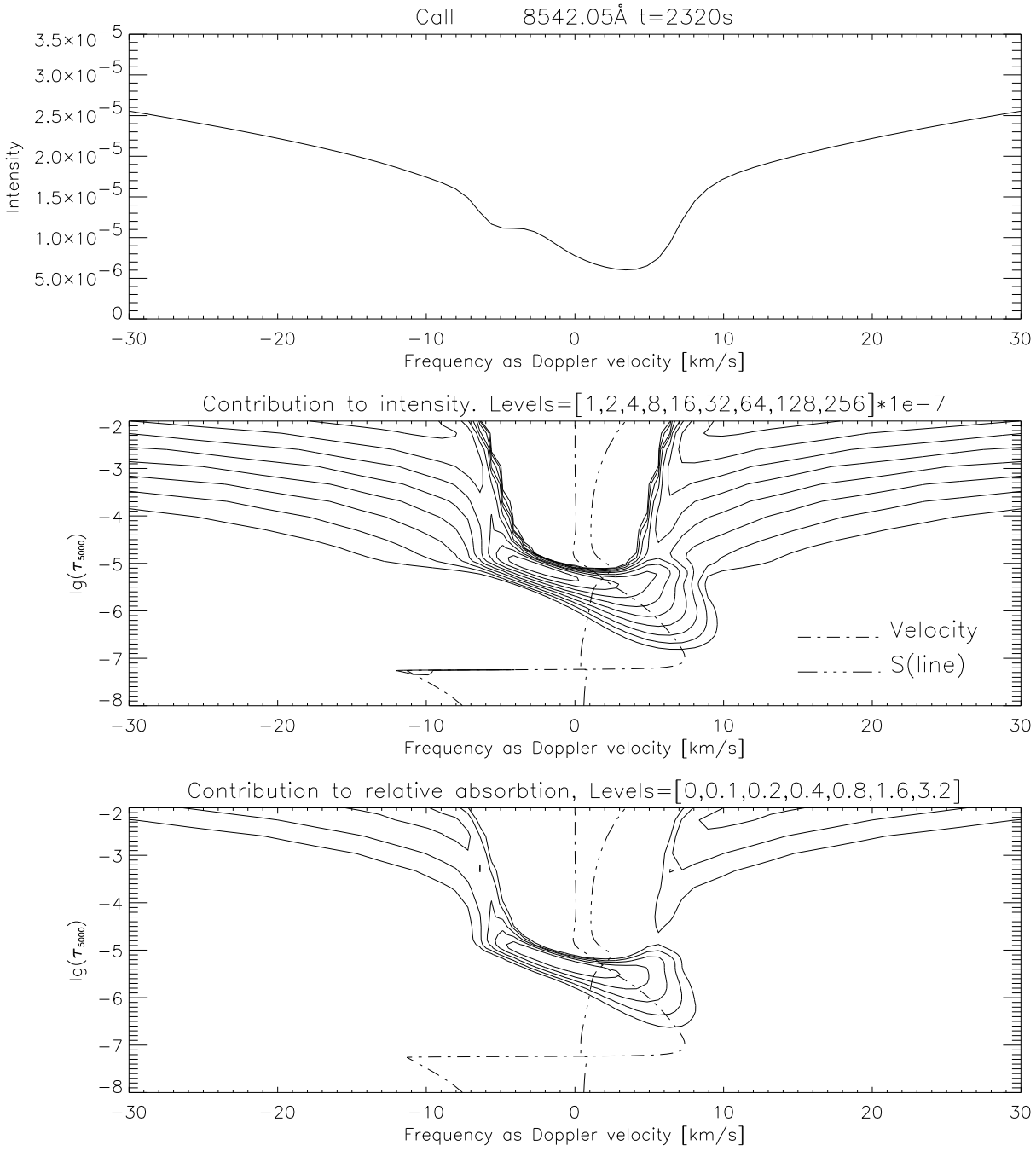

Figure 61: *Upper panel.* Line core region intensity. The frequency difference relative to line center is shown as the corresponding Doppler-velocity. Blueshift corresponds to positive velocity values. *Middle panel.* The contribution function to intensity is shown in the depth-frequency plane as a contour plot. *Bottom panel.* The contribution function to relative absorption or response function to Doppler shift is shown as a contour plot. A slice parallel to the depth-axis through the contour plots at the line core position gives the contribution function to intensity and relative absorption at this frequency. The formation depths to intensity and velocity response depths at the line core are then found. The atmospheric velocity field, and the run of the line source function are also shown.

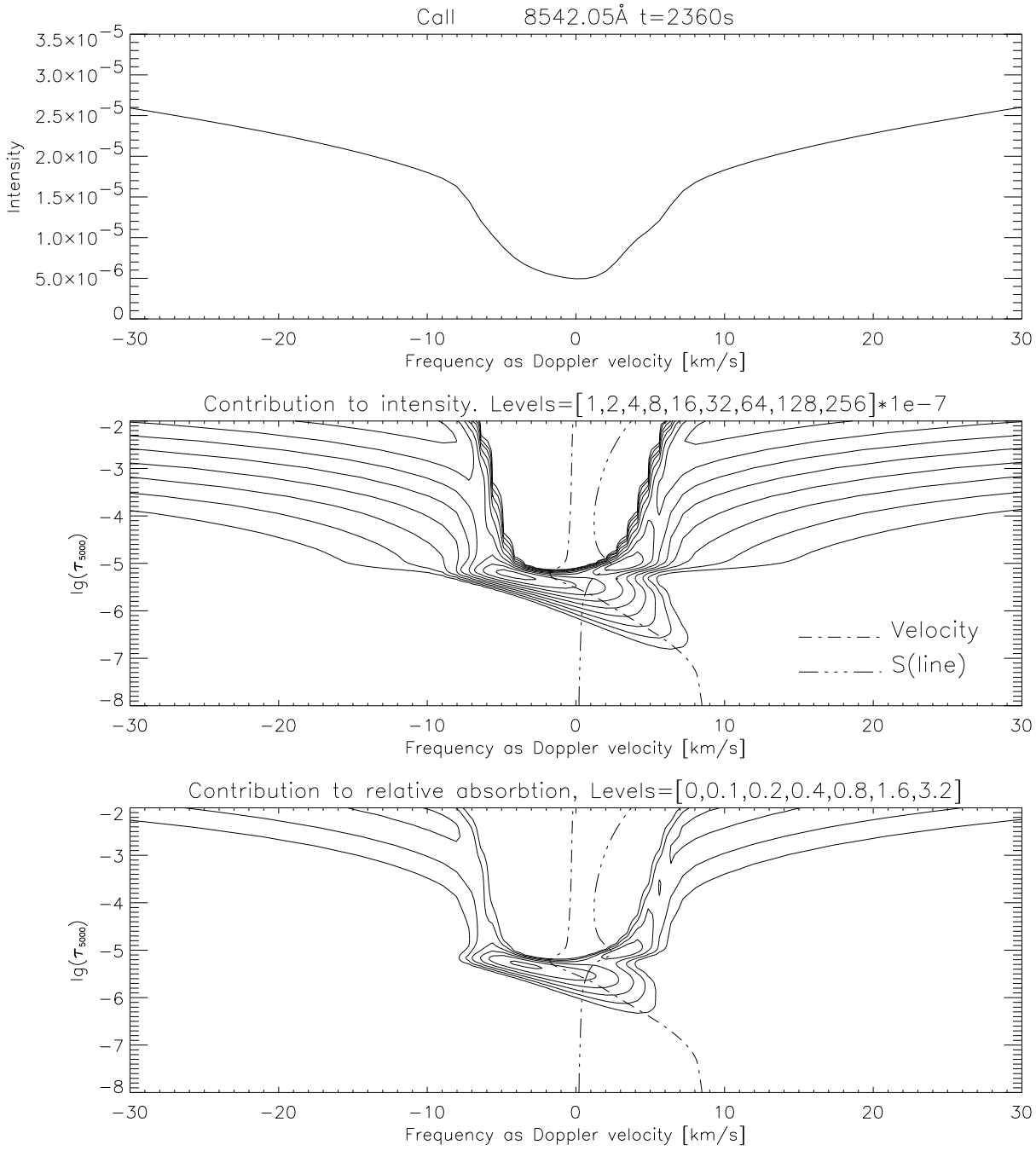

Figure 62: *Upper panel.* Line core region intensity. The frequency difference relative to line center is shown as the corresponding Doppler-velocity. Blueshift corresponds to positive velocity values. *Middle panel.* The contribution function to intensity is shown in the depth-frequency plane as a contour plot. *Bottom panel.* The contribution function to relative absorption or response function to Doppler shift is shown as a contour plot. A slice parallel to the depth-axis through the contour plots at the line core position gives the contribution function to intensity and relative absorption at this frequency. The formation depths to intensity and velocity response depths at the line core are then found. The atmospheric velocity field, and the run of the line source function are also shown.

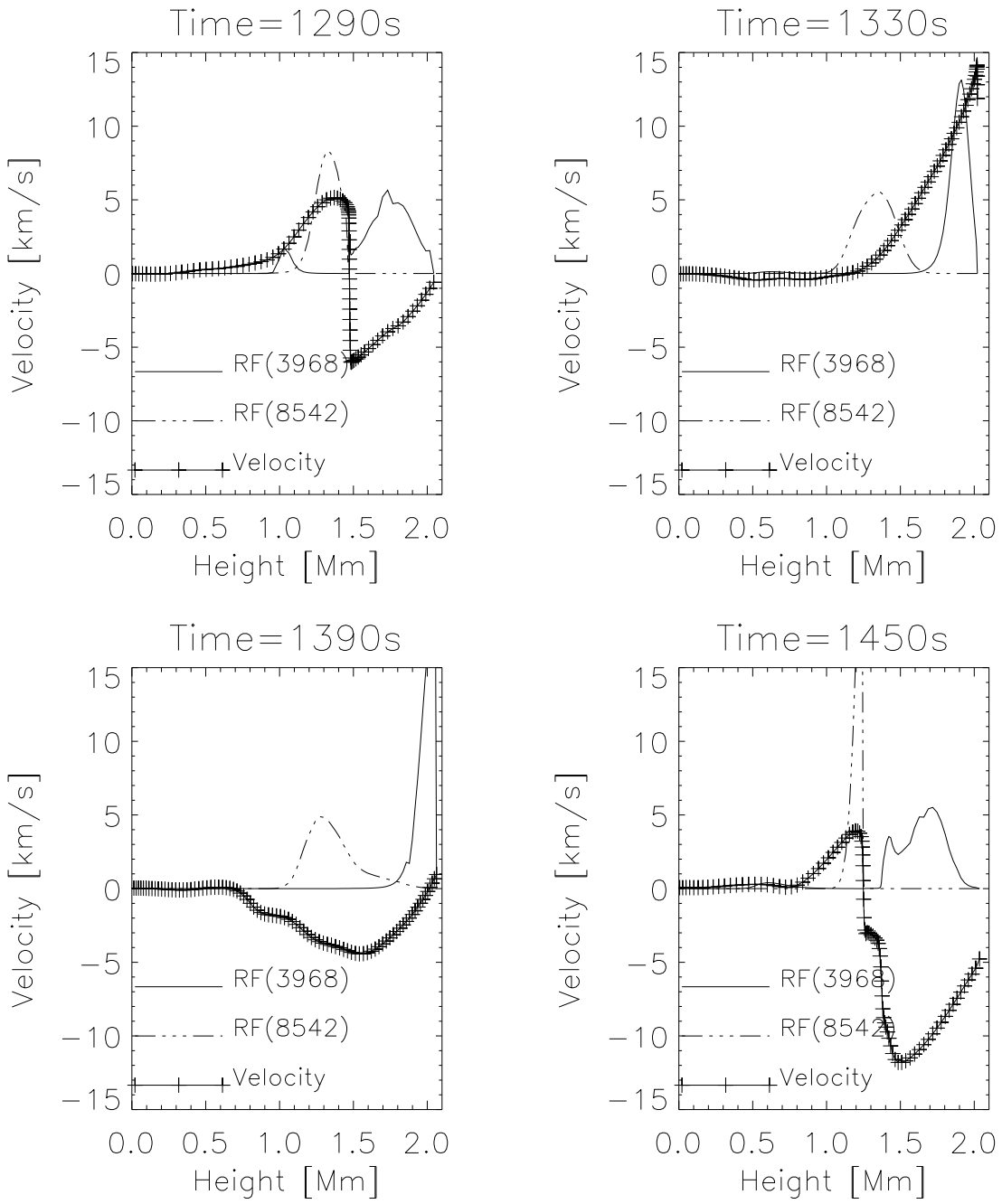

Figure 63: *3968-8542 V-V phase differences.* The response functions to line core Doppler shift (RF) on a height scale are plotted together with the velocity field. The connection between Doppler shift and velocity can then be found. The RF's are equally scaled with an arbitrary constant. *Upper left panel.* The 8542 line is blueshifted, and the 3968 line is maximum redshifted. *Upper right panel.* The 8542 line has a decreased blueshift, and the 3968 line is maximum blueshifted. *Lower left panel.* The 8542 line is maximum redshifted, and the 3968 line has approximately zero Doppler-shift. *Lower right panel.* The 8542 line has a blueshift, and the 3968 line is redshifted again.

7.4 The semiempirical model

In this section we present the semiempirical model of the pre-heated dynamic atmosphere, hereafter model2. The purpose of this model is to compare the semiempirical CaII line profiles with the corresponding time averaged line profiles.

7.4.1 Deviations from the reference radiation temperatures

The reference continuum spectrum is obtained by a time average from 500 seconds to 2470 seconds, which corresponds to 11 periods of 3 minute pulsation period. Relatively small temperature corrections of the order of +/- 20K are obtained after 6 iterations. The average deviation between the semiempirical radiation temperature and the radiation temperature of the time averaged intensity is +/-20 K (figure 66).

The radiation temperature deviations above 2500Å are on the average approximately +/- 5K which corresponds to +/-0.1%. The deviations on wavelengths between 504Å and 2500Å are on the average approximately +/- 50K which corresponds to +/- 1% (figures 64 and 65).

The CaII H and K continuum at 3900Å has a deviation of approximately -1K which is negligible. The continuum of the three infrared CaII lines at 8500Å has a deviation of -3.5K. A negative deviation corresponds to smaller intensity than the time averaged intensity. The deviation increases with increasing formation height, reaching approximately +20K at the temperature minimum region corresponding to approximately 1700Å in figure 65. The radiation temperatures in the inner wings of the semiempirical H,K and IR lines should therefore not have errors more than +20K.

The goal of reproducing the radiation temperature of the time averaged continuum spectrum is thus accomplished.

7.4.2 Accuracy of the temperature structure

We determine the accuracy of the temperature structure by using the radiation temperature response functions to temperature change. This is described in section 4. The radiation temperature response functions are calculated as for model1, and they are shown from 300Å to 3000Å in figure 67. The HeI continuum response functions are not considered in the accuracy calculations because they are also neglected in the semiempirical modelling.

The normalized deviation limits as a function of depth are shown in figure 68. The semiempirical temperature structure with the deviation limits for the average radiation temperature deviation of 20K is shown in figure 69. The radiation temperature sensitivity to temperature chance is relatively small around $lg(column\ mass) = -4.75$ and above $lg(column\ mass) = -6$. The temperature structure in these intervals can therefore not be determined with high accuracy due to the low valued response functions. The use of a polynomial during the iterations provides a smooth and monotone chromospheric temperature structure between the deviation limits.

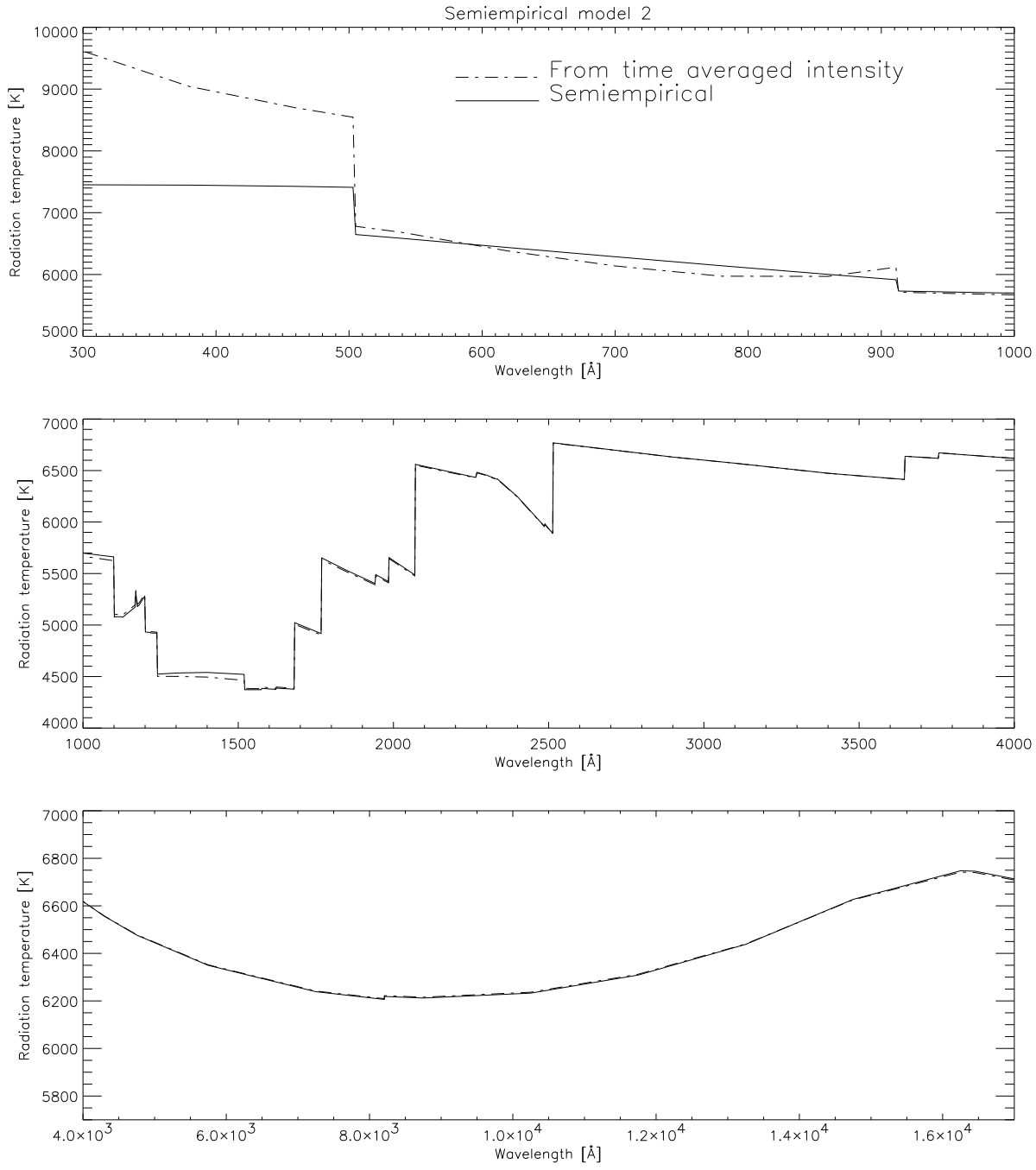

Figure 64: Semiempirical radiation temperature of model2 compared to the radiation temperature of the time averaged dynamic continuum spectrum. Wavelengths shorter than 504Å in the HeI continuum were not considered in the calculations of the temperature corrections, and the deviation here is thus relatively great.

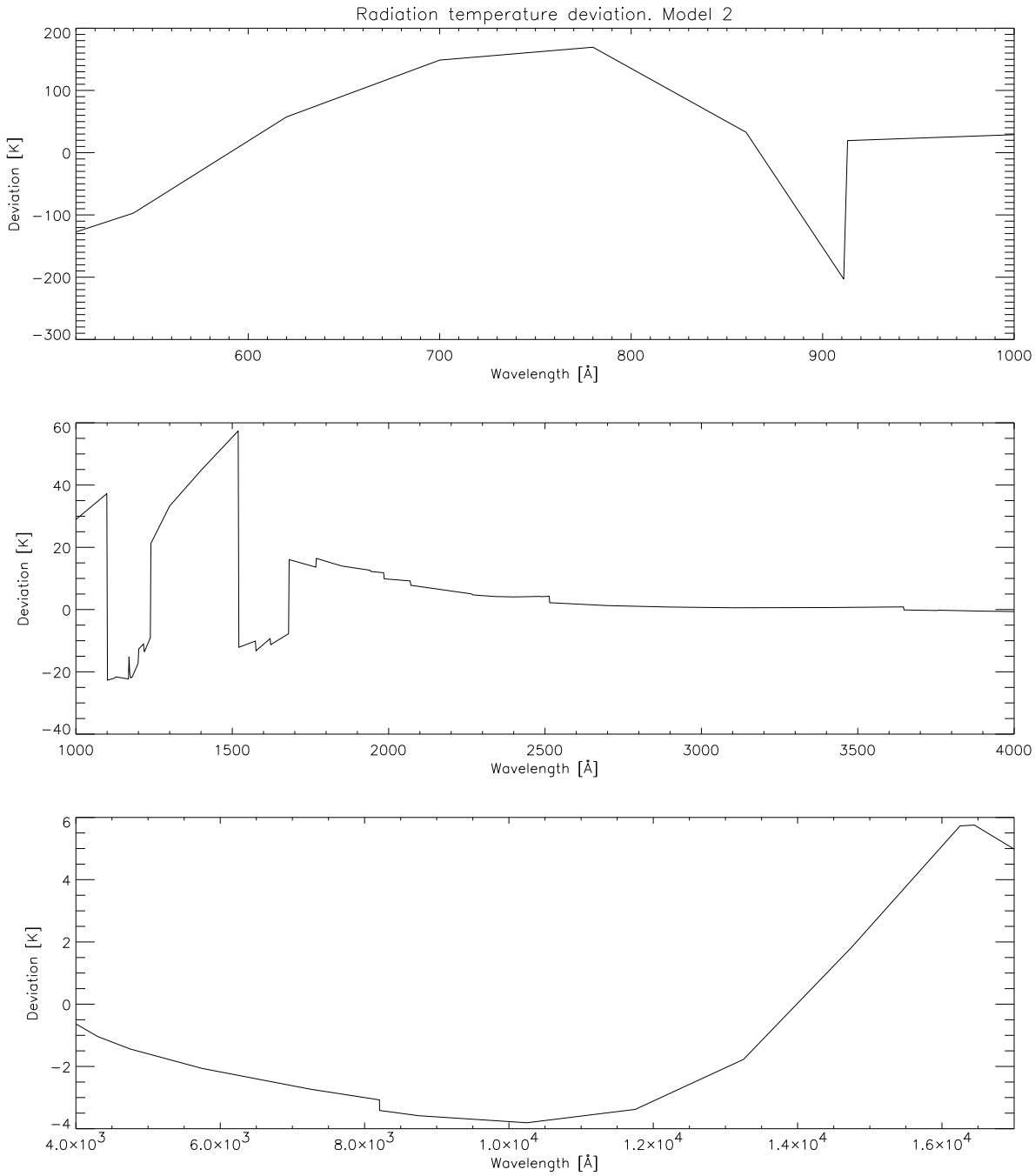

Figure 65: The radiation temperature deviations above 2500Å are on the average approximately +/- 5K which corresponds to +/-0.1%. The deviations for wavelengths between 504Å and 2500Å are on the average approximately +/- 50K which correspond to +/- 1%. Positive deviation values corresponds to higher semiempirical intensities than time averaged intensities.

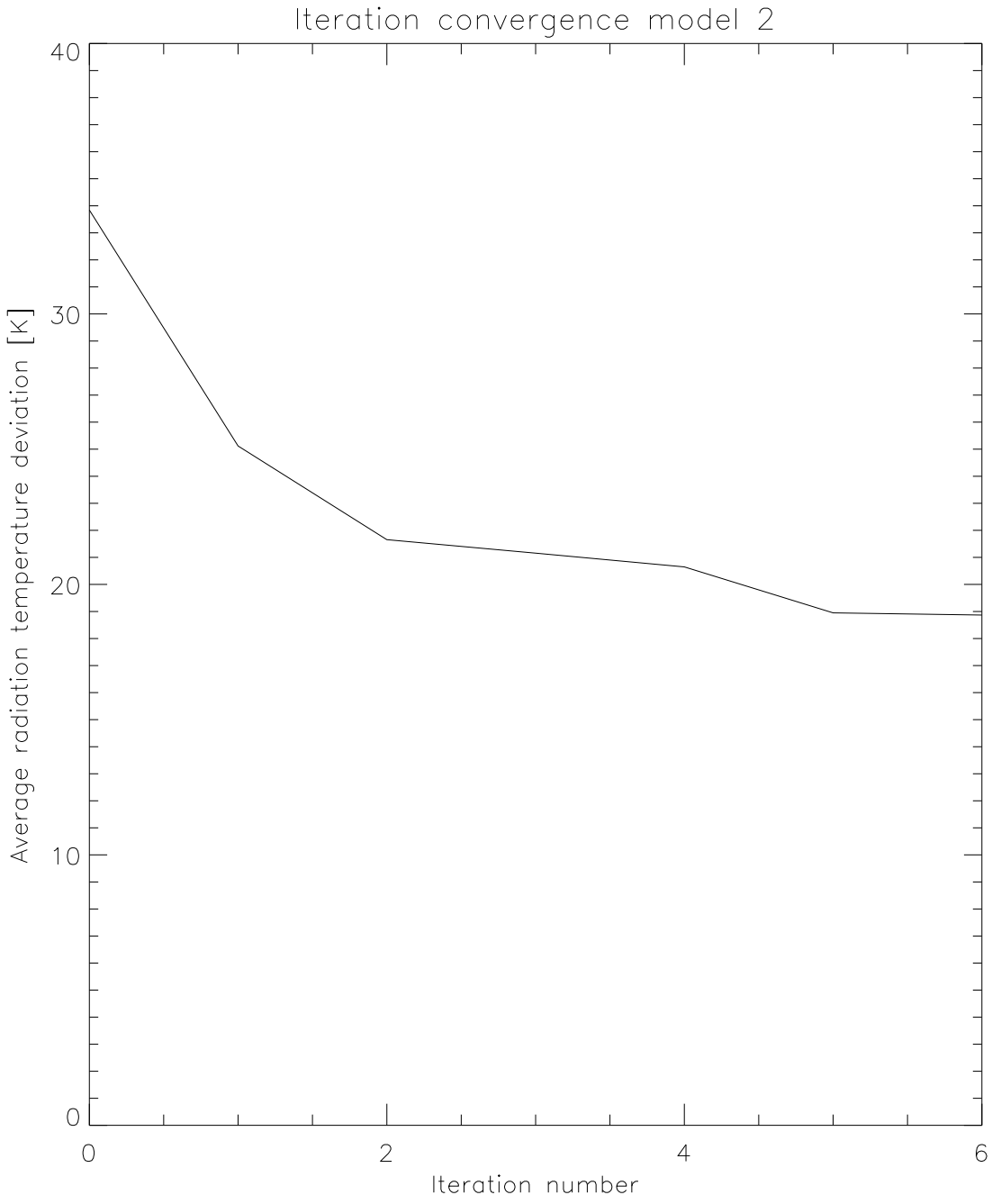

Figure 66: The average radiation temperature deviation seems to converge at approximately 20K. Termination was done after 6 iterations.

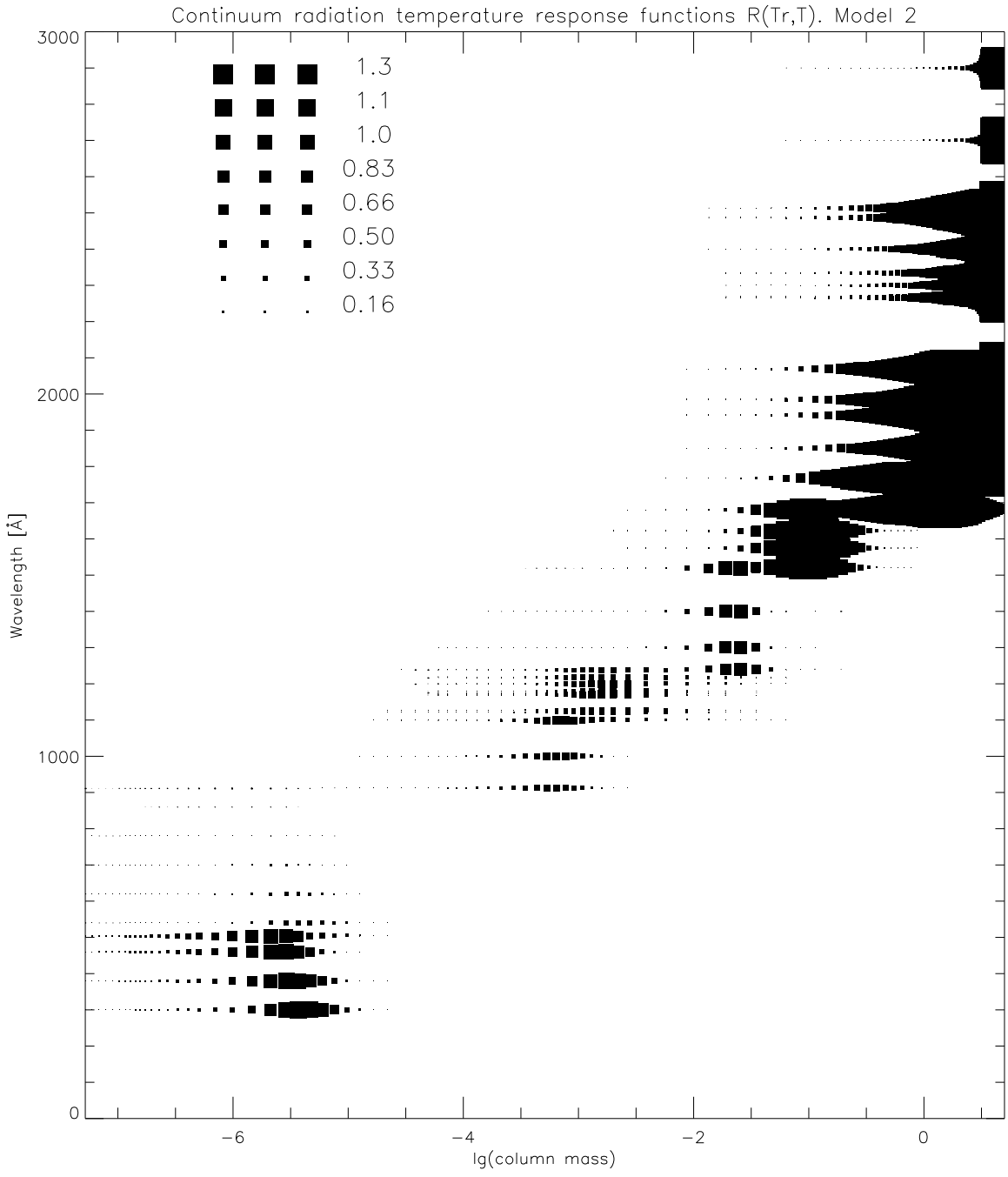

Figure 67: The radiation temperature response functions determine the accuracy of the temperature structure. Small values at a certain depth correspond to an inaccurate determination of the temperature at this depth. Wavelengths below 504Å are not considered in the accuracy calculations because this wavelength interval is excluded from the calculation of the temperature corrections. The accuracy of the uppermost temperature structure is therefore greatly reduced. The values of the response functions are shown in the upper left corner.

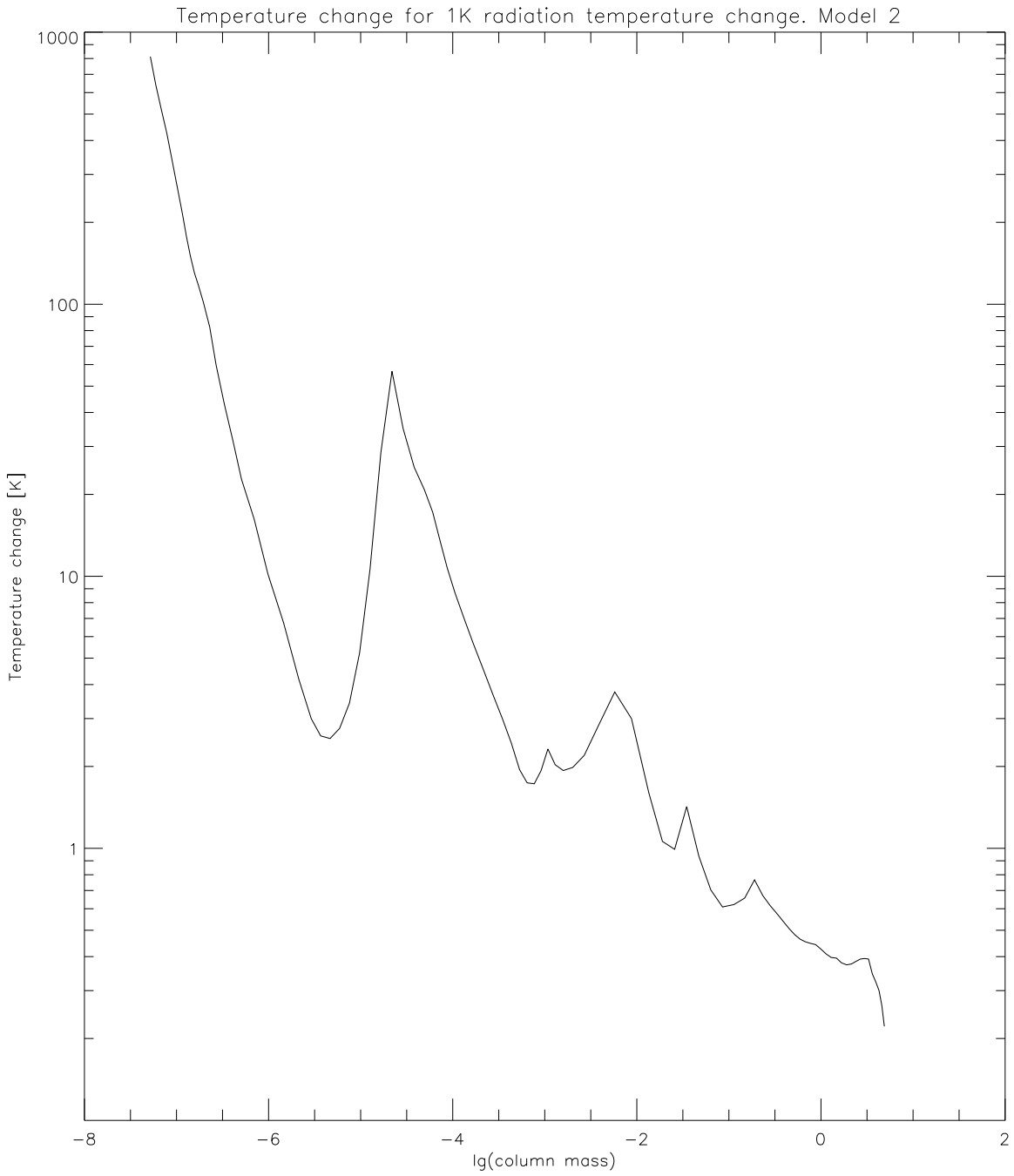

Figure 68: The reciprocal of the maximum valued response functions. This quantity is the normalized deviation limit that gives the atmospheric temperature change in a depth interval of $\Delta lg(column\ mass) = 1$ if a deviation in radiation temperature of 1K over the whole spectrum is to be minimized by the least squares method.

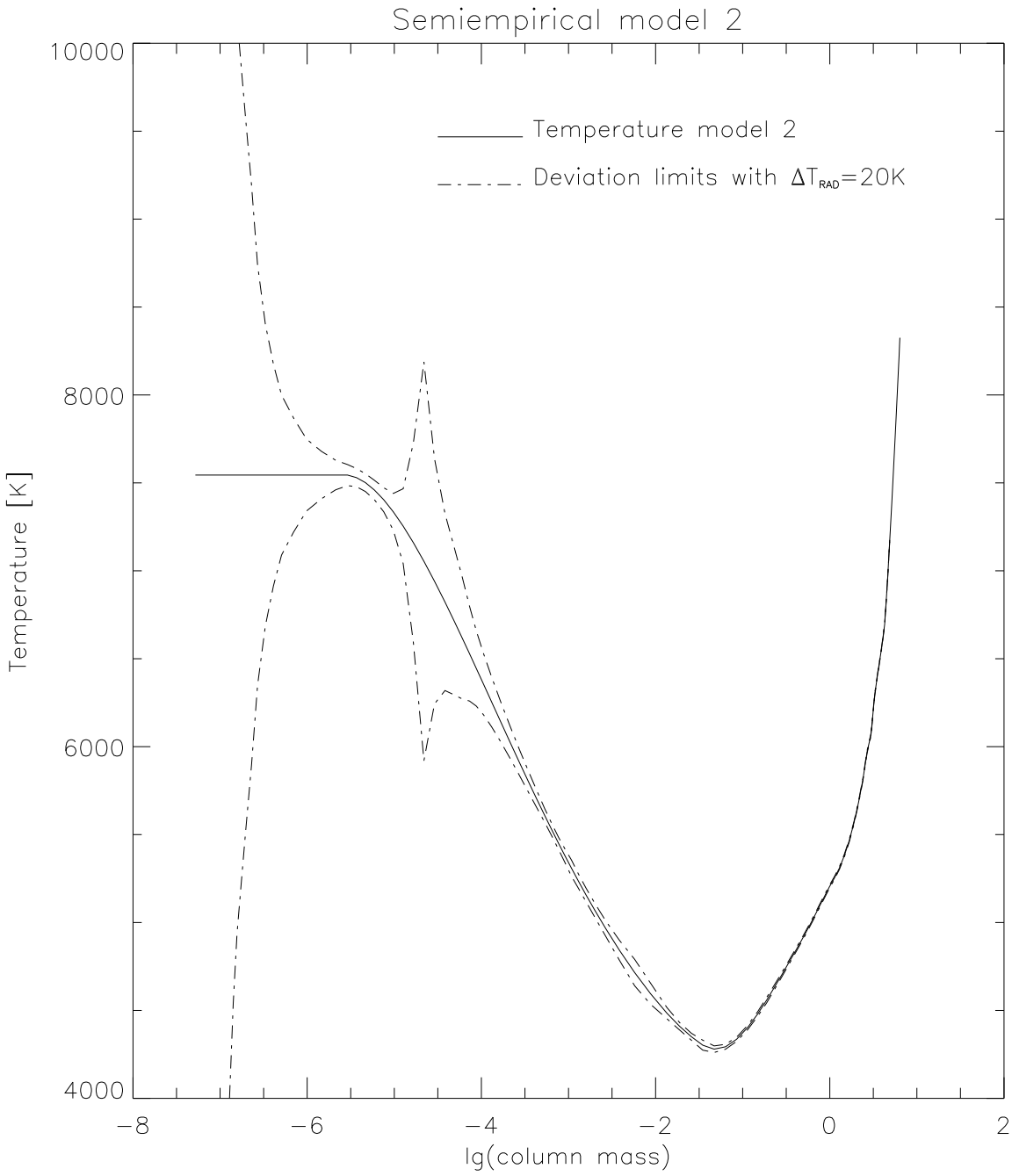

Figure 69: The semiempirical temperature structure (solid) with the deviation limits for a typical radiation temperature deviation of 20K (dotted). The radiation temperature sensitivity to temperature change is relatively small around $lg(column\ mass) = -4.75$ and above $lg(column\ mass) = -6$. The temperature structure in these intervals can therefore not be determined with high accuracy due to the low valued response functions. The use of a polynomial during the iterations provides a smooth and monotone chromospheric temperature structure between the deviation limits.

7.4.3 Comparisons with other semiempirical models

Model2 has a chromospheric temperature rise as for model1. The chromospheric temperatures of model2 are higher than the corresponding temperatures of model1 due to the extra heating term in the energy equation of the dynamic model. The uppermost part of the chromosphere has a lower temperature in model2 compared to model1 (figure 12 and 70).

The temperature structure in the middle and lower chromosphere and temperature minimum region is very similar to the FALa (Fontenla et al. 1993) solar model for internetwork regions. The similarities between Model2 and FALa in the chromosphere indicates that an additional heating term is needed in order to obtain a semiempirical chromospheric temperature rise that is close to solar internetwork models.

The VAL3C (Vernazza et al. 1981) solar model has higher temperatures in the lower chromosphere than model2 and FALa. Even more energy input is thus needed in the lower chromosphere to obtain similarities to the VAL3C model. It must be noted that VAL3C is constructed to reproduce the spatially and temporally averaged continuum intensities over internetwork *and* network regions. Similarities with VAL3C is therefore not expected since our dynamic model has not been made to account for internetwork magnetic fields.

Model2 has higher temperatures in the upper photosphere compared to VAL3C and FALa. There is no transition region since the dynamic model does not include the corona.

A comparison of the radiation temperatures between model2, VAL3C and FALa is given in figure 71. The radiation temperature in the ultraviolet range from 300Å to 1500Å originate from the chromosphere for all three models. Model2 and FALa have similar radiation temperatures in the range from 900Å to 1500Å due to similar chromospheric temperatures. The helium continuum below 504Å is not considered in the semiempirical modelling due to the neglect of helium ionization in the energy equation in the dynamic model. The disparities between model2 and the solar models on the short wavelength side of 504Å is explained by the exclusion of the HeI continuum in the semiempirical modelling, and the lack of a transition region in the dynamic model.

The photospheric radiation for all three models is located in the range from 1500Å to 17000Å. The radiation temperature of model2 in this wavelength range deviates more from the two other models with increased formation height. This is a consequence of the increased deviation in photospheric temperatures between model2 and the two other models with increasing height up to $lg(column\ mass) = 0$ at temperatures of approximately 5000K.

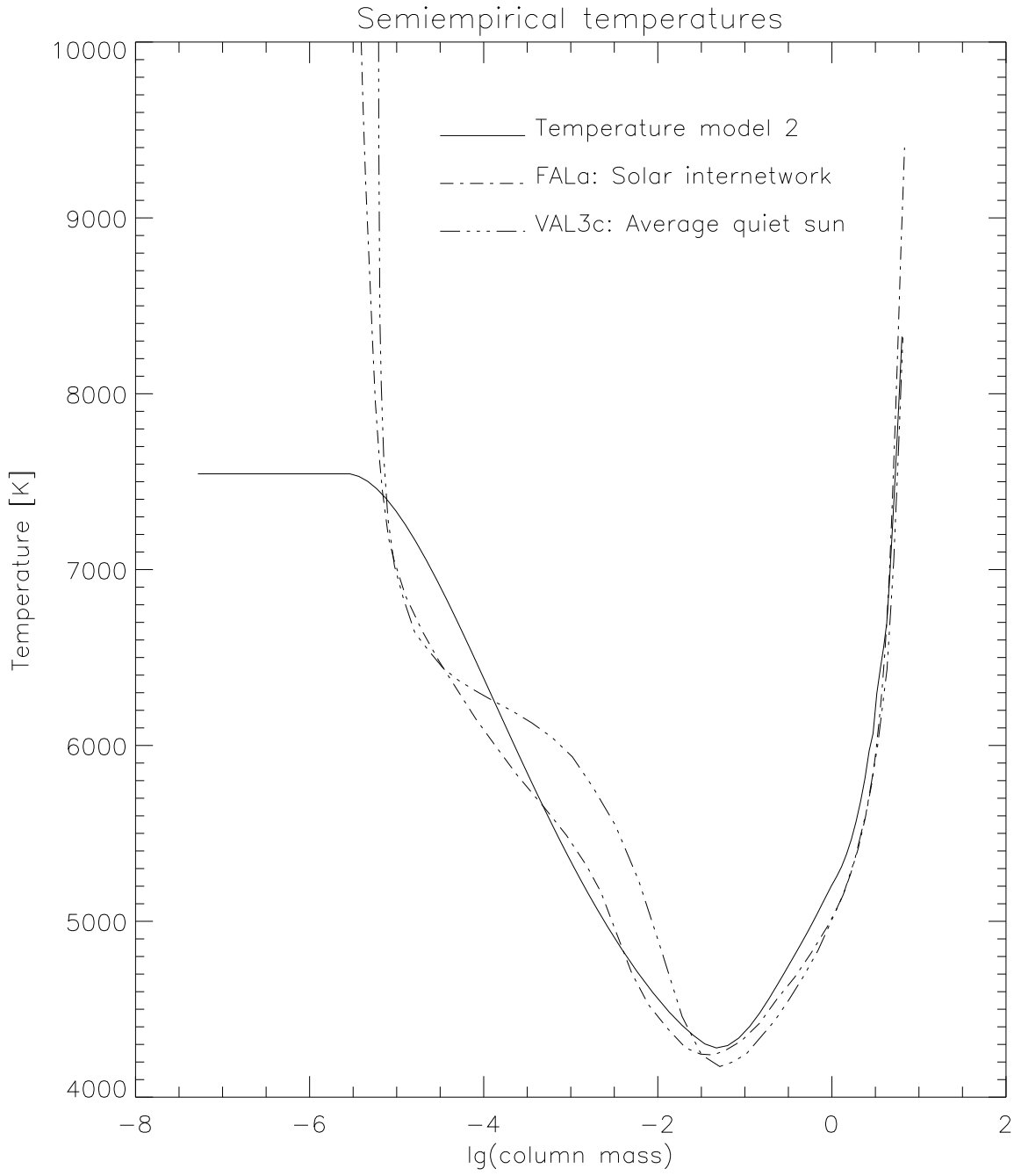

Figure 70: A comparison of semiempirical models. The temperature structure in the chromosphere up to $lg(column\ mass) = -4$ and in the temperature minimum region of model2 is very similar to the FALa solar model for internetwork regions. The VAL3C model has a steeper temperature gradient in the low chromosphere than model2 and FALa.

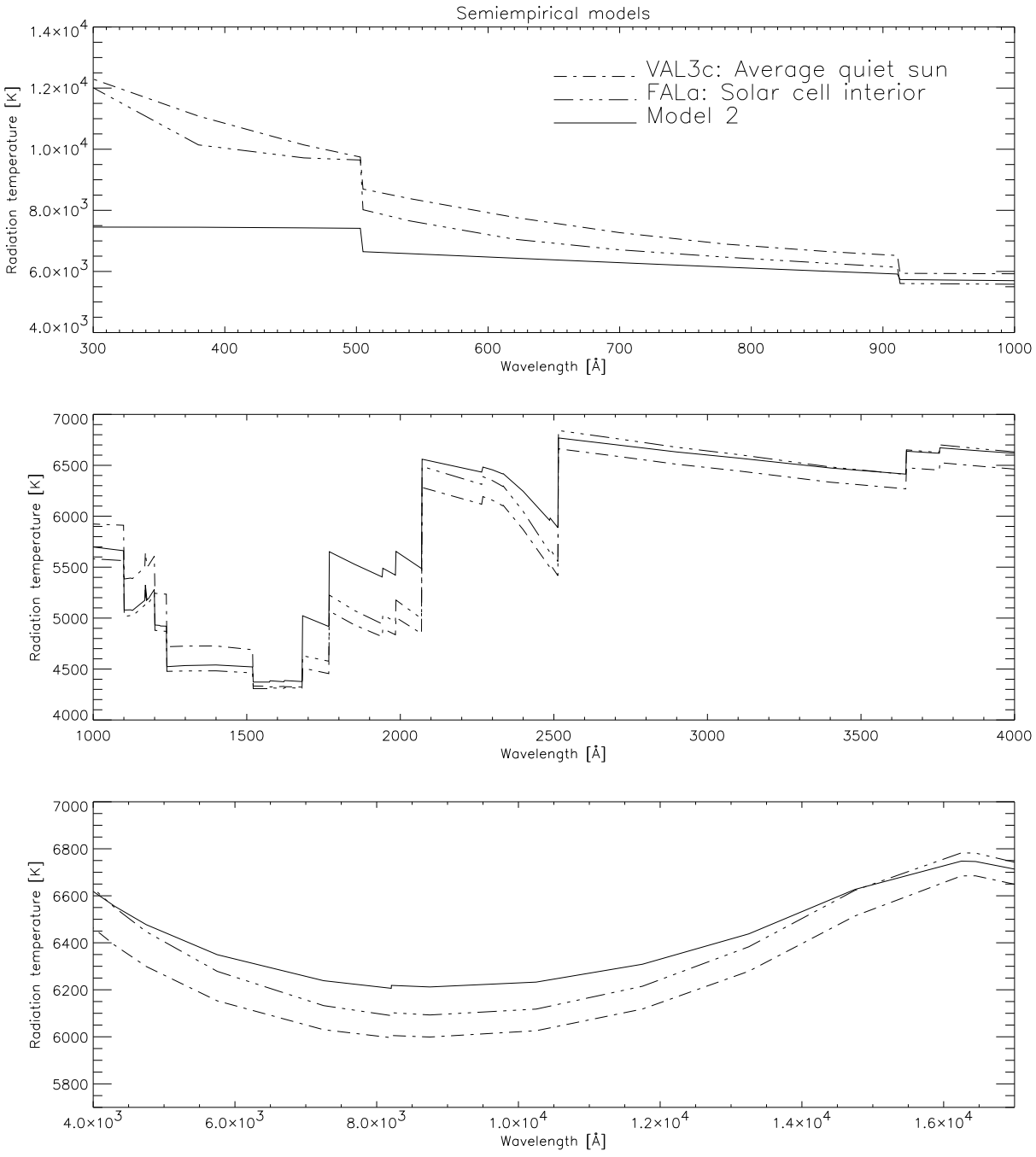

Figure 71: A comparison between different semiempirical radiation temperatures. Model2 and FALa internetwork model (solar cell interior) has the best agreement. The separation between chromospheric and photospheric radiation is located at approximately 1500Å near the SiI bound-free absorption edge for all three models.

7.5 Semiempirical compared to time averaged spectral lines of CaII

In this section we investigate the differences between time averaged line profiles and semiempirical line profiles for the 5 level CaII atom. We denote the line profiles computed from the dynamic time dependent model occasionally as dynamic profiles, and the line profiles computed from the semiempirical model as static profiles. We use the semiempirical model of the pre-heated atmosphere described in 7.4 to calculate the static profiles. The dynamic profiles from the corresponding dynamic atmosphere are time averaged. We compare averaged and static profiles with different microturbulent velocities.

The CaII model is identical in the dynamic and semiempirical model. The comparisons can thus be carried out without taking into consideration uncertainties in atomic parameters and partial redistribution effects, which is the case for comparisons between synthetic and observed profiles. It must also be noted that both models are plane parallel such that three dimensional effects can not be considered.

7.5.1 Microturbulence, mesoturbulence and macroturbulence

Velocity field effects on spectral lines have previously been included in static models by two methods. Both methods assume that no other quantities than the velocity are affected. These methods are therefore not physically consistent, in only taking into account mass motions without altering the thermodynamic variables.

1. *The classical approach.*

   Large scale velocity field effects are included by convolving the synthetic profile by a Gaussian that is parametrized by the macroturbulent parameter. This accounts for random velocity fields on scales larger than a typical contribution function width. Random velocity fields on scales much smaller than a contribution function width is accounted for by including the microturbulent parameter. This is a broadening parameter that determines the width of the opacity profile in the same manner as the most probable thermal velocity. These parameters are adjusted to give the best fit to the observed line profile.

2. *The mesoturbulent approach.*

   Carlsson & Scharmer (1985) used mesoturbulence which allows for typical scales of velocity change in the intermediate range between micro- and macroturbulence. They calculated random velocity fields with different correlation lengths. The emergent intensity from the K-line for 100 realizations was averaged for each correlation length. The microturbulent limit was not reached even if the correlation length was 25 km. The macroturbulent limit was not reached until the correlation length was greater than 3000km. They found that the K-profile in the mesoturbulent regime could not be reproduced by any combination of micro- and macroturbulence. The mesoscale velocities gave a K-line profile with a higher line core intensity, a K2V-K2R separation less than for the microturbulent limit, and K2V and K2R intensities less than for the

microturbulent limit. The peak intensities and separation decreased with increasing correlation length. Their random velocity fields gave naturally symmetrically averaged profiles.

The actual velocities in the RADYN simulations can be considered as mesoturbulence and macroturbulence, but here fully consistent with thermodynamic changes. These changes give an additional effect on the line profiles compared to using the classical and mesoturbulent approaches. Mesoturbulence and macroturbulence is not included in the static calculations, but the typical effects (Carlsson & Scharmer 1985) if it were included, are considered in the comparisons between static and time averaged line profiles.

7.5.2 Method

The RADYN code used in the dynamic simulations can not resolve small scale velocity fields such as microturbulence. Microturbulence is included in the dynamic and static calculations to mimic the effects of such small scale velocity fields. An additional reason is that the observed and averaged H2V peak displacement of approximately 0.1 Å relative to the line core (Cram & Damé 1983) fits better to our corresponding average emission peak if microturbulence is included.

The microturbulence in the dynamic calculation is altered by changing the microturbulence in the atmospheres given by the RADYN calculations. These atmospheres are then run by MULTI to obtain the dynamic profiles.

Three time sequences are calculated, one with zero microturbulence, one with a depth independent microturbulence of 2km/s, and one with a depth independent microturbulence of 4km/s. The dynamic line profiles are then averaged over the same time interval as for the semiempirical reference spectrum.

The same three microturbulent velocities are included in the MULTI computations of the semiempirical line profiles.

7.5.3 Comparisons between semiempirical and time averaged line profiles with different microturbulence

First we compare the time averaged dynamic profiles with the three different microturbulent velocities (figures 72 and 73).

1. *The 3968 line core region.* Increasing microturbulence causes the effects given here. The H2V-H2R separation increases, and both emission peaks are located further from the rest center frequency. The line core region is getting wider. The H2V and H2R intensities decreases. The H3 intensity and the H1 intensities decreases somewhat.

   The line profiles are asymmetric in the line core region with a higher H2V intensity than H2R intensity, which is also evident in internetwork observations. H3 is redshifted relative to the rest center frequency.

2. *The 8542 line core region.* The intensity in the line core decreases, and the line core region is getting wider with increasing microturbulence.

The line profiles are asymmetric in the line core region. The line core at minimum intensity is not significantly displaced relative to the rest center frequency.

The asymmetry in both lines is a direct evidence for systematic or non-stochastic atmospheric behavior in which the time dependent thermodynamics is correlated with gas motions. This can not be reproduced by static models where only random velocity fields (macro-, meso- and microturbulence) are allowed to account for the dynamic effects.

In the remaining discussion, we are primarily concerned with the dependence on microturbulence in both static and dynamic profiles. We look for similar or different behavior between static and time averaged profiles as a function of microturbulence. Microturbulence is here considered as real turbulence on height scales much smaller than a contribution function width, typically 1-10km. Static and time averaged profiles with the same microturbulence are compared.

We are also concerned with whether or not it is possible to use macro- and mesoturbulence to improve the static profiles such that they match at least some features. If this is not possible, one can be tempted to adjust the atomic parameters which can lead to erroneous results. The only reliable modelling approach will then be dynamic simulations.

We choose to compare static and time averaged line profiles for the 3968 and 8542 line. The 3933 line behavior is very similar to the 3968, and the same holds for the 8662 and 8542 line. The 8498 line is left out due to the anomal emission peak at the line core in the dynamic profiles.

The 3968 line core region.

See figures 74-76 during the discussion.

1. *H2V and H2R dependence on microturbulence.* The peak separation increases and the peak intensity decreases with increasing microturbulence in the static profiles. The same holds for the dynamic profiles (cf. figure 72). The averaged H2V is approximately located at the same frequency as the static H2V. The position of H2V is thus an indicator of the value of the microturbulence in both models, provided that it is height independent.

   The time averaged H2V intensities have a smaller variation than in the static case, and the H2V intensities are approximately the same for a microturbulence of 4km/s. Static H2V intensities are greater than the time averaged H2V intensities for the two other microturbulent values.

   The H2R intensity for the averaged profile vary less than for the static profiles, and they have a much lower intensity due to the asymmetry. The intensity peaks are displaced to the red compared to the static profiles. The variation in frequency is approximately the same. The H2 correlation between dynamic and static profiles with respect to microturbulence is thus only evident for the H2V intensity.

2. *H3 intensity and line core width dependence on microturbulence.* The H3 intensity decreases and the line core width increases with increasing microturbulence in the

static profiles. The same holds for the averaged profiles, but the line core regions are wider and the H3 intensities are higher than for the static profiles. The H3 intensities are approximately equal for 4km/s microturbulence. The averaged H3 intensity vary more than for the static profiles.

3. *H1 dependence on microturbulence.* The intensities decrease slightly and the frequencies are approximately constant for the static profiles for increasing microturbulence. The same holds for the averaged H1 intensities, but they have a lower value. The H1V frequencies of the averaged profiles deviates more from the static values compared to the H1R frequencies.

4. *Macro- and mesoturbulent effects on the static profiles.* Convolution with a Gaussian on the static profiles to account for the large scale velocity fields would give a better correspondence to the averaged profiles in the H2V-H3 regions for zero and 2 km/s microturbulence. This is due to the smearing of the narrow emission peaks and narrow H3 regions. Great deviations would nevertheless occur at the H2R region due to the asymmetry of the time averaged profiles.

   If mesoturbulence is applied in the semiempirical atmosphere, the emission peak intensities, and their frequency displacement from the rest center frequency would decrease. The intensity correspondence would thus improve at H2V, but the displacement would lead to less correspondence. Higher intensity in the H3 region would occur and thus lead to an improvement. Neither approach would lead to a satisfactory correspondence at both sides of the line core due to the asymmetry.

The 8542 line core region.

See figures 77-79 during the discussion.

1. *Line core minimum intensity dependence on microturbulence.* Both static and averaged intensities decrease with increasing microturbulence. The intensity is higher and has a greater variation in the averaged profiles compared to the static profiles, as in the case for H3.

2. *Meso- and macroturbulent effects on the static profiles.* Macroturbulent smearing will tend to increase the profile width and increase the minimum intensity. A better correspondence will thus occur at the point of minimum intensity, but it will lead to less correspondence at each side of the line core where the widths already agree. Mesoturbulence will increase the intensity in the region of minimum intensity, and this will improve the static profiles relative to the averaged profiles.

The wing regions.

See figures 80 and 81 during the discussion.

The 3968 wing regions and the 8542 wing regions for the averaged profiles show increased width compared to the static profiles. Figure 80 and 81 show an increased width even in the case for zero microturbulence.

The continuum intensities in both lines are approximately equal, indicating an accurate semiempirical model in the layers of the photosphere where these continua originate. Very small deviations between the semiempirical radiation temperatures and the radiation temperatures of the time averaged dynamic intensities in the continua formed towards the temperature minimum was shown in the discussion of the semiempirical model. These deviations are smaller than the differences in radiation temperatures in the wings. Only the accumulated effect of intensity variations and Doppler shifts of the absorption profile can then explain the deviation between averaged and static line wings.

The semiempirical H-line profiles are convoluted with a Gaussian macrovelocity distribution to account for macroturbulent broadening. The most probable macrovelocity corresponds to the 1/e width of the Gaussian distribution.

A macroturbulent velocity of 110km/s is needed to obtain correspondence with the time averaged profile in the wing regions outside a frequency displacement corresponding to a Doppler velocity of +/- 300km/s. The resulting H3 intensities are approximately a factor two larger than the time averaged H3 intensity, which can not be compensated for by using microturbulence.

This unrealistically high macroturbulence indicates that macroturbulent broadening can not be used to explain the broadening excess of the time averaged profiles.

General comments on meso- and macroturbulent effects on the static profiles.

A satisfying reproduction of the 3968 line by the semiempirical model seems to be impossible due to the strong asymmetric property of the time averaged profile. This comes as no surprise since the dynamic model couples thermodynamic changes to the velocity field. The static approach is only able to handle velocity field effects without taking into consideration this coupling which is very important in this chromospheric line. A better fit for the static 8542 profiles can be achieved by using mesoturbulence. A better fit can not be achieved in the wing regions in the 3968 line using macroturbulence within realistic limits.

7.5.4 The cause of the different variation of the semiempirical and time averaged H3 and H2V intensities as a function of microturbulence

The static and time averaged line profile intensities (figure 72 and 74) have rather different responses to microturbulence. This is clearly seen for H3 and H2V.

The H2V intensity in the static profile vary more as a function of microturbulence and it has a higher value than the corresponding time averaged intensity. The H3 intensity in the static profiles vary less as a function of microturbulence and it has a lower value than the corresponding time averaged intensity. The dependence on microturbulence has to be

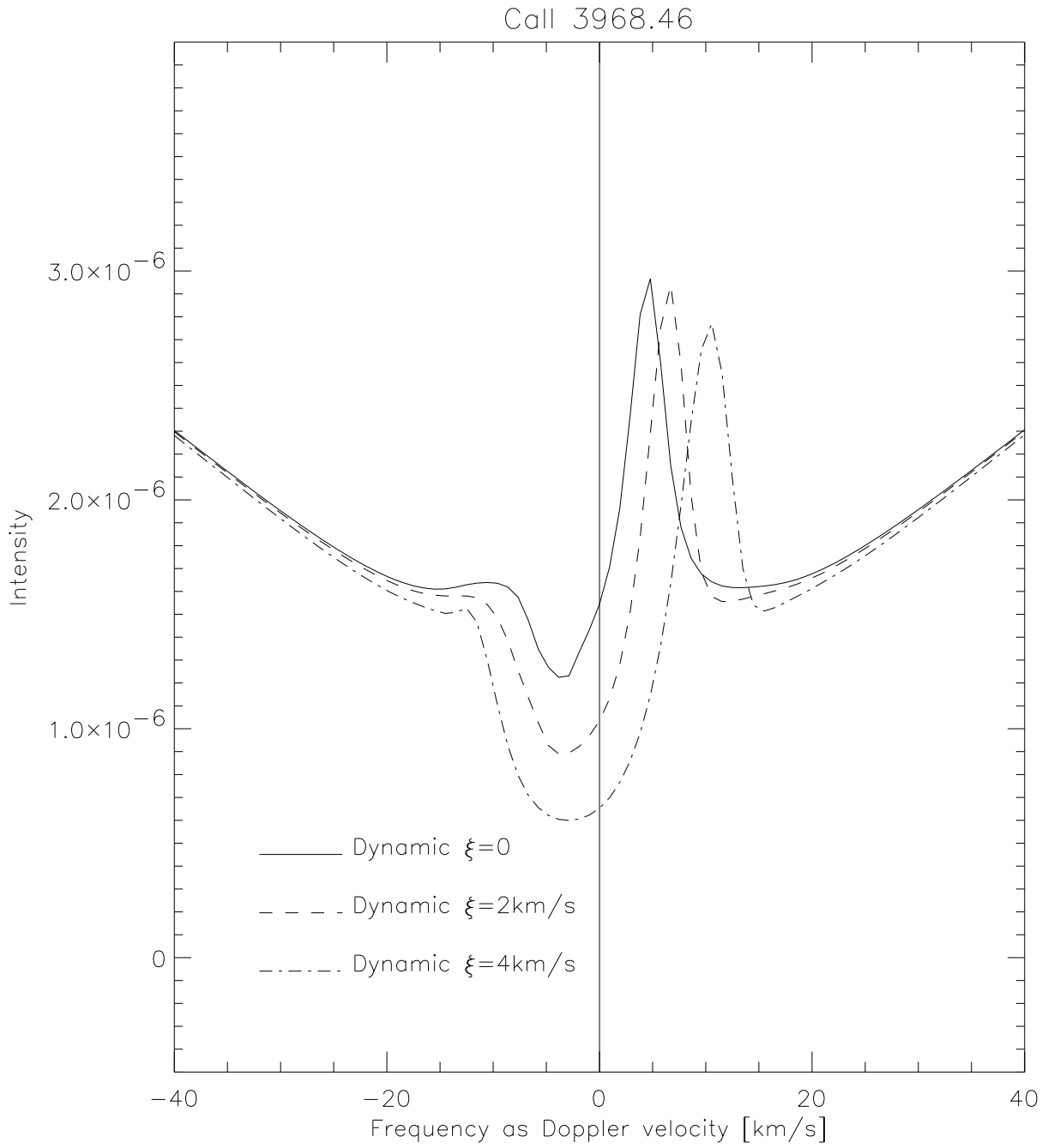

Figure 72: Time averaged dynamic 3968-lines for different depth independent microturbulence. The H2V emission moves further from the rest center frequency, the H3 region is getting wider and the H3 intensity decreases with increasing microturbulence.

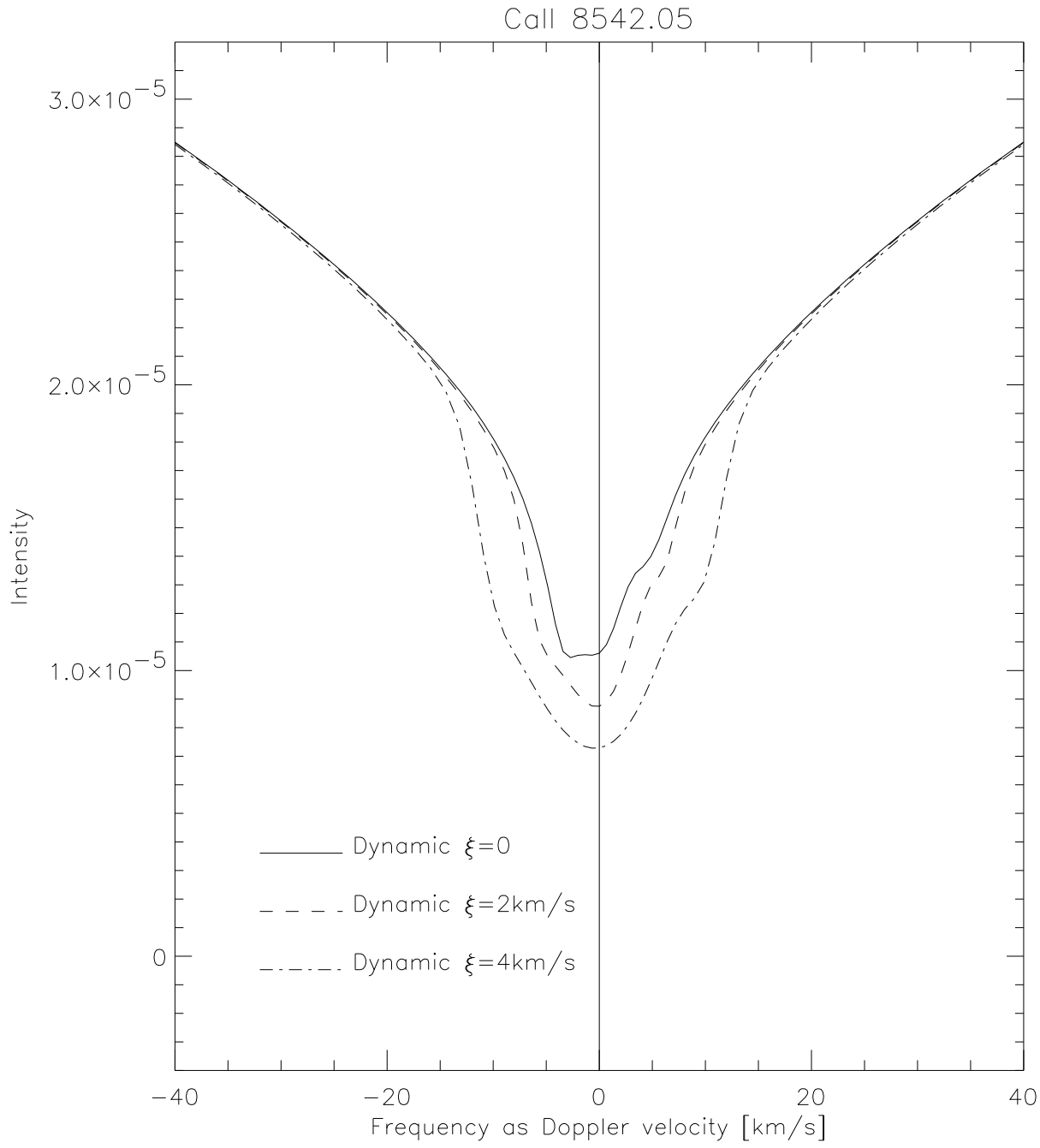

Figure 73: Time averaged dynamic 8542-lines for different depth independent microturbulence. The line core region is getting wider and the minimum intensity decreases with increasing microturbulence.

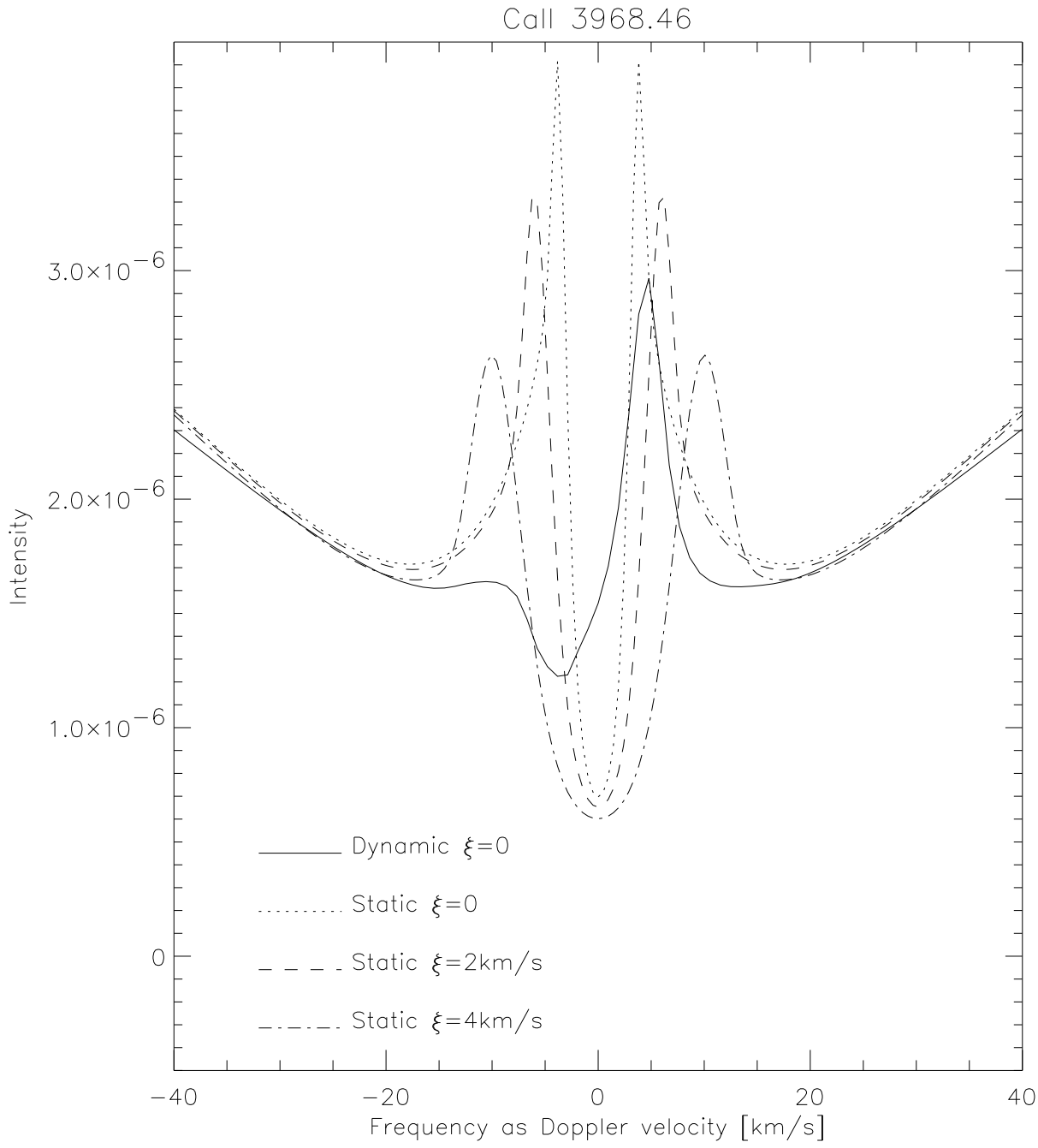

Figure 74: Time averaged dynamic 3968-line for zero microturbulence (solid) compared to the static profiles with 0km/s, 2km/s and 4km/s depth independent microturbulence. Blueshift corresponds to positive velocities.

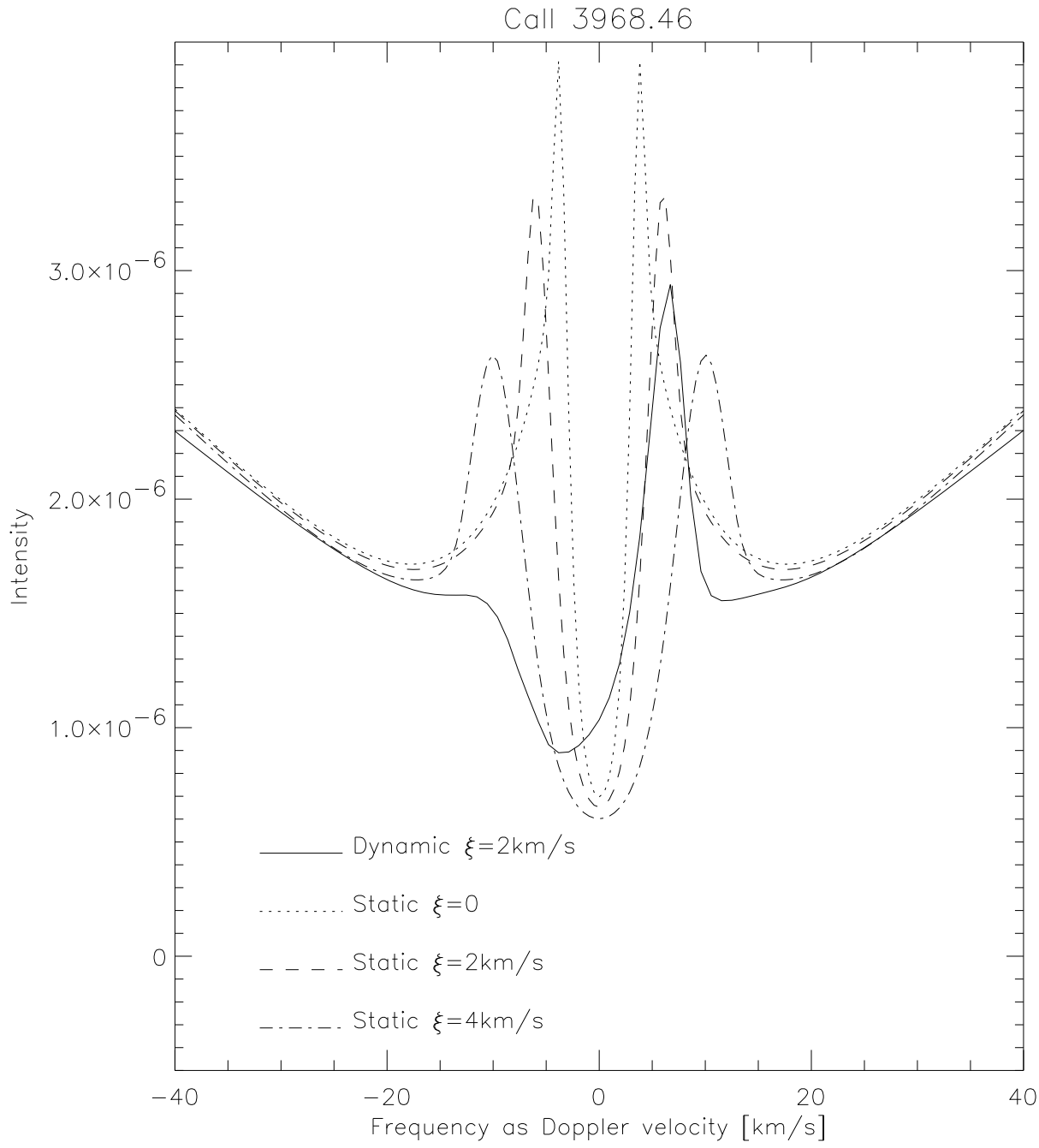

Figure 75: Time averaged dynamic 3968-line for depth independent microturbulence of 2 km/s (solid) compared to the static profiles with 0km/s, 2km/s and 4km/s depth independent microturbulence. Blueshift corresponds to positive velocities.

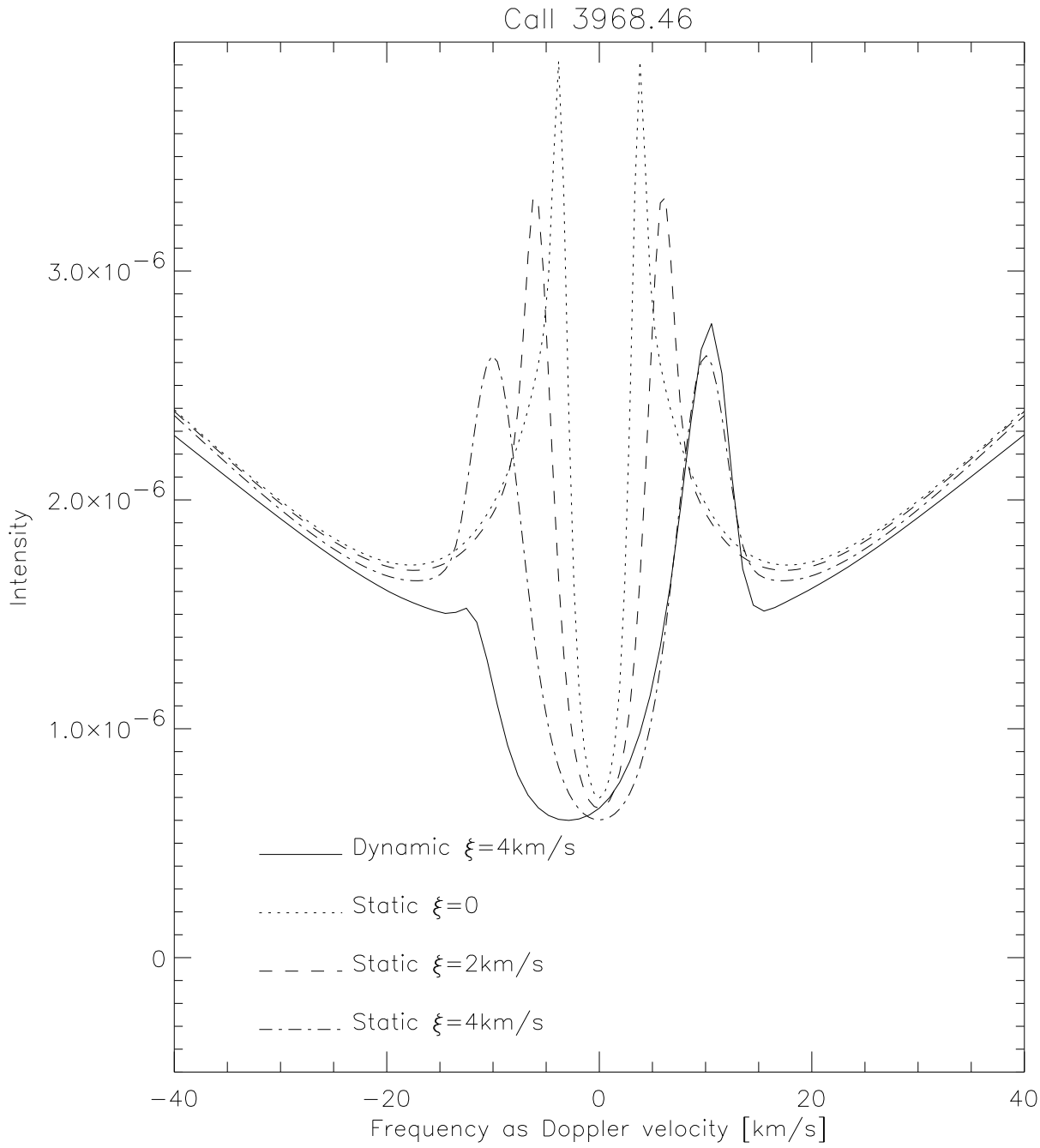

Figure 76: Time averaged dynamic 3968-line for depth independent microturbulence of 4 km/s (solid) compared to the static profiles with 0km/s, 2km/s and 4km/s depth independent microturbulence. Blueshift corresponds to positive velocities.

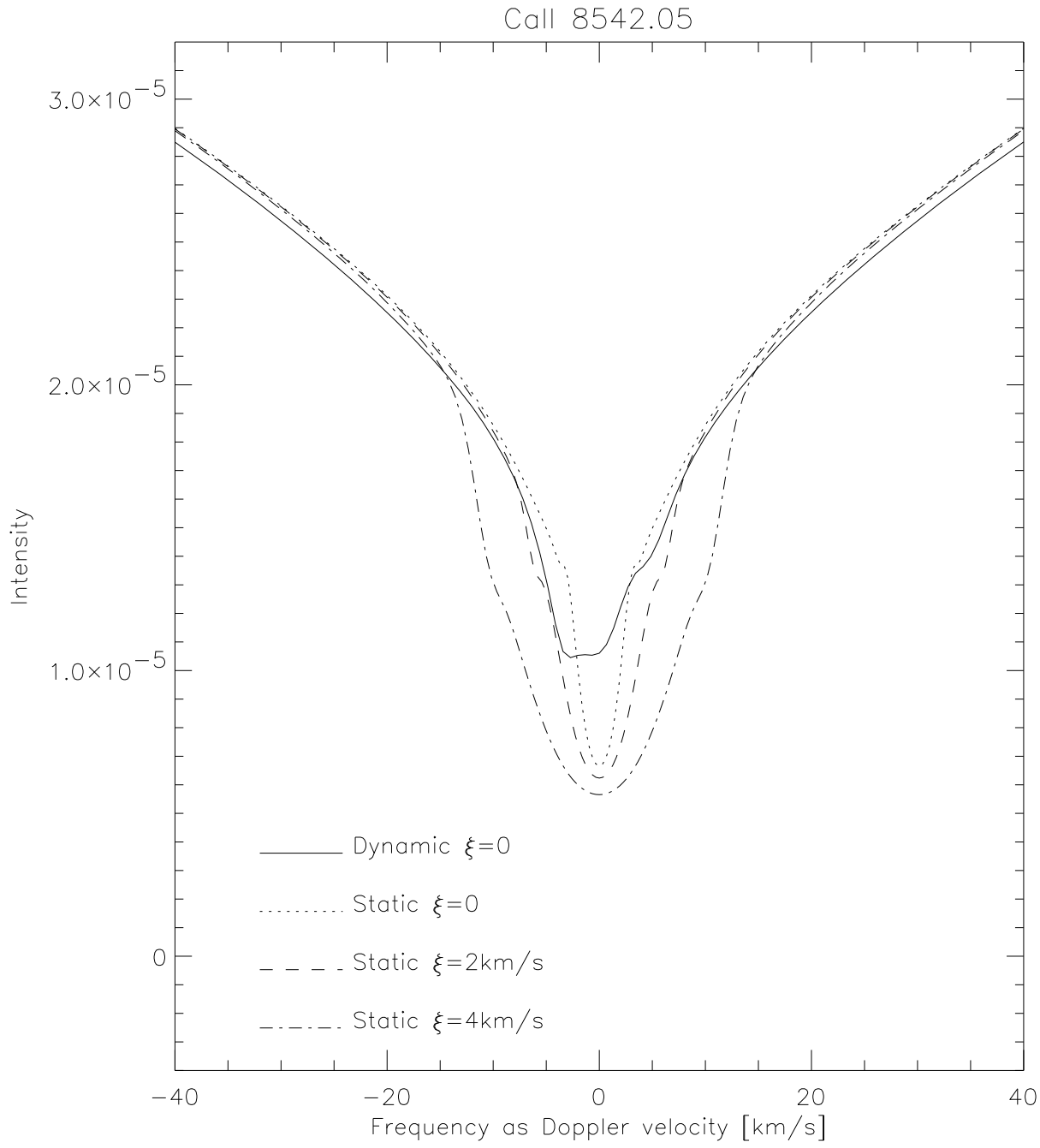

Figure 77: Time averaged dynamic 8542-line for zero microturbulence (solid) compared to the static profiles with 0km/s, 2km/s and 4km/s depth independent microturbulence. Blueshift corresponds to positive velocities.

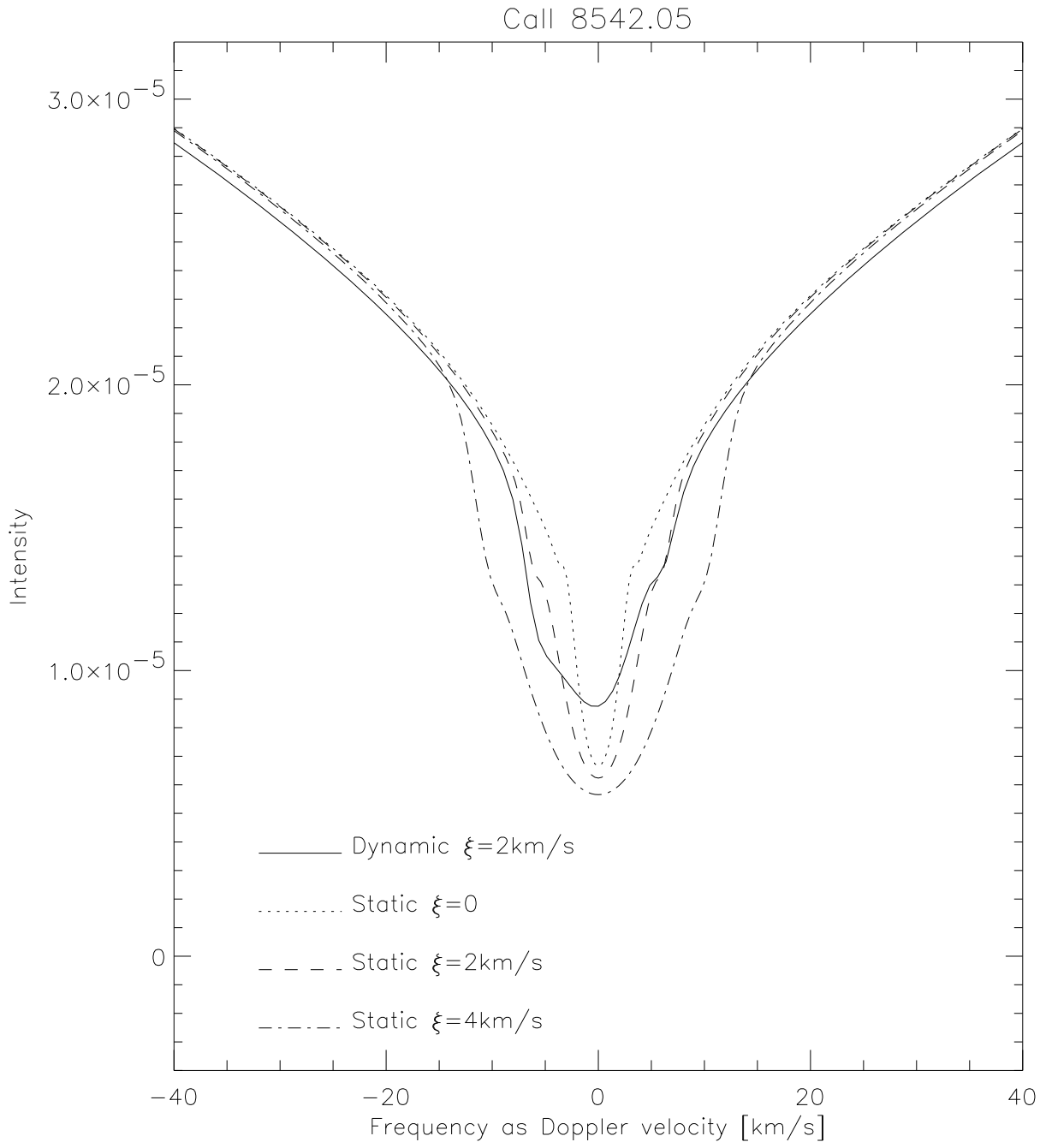

Figure 78: Time averaged dynamic 8542-line for depth independent microturbulence of 2 km/s (solid) compared to the static profiles with 0km/s, 2km/s and 4km/s depth independent microturbulence. Blueshift corresponds to positive velocities.

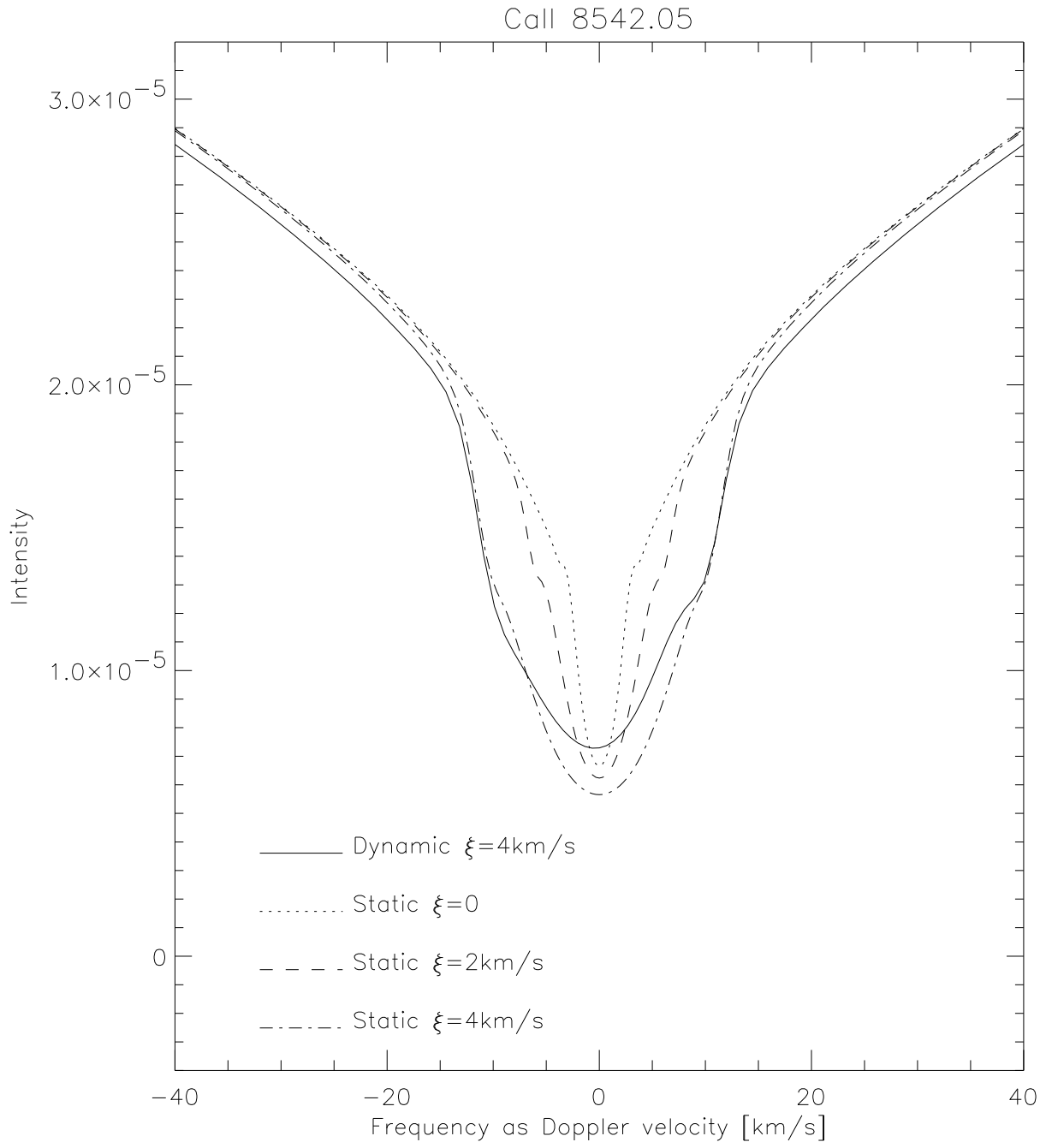

Figure 79: Time averaged dynamic 8542-line for depth independent microturbulence of 4 km/s (solid) compared to the static profiles with 0km/s, 2km/s and 4km/s depth independent microturbulence. Blueshift corresponds to positive velocities.

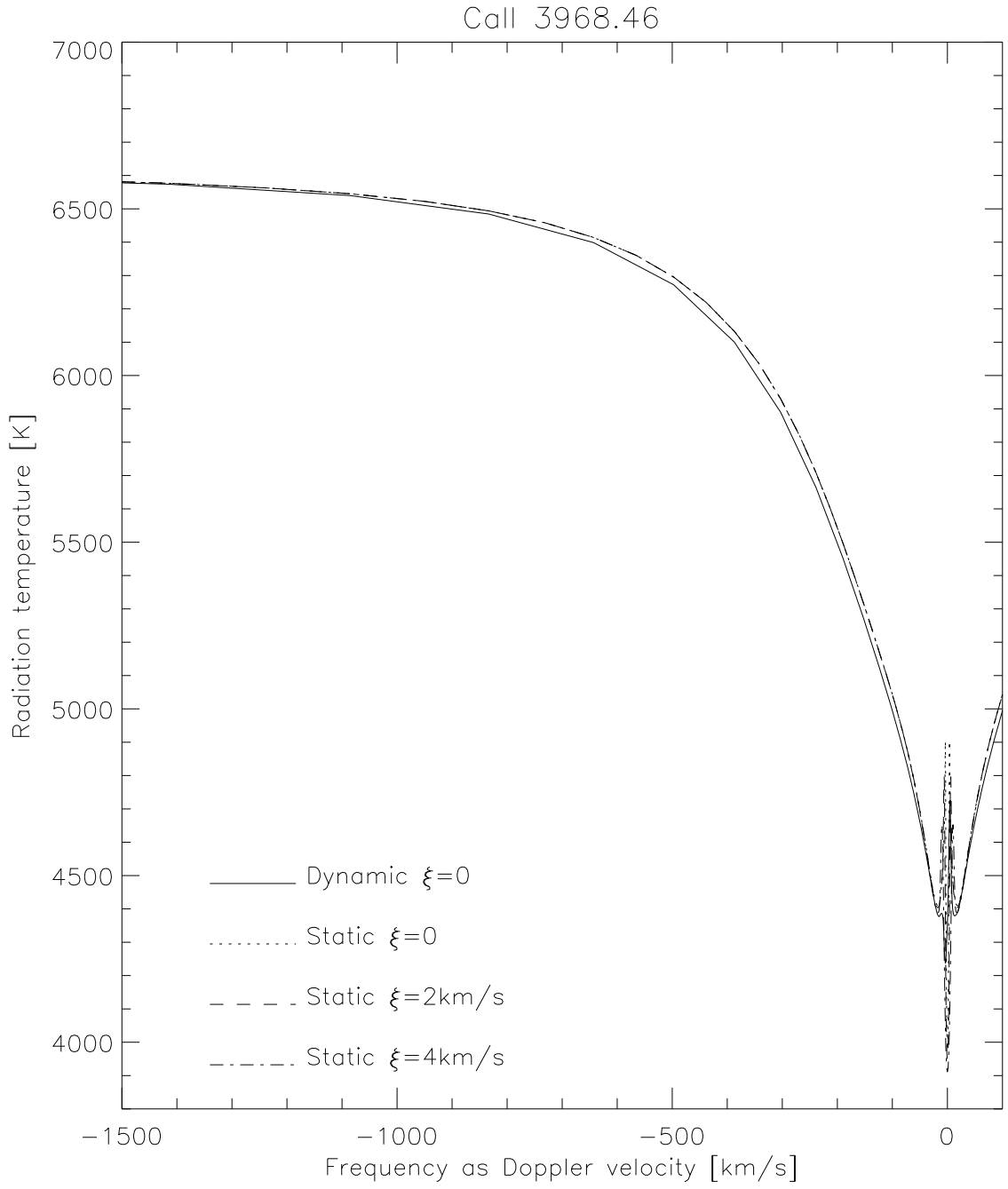

Figure 80: Radiation temperature of the time averaged intensity of the 3968 line with zero microturbulence (solid). The radiation temperature of the time averaged intensity and the corresponding semiempirical value are almost identical at 6580K in the continuum region at -1500km/s. The time averaged profile is wider in the wings than any of the static profiles due to the dynamics. A macroturbulent velocity of 110km/s is needed to obtain correspondence with the time averaged profile in the wing regions outside a frequency displacement corresponding to a Doppler velocity of +/- 300km/s. A satisfactory correspondence can thus not be achieved by using macroturbulence within realistic limits.

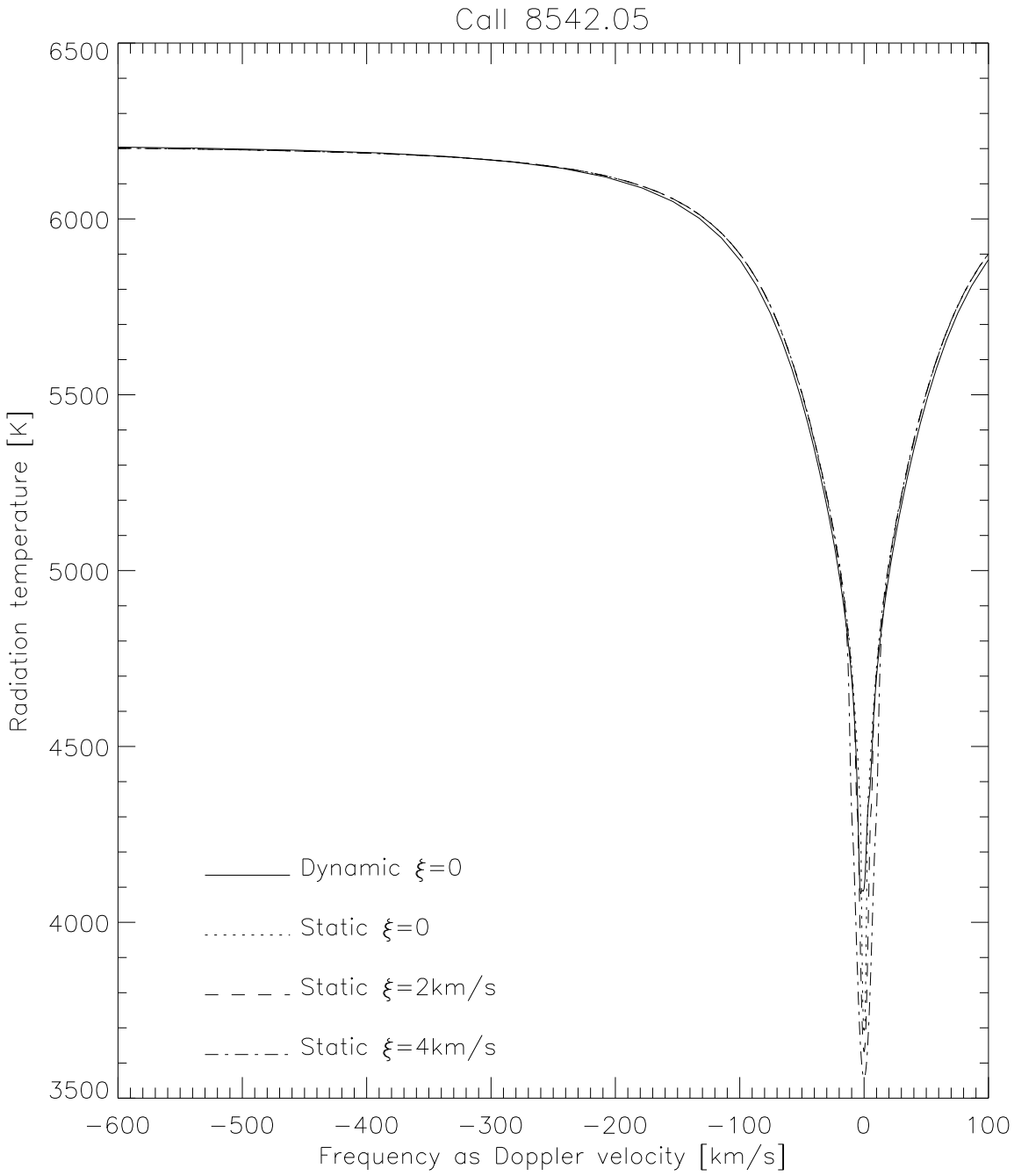

Figure 81: Radiation temperature of the time averaged intensity of the 8542 line with zero microturbulence (solid). The time averaged profile is wider in the wings than any of the static profiles due to the dynamics. The radiation temperature of the time averaged intensity and the corresponding semiempirical value are almost identical at 6200K in the continuum region at -600km/s.

explained in both models in order to reveal the causes of the different behavior.

1. *Static H3 dependence on microturbulence.* The different static profiles can be seen in e.g. figure 74. The contribution functions to intensity and the source functions are shown in figure 82. Increasing microturbulence decreases the line source function due to increased escape probability in the wider opacity profiles. H3 is formed closer to the source function peak due to decreased opacity in the line core. These two effects tend to cancel each other, and the result is that the H3 intensity decreases slightly with increasing microturbulence.

2. *Static H2V dependence on microturbulence.* Wider opacity profiles due to increased microturbulence increase the opacity in the line wings. A higher frequency is thus needed in order to reach unity optical depth at the source function peak. This causes a bright grain location further from the line center, and a wider bright grain.

   The gradients in monochromatic optical depth or equivalently the opacity levels at the H2V frequencies at the source function peaks are approximately the same due to the different frequency displacement. The H2V intensity will then mainly be dependent on the value of the source function which is again dependent on the escape probability. The variation in H2V intensity will therefore be greater than the variation in H3 intensity.

3. *Dynamic H3 dependence on microturbulence.* The intensities at H3 in the time averaged profiles show a decreasing value for increasing microturbulence. The intensities as a function of time at the frequencies of these H3 minima are shown in figure 83. Increasing microturbulence gives an overall lower intensity, but the intensity for zero microturbulence can be less than the intensity for 2km/s and 4km/s microturbulence in short time intervals.

   First, we review the behavior of the contribution function to intensity in order to understand the dynamic intensity formation.

   The centroid of the contribution function to intensity (depth of dominating photon escape) is located approximately at unity optical depth. Increased opacity will increase the altitude of unity optical depth and lead to a location of the centroid at higher altitudes.

   Increased velocity gradient and narrower opacity profiles will increase the opacity gradient along the ray at right angles to the horizontal plane. This leads to a narrower contribution function if a reference scale is considered. Increased opacity levels will increase the value of the contribution function if the source function is held constant.

   A steeper velocity gradient, narrower opacity profiles, and higher opacity levels at the depths of formation will thus lead to higher intensity formed in a relatively small depth interval on the reference optical depth scale.

   A lower opacity gradient will increase the contribution function width. The intensity decreases if the opacity level is too low to compensate for the increased width.

The value of the source function decreases with increasing width of the line wings due to increased escape probability. This is mainly an effect of increased microturbulence in the cases we study here.

Figure 83 shows that the H3 intensity fluctuates between high and low values. At low intensity values (e.g. t=1550s and t=1700s), the formation depths are located in pre-shock regions close to the shock. The source function has a sharp decrease from the local maximum in post-shock regions to relatively low values in pre-shock regions where the intensity is formed. The shock passes the formation depths during the swift transition from low to high intensity. The passage of the shock increases the source function above its local maximum which is now broader. This serves to increase the intensity to the maximum value (e.g. t=1650s).

The intensities at high and low values dominates the time average, and not the swift transitions between. The atmospheric state in these time intervals must therefore be investigated to explain the variation of the time averaged H3 as a function of microturbulence. The formation depths in the relevant time intervals are located at post-shock velocity gradients just above a steepening wave crest or a weak amplitude shock close to the descending part of the source function above its local maximum. The velocity changes from negative values (downward motion) to positive values (upward motion) as a function of height.

The velocity gradient serves to distribute the centers of the opacity profiles at different frequencies, resulting in an inclined "opacity mountain" in the depth frequency plane. Zero microturbulence results in relatively high opacity and opacity gradients at the depths of formation due to narrow opacity profiles, and enhanced source functions due to low escape probability. This leads to a relatively high intensity.

Increasing microturbulence decreases the line center opacity and increases the opacity outside the line core regions. This will broaden the opacity mountain such that the formation height increases at a certain frequency. Increased height of formation will not influence the intensity significantly. The broadening will also serve to decrease the opacity gradients such that the contribution functions widens. Lower opacity at the formation depths and lower source functions due to increased escape probability compensates for wider contribution functions, and the intensity decreases.

The additional effects of decreasing source function and decreasing opacity at the depths of formation with increasing microturbulence, will thus lead in the same direction of decreased intensity. This is due to the influence from wing-opacity close to the line core caused by the velocity gradient. We have thus no cancellation effects here as we have in the static case, in which the line center opacity controls the H3 intensity. The variation of time averaged H3 intensity is then greater than for the static case.

4. *Dynamic H2V dependence on microturbulence.*

Intensity variation. The intensities at H2V in the time averaged profiles show a

decreasing value for increasing microturbulence. The intensities as a function of time at these H2V frequencies are shown in figure 83.

The time intervals of high and low intensity are approximately equal. The time averages are thus mainly controlled by the prominent intensity peaks or bright grains. The intensities for all microturbulent velocities are approximately the same on the rising and falling flanks of the prominent peaks. Increasing microturbulence give lower maximum intensity. The variation of the time averaged H2V intensities as a function of microturbulence is thus mainly set by variation of the maximum intensities.

The maximum intensity is formed in layers where the source function peak is located. The source function is reduced as a function of increased microturbulence due to increased escape probability, as for the static case. The gradient in monochromatic optical depth or equivalently the opacity level at the bright grain frequencies in the grain forming layers is approximately the same due to the frequency displacement, as in the static case. The reduced maximum value of the time dependent intensity as a function of increased microturbulence is thus explained by a reduced source function peak in post-shock regions.

The ratios between the static H2V intensities of different microturbulence are approximately the same as the corresponding ratios between the maximum time dependent H2V intensities. The H2V intensity ratios between the *time averaged profiles* are smaller than for the static profiles. This is explained by the influence from the rising and falling flanks of equal intensity which reduces the ratios of the time averages.

The maximum values of the time dependent H2V intensities are higher than the static H2V intensities. This is explained by higher source function levels caused by the steeper temperature gradient in post-shock regions compared to the gradient of the semiempirical chromospheric temperature rise. The time averaged H2V intensities are lower compared to the static ones. This is explained by the duration of the intensity peaks that is a sufficiently small fraction of the oscillation period.

Displacement and width variation. The H2V displacements relative to the rest center frequency of the time averaged profiles are primarily controlled by the displacement of the bright grains. The position and width of the bright grains is primarily set by the width of the opacity profiles in the post-shock regions, whose variation is controlled by the different microturbulent velocities. Grains with different microturbulence are shown in figures 84-86.

Wider opacity profiles causes an opacity decrease in the line core region and an opacity increase towards the wings. The formation depths close to the core will thus increase, and they will decrease towards the wings. The depth variation of the curves of unity optical depth with increasing frequency will then decrease as can be seen in figures 84-86. This causes a bright grain location further from the line center in order to reach the source function peak, and a wider bright grain. The broadening of the opacity profile causes the same effects for the H2V peaks in the semiempirical model.

The velocities and the velocity gradients at the depths of grain formation are small, and has no significant effect on the position of the bright grains. There is nevertheless small differences of the order of 1 km/s between the static and time averaged H2V position. This can be explained by the small velocities of the outward moving layer associated with the formation depths of the bright grains.

The average frequency displacement from the rest center frequency of the bright grains as a function of microturbulence is shown in figure 87. These frequencies are almost identical to the H2V peaks of the time averaged profile, indicating the dominant influence from the bright grains.

Summary

The cause of the H3 intensity variation in the time averaged profiles and the cause of the static H3 intensity variation as a function of microturbulence are totally different due to the velocity field in the dynamic atmosphere.

The H2V bright grain intensity variation and the static H2V intensity variation as a function of microturbulence can be explained by qualitatively the same processes. This is also the case for the H2V displacement relative to the rest center frequency. The same is true for the time averaged profiles since the bright grains dominate in the time average.

The H2V intensity ratios between time averaged profiles of different microturbulence are smaller than for the static profiles. This is explained by the influence from time intervals of equal bright grain intensity which reduces the ratios between time averaged intensities.

7.5.5 Connections between semiempirical microturbulence and macroscopic dynamics

A better correspondence between semiempirical and time averaged profiles at H3 can be obtained by altering the semiempirical microturbulence. An additional microturbulent contribution will then be introduced in the semiempirical model if the same microturbulence is originally applied in both models. This additional contribution is thus caused by the difference in H3 intensity responses between dynamic and semiempirical models.

It should be noted that the K-line in the semiempirical VAL-model (Vernazza et al. 1981) is used to adjust a height dependent microturbulence. It is likely that an additional microturbulent contribution caused by macroscopic dynamics is present in this case.

7.5.6 Accuracy of the semiempirical line profiles

The chromospheric temperature structure of the semiempirical model could not be determined with high accuracy in the vicinity of $lg(column\ mass) = -4.75$. This corresponds to $lg(\tau_{5000}) = -6$. It is seen from figure 82 that this corresponds to those layers where the source function is decoupled from the Planck distribution (above the local source function maximum). The source function will thus not be very sensitive to the inaccurate temperature here. The source function is close to, and controlled by the Planck function up to

$lg(\tau_{5000}) = -4.5$ which corresponds to $lg(column\ mass) = -2$ where the accuracy of the temperature structure is relatively high.

The intensities in the CaII line core regions are therefore not very sensitive to the temperature uncertainties.

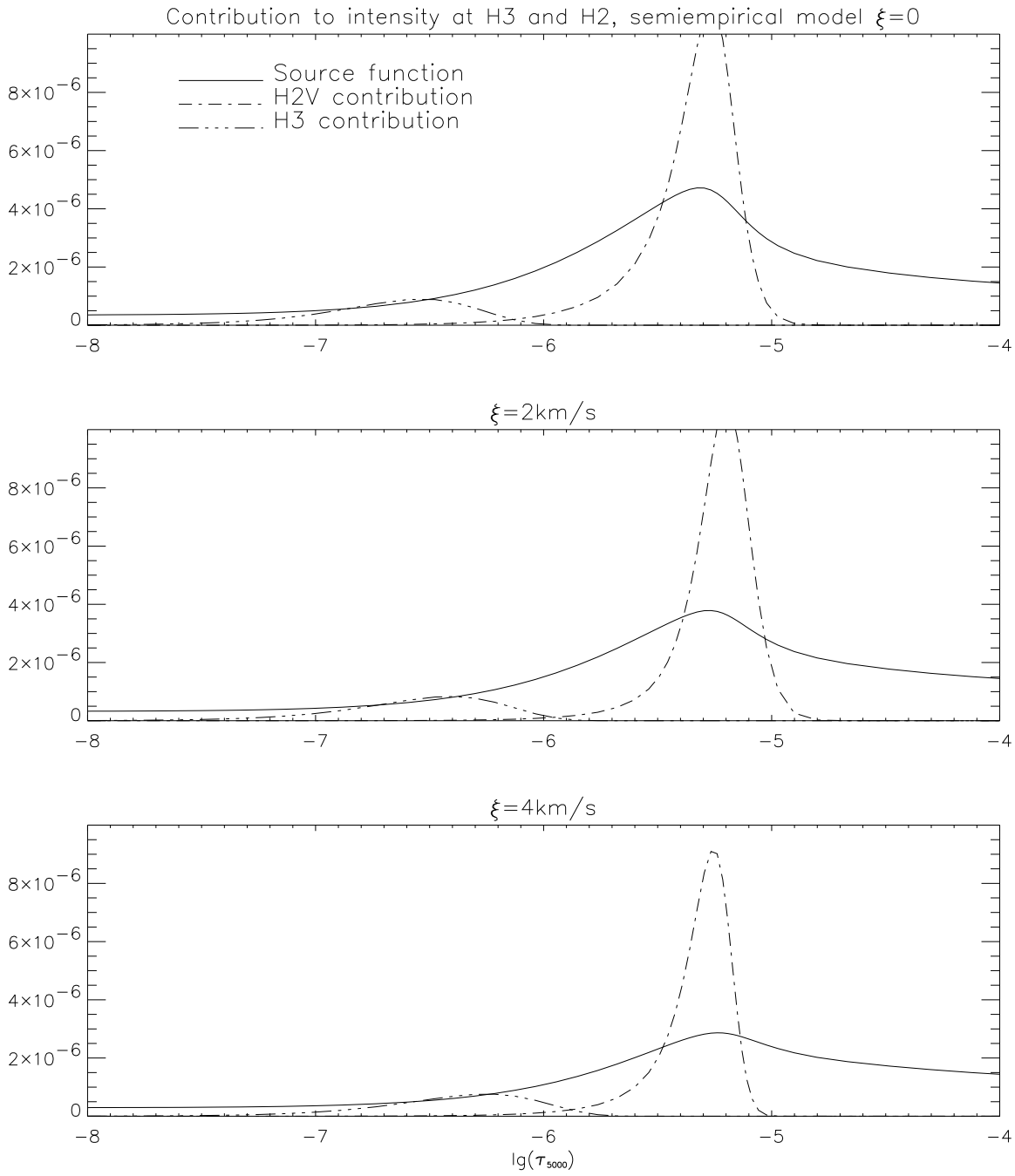

Figure 82: Contribution functions to intensity at H2V and H3 with the three different microturbulent velocities in the semiempirical atmosphere. The line source function is shown in each case. *Upper panel.* Zero microturbulence. *Middle panel.* 2km/s microturbulence. *Lower panel.* 4km/s microturbulence. Increasing microturbulence decreases the line source function due to increased escape probability in the wider opacity profile. H3 is formed closer to the source function peak due to decreased opacity in the line core. This is not enough to compensate for the decreased source function, and the H3 intensity decreases. Decreased source function leads to decreased H2V intensity, but its position in frequency is further from the line core due to increased opacity in the opacity wings.

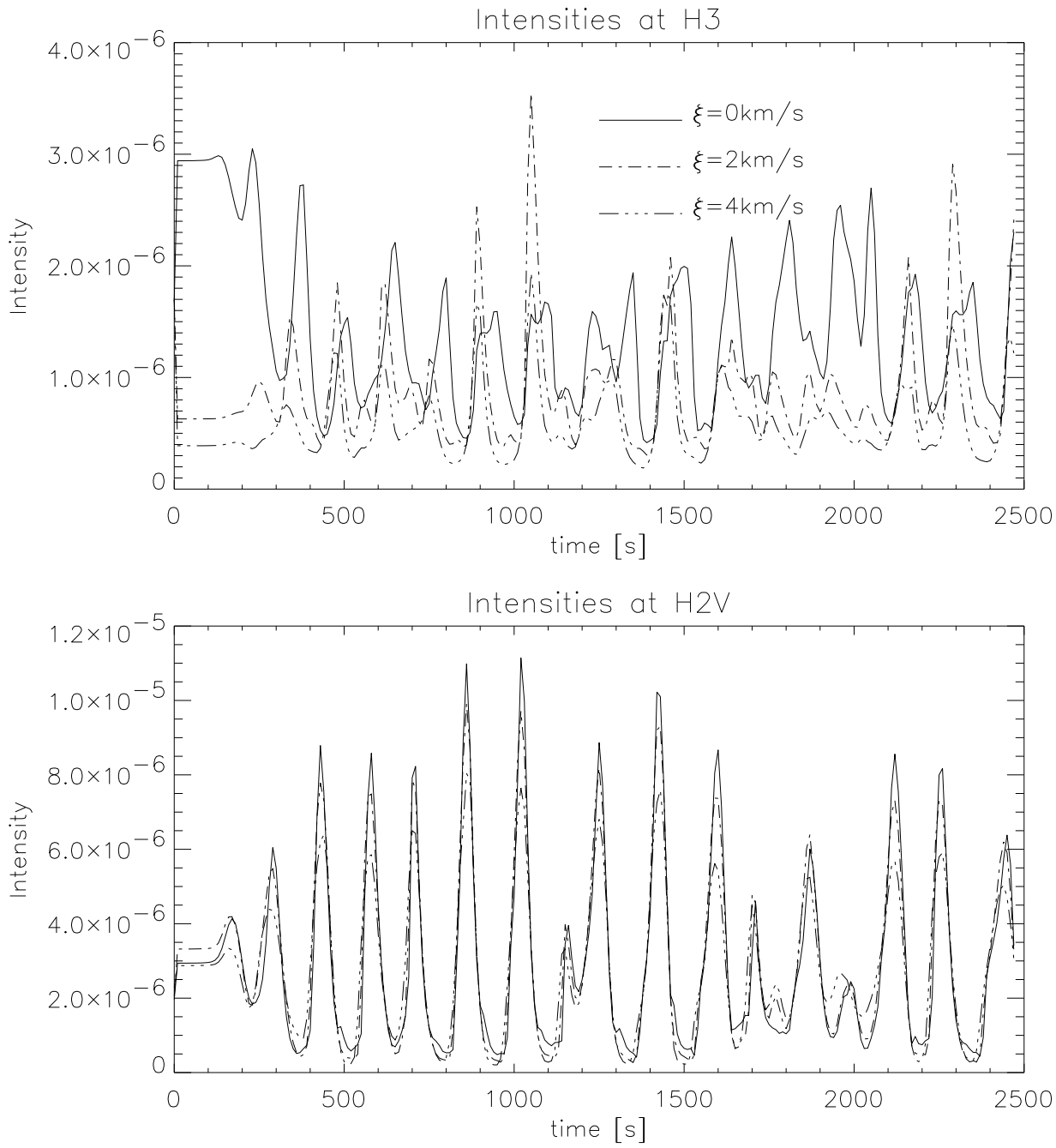

Figure 83: *Upper panel.* Intensities at the frequencies for H3 in the time averaged profiles show a decreasing value for increasing microturbulence. This causes the differences between the time averaged intensities. *Lower panel.* Intensities at the frequencies for H2V in the time averaged profiles show a decreasing value for increasing microturbulence. This causes the differences between the time averaged H2V intensities.

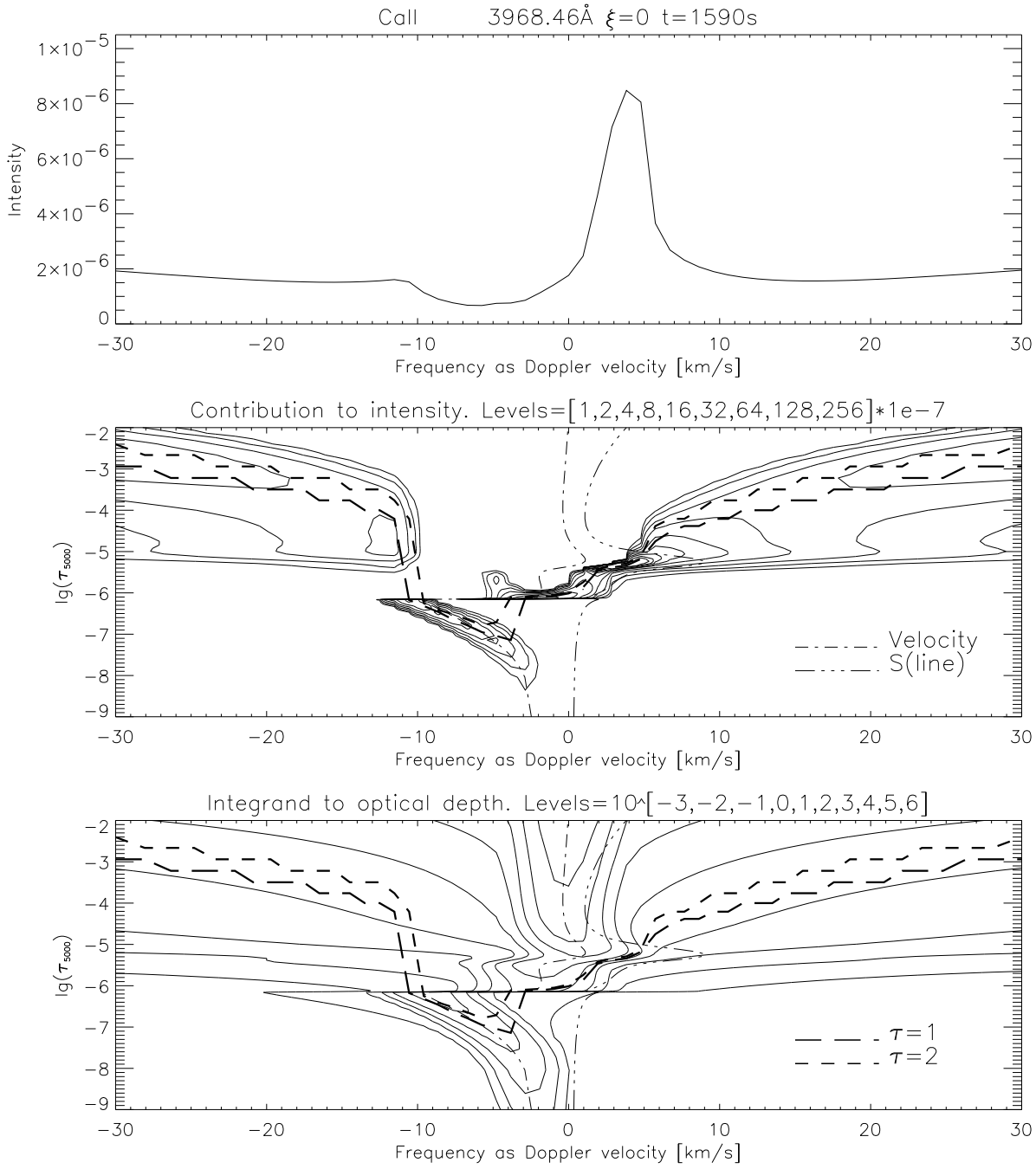

Figure 84: Formation of a bright grain with zero microturbulence. *Upper panel.* Intensity profile in the H-core region. Blueshift corresponds to positive velocities. Frequency is given as the corresponding Doppler-velocity. *Middle panel.* Contribution functions to intensity as a contour plot in the depth-frequency plane. Curves of equal monochromatic optical depth is given together with the velocity and the source function (arbitrary scaled). *Lower panel.* The integrands to monochromatic optical depth on a $lg(\tau_{5000})$ are given to show which layers that controls the curves of equal optical depth. Small spacing between these curves indicates relatively high opacity and high sensitivity to the source function.

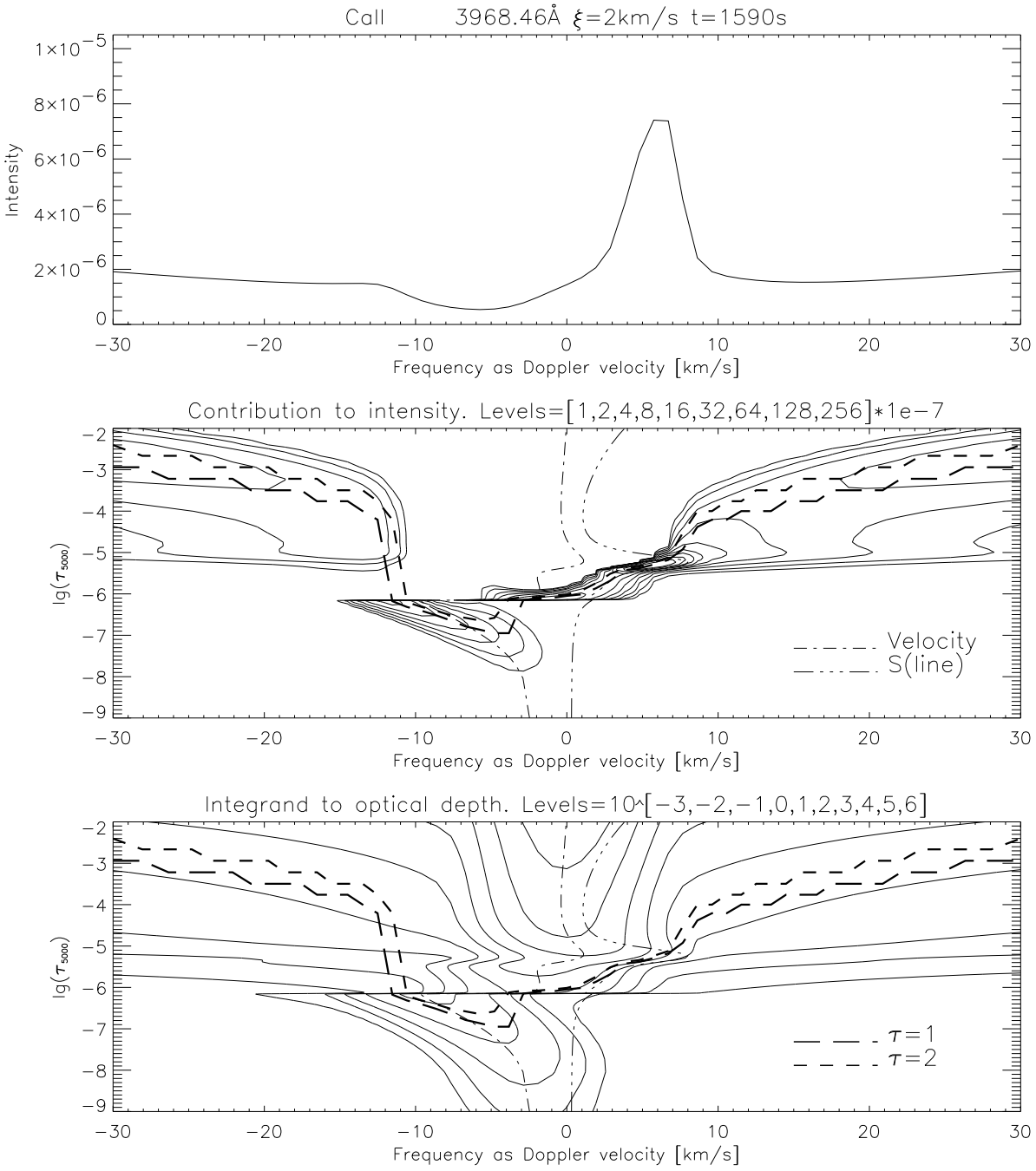

Figure 85: Formation of a bright grain with a microturbulence of 2km/s. *Upper panel.* Intensity profile in the H-core region. Blueshift corresponds to positive velocities. Frequency is given as the corresponding Doppler-velocity. *Middle panel.* Contribution functions to intensity as a contour plot in the depth-frequency plane. Curves of equal monochromatic optical depth is given together with the velocity and the source function (arbitrary scaled). *Lower panel.* The integrands to monochromatic optical depth on a $lg(\tau_{5000})$ are given to show which layers that controls the curves of equal optical depth. Small spacing between these curves indicates relatively high opacity and high sensitivity to the source function.

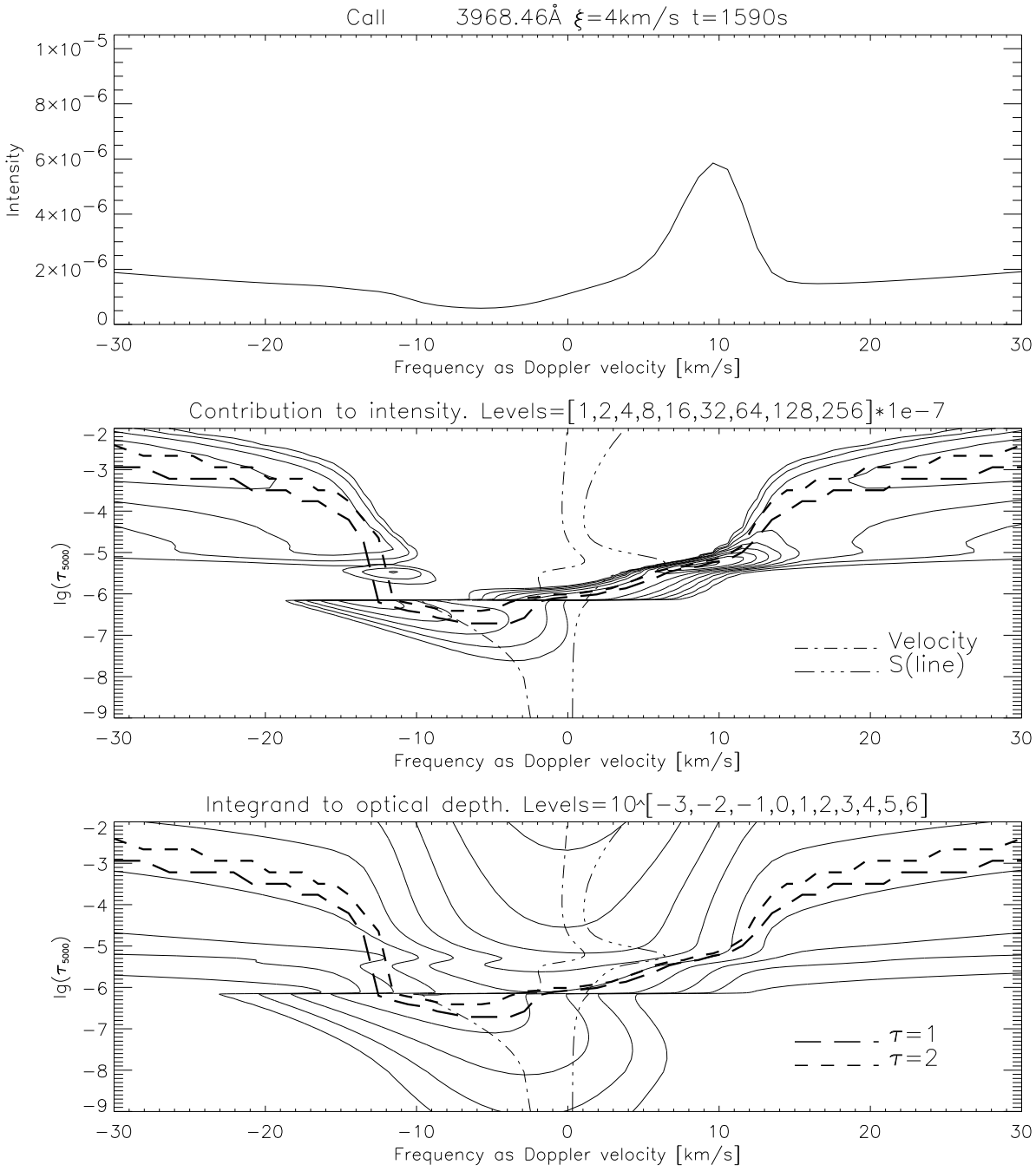

Figure 86: Formation of a bright grain with a microturbulence of 4km/s. *Upper panel.* Intensity profile in the H-core region. Blueshift corresponds to positive velocities. Frequency is given as the corresponding Doppler-velocity. *Middle panel.* Contribution functions to intensity as a contour plot in the depth-frequency plane. Curves of equal monochromatic optical depth is given together with the velocity and the source function (arbitrary scaled). *Lower panel.* The integrands to monochromatic optical depth on a $lg(\tau_{5000})$ are given to show which layers that controls the curves of equal optical depth. Small spacing between these curves indicates relatively high opacity and high sensitivity to the source function.

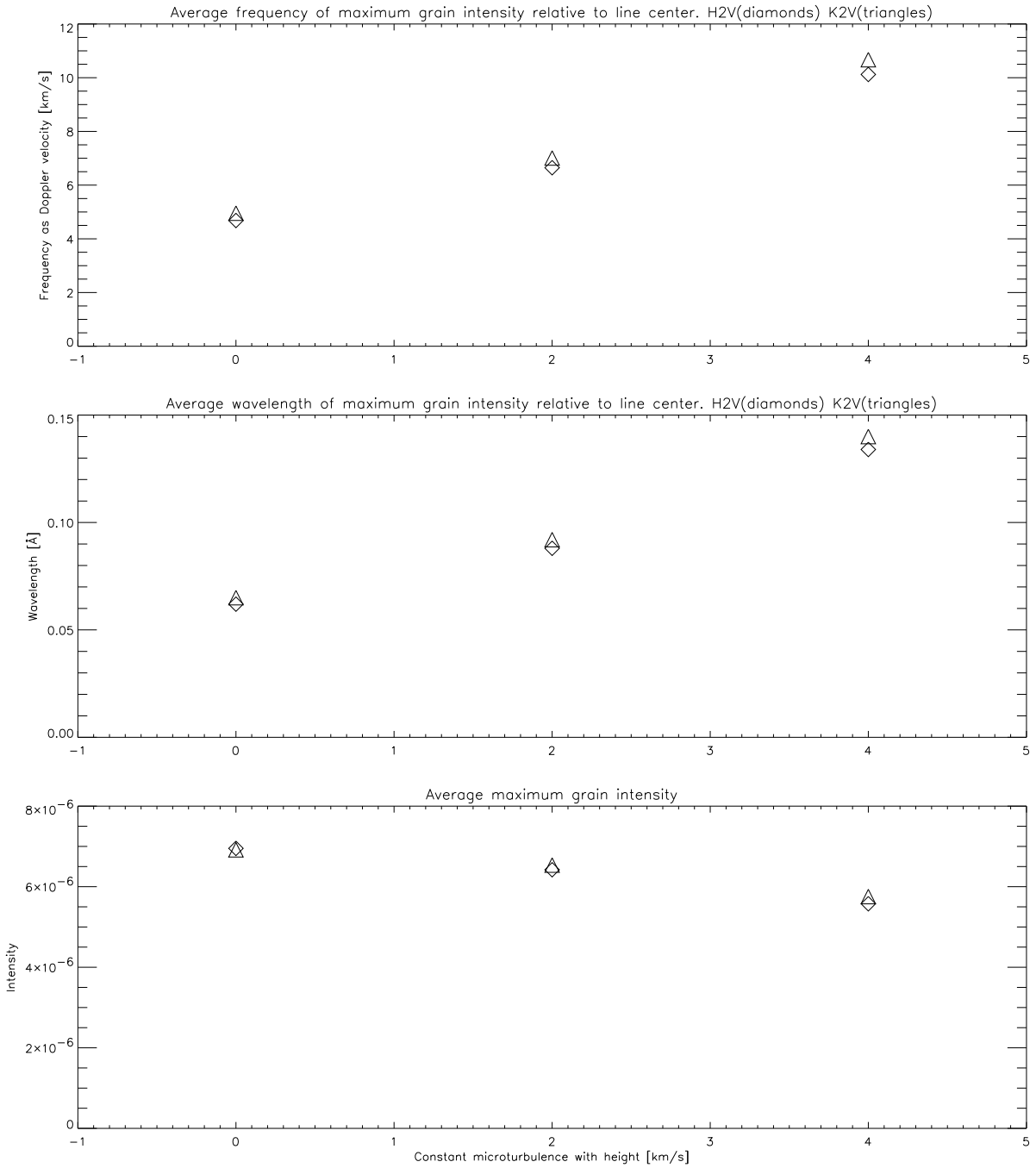

Figure 87: *Upper panel.* Average frequency displacement of H2V and K2V bright grains as a function of microturbulence. *Middle panel.* Average wavelength displacement of H2V and K2V bright grains as a function of microturbulence. *Lower panel.* Average H2V and K2V bright grain intensity as a function of microturbulence. Only the time intervals where the brights grains occurred was considered. A bright grain is defined if the intensity in a specific frequency interval located at the blue side of the line core is above a suitable threshold. The displacements of the peaks are approximately the same as the corresponding quantity for the time averaged profiles.

8 Conclusions

First, we summarize the semiempirical method (section 4) and its properties. Then we consider the results of the acoustically heated model, where we investigate the dynamic energy balance and semiempirical radiative cooling (section 6). Then we conclude about the H2V bright grain formation, the CaII phase relations and the differences between semiempirical and time averaged CaII line profiles of the pre-heated atmosphere (section 7). Finally we make some general considerations about chromospheric heating in connection to the temporal behavior of the CaII lines.

1. *Construction of semiempirical models.*

   We follow the standard method of replacing the equation of radiative equilibrium by a temperature structure that reproduces the averaged continuum spectrum of the dynamic atmosphere. This temperature structure is found by an iterative scheme. Temperature corrections on the previous atmosphere are found by using approximated response functions to radiation temperature. This leads to a multi-dimensional Newton-Raphson method. Several constraints are laid on the solution such that we achieve a smooth temperature structure with one extremal point, the temperature minimum.

   The temperature structure converges to a solution that reproduces the radiation temperatures of the time averaged continuum spectrum within 1%. Typically 5 iterations are needed. The iteration method is quite insensitive to the initial temperature structure.

   The accuracy of the temperature structure is determined on the basis of a typical radiation temperature deviation and the accurate radiation temperature response functions. These accuracy calculations determine the deviation limits of the converged temperature structure.

2. *Dynamic and semiempirical energy balance of acoustic heating.*

   The sources of atmospheric heating are external compression work and viscous dissipation. The terms are caused by shocks in the middle and upper chromosphere, and nonlinear waves in the temperature minimum region and the lower chromosphere. Thermal conduction is negligible compared to these terms. Viscous dissipation and external compression work are approximately of the same magnitude in the middle and upper chromosphere. External compression work is an order of magnitude greater than viscous dissipation in the temperature minimum region and the lower chromosphere.

   The internal energy (the total of thermal energy, exitation energy and ionization energy) increases in the chromosphere during the simulation. The time averaged increase in internal energy has approximately the same magnitude as a function of height as the time averaged radiative cooling. An assumed equality between the heating terms and the radiative cooling will thus be erroneous. This must also be

taken into account in the solar atmosphere at small spatial scales where secular variation in internal energy can be possible.

An internal energy increase indicates that the atmosphere is not in a quasi-static state. Accumulated internal energy will eventually increase the radiative cooling such that a quasi-static state is obtained. This has not been verified by our simulation, since this requires a considerably longer time series.

The semiempirical model contains a chromospheric temperature rise caused by the shock dynamics in these layers. A deviation of typically 1% from the radiation temperature of the reference continuum spectrum is obtained by the semiempirical model. The radiative cooling rates in the dynamic model can then be compared to the semiempirical cooling rates. Hydrogen lines, CaII lines and continua are calculated for both models.

The total semiempirical cooling rate does not deviate more than a factor of two from the time averaged total cooling rate in the middle and upper chromosphere. The deviation is approximately a factor of ten in the temperature minimum region and lower chromosphere.

The semiempirical cooling rate can thus at best be used to estimate the total dynamic radiative cooling in the middle and upper chromosphere, but not in the temperature minimum region and lower chromosphere.

The cooling rates for hydrogen lines, CaII lines and continua are in general different in the two models. The semiempirical model can thus not be used to estimate the cooling distribution among the different contributors in the dynamic model.

Future simulations should be extended such that the energy balance in the quasi-static state of the acoustically heated model can be studied.

3. *H2V bright grain formation.*

The time evolution of the simulated H-line profile agrees very well with the observed behavior when a heating term similar to the VAL3C heating is added to the energy equation. This term is held constant on a column mass scale during the simulation, and we denote this model by the pre-heated model.

We reproduce the "dark whisker" contraction in the wings, the H2V and the K2V bright grains, the Doppler excursions in the line core, the H2V/H2R asymmetry, and the pulsation period close to 3 minutes. The main difference between the observed and simulated profiles is that we get one bright grain almost every 3 minutes contrary to the observed pattern that show an irregular bright grain occurrence.

We study the atmospheric properties during the time of H2V grain formation. One situation is considered where the H2R emission peak is present, and one where it is absent.

We find that the line opacity pattern as a function of frequency and depth is controlled by the atmospheric density and the velocity field. Thermal broadening plays a minor role. The line opacity is determined by the lower level population that is

approximately equal to the CaII density, which in turn is proportional to the total density. NLTE effects are thus not important in controlling the line opacity. Velocity differences of typically 5-10 km/s between pre- and post shock regions have a significant impact on the opacity pattern that controls the bright grain formation.

The grain-forming parts of the source function is controlled by the destruction probability set by the post-shock temperatures, and the escape probability set by the opacity pattern. The source function increases with increasing temperatures behind the shock front if the destruction probability is greater than the escape probability. The escape probability exceeds the destruction probability close to the shock front, and this leads to a decreasing source function as a function of height. A source function peak is thus created. The increase of the escape probability is controlled by the increased escape probability at the blue side of the Doppler core. This occurs by a combined effect of upward motion in post-shock regions, and downward motion in pre-shock regions.

The layers of the atmosphere that contribute most to the emergent intensity are those where the optical depth is approximately unity. This corresponds to one photon mean free path from the upper boundary. The intensity level is increased if the value of the source function is increased or if the opacity is increased in these layers.

The H2V intensity originates in layers of upward motion with relatively small velocity (1-2km/s) in post-shock regions where the source function is peaked. High post-shock density leads to high opacity. These two effects produces the prominent H2V intensity peak. A steep velocity gradient in the post-shock layer widens the emission peak, and the velocity values influence the H2V displacement from the line core. An additional displacement equivalent to 1-2km/s is caused by upward motion in the post-shock region.

Downward motion in pre-shock regions (typically 5-10km/s) provides redshifted opacity profiles. Unity optical depth will reach the depths of the source function peak in the post-shock region at the H2R frequency on the red side of the line core. The opacity here will be smaller compared to corresponding H2V opacity due to the blueshift of the post-shock opacity profiles relative to the pre-shock opacity profiles. This is the reason for the H2V/H2R asymmetry.

Higher velocity differences leads to higher relative blueshift of the post-shock opacity profile and a greater H2V/H2R asymmetry occurs. The H2R peak is thus absent if a high amplitude shock (typically 10km/s) is responsible for the grain formation. Both peaks are formed when a low amplitude shock (typically 5km/s) is responsible for the grain formation. It must be noted that these findings are only sufficient and not necessary for grain formation since we have considered only one dynamic model.

The shock structure is controlled by the radiation-hydrodynamics of hydrogen, the additional heating term, and the velocity field of the lower boundary piston, or equivalently the convective motions of the lower photosphere.

The intensities and frequency displacements of the H2V and H2R grains are promising diagnostics in determining chromospheric shock structure. Future simulations should

be carried out to determine the variation of these quantities as a function of shock strength, pre-heating and lower boundary velocity spectrum.

4. *CaII phase relations.*

   The pre-heated dynamic model is used to study the phase relations between the CaII line core Doppler-shifts and intensities in the Fourier-domain. We use the pre-heated model since the simulated line core fluctuations agree very well with observations.

   We investigate the applicability of linear theory of velocity phase differences of acoustic-gravity waves in an isothermal atmosphere to predict height differences in a dynamic atmosphere. We are only able to study vertical propagation since our model is plane-parallel.

   By measurements of atmospheric velocities at fixed heights, we find that the linear theory becomes inaccurate 500km above $\tau_{5000} = 1$. This is explained by non-linear wave steepening, where high density parts of the waves overtake the low density parts. Linear theory can not be applied above 1000km where shocks are formed. We find that linear theory can predict height differences up to 1000km within 10% deviation from the actual height differences. The predicted height differences are up to 50% less than the actual height differences above 1200km, where the shocks are fully developed.

   We are able to reproduce the simulated Doppler-fluctuations by using the contribution function to relative absorption as a velocity response function. The mean velocity response heights fluctuate several hundred kilometers on time scales equal to the fundamental 3 minute pulsation period of the chromosphere. The mean velocity response heights for the H and K lines vary between 1300km and 2000km due to ballistic motion between short moments of upward acceleration caused by shocks. The mean velocity response heights for the three infrared lines vary between 500km and 1400km. This is in the height range of non-linear wave steepening and shock formation. The 8498-line core contains an emission peak, such that a reliable Doppler-shift signal can not be obtained.

   Wave modes or differences in heights of formation between the CaII lines in the solar chromosphere are commonly determined by using observed Doppler-shift phase relations in the CaII line cores. It is common to use linear theory for velocity phase differences, and to assume fixed velocity response heights in the interpretation of the phase relations. These assumptions have lead to conclusions such as standing waves in the solar chromosphere on the basis of observed V-V and V-I CaII phase relations.

   Our findings of inaccurate linear theory above 500km, the invalidity of it above 1000km, and dynamic velocity response heights, indicate that such interpretations of observed CaII phase relations will be erroneous.

   Simulated V-V and V-I phase relations, phase coherence, intensity- and velocity power spectra are compared with solar observations. We find that the phase relations agree very well with the observed values of internetwork regions. We thus feel justified to say that our dynamic model is a reasonable description of chromospheric dynamics.

We explain the V-I and V-V phase relations by propagating acoustic waves that steepen into radiating shocks at approximately 1000km, in contradiction to the proposed standing waves.

NLTE effects caused by scattering are important for the formation of the line core intensities. These intensities can therefore not be associated with local chromospheric temperatures. Velocity-intensity relations should therefore not be interpreted as velocity-temperature relations in attempts to explain the wave-modes.

The CaII phase relations are promising candidates as diagnostic tools to determine chromospheric dynamics.

5. *Differences between averaged CaII line profiles of the dynamic model and semiempirical line profiles.*

   Time averages of the core regions of the H line and the 8542 line are asymmetric with respect to the rest center frequency. This asymmetry is a direct evidence of non-stochastic atmospheric behavior in which the time dependent thermodynamics is correlated with gas motions. This can not be reproduced by semiempirical models where only random velocity fields (micro-, meso- and macroturbulence) are allowed to account for dynamic effects. These random velocities produce symmetric line profiles.

   It is nevertheless possible to obtain a better semiempirical fit to the time averaged 8542 line core region by applying mesoturbulence in the semiempirical model. A satisfying fit of the core region of the H-line by applying mesoturbulence is impossible due to the strong asymmetric properties.

   Both time averaged lines show increased width in the wing regions compared to the semiempirical profiles. The time averaged wings are also symmetric with respect to the rest center frequency. A satisfactory correspondence between semiempirical profiles and time averaged profiles can not be achieved by using macroturbulence within realistic limits.

   The response to microturbulence is rather different between semiempirical and time averaged line profiles. This is pointed out for the H3 intensities and H2V intensities. The H2V intensity in the semiempirical profile vary more as a function of microturbulence, and it has a higher value than the corresponding time averaged intensity. The H3 intensity in the semiempirical profile vary less as a function of microturbulence, and it has a lower value than the corresponding time averaged intensity.

   The cause of the intensity- and displacement variation of the H2V peak in both semiempirical and time averaged line profiles as a function of microturbulence can be explained by qualitatively the same processes. The cause of the variation of H3 intensity in the semiempirical model as a function of microturbulence is totally different compared to the cause of the corresponding variation in the time averaged profiles due to the velocity gradients in the dynamic atmosphere.

   A better correspondence between semiempirical and time averaged profiles at H3 can be obtained by altering the semiempirical microturbulence. An additional microturbulent contribution will then be introduced in the semiempirical model if the

same microturbulence is originally applied in both models. This additional contribution is thus caused by the difference in H3 intensity responses between dynamic and semiempirical models.

It should be noted that the K-line in the semiempirical VAL-model (Vernazza et al. 1981) is used to adjust a height dependent microturbulence. It is thus likely that an additional microturbulent contribution caused by macroscopic dynamics is present in this case.

6. *Temporal behavior of the CaII lines in connection to chromospheric heating.*

   The temporal behavior of the line profiles is very different for the two dynamic models, and thus very sensitive to chromospheric heating. The acoustically heated model with no additional heating term does not produce any bright grains, and the V-I and V-V phase relations are very different compared to the pre-heated model. Observed phase relations are only comparable to the phase relations of the pre-heated model.

   This suggests that the internal energy of the model chromosphere must exceed a certain threshold in order to reproduce some of the observed behavior. The internal energy of the acoustic model increases during the simulation, but evidently not above this threshold.

   This suggests that H2V grains and phase relations similar to the observed ones can possibly be achieved by an extended simulation of this self-consistently heated model.

   The CaII phase relations are also promising candidates as diagnostic tools to determine the nature and level of chromospheric heating.

9 References

References

Anderson, L. S., Athay, R. G. 1989, ApJ, 336, 1089

Bashkin, S., Stoner, J. O. 1975, Atomic Energy Levels and Grotrian Diagrams, North-Holland Publ. Co., Amsterdam

Biermann, L. 1946, Naturwiss., 33, 118

Carlsson, M. 1986, A Computer Program for Solving Multi-Level Non-LTE Radiative Transfer Problems in Moving or Static Atmospheres, Report No. 33, Uppsala Astronomical Observatory

Carlsson, M., Scharmer, G. B. 1985, in B. W. Lites (ed.), Chromospheric Diagnostics and Modeling, National Solar Observatory Summer Conference, Sacramento Peak Observatory, Sunspot, New Mexico, p. 137

Carlsson, M., Stein, R. 1992a, ApJ, 397, L59

Carlsson, M., Stein, R. F. 1992b, ApJ Let, 397, L59

Cram, L. E., Damé, L. 1983, ApJ, 272, 355

Deubner, F.-L., Fleck, B. 1990, A&A, 228, 506

Dorfi, E. A., Drury, L. O. 1987, J. Comput. Phys., 69, 175

Edmonds, F. N., Webb, C. J. 1972, Solar Phys., 22, 276

Fleck, B., Deubner, F.-L. 1989, A&A, 224, 245

Fontenla, J. M., Avrett, E. H., Loeser, R. 1993, ApJ, 406, 319

Frisch, U., Frisch, H. 1975, M.N.R.A.S, 173, 167

Hale, G. E., Ellerman, F. 1904, ApJ, 19, 41

Ivanov, V. V. 1973, Transfer of Radiation in Spectral Lines, English Language Edition of Radiative Transfer and the Spectra of Celestial Bodies, Special Publication 385, National Bureau of Standards, Washington

Johnson, L. C. 1972, ApJ, 174, 227

Kalkofen, W. (ed.) 1984, Methods in Radiative Transfer, Cambridge University Press, Cambridge, Great Britain

Karzas, W. J., Latter, R. 1961, ApJS, 6, 167

Kulaczewski, J. 1992, A&A, 261, 602

Lites, B. W., Rutten, R. J., Kalkofen, W. 1993, ApJ, 414, 345

Liu, S.-Y. 1974, ApJ, 189, 359

Magain, P. 1986, A&A, 163, 135

Mein, N., Mein, P. 1980, A&A, 84, 96

Menzel, D., Pekeris, C. 1935, MNRAS, 96, 77

Mihalas, D. 1978, Stellar Atmospheres, W. H. Freeman and Co., San Francisco (second edition)

Mihalas, D., Mihalas, B. W. 1984, Foundations of Radiation Hydrodynamics, Oxford University Press, New York

Milkey, R. W., Mihalas, D. 1973, ApJ, 185, 709

Provost, J., Mein, N. 1979, Solar Phys., 64, 43

Rammacher, W., Ulmschneider, P. 1992, A&A, 253, 586
Rutten, R. J., Uitenbroek, H. 1991, Solar Phys., 134, 15
Scharmer, G. B. 1981, ApJ, 249, 720
Scharmer, G. B., Carlsson, M. 1985, J. Comput. Phys., 59, 56
Schwarzschild, M. 1948, ApJ, 107, 1
Shine, R. A., Linsky, J. L. 1972, Solar Phys., 25, 357
Stein, R. F., Schwartz, R. A. 1972, ApJ, 177, 807
Vernazza, J. E., Avrett, E. H., Loeser, R. 1981, ApJS, 45, 635
Vriens, L., Smeets, A. H. M. 1980, Phys. Rev. A, 22, 940

10 Appendix

10.1 The RADYN equations

The RADYN radiation-hydrodynamics code is constructed by Mats Carlsson and Robert F. Stein. Only the results from the RADYN simulations are studied in this thesis. The equations from Carlsson and Stein are thus given for the sake of completeness.

In the chromosphere we can not assume LTE. The population densities can thus not be obtained with the Boltzmann and Saha equations — the full rate equations will have to be solved. Due to the dominance of radiative terms and optically thick lines these equations will contain non-local terms.

It is assumed that the velocity distribution is Maxwellian with the same temperature, T, for all particles. A single fluid description is adopted with a mass density ρ and bulk velocity v.

To make the problem tractable we have to assume a one dimensional geometry. A plane-parallel geometry is assumed with horizontal homogeneity.

The equations to be solved are in Eulerian coordinates:

$$\frac{\partial \rho}{\partial t} + \frac{\partial}{\partial z}(\rho v) = 0 \tag{77}$$

$$\rho \frac{\partial v}{\partial t} + \rho v \frac{\partial v}{\partial z} = -\frac{\partial}{\partial z}(p + Q) - \rho g \tag{78}$$

$$\frac{\partial}{\partial t}(\rho e) + \frac{\partial}{\partial z}(\rho v e) + (p + Q)\frac{\partial u}{\partial z} = \frac{\partial}{\partial z}(F_c + F_r + F_h) \tag{79}$$

$$\sum_k n_{ik} I_{ik} + n_H n_e^{met}(T, n_e) - n_e = 0 \tag{80}$$

$$\frac{\partial n_{ik}}{\partial t} + \frac{\partial}{\partial z}(n_{ik} v) = \sum_{j \neq i}(n_{jk} P_{jik} - n_{ik} P_{ijk}) \tag{81}$$

$$\sum_i n_{ik} = A_k n_H \tag{82}$$

These equations describe respectively the conservation of mass, momentum, energy, charge, the transitional rates, and the conservation of particles.

p is the gas pressure (radiation pressure is thus neglected), Q is the viscous pressure, g is the acceleration of gravity, e is the internal energy, F_c is the conductive flux, F_r is the radiative flux, $\frac{\partial}{\partial z}F_h$ is any additional heating required to give a specific stationary temperature distribution, n_{ik} is the population density of energy level i of element k, I_{ik} is the ionization degree of energy level i of element k (0 for neutral, 1 for single ionized etc), n_H is the population density of hydrogen nuclei, $n_e^{met}(T, n_e)$ is the number of electrons per hydrogen nucleus as a function of temperature and electron density from elements not solved for explicitly, n_e is the electron density, P_{ijk} is the probability of a transition from

energy level i to energy level j in element k and A_k is the abundance of element k on a scale where the abundance of hydrogen is 1.

The internal energy, e, is calculated as the sum of the thermal energy, the ionization energy and the excitation energy. $n_e^{met}(T, n_e)$ is a pre-tabulated function calculated under the assumption of LTE.

The conductive flux, F_c, is calculated according to Spitzer (1962) as

$$F_c = -\kappa_0 T^{\frac{5}{2}} dT/dz. \tag{83}$$

This may not be a good approximation for chromospheric conditions but this term is of little importance at these low temperatures.

The radiative flux divergence is given by

$$\frac{\partial}{\partial z} F_r = -\int\int \chi_{\nu\mu}(I_{\nu\mu} - S_{\nu\mu}) d\nu d\mu \tag{84}$$

where $\chi_{\nu\mu}$ is the extinction coefficient of the matter, $I_{\nu\mu}$ is the specific intensity and $S_{\nu\mu}$ is the source function.

The specific intensity is related to the extinction and the emissivity, $\eta_{\nu\mu}$, through the equation of radiative transfer:

$$\mu \frac{dI_{\nu\mu}}{dz} = -\chi_{\nu\mu} I_{\nu\mu} + \eta_{\nu\mu} \tag{85}$$

The probabilities P_{ijk} can be written as

$$P_{ijk} = R_{ijk} + C_{ijk} \tag{86}$$

where R_{ijk} is the contribution from radiative transitions and C_{ijk} is the contribution from collisions with other particles. The main problem of solving non-LTE problems comes from the radiative transitions, the probabilities of which may be written as

$$R_{ijk} = \begin{cases} \frac{1}{2} \int_{-1}^{1} \int_{0}^{\infty} \frac{4\pi}{h\nu} \alpha_{jik} G_{jik} (I_{\nu\mu} + \frac{2h\nu^3}{c^2}) d\nu d\mu, & \text{if } i > j; \\ \frac{1}{2} \int_{-1}^{1} \int_{0}^{\infty} \frac{4\pi}{h\nu} \alpha_{ijk} I_{\nu\mu} d\nu d\mu, & \text{if } i < j. \end{cases} \tag{87}$$

The expressions for α_{ijk} and G_{ijk} are for bound-bound and bound-free transitions given by:

$$\alpha_{ijk} = \begin{cases} B_{ijk} \frac{h\nu_{ijk}}{4\pi} \phi_{\nu\mu} & \text{(b-b);} \\ \alpha_c(\nu) & \text{(b-f).} \end{cases} \tag{88}$$

$$G_{ijk} = \begin{cases} g_{ik}/g_{jk} & \text{(b-b);} \\ \frac{n_{ik}^*}{n_{jk}^*} e^{\frac{-h\nu}{kT}} & \text{(b-f).} \end{cases} \tag{89}$$

In these equations B_{ijk} is the Einstein coefficient of stimulated emission ($i > j$) and absorption ($i < j$) respectively. $\phi_{\nu\mu}$ is the normalized absorption profile, $\alpha_c(\nu)$ is the bound-free absorption cross-section at frequency ν, g_{ik} and g_{jk} are the statistical weights

and $n^\star_{ik}$ and $n^\star_{jk}$ are the LTE-populations of the two levels. To simplify the notation, the frequency and angle dependencies of α_{ijk} and G_{ijk} are not included in the notation. Note that α_{ijk} is frequency dependent in the bound-free case and both frequency and angle dependent in the bound-bound case ($\phi_{\nu\mu}$ is angle dependent in the observers frame when the velocity-field is non-zero). Note also that G_{ijk} is frequency dependent in the bound-free case.

In the case of complete redistribution, the extinction coefficient $\chi_{\nu\mu}$ and emission coefficient $\eta_{\nu\mu}$ can be written as:

$$\chi_{\nu\mu} = \chi_{\nu c} + \alpha_{ijk}(n_{ik} - G_{ijk}n_{jk}) \tag{90}$$

and

$$\eta_{\nu\mu} = \eta_{\nu c} + \frac{2h\nu^3}{c^2} G_{ijk}\alpha_{ijk}n_{jk}. \tag{91}$$

In these equations $\chi_{\nu c}$ and $\eta_{\nu c}$ are the background opacities and emissivities.

The source function is defined as:

$$S_{\nu\mu} = \eta_{\nu\mu}/\chi_{\nu\mu}. \tag{92}$$

10.2 The SEMI users guide

SEMI is an iterative program that produces a semiempirical stellar atmosphere from observed continuum intensities. The code is implemented in IDL (interactive data language). SEMI uses the NLTE radiation transport solver MULTI (Carlsson 1986) in hydrostatic equilibrium mode. Hydrogen is calculated in NLTE, and the background opacities are calculated in LTE. It is assumed that the user is familiar with the description of MULTI given in Carlsson (1986). The code is available upon request from the author.

INITIALIZATIONS:

These steps are done manually with external procedures separated from the SEMI program:

*Save the reference radiation temperature as TRADIMEAN.DAT

*Make a depth scale file DSCALE that covers the contribution functions in the final atmosphere. This is obtained by trial and errors by using MULTI, the DSCALE2 file and iteration trials with SEMI.

Name of the DSCALE file for usage in SEMI:

dscale.h_semi_XXX XXX=identification number of the atmosphere.

*Make an initial temperature structure to be used in the semiempirical iteration procedure by using MAKE_INIT_ATM. The chromospheric part is parametrized such that the temperature increases as a function of height. The photospheric temperatures, the hydrogen population numbers, electron densities and population numbers are taken from e.g. the initial dynamic model, or a radiative equilibrium model. All of the quantities are interpolated to the DSCALE depth grid.

Name of the atmosphere:

atmos.semi_XXX.000

*Run the initial atmosphere with MULTI in HSE mode by using a suitable batch-file. Continuum frequency points are included in the hydrogen atom file. The resulting files should be named:

1. athse.semi_XXX_000 ;HSE integrated atmosphere.
2. idl1.h_semi_XXX_000 ;Atmospheric quantities, and emergent intensities.
3. idlcnt.h_semi_XXX_000 ;Contribution functions.

*Make a monotone temperature structure as a reference temperature for polynomial fits. Use MAKE_REFERENCE that takes the initial semiempirical structure a basis. The user makes a monotone decreasing temperature structure as a function of height that has smaller values than the initial one in the chromosphere. This temperature structure is saved as REFERENCET.DAT.

SEMI ITERATION STEPS:

These steps are done automatically by SEMI:

*Read the input files:

athse.semi_XXX_n idl1.h_semi_XXX_n idlcnt.h_semi_XXX_n

n is the iteration number.

*Calculate the approximate operator from the response matrix and solve the equations for temperature corrections by using the deviation from TRADIMEAN.DAT.

*Make new atmosphere atmos.semi_XXX_n+1 by correcting athse.semi_XXX_n.

*Use MULTI to produce:

athse.semi_XXX_n+1 idl1.h_semi_XXX_n+1 idlcnt.h_semi_XXX_n+1

*Present the results graphically

*Terminate the process if the user wishes, if not read input files once again. The user determines the convergence criterion.

SECONDARY CALCULATIONS:

*athse.semi_XXX_n+1 is the final semiempirical atmosphere. Use this in further MULTI calculations to produce spectral lines of other atoms than hydrogen.